ELECTRICAL PROPERTIES OF AMORPHOUS SELENIUM BASED PHOTOCONDUCTIVE DEVICES FOR APPLICATION IN X-RAY IMAGE DETECTORS

A Thesis
Submitted to the College of Graduate Studies and Research
in Partial Fulfillment of the Requirements
for the degree of
Doctor of Philosophy
in the Department of Electrical and Computer Engineering
University of Saskatchewan
Saskatoon, SK, Canada
by

GUEORGUI STOEV BELEV
Saskatoon, Saskatchewan

COPYRIGHT

Head of the Department of Electrical and Computer Engineering
Engineering Building, 57 Campus Dr
University of Saskatchewan
Saskatoon, SK, S7N 5A9
Canada

ABSTRACT

In the last 10-15 years there has been a renewed interest in amorphous Se (a-Se) and its alloys due to their application as photoconductor materials in the new fully digital direct conversion flat panel x-ray medical image detectors. For a number of reasons, the a-Se photoconductor layer in such x-ray detectors has to be operated at very high electric fields (up to 10 V μm^{-1}) and one of the most difficult problems related to such applications of a-Se is the problem of the dark current (the current in the absence of any radiation) minimization in the photoconductor layer.

This PhD work has been devoted to researching the possibilities for dark current minimization in a-Se x-ray photoconductors devices through a systematic study of the charge transport (carrier mobility and carrier lifetimes) and dark currents in single and multilayered a-Se devices as a function of alloying, doping, deposition condition and other fabrication factors. The results of the studies are extensively discussed in the thesis. We have proposed a new technological method for dark current reduction in single and multilayered a-Se based photoconductor for x-ray detector applications. The new technology is based on original experimental findings which demonstrate that both hole transport and the dark currents in a-Se films are a very strong function of the substrate temperature ($T_{substrate}$) during the film deposition process. We have shown that the new technique reduces the dark currents to approximately the same levels as achievable with the previously existing methods for dark current reduction. However, the new method is simpler to implement, and offers some potential advantages, especially in cases when a very high image resolution (20 lp/mm) and/or fast pixel readout (>30 s^{-1}) are needed.

Using the new technology we have fabricated simple single and double (*ni*-like) photoconductor layers on prototype x-ray image detectors with CCD (Charge Coupled Device) readout circuits. Dark currents in the a-Se photoconductor layer were not a problem for detector operation at all tested electric fields. Compared to the currently available commercial systems for mammography, the prototype detectors have demonstrated an excellent imaging performance, in particular superior spatial resolution (20 lp/mm). Thus, the newly proposed technology for dark current reduction has shown a potential for commercialization.

ACKNOWLEDGEMENTS

I would first like to thank my wife Mariyana and our two children Stefan and Palmira for their support, encouragement and especially for their patience during this endeavor. For the financial support that made this work possible, I would like to express my deep gratitude to my supervisor Dr. Safa Kasap, NSERC, the University of Saskatchewan, Sunnybrook Health Science Center, University of Toronto, and ANRAD Corporation, Montreal. I would like to extend my sincere gratitude to my supervisor Prof. S.O. Kasap and to my co-supervisor Prof. R.E. Johanson for their guidance and encouragement throughout the course of this work. I would like to thank David Hunter of Sunnybrook Health Science Center, University of Toronto for his excellent work on testing the prototype detectors and for providing me with the results from the tests, as well as for the many and fruitful discussions we have had. Dr. Ziad Shukri and Dr. Habib Mani of ANRAD Corporation deserve a big “thank you” for providing some of the Se alloys used during the study and for all insightful discussions that we have held. A big thank you goes to Dr. D. Tonchev, Dr. K. Koughia, Bud Fogal and Chris Allen for the help with some of the experiments. I would like to extend my gratitude to all the members of Prof. Kasap’s research group with whom I had the pleasure to work in the period 2000-2006 for the stimulating and helpful conversations, as well as for their friendship. Finally, and certainly not least, I would like to thank my colleagues from the chair of Atomic and Nuclear Physics, University of Plovdiv, Bulgaria as well as to my parents and my close relatives in Bulgaria for their unfailing moral support.

TABLE OF CONTENTS

LIST OF FIGURES

LIST OF TABLES

GLOSSARY OF ABREVIATIONS

ALARA	As low as reasonably achievable
AMA	Active matrix array
AMFPI	Active matrix flat-panel imager
a-Se	Amorphous selenium
CCD	Charge coupled device
CMMR	Common mode rejection ratio
CMOS	Complimentary metal-oxide-semiconductor
DC	Direct current
DOS	Density of states
DQE	Detective quantum efficiency
DR	Diagnostic radiology
DSC	Differential scanning calorimetry
DTA	Differential thermal analysis
EHP	Electron-hole pair
EMI	Electromagnetic interferences
ESEM	Environmental scanning electron microscope
ESR	Electron spin resonance
FET	Field effect transistor
GBP	Gain bandwidth product
HEXFET	Hexagonal field effect transistor (known also as vertical field effect transistor)
HV	High voltage
IFTOF	Interrupted field time-of-flight
in, i-n	Intrinsic type/n-type
IR	Infrared
ITO	Indium tin oxide
IVAP	Intimate valence alternation pair
LNT theory	Linear no-threshold theory

LP	Lone pair
MSV mode	Mean square voltage mode
MTF	Modulation transfer function
ni, n-i	n-type/intrinsic type
PCB	Printed circuit board
PET	Positron emission spectroscopy
PIN, P-I-N, pin	p-type/intrinsic type/n-type structur
PTPA	Post transit photocurrent analysis
SALLY	Code name of experimental CCD, DALSA Inc.
SCLC	Space charge limited currents
SELMA	Code name of experimental CCD, DALSA Inc.
SPDT	Single pole double throw
SPST	Single pole single throw
TDI mode	Time delayed integration mode
TFT	Thin film transistor
TLD	Thermoluminiscent detectors
TOF	Time-of-flight
TTL	Transistor-transistor logic
UV	Ultraviolet
VAP	Valence alternation pair

1. INTRODUCTION

1.1 Radiation Detection Techniques

Here we will briefly describe and explain the physics of the different ways in which nuclear and other similar radiation can be indirectly sensed by us, that is, detected and measured. It is fair to say that the advances of the techniques for radiation detection have led to some of the most fundamental advances ever made in science and technology, and have revolutionized many branches of medicine.

1.1.1 Brief History of Radiation Detectors

The collection of the charge that has been created by the ionizing radiation is probably the most important method for the detection of such radiations [1, 2]. Ionization is the process of liberation of free electric charges in a medium with which the radiation interacts. These charges, or at least fraction of them, can then be collected and detected by the application of an electric field to the medium concerned.

The earliest device capable of detecting ionizing radiation was effectively the gold-leaf electroscope but historically its radiation detection capabilities were not realized until after radioactivity was discovered in 1896 [1].

The first ionization detector was developed in 1908 by Rutherford and Geiger at Manchester [1]. Strictly speaking, they made a gas proportional counter, which is an ionization detector with internal charge amplification. Their device was capable of producing a pulse of charge for each particle of radiation incident on the gas inside, instead of measuring the integrated total charge collected as it is done for the ionization chambers. Ionization detectors with a solid as a working medium appeared much later due to a number of difficulties. First really practical counting devices, which were made from materials like silver chloride, cadmium sulphide, and diamond, came in the 1940s and these were followed in 1948 by the first ionization detectors made from liquids [1].

The earliest methods by which ionizing radiation was discovered and investigated investigated did utilize the technique described above. Röntgen's experiments in 1895 with x-rays produced by cathode rays showed that materials can emit visible light when struck by these x-rays. Materials such as barium platinocyanide, when brought towards the tube, gave an intense light emission. Obviously, this initial work did not reveal individual pulses of radiation. This had to wait until 1903, when Crookes and also Elster and Geitel [1] observed zinc sulfide under low magnification, and found that when it was exposed to alpha-particle radiation a number of short-duration scintillations of light could be seen scattered across the surface, rather than a steady, uniform distribution of light. Rutherford and his students made many of their discoveries in nuclear physics by observing scintillations in this way.

The actual discovery of radioactivity by Becquerel in 1896 was made with photographic plates. Röntgen had already found that photographic emulsions responded to x-rays. In his investigations following the latter work, Becquerel found that blackening also happened when uranium salt crystals were left for a few days next to plates which were otherwise unexposed. Emulsions with high spatial resolution which permitted the observation of tracks of individual particles were developed much later in 1930 [1].

The first device for track visualization, however, came much earlier, and was developed in the years up to 1912 [1]. This was Wilson's cloud chamber in which air saturated with water vapor was contained inside a chamber fitted with a movable piston. When the piston descended the air expanded suddenly. This caused water droplets to condense preferentially at the nucleation sites (namely, ions) produced along the track of any ionizing particle passing through the chamber at that time.

The introduction of electronic amplifiers and counting circuits to go with radiation detectors such as ionization chambers, proportional and scintilation counters from late 1920s onwards [1] removed many restriction of the radiation detecting experiments. In due course scintillations themselves could be counted electrically when photomultipliers were introduced. The application of modern pulse amplification, and digital techniques, and of computers has continued to help the development of radiation detection equipment to levels of accuracy and complexity which could never have been foreseen earlier.

1.1.2 Radiation Detector Classification

The operation of any detector basically depends on the manner in which the radiation to be detected interacts with the material of the detector itself. Accordingly, the radiation detectors can be divided in several groups [1, 2].

1.1.2.1 Ionization Detectors

The net result of the radiation interaction in a wide category of detectors is the appearance of a given amount of electric charge, in the detector active volume due to the process of ionization. This charge alters some physical and/or chemical properties of the detector's working medium and thus produces effects which can be measured. Further, ionization detectors can be divided into several groups, depending on the state of aggregation of their working media:

1. <u>Gas filled ionization detectors with typical representatives as follows</u>:
    a. D.C ionization chambers, pulse ionization chambers
    b. Proportional counters, multi-wire proportional counters
    c. Geiger-Mueller counters
    d. Corona and spark detectors and chambers
2. <u>Liquid ionization detectors with applications mainly in high energy physics</u>:
    a. Liquid ionization and proportional chambers
    b. Bubble chambers
3. <u>Solid state ionization detectors with typical representatives</u>:
    a. Crystal and semiconductor detectors
    b. Photographic emulsions
    c. Solid state tack detectors

In photographic emulsions and solid state track detectors the signal appears only after additional processes (development, etching) are applied to the detector. The changes in the detector media are permanent and such detectors exhibit very valuable event storage properties.

1.1.2.2 Radio-Luminescent Detectors

Every time when the alpha, beta or gamma ray strikes the working substance, known as a scintillator, a minute flash of light is produced. Thus the energy of the radiation is transformed into light and this flash of light is the output signal for those detectors. Only in rare cases such weak light signals can be directly observed. Usually they are further detected and amplified by other devices. This is most often a photomultiplier, but photodiodes, photodiode matrices, and charge coupled devices (CCDs) are also used.

The radio-luminescent detectors in which the light signal appears immediately after (10^{-6}-10^{-8} s) the act of interaction with radiation are known as scintillation detectors. The class of scintillation detectors can be further divided into several groups according to the state of aggregation of material of the scintillator itself: gas scintillation detectors, liquid scintillation detectors and solid state scintillation detectors.

In some of the radio-luminescent detectors, the light signal appears only if they are subjected to some additional stimulus, most often a thermal one. These are known as thermoluminiscent detectors TLD. The TLDs, like photographic emulsions, have event storage properties and that is why they are widely used for application like radiation dosimetry. They can be subjected to irradiation (usually x-rays or gamma rays) for several days or even several months. The energy of the incident radiation (some fraction of it) would be stored in the material of the detector. Heating the device through a few hundred degrees liberates the stored energy in the form of light. The amount of light emission is normally in some proportion to the radiation dose received.

1.1.2.3 Miscellaneous Detectors

The basic interaction with radiation for these detectors is neither ionization of the working media nor excitation of atoms or molecules in it that results in the emission of light. There are several detector types in this group [2]:

1. Cerenkov detectors. This category of radiation detectors is based on the light that is emitted by a fast charged particle passing trough an optically transparent medium with index of refraction greater than 1. The light is emitted whenever the velocity v of a charged particle exceeds that of light in the medium through which it is passing. Detectors based on sensing the Cerenkov light are widely used in high energy physics experiments, but have no use for the lower energy radiation.
2. Cryogenic microcalorimeters (Bolometers). Any substance when exposed to ionizing radiation will in principle show an increase in its temperature due to the energy absorbed from the incident particles or photons. In common conditions with ionizing radiation, this temperature rise is too small to be measured unless the radiation exposures are very high. The calorimetric methods become orders of magnitude more sensitive if the temperature rise is measured in miniature samples of material maintained at a very low temperature. For dielectric crystals the heat capacity is proportional to T^3, where T is the absolute temperature. Therefore, the lower the

temperature is, the greater will be the temperature rise per unit absorbed energy. By reducing the temperature to bellow 1K, it is possible to sense the momentary temperature rise due to a single photon or incident particle [2].

3. Superconducting Grain Detectors. The very small heat capacity of materials near absolute zero temperature can be exploited in another way to detect single particles or photons. A number of materials are superconductors at very low temperatures but revert to "normal" conductivity if the temperature is raised. In a very small (diameter of a few micrometers) grain of such a material the energy deposited by an ionizing particle can be sufficient to transform the grain from the superconducting to the normal state and thus enable the event to be detected.
4. Activation foils. These are indirect detectors for neutrons. The neutrons are known to induce radioactivity in some materials. A sample of such a material can be exposed to a flux of neutrons for a period of time and then removed so that the induced radioactivity may be counted, using any of the conventional detectors. The measured radiation can then be used to deduce information about the number and/or energy distribution of the neutrons in the original flux.

1.1.3 Simplified Detector Model. Basic Modes of Detector Operation

The result of radiation interaction in most frequently used detectors is the appearance of a given amount of electric charge within the detector active volume [2]. A simplified detector model is described in [2]. Following the ideas in that work we assume that a charge Q appears within the detector at time $t=0$ due to interaction of a single particle or quantum of radiation. This charge is then collected to form the basic electric signal. The latter is accomplished through the application of an external electric field which causes positive and negative charges that have been created by the radiation to flow in opposite directions. The time required to fully collect the charge varies greatly from one detector to another. These collection times depend on the drift mobilities of the charge carriers and on the average distance that must be traveled before to reach the collection electrodes. The response of the detector to a single particle or a quantum of radiation will be a current that flows for a time equal to the charge collection time t_c. The time integral over the duration of the current must be equal to the collected charge Q

$$Q = \int_{t=0}^{t_c} i(t)dt\,. \tag{1.1}$$

We have assumed that the event rate is low enough, so each individual interaction gives rise to a current that is distinguishable from all others. The magnitude and the duration of each current pulse may vary depending on the type of interaction and the current pulses normaly have different forms. The arrival of the radiation quanta is a random process governed by Poison statistics, thus the time intervals between successive current pulses are also randomly distributed.

There are three general modes of detector operation [2]. The tree modes are called pulse mode, current mode and mean square voltage mode (MSV mode). First two modes of operation have many practical applications, including in medical x-ray image detectors. The most basic details of these modes of operation will be given below.

In pulse mode of operation, the measurement instrument is designed to record each individual quantum of radiation that interacts with the detector. In common applications the total charge Q is recorded since the energy deposited in the detector is directly related to Q. All detectors designed to measure the energy of individual radiation quanta must operate in pulse mode. Such applications are known under the term of radiation spectroscopy. The scintillation detectors used in the imaging of brain and its functions in positron emission spectroscopy (PET) are example for medical detectors operating in the pulse mode of operation.

At very high event rates (such as during an x-ray imaging procedure), pulse mode of operation becomes practically impossible because the current pulses from successive events overlap in time. For such cases, the most suitable alternative measurement technique is that which respond to the time average taken over many individual events. This approach leads to the current mode of operation.

Let us assume that detector has a fixed response time t_r. The recorded signal from a sequence of events will be a time dependent current [2] given by

$$I(t) = \frac{1}{t_r} \times \int_{t-t_r}^{t} i(t')dt'\,. \tag{1.2}$$

The response time t_r is typically a fraction of a second or greater, so that the effect is to average out many of the fluctuations in the intervals between individual radiation interactions, and to record an average current. The current depends on the product of the interaction rate and the amount of charge created per one interaction. In the current mode, this time average of the individual current bursts is recorded as the basic signal. There is a statistical uncertainty in this signal due to the random fluctuations in the arrival time of the event. The choice of large T will minimize the statistical fluctuations in the signal but will also slow the response of the detector to the rapid changes in the incident radiation.

The average current is given by the product of the average event rate and the charge produced per event

$$I_o = rQ = r\frac{E}{W_{\pm}}q\,, \tag{1.3}$$

where r is the event rate;

$Q = \frac{E}{W_{\pm}}q$ - charge produced for each event;

E - average energy deposited per event;

$W_{\pm}$ - average energy required to produce a unit charge pair (e.g. electron-ion) and

q=1.6x10^{-19} C – the charge of the electron.

For steady-state irradiation of the detector this average current can also be rewritten as the sum of a constant current I_0 plus a time dependent fluctuating component $\sigma_i(t)$. Here $\sigma_i(t)$ is a random time-dependent variable that occurs as a consequence of the random nature of the radiation events interacting within the detector.

The vast majority of detectors involved in the digital x-ray imaging are used in current mode of operation.

1.2 X-ray Detectors for Projection Radiography

The x-rays discovered by Wilhelm Röentgen in 1885 are probably the scientific discovery with the fastest practical implementation that provided medical practitioners with a very convenient non-invasive procedure to obtain diagnostic information. Only weeks after the actual discovery, x-rays have been applied for the purposes of medical imaging and diagnostics and led to the development of a new branch in medical sciences which is known today as Diagnostic Radiology (DR). DR always was and still is a dynamically developing part of medical practice. This rapid development is due mainly to two reasons: the constant need of high quality images containing as much diagnostic information as possible and the need to obtain the diagnostic information with as little x-ray exposure of the patient as possible. The first of these two reasons is self-explanatory but the second one needs to be clarified further. X-rays like any other form of ionizing radiation can cause damage to the living tissue. The first evidence that x-rays, can cause malignant changes in the living tissue appeared soon after Röentgen's discovery. After the end of World War II, studying the effect of radiation on the survivors of the atomic bombing of Hiroshima and Nagasaki and the data collected from experiments with mammals during tests with nuclear weapons, a theory was proposed, which presumes that the detrimental effects of radiation are proportional to the dose, and that there is no dose which can be considered as harmless. That theory, known as LNT (linear no-threshold), was chosen by the International Commission on Radiological Protection in 1959 as the basis for its rules of radiation protection [3] and since then it has become a pillar of the international theory and practice of radiation protection. Today all examinations involving ionizing radiation must obey the ALARA principle, which simply means that the diagnostic information has to be obtained with "as low as reasonably achievable" exposure of the patient to the ionizing radiation.

Despite the introduction of a large number of alternative imaging modalities, projection radiography is still one of the most commonly used techniques in the health care centers. The development of better detectors for that imaging modality is a topical research problem. In a projection radiography examination, the incident radiation is either from a point source, or it is a parallel beam, which will therefore cast a "shadow" of the object on the recording detector. The contrast in the image is due to the different amounts of absorption of the x-rays in different tissues and parts of object. The detector after the exposure must store the information and develop an image, visible for the human eye.

Imaging detectors and techniques that are most commonly used and that are currently undergoing very promising development are described in the next part of this subsection.

1.2.1 X-ray Film and X-ray Screen/Film Combination as Imaging Detectors

The use of photographic film as an x-ray image detector dates back to the discovery of x-rays in 1895. With little modification still remains an important technique in the present time.

Ordinary photographic film consists of an emulsion of silver halide grains (silver bromide being one example) suspended in a matrix and supported with a backing of glass or cellulose acetate film. The action of ionizing radiation in the emulsion is similar to that of visible light. Some of the grains will be "sensitized" through the interaction of the radiation with the silver halide molecules. The sensitized grains remain in this state indefinitely, thereby storing a latent image of the track of the ionizing particle through the emulsion. In the subsequent development process, all sensitized grain are converted to metallic silver, vastly increasing the number of affected molecules to the point that the developed grains are visible. Following development, the emulsion is fixed by dissolving away the undeveloped silver halide grains. During the final washing step the processing solutions are removed from the developed emulsion. Radiographic emulsions are typically 10-20 μm thick with grains up to 1 μm in diameter [2]. The silver halide concentration amounts to about 40% by weight. In some cases the sensitivity is increased by applying the emulsion to both surfaces of the base film.

This detection technique is known as "*direct film radiography*". The greatest advantage of the direct film is its high spatial resolution. Some films are capable of imaging with resolution several hundred lp/mm which is well out of reach for the modern digital image detectors. However, direct sensitivity (the efficiency) of the radiographic emulsion for x-rays is at best a few percent. That leads to ineffective use of the x-ray beam and invariably to higher patient doses.

In almost all medical radiographic applications, additional steps are taken to enhance the sensitivity of the emulsions. One method is to sandwich the film between foils made from materials with high atomic number. Photoelectric or Compton interactions within these converter foils may then contribute secondary electrons, which add to those created within the emulsion itself. Alternatively, and more commonly, is to sandwich the film between two intensifier screens which consist of light-emitting phosphors of high atomic number. X-ray interactions within the screen create visible light through the fluorescent scintillation process, which then leads to additional sensitization of the emulsion. Because emitted light rays travel in all directions, a compromise must be struck between sensitivity and spatial resolution in choosing the thickness of the screen. In typical situations, the sensitivity of such screen/film combination ("indirect film") can be increased by a factor of 10 through the use of such intensifier screens. This comes at the expense of lower spatial resolution, which normally does not exceed 10-15 lp/mm.

Today about 60% of x-ray imaging is accomplished with film/screen (indirect film) systems. The cassettes are loaded with film and taken to the examination room, then to the x-ray equipment, and after exposure they are returned to the darkroom for the development before a final image can be viewed. This is time consuming and the acquired image is in analog form.

A future digital system must conveniently eliminate that waiting time and transfer the present process to the digital domain.

1.2.2 Flat-Panel X-Ray Image Detectors – The Most Promising Imaging Technology for Radiography

An ideal x-ray diagnostic system would permit the instantaneous acquisition of an x-ray image directly in digital form with the least number of x-ray photons.

There are various transitional digital systems based on the use of photostimuable phosphor plates (computed radiography CR systems), x-ray image intensifiers optically coupled to charge coupled device (CCD) arrays, and phosphor screens optically coupled to CCDs [5]. With photostimuable plate systems, the x-ray image is captured on a photostimuable plate, which must then be taken and scanned by a laser system in order to digitize the image information. The principle of operation of these detectors is very similar to the TLD described previously in subsection 1.1.2.2. However, this is just as time consuming as the conventional film/screen systems and furthermore the image quality is not as good. With x-ray image intensifier systems, the image is obtained instantaneously but the image quality for radiography is also poorer than that for film/screen cassettes. Further, the x-ray image intensifier is bulky and extremely expensive which limits its use to situations where the real time aspects of the image are most important. The basis of optically coupled CCD systems involves the use of a structured screen (such as Tl activated CsI phosphor), which is able to detect x-rays, converting them to light, which in turn is collected by tapered optical fibers. This reduces the image size by a factor of 2 to 4 and matches the size of the CCD array, typically no larger than 2 x 2 cm to the required field of view of the clinical task. Thus, for fields of view larger than 10 x 10 cm several CCDs must be used together in order to obtain a detector of sufficient size for many clinical studies.

An active matrix flat-panel imager (AMFPI) using active matrix thin film transistor (TFT) arrays is the most promising technology for digital X-ray imaging due to its compact size, rapid readout and better imaging performance compared to screen-films [6-9]. Based on the materials used for x-ray detection, AMFPI are divided into two main categories: direct and indirect conversion type. As shown in Figure 1.1, the direct detection AMFPI employs a uniform layer of x-ray sensitive photoconductor, most often amorphous selenium to directly convert part

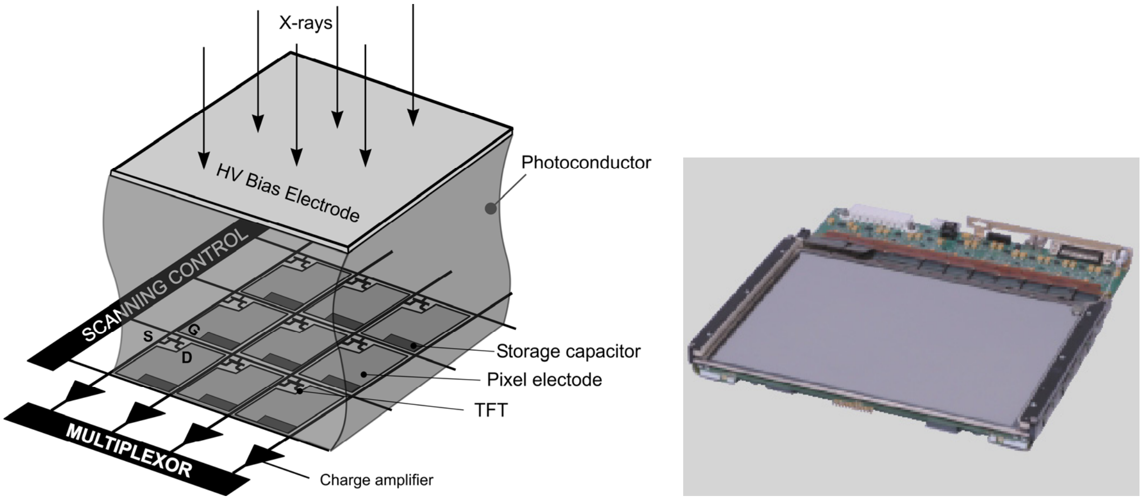

Figure 1.1 Schematic diagram illustrating the concept of direct conversion AMFPI (left). Anrad Corporation SMAM a-Se based flat panel detector for digital mammography (right). The detector has an image area 17 cm × 24 cm , detective quantum efficiency DQE of 65% at 1 lp/mm and modulation transfer function MTF of 50% at 5 lp/mm (Courtesy of Anrad Corporation).

of the energy of the incident x-rays to charge, which is subsequently electronically read out by a two-dimensional array of TFTs. During readout, the scanning control circuit generates pulses to turn on the TFTs one row at a time, and transfer image charge from the pixel to external charge sensitive amplifiers. These are shared by all the pixels in the same column. Each row of the detector typically takes ~20 μs to read out. Hence a detector with 1000×1000 pixels can be read out in real-time (i.e. 30 frames/s).

The indirect AMFPI uses a phosphor such as cesium iodide (CsI:Tl) to convert x-ray energy to optical photons, which are then converted to charge by integrated photodiodes at each pixel of the TFT array. The charge image is read out in the same fashion as in the direct detectors. Structured scintillators (Figure 1.2) are used to reduce the lateral spread of the light emitted during the scintillation events and hence to improve the spatial resolution of indirect AMFPI. Despite their differences, both AMFPI methods offer better image quality than screen-films and computed radiography systems [9].

However, it is currently believed that the direct method has the advantages of higher image resolution. Additional advantage is that the direct approach requires simpler TFT array structure that can be manufactured in a standard facility for active matrix liquid crystal displays.

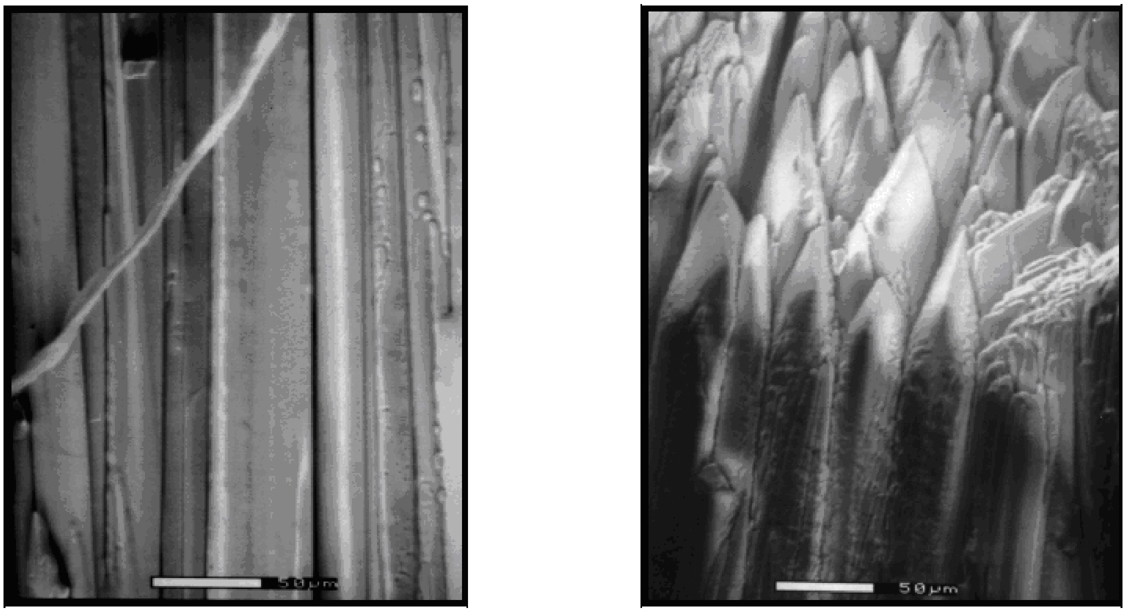

Figure 1.2 ESEM (environmental scanning electron microscope) micrograph of 2000 μm CsI(Tl) film[10]. The photograph on the left side shows the central portion of the film, while the one on the right side shows the film surface.

At the moment AMFPIs satisfy almost completely the requirements for general radiology and many of the requirements for application in mammography. Breast imaging is very difficult because the radiologist must be able to distinguish between several types of soft tissue with very similar x-ray absorption properties. The contrast in the image is low and the problem with scattered radiation in the breast is very serious. The smallest objects of interest are micro-calcifications which are only about 80-100 μm in size. Such small objects are nearly "invisible" for all currently existing AMFPIs. In the indirect conversion flat panel detectors, the lateral light scatter limits the spatial resolution of these detectors to a level that is insufficient to observe the micro-calcifications in the breast. The pixel size in the direct conversion flat panel detectors that are available in the market (Figure 1.1) is 70 μm. Such pixel size theoretically might allow imaging of 80-100 μm objects but in practice the micro-calcifications disappear in the noise of the detector system. The pixel size that will make the micro-calcifications in the breast visible is 20 μm or less [11]. Regular production of AMA with such small pixel sizes is unachievable with the current hydrogenated amorphous silicon technology for a number of reasons (see Appendix A).

During the last 6-8 years, an attempt is being made to develop second-generation direct conversion detectors for digital mammography with very high spatial resolution [13]. These detectors utilize charge coupled devices (CCDs) as the image readout electronic circuit and a photoconductor as the detector working media. This approach benefits from the higher intrinsic resolution of photoconductors (compared to scintillators) as well as from the higher resolution of the readout device (pixel sizes 20×20 μm and much smaller are readily achievable). Another advantage is the low readout noise that is characteristic for the CCD devices. With the current semiconductor technology, charge coupled devices with image areas like 11 cm by 1 cm are readily achievable. Typical image size of interest for mammography is 18 cm by 24 cm or bigger. Such sizes are achievable, if 2-3 CCD chips are butted together to form a "slot detector". The x-rays are collimated in the form of a very narrow beam incident to the detector and the 2-dimentional image is obtained as the x-ray source – detector assembly mechanically scans the breast. This method is known by the name *slot-scanning technique* for x-ray imaging. During the image acquisition the CCDs are operated in Time Delayed Integration TDI mode to increase the sensitivity of the detector and to reduce the patient dose.

The disadvantage of such a technique is obvious – the presence of mechanically moving parts and the inefficient use of the x-ray field generated by the x-ray tube. However, the slot scanning method has some distinct advantages compared to the standard technology for breast imaging. First, the scanning mode allows dose efficient elimination of the scattered radiation and second it makes possible imaging with a detector of a much smaller area. Fabrication of high-resolution detectors with a large image area is a very low yield process and hence very expensive. From this point of view, the CCD "slot detector" will be less expensive and will have a better resolution than a AMFPI.

More detailed description of the slot scanning technique for x-ray imaging, TDI readout mode and pixel structures of direct conversion CCD detectors is given in Appendix A.

Various candidate photoconductor materials, namely CdTe, CdZnTe, PbI2, HgI2 and a-Se, have been investigated for potential applications in such high-resolution CCD detectors. From the latter photoconductors, a-Se has been demonstrated to exhibit the most promising performance [12] and was chosen as the photoconductor in an attempt to develop a high-resolution detector for mammography based on the slot scanning technique [13].

The work that will be presented later in this thesis was directly related to the research efforts to develop such detector. The development of the detector involved extensive research on the electrical properties of a-Se, which was an integral part of the thesis project.

1.3 Direct Conversion Detectors Based on a-Se – The Dark Current Problem

A simplified pixel structure of a direct conversion x-ray image detector is shown in Figure 1.3. The x-rays arriving to the detector interact with the photoconductor layer and a number of electron-hole pairs are formed in this layer. The electrons and holes are separated by the applied electric field and collected at the detector electrodes. The amount of charge collected in the pixel charge storage device is proportional to the intensity of the x-rays arriving at the pixel. Thus the x-ray image is stored as a distribution of electric charge in the readout device. After the x-ray exposure, the charge collected at each pixel is measured and the final x-ray image is stored in the computer.

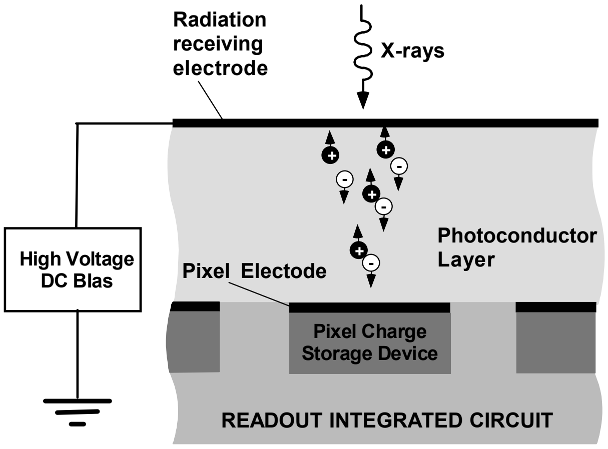

Figure 1.3 A simplified pixel structure of a direct conversion x-ray image detector.

The charge collection process requires the application of an electric field. When an electric field is applied to the photoconductor, a small current will flow through it even in the absence of any radiation. The current through the photoconductor in the absence of x-ray radiation and light is called the *dark current*. The dark current limits the smallest amount of x-ray radiation that can be detected by the pixel, shrinks the dynamic range of the detector and introduces noise in the x-ray image. For these reasons, the dark current has to be kept as small as possible.

However, the a-Se photoconductor layer has to be operated at high electric fields. The main reason for a large operating field is that the photogeneration process in a-Se is field dependent. The electron-hole pair creation energy $W_{\pm}$ is a function of the applied electric field and good x-ray sensitivity can only be achieved by the application of high fields. In addition, the electron and hole traps that are present in a-Se impose certain limitations on the process of charge collection. If significant amount of charge is trapped in the a-Se film, artifacts in the image known as *lag* and *ghosting* can appear.

Acceptable x-ray sensitivity and acceptable levels of lag and ghosting can be achieved only if high enough voltage is applied across the a-Se layer. For the reasons specified above, the a-Se layer is operated at high electric fields: 3-10 V μm^{-1}. At such high fields, the dark currents are intolerably high (in many cases bigger than the x-ray generated signal) and special measures must be taken to reduce the dark current in the a-Se layer to a reasonable level.

The exact nature of the dark current in a-Se is not fully understood. However, the dark current has two components; one due to the thermal generation of free carriers in the bulk of the a-Se film and the second one is due to carrier injection from the metal contacts into Se. Some initial work suggests that the magnitude of the dark currents is dominated by the charge injection from the metal electrodes [14]. Due to the latter reason, all the methods for dark current reduction at present rely on the fabrication of a thin blocking (trapping) layer between the Se photoconductor and the metal electrode. In some cases the trapping layer consists of a special insulating dielectric layer. For example, Hologics/Lorad are using this technique for dark current reduction in their medical x-ray image detectors. The charges injected from the metal contacts are trapped in the insulating layer and the current injection from the metal into a-Se is thereby blocked. An alternative explanation is that the insulator layer has a large bandgap so that the charges can not be easily injected from the electrode into the a-Se. When a dielectric is used as a trapping layer, the charge generated by the x-ray exposure is also trapped in the blocking layer. The trapping of charge is very deep and the detectors in which this technique is involved require a system reset procedure, for example soaking with light to eliminate the trapped charge in the dielectric layer. It is evident that such detectors cannot be used for real time x-ray imaging. The thickness of such a blocking layer must be thick enough to prevent charge tunneling through the dielectric. The presence of such a thick blocking layer will have negative impact on detector performance for reasons that will be explained later.

For dark current minimization, ANRAD Corporation and others have used multilayers, which are a structural analogue of the pin diode structure, that are reverse biased as shown in Figure 1.4.

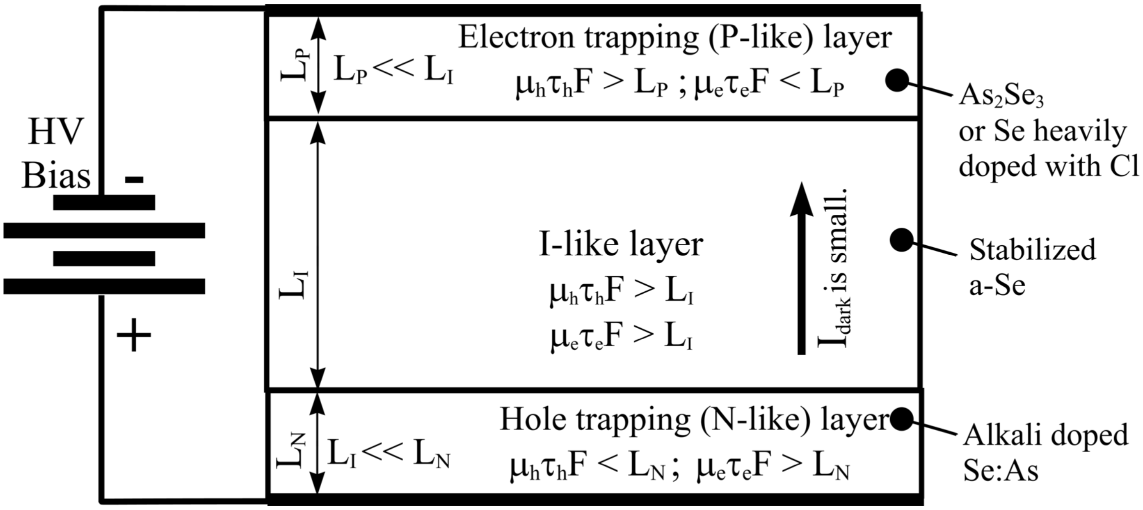

Figure 1.4 The ideal a-Se multiplayer analogue of a pin structure.

The p- like layer in Figure 1.4 is produced from an a-Se that has been doped to have good hole transport but to trap electrons; the i- like layer transports both holes and electrons, and the n- like layer transports electrons but traps holes. The p- like layer can also be As_2Se_3 film which is p-type. The p- like layer is connected to the negative bias terminal and the n- like layer to positive one. The p- and n- like layers are normally thin compared with the i- like layer, which is thick. Thus the x-rays are absorbed mainly in the i- like layer. P- like layer and n- like layer are a-Se layers that have been alloyed and doped to give those layers their characteristic electronic properties. The n- like layer is usually an alkali (Na) doped a-Se alloyed with a few percentages of As for stability. The p-like layer is usually a halogen (Cl) doped a-Se, and some As for stability. However, as mentioned above it can also be a-As_2Se_3. The multilayer structure functions in the following way. Both hole and electron injection from the metal electrodes is blocked. The holes injected from the positive electrode are trapped in the n- like layer and the electrons injected by the negative electrode are trapped by the p- like layer. Due to the charge trapped in these layers the electric field near the electrodes decreases. The injection currents are strongly dependent on the electric field at the electrodes and thus the charge injection in the sample is strongly reduced, which minimizes the dark current. At the same time, electrons and holes created in the i-like layer by the x-ray radiation will pass without trapping through the n- like layer and through the p- like layer respectively. There will be no loss of x-ray induced signal due to trapping in the blocking layers which is an advantage compared to the case when an insulator is used to block the current injection from the electrodes.

The multilayer structure seems to be a more promising approach for dark current reduction in a-Se detector films; however it has its own disadvantages. The production of such a structure involves depositing 3 different layers to achieve a pin- like structure. Obviously, the device preparation technique is difficult and requires the right dopants in right combinations to produce the p- like layer, n- like layers and i- like layers. The long-term stability of such structures can be a problem because Na doped amorphous Se tends to crystallize. Another, problem with sodium is that that when high electric fields are applied to the pin- like structure, sodium ions will tend to drift towards the negative electrode and hence out of the n- like layer into the i- like layer. This will obviously change the properties of the i- like layer and can cause another set of problems affecting the long-term stability of the structure. The real p- like layers and n- like layers are not ideal and their transport properties are usually far from the ideal ones shown in Figure 1.4. The lifetime of the holes in the n- like layers and the electrons in the p- like layers is not zero. So the thickness of an efficient trapping layer is finite and must be greater than the average distance that the carrier travels before being deeply trapped (carrier Schubweg). Because the drift mobility of the holes in a-Se is much greater than that of the electrons, thin n- like layers are more difficult to prepare. For an n- like biased at 5-10 Vμm^{-1}, the typical thickness of the blocking layer should not be smaller than 10-15 μm. In addition, due to the heavy As doping, the electron transport in the n- like layer should be in general much worse than that in the i- like layer, so a significant amount of electrons are also lost in the n- like (trapping and recombination).

In some cases, x-ray image detectors that collect electrons on the pixel electrodes can benefit from cheaper AMA and CCDs that are readily available. However, in that case the electrons have to pass through the at least 10-15 μm thick n- like layer before reaching the pixel electrode. High resolution detector will have small pixel size 20 μm and less. The a-Se film of

200 μm is commonly used for mammographic detector applications. This means that the aspect ratio (pixel size to photoconductor thickness) of such detectors will never exceed 0.1. The "small pixel effect" [15] becomes significant for such aspect ratios and that causes additional complications. The analysis of that effect [15-18] shows that the x-ray generated charges contribute to the signal only when they are moving in the vicinity of the pixel electrode, i.e. one pixel size away from the pixel electrode. The consequences of that are twofold; first, practically only the electrons contribute to the signal formation (radiation receiving electrode is negatively biased) and second, electron transport in the n- like layer becomes extremely important since more than 80% of the signal is formed when the electrons are moving through that layer. Alkali doped n- like layers, are stabilized with the addition of about 2% As. It is very well known that As decreases the electron mobility in a-Se by inducing a lot of shallow traps (0.4-0.6 eV from conduction band edge). That is highly undesirable in the case of real-time systems, and especially when CCD working in TDI mode is used as a readout circuit. In such cases the rows are shifted in the TDI direction more than 1000 times per second. At that fast readout speed, the low mobility of the electrons in the n- like layer may cause severe degradation of the image performance. In other words, it seems that it might not be possible to apply the alkali doped n-like layers for dark current control in a-Se based x-ray detectors with a TDI CCD readout circuit collecting electrons.

1.4 Research Objectives

The research work that will be described in this document was directly related to the investigation of the possibilities to create a high-resolution (20 lp mm^{-1}) direct conversion digital x-ray detector utilizing a-Se as a photoconductor and a CCD readout circuit for applications in mammography.

The main objective of the research work was to investigate the possibilities for dark current minimization in selenium based photoconductor structures without any significant deterioration in their imaging performance through systematic studies on the charge transport in a-Se films as a function of deposition conditions and alloying as well as through studies of dark currents in various single and multilayered a-Se devices.

In the search for the dark current reduction technique that will give comparable or better results than the pin- like a-Se based structures, more than 300 vacuum depositions of a-Se were performed and numerous metal/a-Se/metal structures were produced. Commercial metal/a-Se/metal structures were also investigated. The experiments that were carried out can be classified in the main groups:

- Investigation of charge transport in a-Se as a function of alloying
- Investigation of charge transport in a-Se as a function of deposition conditions
- Investigation of dark currents (I-t and I-V curves) in single and multi layered metal/a-Se/metal structures
- Investigation of dark currents (I-t and I-V curves) in metal/a-Se/metal structures as a function of the metal electrodes
- Production of prototype x-ray image detectors utilizing the newly developed technique for dark current minimization.

Based on the results of the experiments mentioned above, we have been able to propose and test a new technology for the fabrication of multilayer a-Se structures with low dark currents suitable for application in high-resolution x-ray image detectors. The new technology eliminates the need of doping with alkali elements to suppress the hole transport in the n- like layer and all associated complications that have been already described at the end of subsection 1.3. The newly proposed method offers several potential advantages over the existing technologies for dark current reduction. The initial test results were very promising and a patent application was filed.

1.5 Scope of the Thesis

This chapter of the thesis has provided introductory information. The chapter started with a brief historical overview on the development of the methods for the detection of ionizing radiation. That was followed by a classification of the existing radiation detectors in several main groups and an introduction of a simple detector model applicable to most detectors producing an electrical output signal. The chapter continued with a brief description of the most commonly used detectors for x-ray projection imaging – screen/film cassette. The most promising technology for digital x-ray imaging based on the active matrix flat panel imagers of direct and indirect conversion type was described next. The need of high resolution direct conversion detectors and a way for their practical realization were described next. Amorphous Se is the most promising candidate for application as photoconductor in such high resolution digital x-ray image detectors. For latter reasons, the ways to control the dark current to a tolerable level in a-Se based photoconductors layers have been briefly covered together with the disadvantages inherent to those methods. The chapter concludes with the description of the research objectives and structure of the thesis.

The remainder of this thesis is divided into five chapters. In Chapter 2, the properties of Se that are of significant importance for understanding the results of this work are described. These include: short description of the different crystalline and non crystalline forms of Se with some of their physical properties; description of the structural defects in a-Se; band structure of a-Se is described with emphasis on the density of electronic states in the band gap of that material. The chapter concludes with the description of the properties that make a-Se a good photoconductor material for x-ray image detectors.

Chapter 3 provides description of the theory of transient photoconductivity measurements which is vital for proper interpretation of the results from Time-of-Flight (TOF) and Interrupted Field Time-of-Flight (IFTOF) experiments which were essential part of the research work.

Chapter 4 describes the experimental procedures used to conduct the research. The chapter starts with the description of the fabrication process for the production of metal/a-Se/metal devices and equipment involved in that process. The discussion is then shifted to the equipment and the experimental procedure used for the measurement of dark currents in metal/a-Se/Metal structure. The TOF and IFTOF experimental setups are described next as means to obtain information about charge transport in the investigated a-Se films.

Chapter 5 is devoted to the presentation of the main results from the research as well as to their discussion. The experiments are grouped in the same way as described in subsection 1.4 and the discussion follows the order presented there.

Chapter 6 presents the conclusion from the work together with the suggestions for future work.

2. PROPERTIES OF SELENIUM

2.1 Structure of Selenium

Selenium is a member of group VI of the periodic table. The set of elements which are located in that group are called chalcogens. Selenium (Z = 34) has twenty eight electrons occupying the completed inner core shells. Two of the six electrons in the outermost shell occupy the 4s subshell and the other four outer electrons occupy the 4p subshell. The two electrons in the 4s-states form an lone pair (LP) state and do not participate in bonding. Chalcogen elements normally have a p-state lone pair in addition to the s-state lone pair, and these are both commonly referred to as non-bonding states. This leaves two valence electrons in the p-states that are available for covalent bonding with other atoms to form a solid. Therefore, Se atoms in a solid have a two-fold coordinated bonding configuration with an optimum bond angle of 105° [19]. The bonding configuration for Se in realty is quite flexible, because in the condensed state, under normal pressure, selenium can exist in many different allotropic forms [20-22]. More than four different crystalline modifications have been described and obviously at least 4 different liquid forms can be produced by heating the mentioned polymorphs above their specific melting temperatures. The non crystalline solid state forms of Se are known as "amorphous" (red, black and brown) and "vitreous" (produced by melt quenching). Most of the authors use the terms "amorphous" and "vitreous" as synonyms when referring to the non-crystalline solid forms of Se. However, the variety in the properties of the existing non-crystalline forms of Se requires the introduction of better terminology that avoids the confusion between “amorphous" and "vitreous" [21].

The purpose of this subsection is to provide more detailed information on the structure of solid state forms of selenium and especially about its non-crystalline forms.

2.1.1 Crystalline Polymorphous Modifications of Selenium

The summary of allotropic selenium forms and some of their characteristics is given in [21] and are presented in Table 2.1. Several crystal modifications are possible: trigonal Se (hexagonal according to some authors) constructed from Se_n chains with meting point $T_m = 217$ °C; α-monoclinic consisting of Se_8 rings with $T_m = 144$ °C; β-monoclinic consisting of

Se_8 rings with $T_m = 100$ °C; γ-monoclinic constructed from Se_8 rings, rhombohedric consisting of Se_6 rings with $T_m = 120$ °C; orthorhombic Se possibly constructed from Se_7 rings; and α- and β-cubic Se [21] produced in form of films.

Table 2.1 Allotropic forms of Selenium as summarized in [21].

Name	Molecular Structure	Bond length, pm	Bond angle, deg.	Coordination number K_1	Unit cell constants			Transformation temperature *T*, °C	Density, gcm^{-3}
					***a*, pm**	***b*, pm**	***c*, pm**		
Crystalline									
Trigonal	Spiral chains, Se_n	237	103.1	2	436.6	-	495.4	Melting 217-221	4.819
α-monoclinic	Rings Se_8	232	105.9	2	905.4	908.3	1160.1	Transforms into trigonal form 140-160	4.390
β-monoclinic	Rings Se_8	324	105.5	2	1285	807	931	Transforms into trigonal form 140-180	-
α-cubic	unknown	297	-	6	297.0	-	-	-	
β-cubic	unknown	248	-	4	575.5	-	-	-	
Rhombo-hedric	Rings Se_6	235	101.1	2	1136.2	-	442.9	Transforms into trigonal form 120-135	4.710
Ortho-rhombic	Se_7 rings	-	-	-	263.2	688	434	Transforms into trigonal form 105	
Non-Crystalline									
Red amorphous	Rings	233		~2.4	-	-	-	~T_{room}	4.270
Black amorphous	-	-		-	-	-	-		
Vitreous	-	233 246	105	2.0-2.2	-	-	-	Softens at ~30	4.280
Melt									4.010

The trigonal Se consists of spiral chains with the trans-configuration arrangement of atoms in the 4-member fragment of the chain shown in Figure 2.1. The spiral chains with identity period 3 are connected in the trigonal crystal lattice with the following parameters for the unit cell: a=436.8 pm, c=495.8 pm. The valency angle θ is equal to 103.1degrees. The dihedral angleϕ , characterizing the degree of the chain twisting, reaches 100.6 degrees, approaching to the value of the angle in the Se_8 molecule [21]. Red monoclinic selenium is characterized by the cis-configuration in the arrangement of four sequentially bonded atoms in the circular molecule of Se_8. The monoclinic unit cell of α- and β-selenium contains four Se_8 molecules, γ-selenium – eight [21]. α-monoclinic selenium has the following parameters for the unit cell: *a*=905.4 pm, *b*=908.3 pm, and *c*=1160 pm. The valency angle is equal to 105.9 deg, the dihedral angle - 101.0 deg [20]. Data on rhombohedric Se_6 are given in Table 2.1. The dihedral angle is 76.2±0.4 deg. The hexagonal unit cell contains 3 molecules of Se_6 [22].

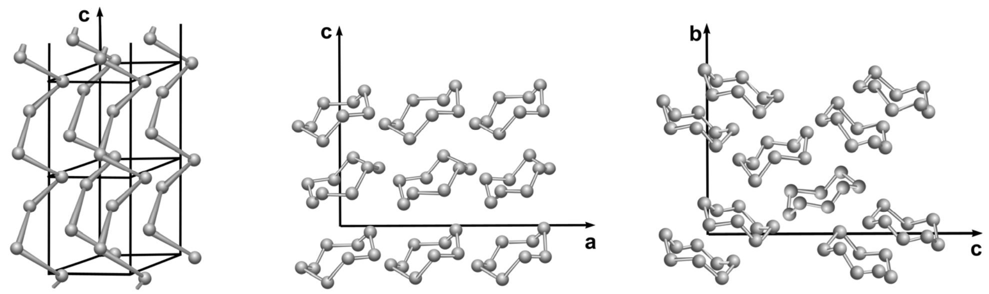

a) Trigonal Se **b) β-monoclinic Se** **c) α-monoclinic Se**

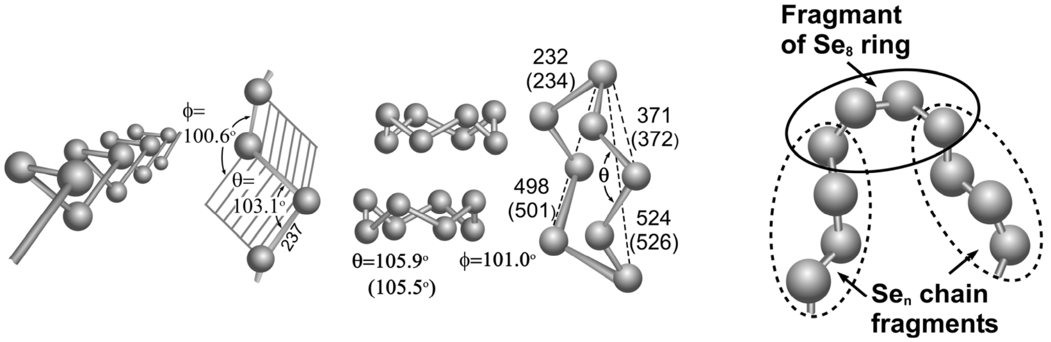

d) Se_n chain and its preiod **e) Se_8 rings of α- and (β-) Se** **f) a-Se molecule build from ring-like and chain-like fragments**

Figure 2.1 Molecular structure of several selenium allotrope forms. The distances are given in pm. Data were taken from [20], [21] and [23].

The thermodynamically stable allotropic modification of selenium is trigonal selenium. The monoclinic crystalline forms of Se transform into trigonal as the temperature increases. The beginning of such transformation is registered after heating at 70 °C for 600 min [23]. The rhombohedric Se transforms into trigonal at temperatures above 105°C.

α-monoclinic Se melts at 144 °C and spontaneously transforms into trigonal selenium; β-modification melts at temperatures higher than 100 °C [20]. The curves of the differential scanning calorimetry (heating rate of 10 °C/min) of rhombohedric selenium show the endothermic melting peak at 120 °C [22]. All these transformations are irreversible which demonstrates the monotropic character of the transformations. The heating of the hexagonal althropic form of Se leads to its melting at 217 °C with the enthalpy of fusion as 6.23 kJ mol^{-1} [20].

2.1.2 Non Crystalline (Amorphous) Forms of Selenium

2.1.2.1 Vitreous Selenium

The vitreous modification of Se can be readily produced in the form of relatively large samples provided that the crystallization promoting impurities can be eliminated by quench cooling the melt with sufficiently high rate (the critical rate is about 20 °C min^{-1}) [20]. The glass transition temperature of such samples is about 40 °C. Their density is about 4.280 g cm^{-3}. During the sixties it was considered that vitreous selenium was a mixture of two types of molecules that are connected by Van der Waals forces: polymeric spiral Se_n chains like the ones in trigonal Se and 8-member ring molecules like the ones in monoclinic modifications of crystalline selenium (see Figure 2.1). The ring to chain ratio in vitreous selenium depends on the temperature of the melt from which the samples were produced. That model for the structure of the melt and of the vitreous form of Se was based on indirect evidences. Se has very high viscosity around its melting point. Close to that temperature the only stable polymorph of Se is the trigonal Se constructed from Se_n chains. It was presumed that the chain structure is preserved in the melt and, by analogy with sulfur, the high viscosity of the melt was attributed to long Se_n chain molecules (n can be as big as 10^4-10^5 [24,25]). The viscosity of liquid selenium decreases with increasing temperature. That experimental fact is interpreted in terms of decrease of the average length of Se_n chain with increasing temperature. The presence of Se rings in vitreous Se and possibly in the melt was inferred from the partial solubility of vitreous Se in carbon sulfide CS_2. It is known that trigonal Se does not dissolve in CS_2 under all experimental conditions while monoclinic crystalline forms of Se dissolve completely in CS_2. On the basis of such observations it was assumed that CS_2 selectively dissolves only the Se_8 ring fractions of vitreous Se. The first attempts to measure "ring-chain" equilibrium in the Se melt were pioneered by Brieglieb and date back to 1929 [21]. He prepared vitreous selenium samples by quench cooling the melt from 217°C and from 427 °C. The samples produced were extracted with CS_2 and it was found 40% Se_8 rings for the samples quenched from (217°C) and only 18% for the sample quenched from 427°C. However as described in [21], in 1970s it was found that IR spectra of vitreous Se samples produced in the way described above are not significantly different. More importantly, the IR spectrum does not change after extraction with CS_2. In his works, Lucovsky [19] has shown that vitreous selenium dissolves in CS_2 only if illuminated with light having photon energies greater than 2.3 eV ($\lambda < 540$ nm) while α-monoclinic selenium dissolves easily and the dissolution speed does not depend on the presence of illumination. Briegleb does not comment on this fact. Lucovsky was eventually able to interpret the molecular spectra of vitreous selenium on the assumption of a chain structure with random distribution of cis and trans linkages. A section of a chain of this type is illustrated in Figure 2.1-(f). The experimental radial distribution function measured in different x-ray, electron and neutron diffraction experiments on vitreous selenium at that time coincides rather well with the curves calculated in accordance with the latter structural model and the existence of separate monomeric Se_8 rings in vitreous selenium gradually became questionable. Such a conclusion was probably premature because at present, some researchers [26] support the understanding that based solely on diffraction data, it is not possible to determine if amorphous selenium consists of long chains, Se_8 rings, or a mixture of both.

However, in 1989, Miyamoto [22] grew a selenium crystal from the saturated solution of CS_2 that was identified with the help of the x-ray analysis as a new allotropic rhombohedric modification of selenium that is constructed from Se_6 rings (see Table 2.1). According to Miyamoto, the probability for formation of Se_6 rings during the crystal growth from CS_2 solution is very small. He thinks that these molecules came from dissolved vitreous selenium. Further, Miyamoto proposed a new model of vitreous selenium consisting of three types of molecules: Se_8 ring, Se_6 rings and polymeric chains. The content of each molecular component depends on the method of glass production. It has to be noted that the amount of monomer (ring molecules) content is much lower than the one proposed from Briegleb. For example a resent Raman scattering study [27] have shown that the monomer content does not exceed 15% close to the glass transition temperature of vitreous selenium. The monomer content has week temperature dependence and extrapolates nicely to the dissolution data of Popov [28]. The latter author used CH_2I_2 as a solvent that dissolves only selenium rings and found that sample of vitreous selenium quenched from 250 °C have only about 5% rings while the content in samples quenched from 400 °C drops to only about 1%.

Based on part of the information presented above, Minaev [21] have drawn the conclusion that vitreous selenium is constructed mainly of tangles of chains consisting of fragments of rings (Se_8 and Se_6) and fragments of chains of trigonal selenium. Separate Se_8 and Se_6 rings are also present to much lesser extend.

2.1.2.2 Non-Vitreous, Non-Crystalline Selenium

In his paper [21] Minaev, mentions several non-crystalline non-vitreous forms of "amorphous" selenium: red, black (Table 2.1) and brown, and of course a-Se produced by vacuum deposition technique. Red "amorphous" selenium according to Feltz [20] can be prepared by direct precipitation of Se from acidic serenity solutions, for example according to the reactions

$$\begin{aligned} &H_2SeO_4 + N_2H_4 \longrightarrow Se + H_2O + N_2 \\ &H_2SeO_3 + 2\,SO_2 + H_2O \longrightarrow Se + 2\,H_2SO_4 \end{aligned} \tag{2.1}$$

or by quenching Se vapors to a temperature of about 85 K. Little is known about its structure. As explained in the previous subsection, the solubility in CS_2 can not be considered as evidence for the existence of ring molecular units. The enthalpy change on transition to trigonal Se at room temperature (298 K) is 12.5 kJ mol^{-1}. This value is 2.5 times higher than the one connected with the crystallization of vitreous selenium. The higher energy content of red "amorphous" Se is probably due to a higher content of distorted configurations in the polymeric Se_n chains such as cis linkages with distorted dihedral angles, which leads to ring closure to Se_8 molecules in combination with the action of the solvent. The process is known in sulfur chemistry. When heated, the red "amorphous" Se transforms into black "amorphous" selenium at about 37 °C. The conversion is endothermic with enthalpy of about 0.4 kJ mol^{-1} [20]. The structure of black "amorphous" Se has not been investigated well enough. The infrared spectra of red and black "amorphous" Se are almost identical [20] as shown later in Figure 2.4 .

Vacuum evaporation produces amorphous selenium thin films, which have been investigate extensively in relation to their application in electrophotography in 1970s and more recently in x-ray medical imaging. Evaporated layers of selenium dissolve completely in CS_2 and are red transparent if they are not too thick.

Se vapors have complex composition. For example close to 330 °C the main constituents are Se_6 and Se_5 molecules, together with Se_8, Se_2, and Se_7 molecules. The former two remain at nearly constant concentrations up to 730 °C. The fraction of Se_2 and Se_3 molecules increases with increasing temperature at the expense of larger molecules. The resulting amorphous selenium layers are expected to have different structure depending on the evaporation and condensation conditions, such as source and substrate temperatures, evaporation rate etc. Trace impurities can inhibit or promote the crystallization tendencies which exist for all forms of non-crystalline selenium, and it is often very difficult to suppress the formation of nano- and micro-crystalline inclusions in vacuum evaporated Se layers [29, 30].

Popescu [21] divides non-crystalline vacuum deposited selenium into two forms: a-Se-I and a-Se-II. The first group includes samples deposited on a substrate kept at low temperatures, in the second group selenium produced at high temperatures and bulk vitreous selenium. Analyzing previous information on the structure of selenium based on IR-spectroscopy, Raman-spectroscopy, differential thermal analysis and other methods together with his own information based on x-ray scattering experiments, Popescu has come to the conclusion that the non-crystalline selenium structure consists of 8-member ring monomers and chain polymers. The main constituent of a-Se-II are selenium polymer chains while a-Se-I is build predominantly from Se_8 rings. Popescu investigated samples prepared at substrate temperatures in the range from 30 ^{o}C to 70 ^{o}C. The ratio "chains-rings" reached maximum at 50 ^{o}C. Further, the author has mentioned that the transformation of a-Se-I into a-Se-II is possible if the samples are annealed.

Takahashi et al. have investigated the properties of highly disordered amorphous selenium deposited on cold substrate held at 77 K by UV photoemission spectroscopy [31]. In order to explain the observed spectra and their irreversible thermally induced changes, the authors have proposed a new structural model for a-Se. According the latter model a-Se consists of regular very short (about 10 atoms) chains (clusters). The dihedral angles inside each short chain are the same as in trigonal Se while the bond angles are slightly distorted. The clusters are connected to one another with dihedral angle that differs than the one in trigonal selenium. Such model is in relatively good agreement with the data about Se vapor presented above because at 77 K Se molecules are immobilized almost immediately after their arrival at the surface of the film.

2.1.2.3 Structure of Non Crystalline Forms of Selenium

The structure of all amorphous forms (noncrystalline solid forms) is not fully understood in spite of several decades research. One of the most recent attempts to explain the structure of noncrystalline forms of selenium and their transformations with temperature and time is due to

Minaev and his concept for the polymeric-polymorphoid structure of the glass [21]. According to this concept, all forms of non-crystalline selenium are constructed of copolymerized in the greater (vitreous Se) or lesser extent (the other noncrystalline forms of Se) structural fragments of crystal lattices (polymorphoids) of trigonal, monoclinic and sometimes rhombohedric modifications without a long range order. Thus chain structures are formed. Some segments of these chains will have the trans configuration characteristic for trigonal selenium, while other segments will have the cis-configurations characteristic for Se_8 and Se_6 ring molecules from which the monoclinic and the rhombohedric modifications of selenium are built. The average coordination number for amorphous selenium measured for example in [32] is about 2.2. This means that some of the chains form "stars", in which threefold and fourfold coordinated selenium atoms are located. Besides the chain structures the non-crystalline selenium contains, in the greater or lesser extent, separate eight-member and six-member ring selenium molecules.

The concentration ratio of different polymorphoids is a fundamental characteristic of condensed selenium. Under factors like irradiation, pressure, temperature, time etc., the inter-transformation takes place between the polymorphoids of different polymorphous forms and the ratio of the concentration of different polymorphoids is altered. It seems as if the non-equilibrium selenium "memorizes" all inherited crystalline modifications and relaxes in the direction of formation of polymorphoids of the crystal modification stable under the given conditions.

This concept is not well established but is capable of explaining many structural properties and experimental facts related to different transformations of the non-crystalline forms of Se including the effects of temperature and ageing [21].

In conclusion we have to say that the structure of a-Se is not unique. The review above suggests that huge variations in structure and in properties of a-Se are possible depending on the properties of the staring selenium material (origin, purity, preparation conditions, ageing history, etc.), sample preparation conditions and post-treatments of the sample (storage conditions, annealing, ageing, etc.).

2.1.2.4 Structural Defects in Amorphous Selenium

The main reason for the structure and for the semiconductor properties of Se is its twofold coordination and van der Waals interactions between the molecular units (chains and rings). In crystalline, in amorphous and in liquid selenium the majority of the atoms are bonded to two nearest neighbors. Any deviation from that bonding configuration can be considered as a defect in the structure of Se. Obviously, the atoms at the ends of Se chains are singly coordinated. These defects are the only possible under-coordinated structural defects in Se. A Selenium atom can form from 1 to 4 bonds in his normal valency configuration and up to 6 bonds in its "hyper-valent" configuration (SeF_6 for example). Such properties makes the existence of many over-coordinated defects possible and thus the average coordination number slightly in excess of two measured in many experimental works (see for example [32]) seems natural.

The existence of structural defects in chalcogenide glasses gives rise to very interesting properties. There is evidence from electronic and optical phenomena that amorphous selenium has a significant density of gap states with Fermi level E_F pinned near the center of the optical gap. Singly occupied defect states near E_F would be expected but the absence of Electron Spin Resonance (ESR) signal or paramagnetism rules out their existence [33, 34].

Among the numerous publications with regard to defects in a-Se are the models developed by Street and Mott [35], Kastner and Adler and Fritzsche [36] and Vanderbuilt and Joannopoulus [37,38] that have received most of the attention of the scientific community. Using the idea of Anderson [39] on defects with negative correlation energy (negative U defects), Street and Mott proposed the idea that the dangling bonds D^0 generated naturally by breaking bonds homolytically can lead to charged defect centers:

$$2D^0 \rightarrow D^+ + D^-, \tag{2.2}$$

where D denotes a defect without any reference to coordination or geometry. The authors have assumed that the reaction is exothermic by means of significant phonon contribution.

Kastner, Adler and Fritzsche have tried to analyze the coordination environment and electronic structure of these defects. From the exothermic nature of the reaction in Eq. (2.2) they have concluded that all defects generated by homolytic bond scissions will eventually transform into pairs of threefold coordinated positively charged defect centers C_3^+ and singly coordinated negatively charged defect centers C_1^-. In that notation C denotes Chalcogen atom, subscript and the superscript represent the coordination and the charge of the centre respectively. The pair $C_3^+ - C_1^-$ is known as a "valence alternation pair" or VAP. It was assumed that the lowest-energy neutral defect is the three-fold coordinated atom C_3^0. An essential feature of the proposed model is that even C_3^0 defect will spontaneously change by the exothermic reaction to form a VAP

$$2\,C_2^0 \rightarrow C_3^0 + C_1^0 \rightarrow \left(C_3^+ + C_1^-\right). \tag{2.3}$$

If in the so formed VAP C_3^+ and the C_1^- atoms are near each other then a strong Coulomb attraction exists between them. This type of VAPs are assumed to be stable and are called "intimate" (non random) valence alternation pairs or IVAPS. The defect states with lowest energy in the theory are either doubly occupied or unoccupied. Such defects do not carry a net spin. This explains the absence of dark ESR signal and why the low-temperature material is diamagnetic. The paramagnetic behavior at medium temperature is presumed to arise from the electronic excitation of C_1^- and C_3^+ defects to form neutral C_1^0 and C_3^0 defects carrying net spins. The unusual properties of lone-pair semiconductors, including Se, such as reversible photostructural changes, photoinduced diffusion, crystallization, phase separation and decomposition are all believed to be strongly connected to the bond switching and the chemical reactivity associated with the photo-excited VAPs. The VAP model has been verified by some molecular-dynamic simulations [40] and more reliably by some experiments. For example, the ESR experiment by Kolobov et al. [41] is believed to give a direct experimental evidence for the existence of negative-U centers and valence alternation in amorphous selenium. The latter authors have observed two different kinds of electron spin resonance (ESR) signals, triclinic and isotropic, in amorphous Se under photoexcitation at 20 K with a concentration of up to 10^{20} cm^{-3}. ESR signal annealing behavior suggests that isotropic centers are not stable and are converted into triclinic defects. The defects are identified as singly and triply coordinated Se defects. These results in the opinion of the authors of [41] present direct experimental evidence for negative-U centers and valence alternation in amorphous selenium.

However, the average coordination number in a-Se is about 2.2 [32] and that can not be explained in terms of predominant VAP defects simply because the average coordination number of a VAP is exactly 2. In addition, Vanderbuilt and Joannopoulus [38], by means of mathematical simulations, have found that the energy necessary for the creation of defects in the framework of VAP theory is bigger than the binding energy E_b and from the bandgap energy E_g for practically all VAP configurations with one exception. If the calculations are correct the VAPs can not be the predominant type of defects in a-Se.

On the basis of the results of Vanderbuilt and Joannopoulus, and some chemical evidence, Steudel [42] have suggested that the hypervalent configurations $C_3^d - C_1^d$ and C_4^0 shown in Figure 2.2 are the most probable defect structures in a-Se. The subscript *d* denotes that the bond between the threefold coordinated atom and the singly coordinated atom is double. The existence of the defect $C_3^d - C_1^d$ has not been confirmed so far, but some evidence for existence of C_4^0 defects has been provided by molecular-dynamic simulations [43] and the "footprints" of such fourfold coordinated defects have been found in the IR spectra of red "amorphous" selenium [45].

Hohl and Jones [43] in their first-principle molecular-dynamic simulation have found that the concentration of threefold coordinated defect is 4 times bigger than the concentration of singly coordinated defect sites. According to the authors the defects of the type C_3 have the tendency to pair and form a new defect in the structure C_3-C_3 as shown in Figure 2.3. Almost 82% of the C_3 defects were found in pairs C_3-C_3. About 12% of threefold coordinated defects were in VAP pairs C_3-C_1 and the rest 6% existed as isolated C_3 sites. Some isolated C_1 defects were found to exist together with C_4^0 defects that had almost the same structure as proposed by Steudel.

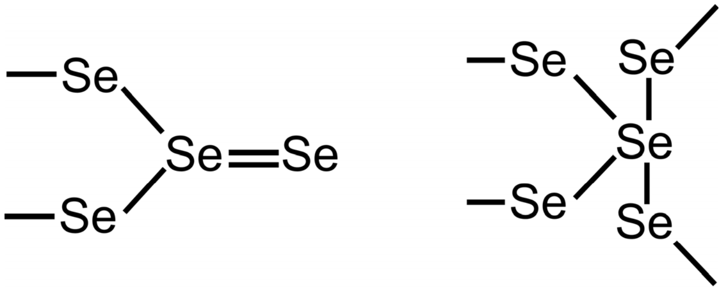

C_3^d—C_1^d C_4^0

Figure 2.2 Hypervalent defect structures in a-Se as proposed by Steudel [42].

The simulation methods used in this work were later criticized by Xiaodong Zhang, D.A. Drabold [40]. They argued that the described system is not well relaxed and have found that the well relaxed Hohl and Jones model contains only six defect states: two IVAPs C_3-C_1, one C_3 and one C_1 defect.

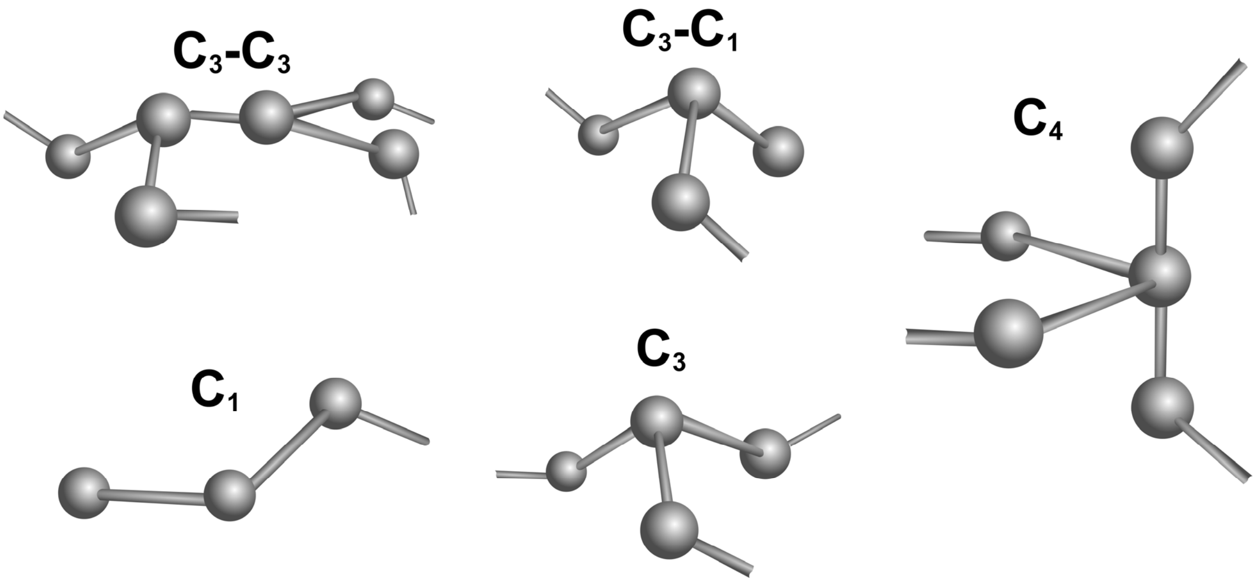

Figure 2.3 Diagrams of the defects encountered by Hohl and Jones in their molecular-dynamic simulation of liquid and amorphous selenium [43]. Their simulations find a new candidate for the predominant defect structure; a pair of threefold coordinated atoms C_3-C_3 and confirms the existence of fourfold coordinated defects C_4.

In our view molecular-dynamics simulations are not reliable methods for the determination of defect concentrations. Most of the calculations were performed on systems of 64 atoms (on 216 atoms more recently). A single Se chain can have as much as 10^4-10^5 atoms. Simulation based on models containing more than ~4000 atoms are not possible at the present time. The results of the simulations based on models containing 64 atoms can easily became compromised by severe scale effects. So, the calculated equilibrium concentration of defects and densities of the electronic states are not very reliable. However, having in mind the bonding flexibility of Se and the variability of its structure and properties, probably all of the defect structures proposed so far can be found in a real a-Se sample.

In support of the thoughts presented above we can mention that Dembovsky and Chechetkina [44], have proposed very similar defects to the ones shown in Figure 2.3 under the name "quasi-molecular defects". More recently, Zyubin et al. [45] have done quantum-chemical simulation of different defects appearing in a-Se. The stress was placed on three types of defects sites: IVAPs, C_4^0 and $-Se-Se_6-Se-$ defect (that is actually a pair of C_3 defects). The defects, the way in which they are formed, and their stability are shown in Figure 2.4 . The authors have further calculated the infrared absorption spectra for the different realizations of these defects. As a result they were able to find the "footprints" of the defects in experimentally measured spectra of a-Se samples as shown in Figure 2.4. The positions of weak additional minima in the experimental transmittance spectra of "red" and "black" amorphous selenium are in good agreement with the most intensive vibrational frequencies of the "hypervalent defects". The picture is consistent with the known structure of red and black "amorphous" selenium and the appearance of the minimum caused by the formation of IVAPs in the structure of the black a-Se is expected. The small intensity of these additional absorption bands suggests low concentration of such defects [45].

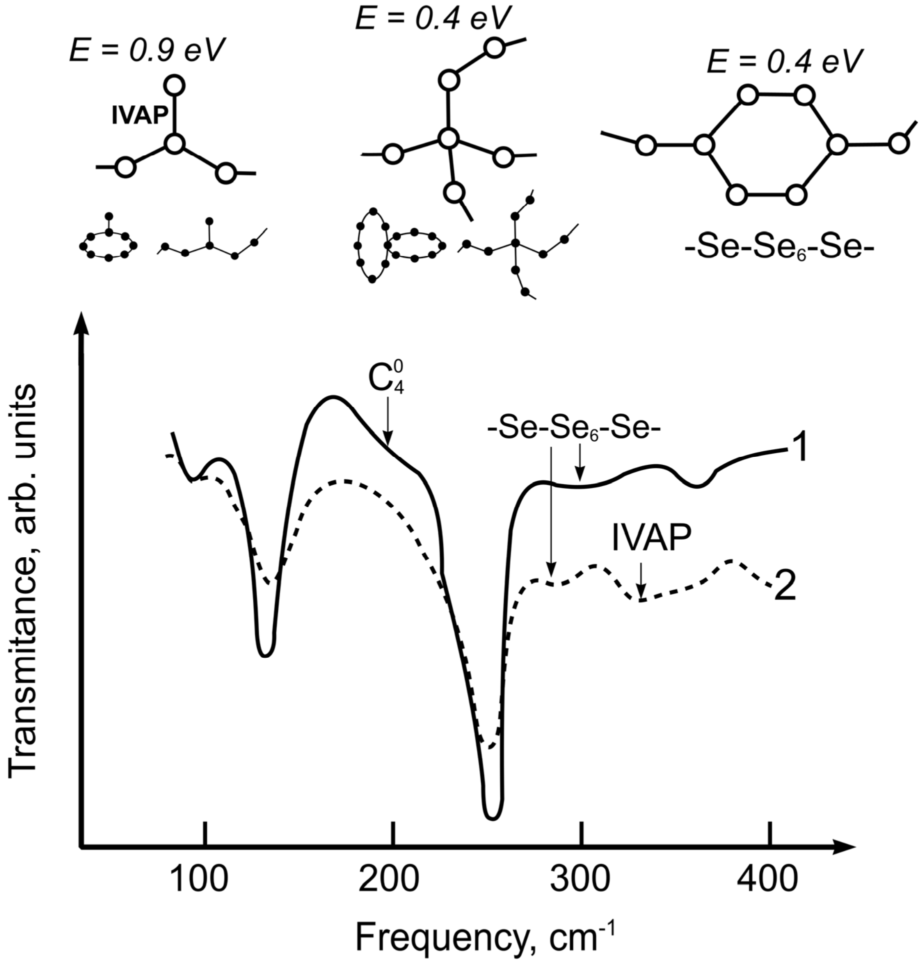

Figure 2.4 Defects in a-Se [45]: geometry, formation, stability and their "footprints" on the experimental infrared spectra of red (1) and black (2) "amorphous" selenium.

The defects described so far are native "atomic" defects in a-Se, i.e. deviations from the normal bonding configuration in Se. We have to admit that other defects can exist in a-Se related to the presence of different impurity atoms. Such atoms will generally have a valency that is different than that of Se and therefore will form under and over coordinated defects in its structure similar to the ones described above. One very important difference however has to be recognized. The size of such impurity atoms can be greatly different than the size of Se atom and this can trigger different size effects, formation of crystallization nuclei being one example.

It is almost impossible to produce ideal a-Se. In most cases it is impossible to totally suppress the formation of nano- and micro- crystal in the a-Se matrix [29]. Such crystalline inclusions represent another type of defect in the a-Se structure. Their concentration can be quite high – up to 10^{13}-10^{14} cm^{-3} and to complicate the situation even further they can belong to one of the numerous crystal modifications summarized in Table 2.1.

In the present time, the known data are insufficient and does not allow us to conclude which are the predominant types of defects in a-Se. The concentration and the nature of the structural defects in a-Se most probably depend, on the starting Se material, on alloying and doping, on the sample preparation technique, on storage conditions, etc. In addition, the concentration of different defects changes as the sample ages. The latter partly explains why the properties of a-Se are so difficult to investigate. Many of the properties of a-Se are strong functions of a very long sample history that includes in it the history of the starting Se material. In most of the cases such long history dependence is impossible to be followed exactly .What is worse, is that in some cases, sample history is totally neglected by most researchers. This is one of the reasons that substantially diverse results related to different properties of a-Se have been published in the literature.

2.2 Electronic Density of States in the Band Gap of a-Se

Although several points of view exist in the scientific literature [46], most of the researchers working with amorphous and crystalline selenium tend to interpret their experimental results in the framework of the band model for the semiconductors. Selenium is the only material that exhibits "semiconducting" properties in its crystalline, amorphous and liquid (near the melting temperature) states. This unique behavior is related to the molecular structure of selenium, which generally plays a key role for liquid and amorphous semiconductors [47]. As described in the previous subsection, the nearest neighbor distance and bond angles turn out to be very similar for the above phases of selenium. The predominant two fold coordination is the main reason for the semiconducting behavior of selenium as can be seen from the simple bond orbital model for this element. The electronic configuration of Se is $4s^2 4p^4$. Two out of the 4 p-electrons are involved in covalent intra-chain or intra-ring bonding. They form σ-type bands in the energy range 3-7 eV below the top of the valance band. The corresponding σ* untibonding states form the conduction band. The two low laying 4s electrons hardly participate in the bonding and the remaining two 4p electrons enter "lone pair" states which form the top portion of the valance band (0-3 eV below the band edge). This simple qualitative picture has been confirmed by calculations and photoemission experiments for crystalline, amorphous and liquid selenium [48, 49].

No significant tailing of the valence band edges into the band gap was observed for both amorphous and liquid selenium in the vacuum photoemission studies of Nielsen and Greuter [48, 49]. Their experiments suggest that the valance band edges are rather narrow with tailing of the order of ~ 0.1 eV. Such result is to be expected because; the top portion of the valence band is constructed from "lone pair" orbitals, which do not participate in bonding and that can qualitatively explain their relative "inertness" to the amount of structural disorder. The amount of tailing at the conduction band edge might be different for liquid and amorphous selenium and is expected to be bigger than the one at the valence band edge, since the conduction band in Se is build by σ* untibonding states and larger distortions are expected as a response to fluctuations in local bonding geometry.

For a-Se films produced by vacuum evaporation Nielsen has estimated the upper limit of the density of states in the gap as 10^{20} $eV^{-1}cm^{-3}$ [48]. In the same work he has found that the density of states in the gap around the Fermi level is less than 2×10^{14} $eV^{-1}cm^{-3}$ and that the density of surface states is less than 10^{10} $eV^{-1}cm^{-3}$. The last number means less than one site per 10^5 surface atoms which is in agreement with the idea that the valence requirements are fulfilled for all the atoms in a-Se films.

One of the most often cited models describing the density of states (DOS) in the gap of a-Se and being in good agreement with the data from the photoemission measurements described above has been proposed by Abkowitz [50] in 1988. The later model is a natural extension of Marshall and Owen model [51] describing the density of states in the gap of the amorphous As_2Se_3. The main features in the density of state distribution proposed by Abkowitz are illustrated in Figure 2.5. In addition to the quickly decaying band tails four sets of states with relatively narrow distributions on the energy scale are present in the model. The set of states situated close to the band edges act as shallow traps for charge carriers in a-Se. Such set of shallow traps known to control the mobilities of holes and electrons in selenium through the process of multiple trapping and detrapping in these states. The position of the shallow trap peaks have been derived from the analysis of the temperature dependence of the mobility of the holes and electrons in time-of-flight transient photoconductivity measurements performed by Kasap and Juhasz [52]. The positions of the traps near the Fermi level have been determined from the analysis of time-resolved xerographic measurements in a-Se films. These deep sites act as deep traps for the charge carriers because the thermal release time from them is much longer than the time scale of the associated experiment. Thus, their concentration determines the lifetimes of charge carriers in amorphous selenium.

Each of the four main trap levels is probably related to certain types of defects in a-Se. Numerous intrinsic structural defects can exist in a-Se as described in the previous subsection. Vast variety of extrinsic defects due to impurities and doping are also possible. The energy levels of both intrinsic and extrinsic defects in selenium are not known. Although many authors have tried to relate certain set of traps to the defects in Se such as VAP for example, the suggested relations up to date are mostly speculative.

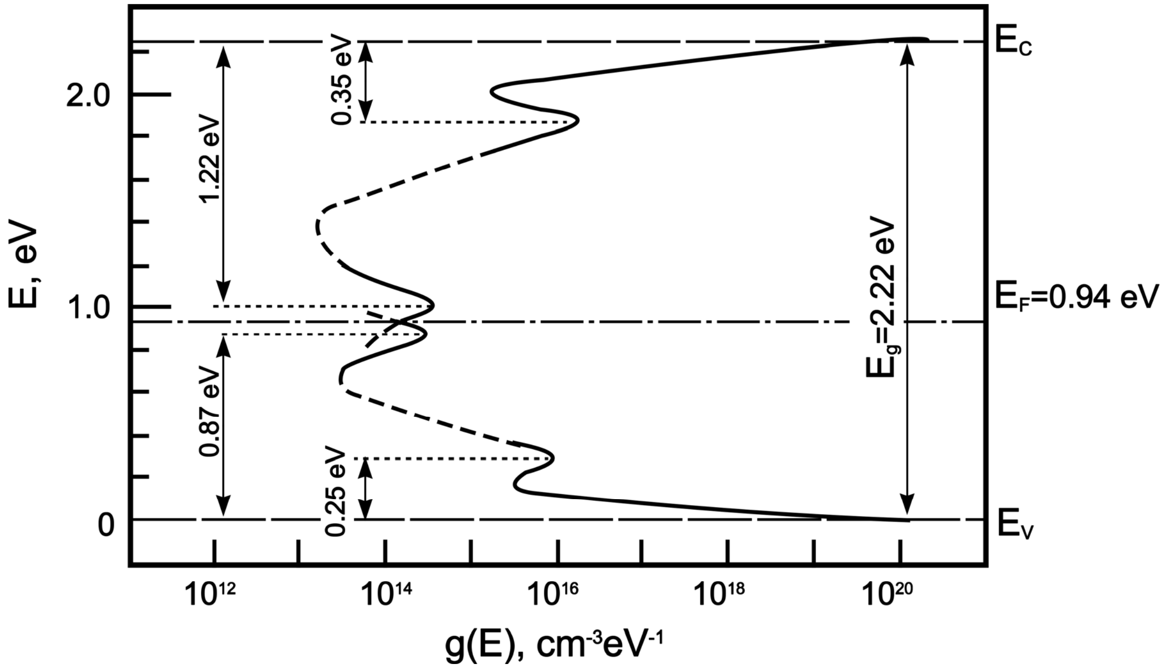

Figure 2.5 Density of electronic states in amorphous selenium proposed by Abkowitz in [50].

A study of the scientific literature on a-Se before Abkowitz's paper [50] will reveal that many researchers have interpreted carrier transport in a-Se in terms of several relatively narrowly distributed or even discrete trap levels. For example, in 1967 Blakney and Grunwald [53] analyzing the shape of TOF transient photocurrents in a-Se films have concluded that the electron transport in a-Se can be interpreted in terms of 3 discrete levels of traps. The position of two of those levels, coincide rather well with the positions in Abkowitz's model. The third set of traps, according to Blackney and Grunvald positioned between the trapping levels proposed by Abkowitz at about 0.40-0.48 eV below the bottom of the conduction band. In 1969 Turgul Yasar [55], studying the transient polarization currents in a-Se, found that the hole transport in his experiment is controlled by two levels of traps 0.48 and 0.8 eV above the edge of the valence band. In 1977 Noolandi [56] found that 3 trapping levels for holes needed to fit his experimental TOF data for holes with precision better than 5%. All these works suggest that an intermediate third level of trap exists for both holes and electrons in a-Se. These trap levels are positioned somewhere in between the shallow traps controlling the mobility and the deep traps controlling the lifetime of the carriers in Abkowitz's model.

The knowledge on DOS distribution in the bandgap of a-Se until early 1990s can be summarized as follows. The DOS distribution in a-Se is quite shallow. This means that both the valence and the conduction band edges are relatively sharp. Band tailing in the bandgap is relatively small. The distribution of the tail states in the gap can be as narrow as 0.1 eV [48, 49] both near valance and the conduction band edges. At least three different discrete or relatively narrowly distributed set of traps are present in the gap of a-Se for both holes and electrons. The peaks in the DOS distribution around 0.25 eV above E_V and 0.35 eV below E_C (see Figure 2.5) are known to control the mobility of holes and electrons in a-Se respectively. The existence and positions of these shallow peaks were determined based on the interpretation of the TOF data of Kasap and Juhasz [52] and in more direct micro stripline experiments performed by Orlowski and Abkowitz [53]. Very similar mobility controlling peaks are present in [53] and [56]. The deep peaks near the Fermi level in Figure 2.5 control the lifetime (the deep trapping time) of the holes and electrons in a-Se. Their existence, amplitude and positions were confirmed by time-resolved xerographic residual and dark depletion potential measurements in [50], transient polarization currents data in [55] and by the technique of thermally stimulated currents for example in [57]. Similar deep sets of traps are present in [53] and [56]. Finally, a number of researchers have suggested that third set of trap exists for both holes and electrons in a-Se. These sets are not shown in Figure 2.5 and are missing in Abkowitz's model and have been neglected by the researchers for many years. According to the authors of [53, 55 and 56] these intermediately deep set of traps are located in the range 0.4-0.5 eV from the band edges for both holes and electrons.

The knowledge about the DOS distribution in the gap of a-Se has not improved significantly since the end of 1980s and remains controversial even today although significant number of works has been published in the field during the last 7-8 years.

Starting in 1999 a group of researchers headed by Adriaenssens have published considerable number of papers on the subject; works [58-65] being only part of the cycle. These researchers have used their post transit photocurrent analysis PTPA technique (see section 3.3.7.3 for details) to map the DOS distribution in the gap of a-Se. Based on that method Song and coworkers [58] have rediscovered the long neglected set of traps described at the end of the previous paragraph. PTPA gave the following positions for the "new" peaks: 0.4-0.5 eV above the valence band edge and 0.55-0.65 eV below conduction band edge. The energy positions of these two peaks do resemble $\frac{E_g}{4}$ and $\frac{E_g}{3}$ and that lead the authors to the idea to interpret their results in the framework of the standard "negative U" [39] model for a-Se [36]. The measured DOS distribution was explained in terms of VAP (a pair of C_1^- and C_3^+) existing in a-Se. Thus the first peak was related to the C_1^- defect states in a-Se and second one - to C_3^+ ones. The picture was almost perfect except that the original model of Abkowitz (Figure 2.5) had in it two other set of peaks at absolutely different positions, which obviously had to be related to other distinctly different defect types and what is more important these peaks do not fit in the standard negative U model of a-Se. The researchers in Adriaenssens's lab decided to overcome that last obstacle by questioning the existence of the peaks in Abkowitz's model, although all of those peaks are well out of reach of the experimental technique used by them. This gave birth to the speculation [58] that the set of the two shallow peaks in Figure 2.5 was entirely due to the misinterpretation of the experimental TOF data by Kasap and Juhasz. The basic idea was to show that there exists another interpretation of the experimental data that does not require the existence of shallow peaks superimposed on the band tails as in the Abkowitz's model. Based on the results of previous experiments and modeling [66-68], the authors of [58] have concluded that drift-mobility activation energy curves from the data of Kasap and Juhasz "should be interpreted as evidence for a continuous featureless distribution of tail states in which the MT (multiple trapping) transport takes place, with smaller field dependences indicating steeper tails, and vice versa". Finding explanations for the "false" appearance of the peaks near the Fermi level in Abkowitz's model of DOS distribution in a-Se was not so easy, because even the data in [58] give indication that such peaks can exist. However, the authors have done quite well suggesting that these peaks could appear due to "artifacts" in both the xerographic experiments of Abkowitz and in their own measurements.

The DOS distribution for a-Se that originated from [58] was "refined" in several other papers and is presented in Figure 2.6. However, the explanation for the absence of shallow and deep peaks (equivalent to the ones proposed by Abkowitz's) in the DOS distribution of a-Se presented in Figure 2.6 were highly speculative and naturally the model presented in the figure did not last for very long time. Indeed, researchers from the same group have found evidence for existence deep set of traps located close to the equilibrium Fermi level in a-Se analyzing steady state photoconductivity currents in that material at low temperatures [62].

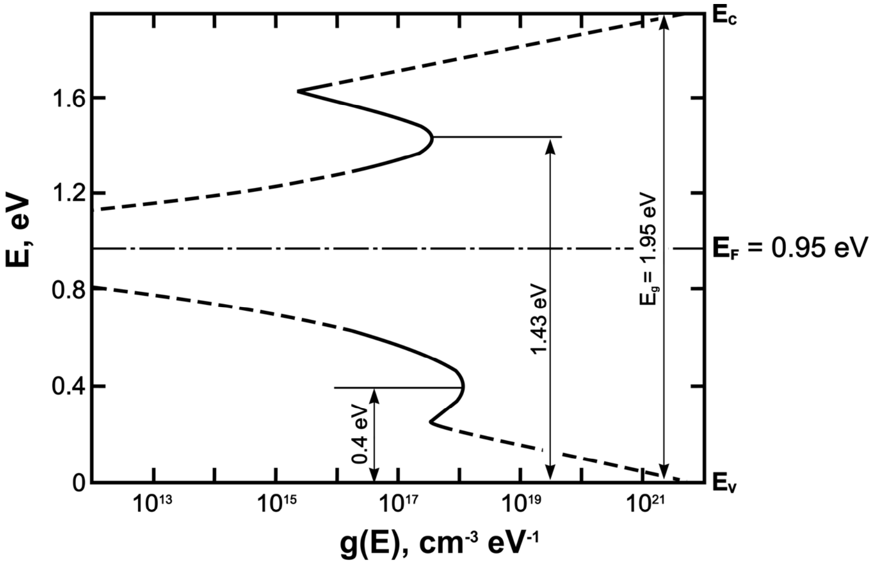

Figure 2.6 Density of states in a-Se deduced from steady state and transient photoconductivity measurements by Adriaenssens's group of researchers. The position and the width of the peaks are taken from [60,61]. The distribution of tail states may, to first approximation, be described by as steep exponential with a characteristic width of ~24 meV at the valence band and a more steeply declining functional of similar width at the conduction band. The full curves correspond to the energy range that is accessible in the post transit time-of-flight experiments.

Again work published by the same group [64], discusses the existence of similar deep relatively discrete states in the gap of a-Se. What is more interesting in the very same work [64] they claim that have found evidence for existence of a discrete defect level about 0.28 eV below the conduction band edge of a-Se.

Further the same group, under the influence of ideas presented by Koughia et al [69-70] which will be discussed later in this section, has tried to model the DOS distribution in the gap of a-Se near the conduction band as a sum of an exponent and three Gaussians [65]. That implies that three distinctly different set of electron traps (defect levels) exist in the band gap of a-Se. The positions of these traps were found to be 0.3 eV, 0.48 and below 0.65 eV from the conduction band edge. The characteristic width of the exponent in the same work was found to be 20 meV.

We can summarize the developments on the DOS distribution in the bandgap of a-Se as follows: a-Se has relatively sharp bandgap edges compared to the rest amorphous semiconductors. It seems that there are at that least 5 different sets of defects positioned in the gap; three of them act as electron traps and two as hole traps. What is left to completely confirm the situation known from the end of 1980s is to prove once again that shallow hole traps exist ~ 0.25 eV above the valence band edge.

Other recent works that have attempted to reveal the "real" electronic DOS distribution in the bandgap of a-Se are due to Koughia et al. [69-71]. The approach is very similar to the one described by Noolandi in [56]. It is based on an approximate numerical inversion of the Laplace transform of the theoretically calculated photocurrent for a given DOS distribution and comparing the result with the experimentally obtained photocurrent traces. There are two main differences in the approaches of Noolandi and Koughia. First, Koughia is using a technique for the approximate inversion of the Laplace transform that is different than the one used by Noolandi. Second, while Noolandi is seeking DOS distribution in the form of sum of discrete trapping levels, Koughia is trying to represent the DOS distribution as a nearly continuous function; to be more precise as a sum of predefined functions (a sum of spline functions in the earliest work, which was changed to a sum of an exponential and several Gaussians in later works). The basic results of the research efforts in [69-71] are presented in Figure 2.7.

The distribution above the Fermi level is in good agreement with the existing experimental data. In addition to the sharply decaying tail states, two relatively narrowly distributed peaks located at 0.3 and 0.5 eV below the band edge exist in the proposed model. From the TOF data, only the integral concentration of the deep states (further than 0.65 eV away from the band edge) can be determined. Although, the exact distribution of these states can not be determined from the experimental data their existence is justified.

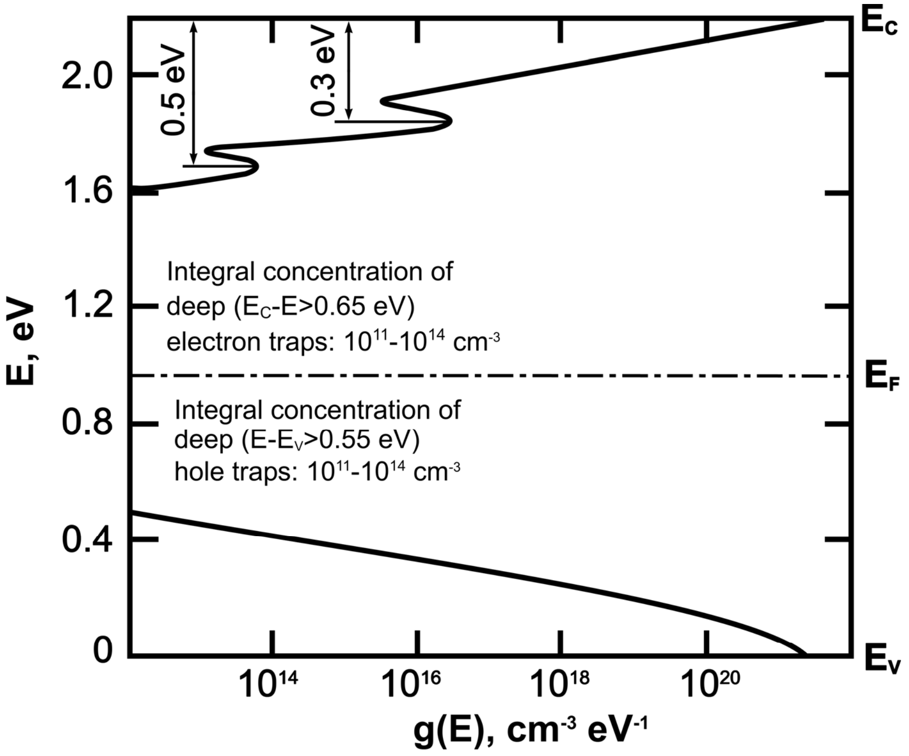

Figure 2.7 The asymmetric DOS distribution in the gap of a-Se proposed by Koughia and coworkers [69-71]. The distribution above the Fermi level is very close to the one known in the late 1980s - sharp exponential tail with a characteristic width of 20 meV , two relatively sharp peaks at 0.3 and 0.5 eV below E_c, and a set of deep states situated more than 0.65 eV below E_c. Surprisingly, the distribution near the valence band edge is featureless and to first approximation can be presented by a single exponent for the energies starting 0.2 eV above E_v. A set of deep hole traps situated more than 0.55 eV above the valence band is a feature of the proposed distribution.

However, the distribution near the valence band edge is considerably different from the most common views presented in the scientific literature. The distribution of the electronic states near the valence band edge is "flat", meaning that it has no features. Actually, 0.2 eV away from the band edge, the distribution can be approximated with a single exponent. Some deep states with integral concentration in the range 10^{11} - 10^{14} cm^{-3} are confirmed by the analysis of the experimental data though their exact distribution cannot be resolved due to the limited timescale of the experiments. The distribution of hole traps bares no resemblance to the models proposed by Abkowitz (Figure 2.5) and Adriaenssens (Figure 2.6). However, the calculated distribution is in good agreement with the DOS distribution near the valence band proposed by Naito et al. [72].

The DOS model proposed by Koughia and presented in Figure 2.7 correctly predicts the dependence of carrier mobility (μ) on temperature (T) at different electric fields (F). The calculated $\mu(1/T)$ curves at different fields F coincide well with the experimental data which is a merit of the proposed distribution. On the negative side, the distribution of electronic states near the valence band edge proposed by Koughia, predicts more tailing than it was experimentally observed in [48, 49]. The valence bands in a-Se and in trigonal allotrope of crystalline Se are build by lone pair orbitals and for reasons explained in the beginning of this subsection and acknowledged in [71] should have a lot of similarities. It is known that, in trigonal Se there exist three types of hole traps 0.09, 0.21 and 0.47 eV above the valence band; see [76] for example. The analogs for the later two levels might be with very low concentrations in a-Se but is difficult to imagine that their existence is totally masked by the disorder in a-Se, because a number of other researchers, as previously described have found some prove for their existence in a-Se.

Only the future will show how correct is the DOS distribution of electronic states above the valence band proposed by Koughia and how the exact DOS distribution of a-Se will look like. However, there are a few general remarks on the mathematical nature of the techniques that are used to recover the DOS by different authors that we will like to comment below. First, there are several mathematical techniques which are based on approximate inversion of the Laplace transform of the photocurrent. For the calculation of the DOS distribution in the range 0.1-1.0 eV away from the band edge one will need to record and analyze TOF photocurrent ranging in time about 15 orders of magnitude (10^{-11}-10^{4} s). Recording transient photocurrent with the necessary precision over such huge range is on its self a challenging experimental task. Finding an approximate inversion of the Laplace transform that will give acceptable precision in such huge time range is an extremely difficult mathematical mission. Second, most of the authors usually acknowledge that the problem is ill-conditioned and the DOS derived “satisfies all requirements that define generalized solutions of so-called *ill-posed* problems". However, in the majority of the works on recovering the DOS in a-Se a proper regularization technique is never systematically applied, although in general most of the methods bare some elements of regularization. For example, in [69-71] the author searches a solution (DOS distribution) that has a certain predefined form (sum of splines or sum of a exponential and several Gaussians) and that is known as "quasisolution" in the sense of Ivanov [73]. However, in such situations one never knows how well the compromise between stability and sensitivity is struck. The computed solution can easily be "over smoothed" (revealing less structure than the really existing one) or "under regularized" – showing more structure than the one that can be found in the real solution. Technique, like Monte Carlo simulations that is in many cases used by the authors to check the calculated solution is incapable of distinguishing between "over-smoothed" and "under-regularized" solutions. Third, a problem that is often neglected is the lack of short term and long term experimental data that are out of reach for the particular experimental setup used to record the photocurrents. For example, the authors of [71] have indeed analyzed TOF data from many different sources, however for all these sources the short term portion (10^{-11} - ~10^{-6} s) of the TOF waveform is missing due to the limited instrumentation response time. Such lack of short-term data has been shown to lead to miscalculation of the DOS distribution function [74, 75]. In 1999 Nagase et al. [74] have demonstrated that calculation based on Laplace transform technique using waveforms that do not contain data for times shorter than 10^{-6} s can fail to return existing deeply lying (up to 0.5-0.6 eV from the band edge) peaks in the DOS. The lack of short term data actually explains the good agreement between the DOS distributions near the valence band calculated in [71] and in [72] by the use of different numerical techniques for solving the same set of multiple trapping equations. The analyzed photocurrents, in both works, are missing the short time data and according to [74] the calculated solutions will contain no peaks in the energy interval from 0 to 0.6 eV away from the valence band.

The highly controversial situation with regard to the DOS distribution in the bandgap of amorphous selenium is direct consequence of our lack of satisfactory understanding of the structure of a-Se which was described in subsection 2.1. The works published after late 1990s although relatively big in number failed to significantly improve the understanding about DOS in the gap of a-Se. The most important group of reasons for that failure is the fact that most of the researchers failed to understand completely the underlying limitations of the problem for the recovery of the DOS distribution function from experimentally measured photocurrent. The DOS distribution function and the experimentally accessible currents are related through some sort of Fredholm integral equation of the first kind which can not be solved in a closed form. Finding a numerical solution of such integral equations is known to be an ill posed problem, in some cases severely ill posed problem. This term means that the solution may not exist, may not be unique and may not continuously depend on the input data. Strictly speaking there is an infinite amount of information about the DOS distribution function that can not be recovered from the experimental photocurrent. The amount of information that is recoverable is limited by the signal to noise ratio (SNR) of the experimental data. The SNR ratio with which the current is measured in any of the published works probably does not exceed 20 and that is far away from being sufficient for high resolution analysis no matter what numerical algorithm is used to calculate approximately the DOS distribution function. The situation is even worse because the photocurrent data are incomplete. The photocurrents can not be recorded for periods very shortly after the excitation, and the currents can not be reliably followed for sufficiently long times after the excitation due to various limitations. Thus, the low quality of the experimental data, limits the amount of information about the density of states that can be recovered through analysis of the photocurrent. This limit is fundamental and the resolution can not be improved by the implementation of better numerical algorithms. Through a detailed analysis that is beyond the scope of this work, one can show that based on the quality of the published data, the DOS distribution function can be recovered with precision that is quite low, probably not better than 6-10 degrees of freedom. Any attempt to recover more information about the DOS distribution function can not be justified mathematically. Such low resolution is not sufficient to describe even the general case of 3 discrete trapping levels and so, none the DOS distributions described in the subsection can be strictly justified mathematically because they are trying to recover a structure that is well beyond the fundamental limits imposed by the quality of the experimental data. The situation is even worse due to the ill posed nature of the problem. It can be shown that one and the same set of experimental data can be fitted by more than one combination of discrete trapping levels and in the same time by at least one continuous distribution of traps. Among those solutions the researchers involved in studying DOS distribution in various amorphous semiconductors will normally select the one that fits best (with smallest error) the experimental data. It can be demonstrated, however, that the error of the fit alone is not a sound criteria for selecting a solution of an ill posed problem.

DOS distribution in the gap of a-Se is obviously a theoretical problem that requires much more careful studies in the future. On the positive side most problems in which a-Se is involved as an x-ray photoconductor can be successfully modeled in terms of only two effective trapping levels: one shallow that controls the mobility of the carriers and one other - a deep one that defines the lifetime of the carriers under the given experimental conditions. Thus the whole discussion in this subsection has only theoretical significance.

2.3 Amorphous Selenium as a Photoconductor

Any material that possesses a certain amount of photoconduction can be applied as a radiation detector. A material is a photoconductor if free charges can be generated in it when it absorbs radiation and if the generated free carriers can be transported trough that material by the application of an electric field to form a measurable electrical signal. Free carriers can be generated in amorphous selenium under irradiation with many different radiations such as light, x-rays, gamma rays, α- and β- particles, and probably by other charged particles. Both electrons and holes can travel in a-Se under the influence of an applied electric field. This obviously makes a-Se a good photoconductor and the purpose of this subsection is to provide some data related to the photoconductive properties of a-Se.

2.3.1 Optical Photogeneration in Amorphous Selenium

Any incident optical photon with sufficient energy can with certain probability excite an electron from the valence band into the conduction band. The probability that absorption occurs is determined by the optical absorption coefficient α of the material. This value depends on the incident photon energy and the magnitude of the DOS at the band edges. The absorption is extremely small if the energy of the incident photon is less than the band gap of a-Se. As the energy of the incident photons increases to the value of the bandgap and above, the magnitude of the absorption coefficient abruptly raises.

Experimental studies have shown that shown that the optical absorption coefficient of a-Se exhibits an Urbach edge of the form

$$\alpha(E) = A\exp\left(\frac{E}{\Delta E}\right), \tag{2.4}$$

where E is the energy of the incident photons, and A and ΔE are constants. Such behavior was explained following [77] in terms of optical transitions between tail states and extended states. The values of constants A and ΔE in this study were found to be ~7.35×10^{-12} cm^{-1} and ~ 0.058 eV respectively. At higher photon energies, as described in [78] the absorption coefficient obeys

$$\alpha E \propto (E - E_0), \tag{2.5}$$

where E_0 is the optical bandgap of a-Se with a value of 2.05 eV at room temperature.

A dependence following Tauc's law

$$\alpha E \propto (E - E_0)^2 \tag{2.6}$$

with $E_0 = 1.95\, eV$ has also been observed experimentally [79].

The dependence of the absorption coefficient of a-Se on the photon energy can be readily measured experimentally and a data set from such measurements that partly illustrates the dependences outlined above is shown in Figure 2.8.

The absorption of an optical photon results in the generation of an electron-hole pair (EHP); an electron excited to the conduction band leaves a hole, in the valence band. These optically generated charge carriers can contribute to the conduction current in the presence of an electric field only if the electron and the hole are separated by the applied electric field before having a chance to recombine. The probability of successful separation is given by the quantum efficiency

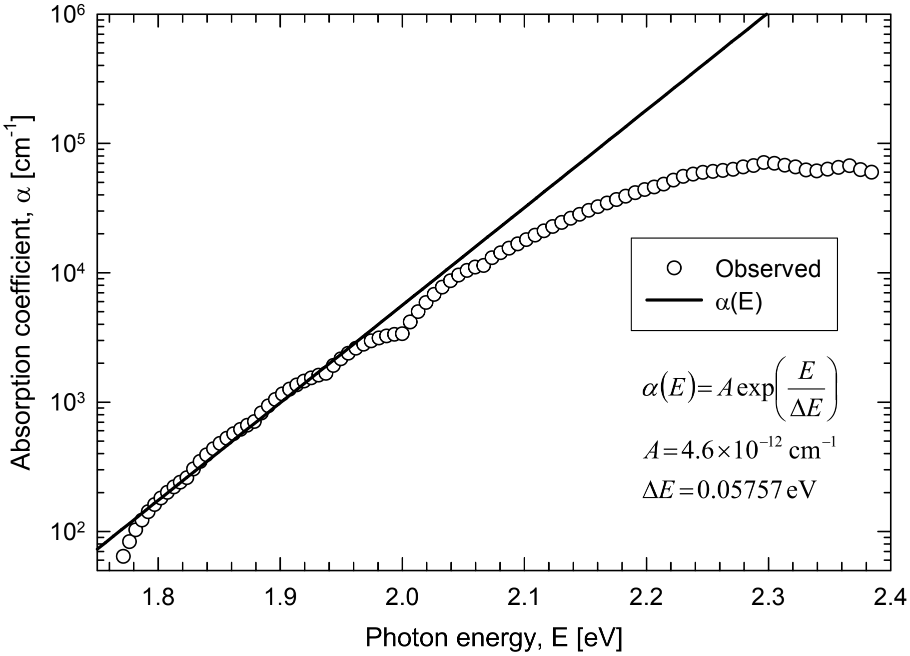

Figure 2.8 Experimentally measured optical absorption coefficient of a-Se. The measurements were done on PE Lambda 900 spectrophotometer using 10 μm thick vacuum deposited a-Se film.

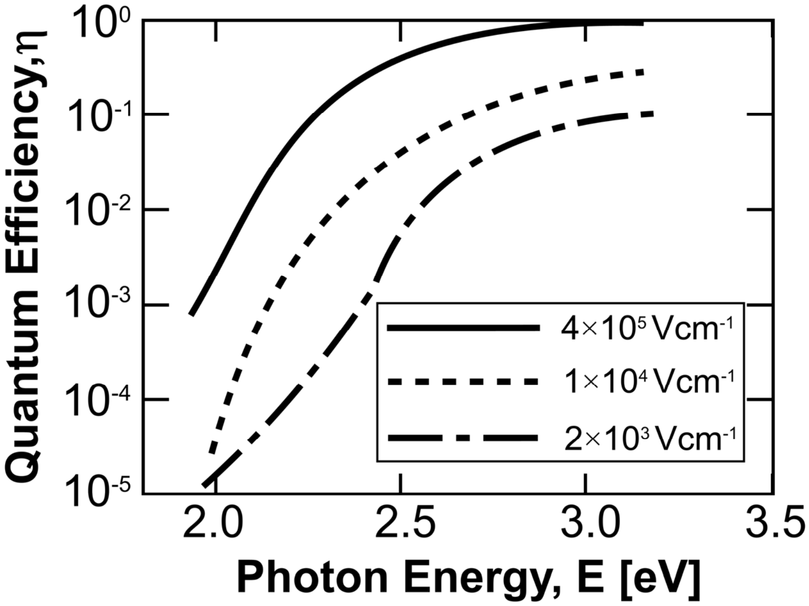

Figure 2.9 Quantum efficiency in a-Se as a function of incident photon energy at several different applied fields. Data were extracted from [80].

η which is another important optical parameter of semiconductor materials. The quantum efficiency in a-Se has been found to exhibit a strong field dependence, even for photon energies well above the optical gap.

The mechanism behind the field dependent quantum efficiency observed in a-Se can be explained by the Onsager theory for the dissociation of photogenerated EHPs [80]. The Onsager theory essentially calculates the probability that an EHP will diffuse apart for a given electric field *F* and temperature *T*. The quantum efficiency shown in Figure 2.9 can be expressed as product of two quantities. The first one is the efficiency of the intrinsic photogeneration process that depends strongly on the energy of the incident photons and the second one is the probability that the generated EHP is separated which depends on the applied field, on the temperature and on the initial separation between the electron and the hole in the pair.

2.3.2 X-ray Photogeneration in Amorphous Selenium

The penetration and the energy deposition by high energy photons can be conveniently calculated using two basic quantities: the mass attenuation coefficient $\frac{\mu}{\rho}$ and mass energy-absorption coefficient $\frac{\mu_{en}}{\rho}$. The mass attenuation coefficient $\frac{\mu}{\rho}$ relates the flux density of the incident photon beam Φ_0 to the flux density of the emerging beam Φ, when a narrow beam of high energy photons penetrates a material with density ρ and mass thickness x through the usual exponential attenuation low

$$\Phi = \Phi_0 \exp(-\frac{\mu}{\rho} x), \tag{2.7}$$

where x is the mass thickness of the material (the mass per unit area), that can be found by multiplying the normal thickness of the material L by its density ρ. The mass attenuation coefficient is proportional to the total cross section for interaction per unit atom $\sigma_{\text{tot.}}$ Since the interaction of photons with matter can follow several different channels, the total cross section for interaction is a sum of the interaction cross sections for the different channels involved

$$\begin{gathered}\sigma_{\text{tot}} = \sigma_{\text{photo effect}} + \sigma_{\text{coherent scattering}} + \sigma_{\text{incoherent scattering}} + \\ + \sigma_{\text{pair and tripplet production}} + \sigma_{\text{photonuclear reaction}}\end{gathered}. \tag{2.8}$$

The interaction types accounted for in the last equation are: the atomic photo-effect, coherent (Rayleigh) and incoherent (Compton) scattering, electron-positron (e^--e^+) pair and triplet ($2e^-$-e^+) production and photonuclear reactions. The probability for each interaction to occur depends on the energy of the incident photons and on the average atomic number Z of the attenuating material. Obviously, the x-rays involved in medical diagnostics (16-140 keV) have energies that are well below the thresholds for pair production and nuclear reaction processes and thus only the first three terms in the right hand side in last equation have non zero contributions. The most significant interaction channel for that energy range is the atomic photoeffect. The cross section for photoeffect also depends strongly on the atomic number Z ($\sigma_{\text{photoeffect}} \propto Z^{4.5}$) of the absorbing material and a good material for x-ray detection should have as high Z as possible.

The mass attenuation coefficient of Se for photons with energies in the range 1 keV – 1 MeV is plotted in Figure 2.10. The location of the K edge (12.658 keV) makes Se a very suitable material for the detection of x-rays used in mammography (15-22 keV). Over the energy range of diagnostic x-rays 16-140 keV the value of the mass absorption coefficient decays more than two orders of magnitude. It is apparent from Figure 2.10 that high x-ray sensitivity of a-Se based detectors designed for general radiography can be achieved by involving 4-5 times thicker a-Se layers for x-ray detection, than the ones used in mammography (only 200 μm).

The mass energy-absorption coefficient for Se is also plotted in Figure 2.10. That quantity multiplied by the energy fluence of the incident photon flux will give the total energy deposited by the photons in the material. Note that not all photons that will interact with the material will deposit all their energy in the material. The initial interaction can result in the formation of secondary photon (Compton photons, fluorescent x-rays, annihilation gamma quanta, bremstramhlung photons etc.) radiations that can escape the material without further interaction and carry some of the incident energy away. For latter reason, the values of $\frac{\mu_{en}}{\rho}$ shown in Figure 2.10 are somewhat lower than the corresponding values of the mass absorption coefficient $\frac{\mu}{\rho}$. The difference between these two quantities becomes more evident for higher energies of the incident photons since as the energy of the incident photon increases more and

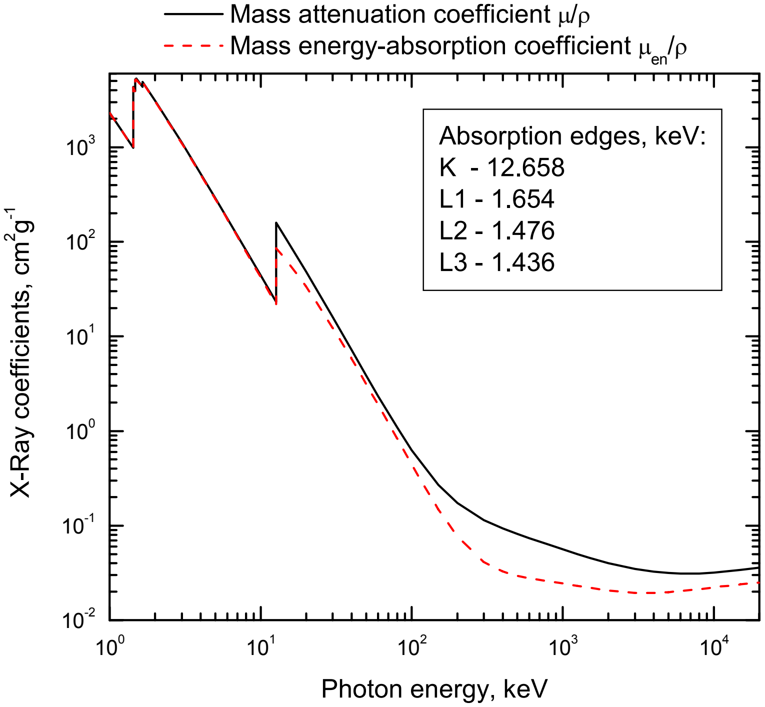

Figure 2.10 Mass attenuation (μ/ρ) and mass energy-absorption (μ_{en}/ρ) coefficients of selenium for x-rays and gamma rays with energies in the range from 1 keV to 20 MeV. Data were taken from National Institute of Standards and Technology (NIST) website (http://physics.nist.gov/PhysRefData/XrayMassCoef/cover.html on 12/04/2006).

more energetic secondary photons are created and the probability of them escaping the absorber material without further interaction also increases.

In the case of an a-Se photoconductor and diagnostic x-rays two channels for energy loss have practical importance: K-fluorescence and Compton photon escape.

The minimum amount of energy absorbed by the incident radiation that is needed to create a single EHP is termed EHP creation energy $W_{0\pm}$ and determines the intrinsic sensitivity of the material used as a radiation detection medium. $W_{0\pm}$ is also called the ionization energy of the medium. The photogeneration efficiency η can be redefined as the fraction of EHPs which do not recombine relative to all EHPs created by an incident photon. The latter definition is better suited for a photogeneration process initiated by an x-ray or a gamma-ray (thousands of EHP created by a single photon).

The average energy $W_{\pm}$ per freed EHP (EHP that escapes recombination and can be potentially successfully collected) is given by

$$W_{\pm} = \frac{W_{0\pm}}{\eta} . \tag{2.9}$$

The amount of energy ΔE absorbed by the material from the radiation and the electric charge ΔQ that can be are related by the quantity $W_{\pm}$ through

$$\Delta Q = q\frac{\Delta E}{W_{\pm}} , \tag{2.10}$$

where q is the charge of the electron.

Typically $W_{0\pm}$ increases with the bandgap E_g of the photoconductor and for crystalline semiconductors it follows the Klein rule [81]

$$W_{0\pm} \approx 2.8\, E_{\mathrm{g}} + \varepsilon_{\mathrm{phonons}} , \tag{2.11}$$

where $\varepsilon_{\mathrm{phonons}}$ is a phonon energy term that involves multiple phonons. For amorphous semiconductors as suggested by Que and Rowlands [82], the relaxation of conservation of momentum rule leads to

$$W_{0\pm} \approx 2.2\, E_{\mathrm{g}} + \varepsilon_{\mathrm{phonons}} . \tag{2.12}$$

However, $W_{\pm}$ in a-Se, as in a number of other low-mobility solids, depends both on the applied field F and energy E of the incident photons because the photogeneration efficiency η supposedly depends on both of these quantities. There have been numerous experiments, with a wide range of conflicting results devoted to measuring $W_{\pm}$ in a-Se as a function of applied electric field and the energy of the incident photons. One of the most recent and most detailed experimental works is due to Blevis et al. [83]. In the latter work the authors have used various monoenergetic photon sources and have clearly shown that $W_{\pm}$ depends on both energy of the incident photons and on the applied electric field across the a-Se layer. However, even that set of experimental data is not complete because the dependence of $W_{\pm}$ on temperature has not been investigated.

Several mechanisms have been suggested to be responsible for the field and x-ray energy dependence of the photogeneration efficiency η and hence $W_{\pm}$ in a-Se. Among these are geminate (Onsager) recombination (see for example [82]), columnar recombination [84] and combination of both [86]. The controversy with regard to the relative importance of proposed recombination mechanisms is still an ongoing research topic together with the question about the saturated value of the EHP creation energy $W_{0\pm}$.

The usual way to find $W_{0\pm}$ from $W_{\pm}$ versus electric field F data is to extrapolate to infinite electric field plotting $W_{\pm}$ vs $1/F$. Part of the data of Blevis et al. [83] replotted in that way is presented in Figure 2.11. Although the lines corresponding to different x-ray photon energies have different slopes they all converge to $W_{0\pm}$ in the range 6-8 eV and that value is relatively independent from the energy of the incident photons. Previous measurements by Kasap and coworkers have resulted in $W_{0\pm} \approx 6\,\text{eV}$ for x-ray beams with average energies in the range of 32-53 keV [84]. Application of Klein rule with $E_g = 2.22$ eV and $0.5\,\text{eV} \le \varepsilon_{\text{phonons}} \le 1.0\,\text{eV}$ (the latter taken from [81]) gives $6.71\,\text{eV} \le W_{0\pm} \le 7.16\,\text{eV}$ whereas Que and Rowlands rule gives $5.38\,\text{eV} \le W_{0\pm} \le 5.89\,\text{eV}$. The scatter in the existing experimental data makes very difficult to assign any of the described models to $W_{0\pm}$. However, it is instructive to mention that, as suggested in [85], there might exist a very simple explanation for $W_{0\pm} \approx 6-8\,\text{eV}$. Values in that range may simply represent the energy for an electron excitation from the peak in the density of valence band states to the peak in the density of conduction band states. More experiments, especially on the temperature dependence of $W_{0\pm}$ are needed to understand the origin of the EHP creation energy in a-Se.

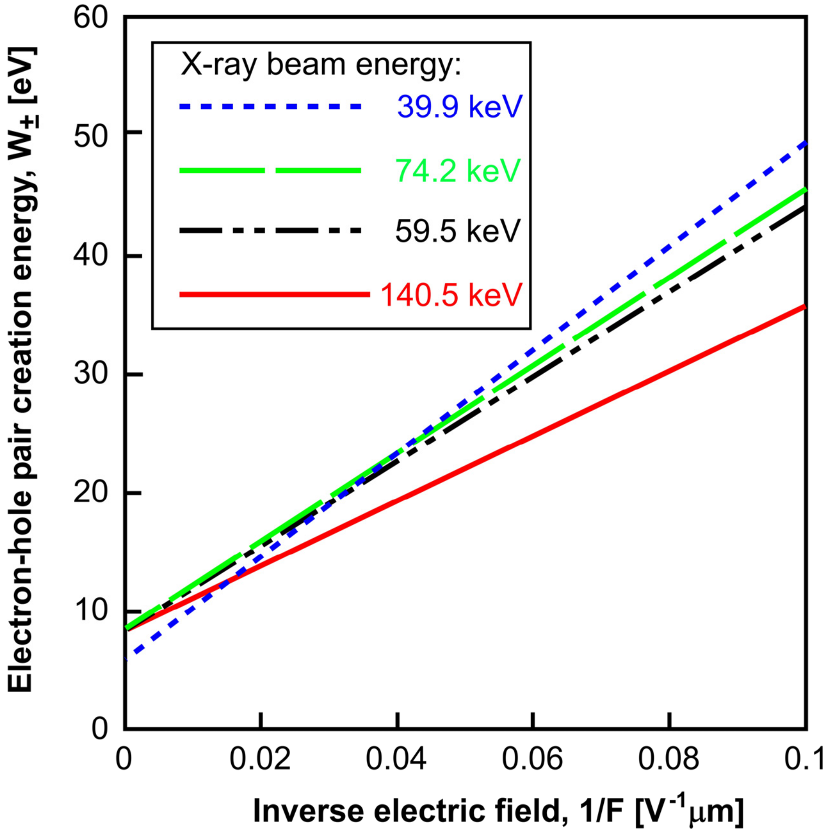

Figure 2.11 Electron-hole pair creation energy $W_{\pm}$ in a-Se for different applied fields and different beam energies. Data were selectively extracted from [83].

The EHP creation energy discussed above addresses the issues with the intrinsic sensitivity of a-Se as an x-ray photoconductor and can help us determine the minimum amount of radiation measurable by a direct conversion a-Se based x-ray detector. Another quantity of interest, especially for imaging detector applications, is what is the intrinsic spatial resolution of a given detector material. An x-ray interacts with the detector material in one point, say atomic photoeffect. Most of the energy of the x-ray is thus transferred to a single electron which starts its trajectory inside the a-Se layer. That electron through a chain of interactions will create huge number (e.g. thousands) of EHPs until fully stopped in the a-Se layer. The question that arises is how well localized in space is, the latter process. In other words, over what volume of the film are the EPHs dispersed as a result of their creation by a single x-ray photon? Obviously if the stopping power for charged particles, $\frac{dE}{dx}$, of the detector material is bigger, the photoelectron will be stopped over a shorter distance and the ionization track produced by a single x-ray photon will be better localized in space. Thus, detector materials with higher stopping power will be capable of imaging with higher spatial resolution.

A clear answer for the question for the intrinsic spatial resolution of a-Se can be readily given by a Monte Carlo simulation of the photoionization process in a-Se as it is done for example in [86]. A typical ionization track initiated by a single x-ray photon with energy of 140 keV as simulated in the latter work is presented in Figure 2.12. Note that all the EHPs created by the x-ray photon are localized in space in a volume of only approximately 8 × 8 × 8 μm. This result clearly illustrates the very high intrinsic spatial resolution of a-Se. For mammographic x-ray beams, the size of the ionization track initiated by a single x-ray photon will be even better confined in space compared to the one shown in Figure 2.12 because the energy of the incident

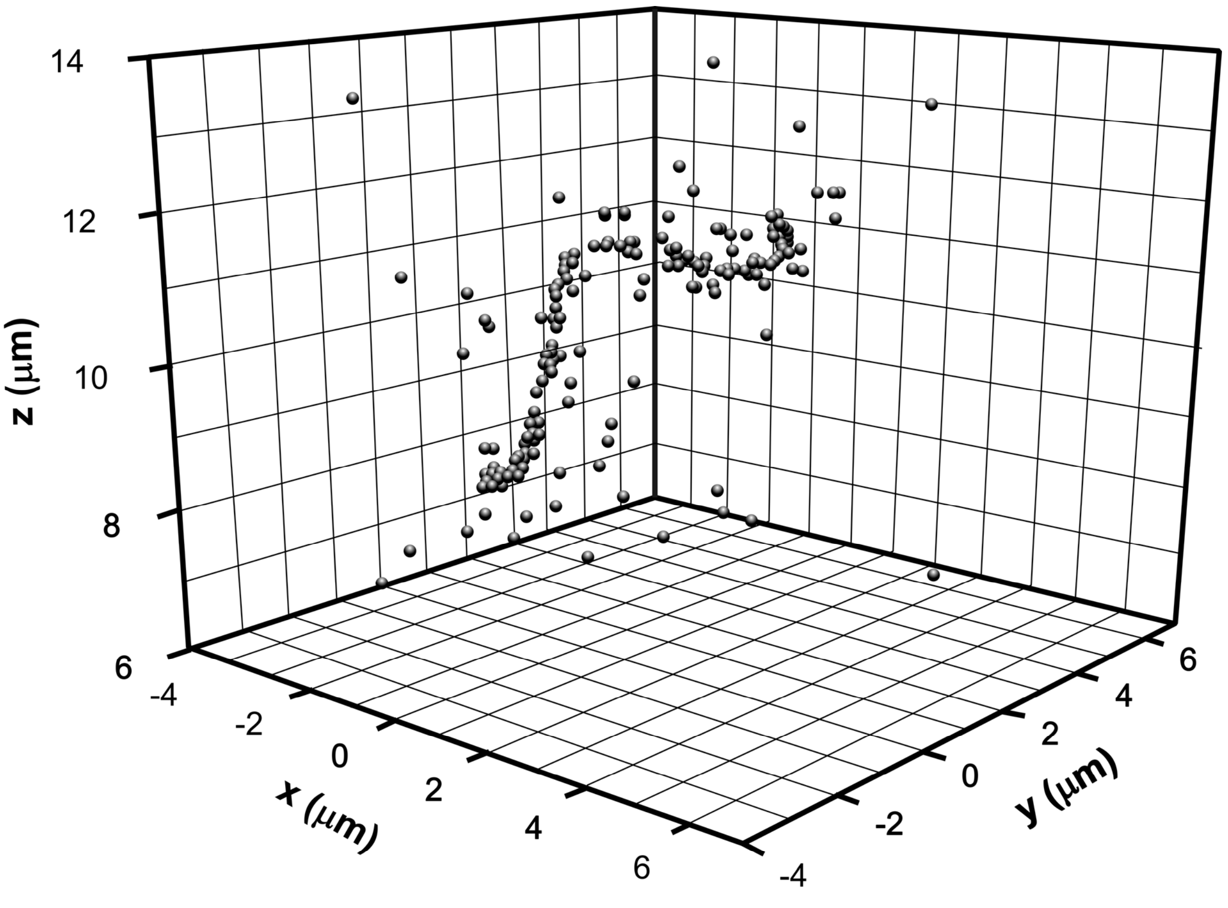

Figure 2.12 Sample ionization track initiated by140 keV x-ray photon in a-Se film as simulated in [86]. The spheres represent the initial positions where the EHPs were created. All the charge is confined in less than 8× 8 × 8 μm which illustrates the intrinsic resolution limit of a-Se at 140 keV.

x-ray photons will be roughly seven times smaller. Thus the intrinsic resolution of the direct conversion a-Se based image detector working with such x-ray beams will be limited purely by the size of the pixels of the readout circuit involved, provided that a sufficiently high electric field is applied across the a-Se photoconductor layer to ensure the collection of all the photogenerated charge with negligible deep trapping. If some of the photogenerated carriers become trapped, then these trapped carriers can induce charges on neighboring pixels and spread the information, i.e. lead to a reduction in the resolution of the detector.

2.3.3 Charge Transport in Amorphous Selenium

As explained earlier in this chapter, most of the researchers working on a-Se have chosen to interpret their results within the framework of band transport formalism. Unfortunately, as explained in section 2.2, the distribution of electronic states in the band gap of a-Se remains highly controversial even today and that makes the exact treatment of the charge transport in a-Se a very difficult task. However, for most practical cases, the electron and hole transport in a-Se can be treated approximately with a precision that is sufficiently high for the application of that material as a radiation detector in terms of only two effective trapping levels for each type of carrier. The first of those two trapping levels is close to the band edge and represents a set of shallow traps that controls the effective mobility of the carriers. The other level represents a set of deep traps, which controls the effective carrier lifetime (deep trapping time) and hence the average distance that a carrier can travel at a given electric field before being deeply trapped (carrier Schubweg). These two set of traps need not to be discrete sets of traps but can be a distribution of traps as well that satisfy the definitions of “shallow” and “deep”.

The experimental facts that both electrons and holes can move in a-Se, that the mobility is thermally activated at low temperatures [52, 87], and that the mobility is shallow trap controlled [88] can be explained in terms of many DOS functions: discrete levels near the band edge [54], narrowly distributed set of traps near the band edges [56], exponentially decreasing band tails [66-68], superposition of a sharply decaying exponent and a discrete or narrowly distributed set of states that forms a peak in the resultant DOS function [50, 65, 69-71], a distribution with a shape similar to the one proposed in references [71, 72] that describes the DOS near the valence band of a-Se, and probably by many other distributions. However, for practical calculations, all these possible DOS distributions near the band edge can be represented by a suitably positioned single discrete *effective* level of shallow traps. In the presence of such a level of traps, the effective mobility of the carriers is known to be shallow trap controlled which means that the effective mobility μ of the carriers is the microscopic mobility in the extended states μ_0 reduced by the transport parameter θ

$$\mu = \theta\mu_0 \,. \tag{2.13}$$

The above equation is derived in detail in section 3.3.4. The transport parameter depends on the shallow trap energy depth, on their concentration, on the temperature and applied electric field and has values that are less than one. The values for the microscopic mobilities for holes and electrons are known to be 0.3-0.4 cm^{2}V^{-1}s^{-1} and 0.1 cm^{2}V^{-1}s^{-1} respectively [52, 89, 90]. At room temperature, for a commercial material, and practical electric fields, the most commonly observed effective mobility for holes is in the range 0.09-0.16 cm^{2}V^{-1}s^{-1}. For electrons, under the same conditions the observed effective mobility ranges from 0.001 to 0.007 cm^{2}V^{-1}s^{-1}. The values of the transport parameter θ under such conditions can be calculated to be ~ 0.3-0.4 for holes and about one order of magnitude smaller for electrons.

The equation that describes the effective carrier mobility at different temperatures for the case of a single level of traps is

$$\mu = \mu_0\left[1+\frac{N_\mathrm{t}}{N_\mathrm{band}}\exp\left(\frac{E_\mathrm{t}}{kT}\right)\right]^{-1} \approx \mu_0\,\frac{N_\mathrm{band}}{N_\mathrm{t}}\exp\left(-\frac{E_\mathrm{t}}{kT}\right). \tag{2.14}$$

Here N_t is the concentration of shallow traps, $N_\mathrm{band.}$ is the density of states at the band edge, E_t is the distance from the band edge, k is Boltzmann's constant and T is the absolute temperature. The asymptotic behavior at sufficiently low temperatures has a clear Arhenius form. If the last equation is fitted to the experimental mobility vs temperature data [52] one can determine that the effective trapping level that controls hole mobility which is located 0.28 eV above the valence band edge while the one controlling the electron mobility is located approximately 0.35 eV below conduction band edge (see Figure 2.5 Density of electronic states in amorphous selenium proposed by Abkowitz in [50].).

Similarly, the exact and currently unknown distributions of deep localized states above and bellow the Fermi level can be replaced by discrete effective levels that would control the effective lifetime of the carriers. Once trapped in such a deep state, the carrier is immobilized and can not contribute to the conduction process until it is thermally released. Since, these traps are very deep, the average release time associated with them is very long compared to the timescale of the usual measurements in which a-Se is involved. In other words, once the carrier is deeply trapped it is practically lost from the conduction process. The average time that the carrier exists in the sample before falling into such a deep trap (the deep trapping time) is the effective lifetime τ of the carriers as observed in experiments. The effective lifetime depends on the integral concentration of deep traps in the material and on their capture coefficient. Thus, the integral concentration of deep localized states is a very important characteristic of the material since it controls the carrier lifetime and through it the carrier mobility-lifetime product (carrier range) $\mu\tau$. The latter quantity multiplied by the applied electric field gives the average length that a carrier is capable of traveling through the material, $\mu\tau F$, or the carrier Schubweg. Maximum detector sensitivity can be achieved when the carrier Schubweg is much larger that the thickness of the x-ray photoconductor material at practical applied electric fields. Due to the low integral concentration of deep localized states in a-Se both electrons and holes can be successfully collected in this material and x-ray detectors with thickness of about 1000 μm are commercially available.

The current belief is that both deep and shallow localized states are due to various defects in the structure of a-Se that are thermodynamically stable at room temperature [91-93]. Experiments at Xerox in the 1980s showed that these states are derived from equilibrium defects [91] and, therefore, cannot be eliminated by careful preparation methods or by the purification of the source material.

The effects of impurities and alloying elements on the transport properties of a-Se have been extensively studied. Pure a-Se is unstable and tends to crystallize over a period of time, which varies from months to years depending on the ambient conditions and the origin of a-Se [94]. It was found that the rate of crystallization could be reduced by alloying pure a-Se with small amounts of As (0.2%-0.5%). Since As atoms have a valency of III, they are triply bonded and link Se chains which increases the viscosity of the amorphous structure and prevents crystallization. However, the addition of As affects also the electronic transport in a-Se: the hole lifetime decreases while electron lifetime increases. Such changes are generally compensated for by adding a halogen (e.g. Cl) in the parts per million (ppm) range which improves the hole lifetime and deteriorates the electron lifetime.

A thermally stable film with balanced hole and electron transport can be achieved by properly adjusting the amount of As and Cl in the material. The resulting material is called *stabilized* a-Se, and the nominal composition is indicated, for example, as a-Se:0.3%As:20ppm Cl. The compensation effect of As and Cl on the charge transport properties of a-Se photoconductors is currently being studied as there are fundamental issues that have yet to be fully resolved [52, 95]. However depending on the properties of the starting pure selenium material and deposition conditions the charge transport observed in films produced from different stabilized a-Se alloys (0-0.7% As and 0-40 ppm Cl) demonstrate huge variations in their electronic transport properties as summarized in Table 2.2 . The mechanism by which different additives alter the electron transport in Se is not exactly known, although many attempts have been made to explain the changes in terms of defect forming reactions as it will be explained later in chapter 5.1.

Table 2.2 Variation in the electronic transport properties for stabilized a-Se films.

Carrier Type	**Mobility, $cm^2V^{-1}s^{-1}$**	**Lifetime, μs**	**Mobility-Lifetime Product, cm^2V^{-1}**	**Schubweg at 5 V/μm, mm**
Holes	0.1-0.16	0.3-300	3×10^{-8}-3.9×10^{-5}	0.015-20
Electrons	0.002-0.007	10-1000	2×10^{-8}-3.5×10^{-6}	0.01-1.8

2.4 Summary

In this chapter we have reviewed the present understanding on the most important properties of amorphous selenium with regard to its application as a photoconductor. The chapter starts with a brief description of the structure and properties of different crystalline and noncrystalline forms of Se. The existence of so many different crystalline forms explains why the structure of noncrystalline Se is very complicated and preparation method and history dependent. The complicated structure of the different noncrystalline forms of Se has been studied by all existing experimental techniques over several decades. In spite of the advances in the methods for examining the structure of materials, the structure of a-Se is still not fully understood.

The same applies to the exact structure of defects in a-Se, which is still highly controversial. Many authors believe that VAPs are the only type of thermodynamically stable defects in a-Se and conveniently forget that all structural studies return an average coordination number of 2.1-2.2. Average coordination number of 2.1-2.2 means that the defects in the structure of a-Se must on average have more than twofold coordination. If all defects were VAPs only, the average coordination number would be exactly two.

The explanation of the electrical properties of a-Se is within the framework of the multiple trapping controlled band theory of amorphous semiconductors have been briefly discussed. As described in the chapter, such approach can explain many experimental facts, but the scientific literature is still full of controversies, the DOS in the bandgap being one example.

At the end of the chapter, the properties of a-Se as an x-ray photoconductor have been outlined. These include a short description of its optical and x-ray absorption properties, x-ray photogeneration properties and finally charge transport in stabilized amorphous selenium.

The unique molecular structure of Se, defines certain short range order and that gives a formal base for application of band theory of solids and in particular the band theory of amorphous semiconductors for the explanation of its properties. However, the same molecular structure does not exclude other possibilities. For example, a-Se can be treated as a molecular semiconductor or as a polymer. Some isolated attempts of such treatments can be found in the literature but a more completed theory based on latter understanding is absent.

This lack of fundamental understanding of the properties of a-Se makes the fabrication of devices based on that material difficult because the whole technological processes are based on almost empirical knowledge and on the properties of the starting Se material. Although that technologists have learned how to prepare a-Se films with desired electronic transport and other properties, this process is far removed from the exact science of single crystal semiconductors and involve many trial and error experiments, which places it closer to art than to an exact science.

3. THEORY OF TIME OF FLIGHT TRANSIENT PHOTOCONDUCTIVITY TECHNIQUE

3.1 Introduction

Transient photoconductivity technique in different variants is widely used to investigate different properties of amorphous semiconductors. Most of the proposed DOS distributions for a-Se described in section 2.2 are based on different type of approximate analysis of Time-of-Flight (TOF) transient conductivity data. The conventional TOF technique has widely been used through out the study to determine mobilities and lifetimes of electron and holes in vacuum deposited a-Se films. This chapter is devoted to the description of the basic principles and mathematical theory behind the TOF transient photoconductivity technique.

3.2 Time of Flight Technique – Basic Principals

The Time of Flight Technique (TOF) has been pioneered by Spear and coworkers in 1968 [96] and since then has been widely used with some modifications to study the carrier transport in low-mobility materials. The basic ideas behind this experimental technique are demonstrated in Figure 3.1.

The explanations that follow and the shape of the TOF waveform shown in Figure 3.1 are based on the assumption that the sample capacitance and the capacitance of the electronic circuits are very small and can be neglected. In this case the TOF signal measured across the sampling resistor R is directly proportional to the photocurrent that flows in the sample. This measurement mode is known as current mode TOF and only this type of TOF measurements will be discussed further in this work.

As illustrated in Figure 3.1, the excess charge carriers of both signs are created in equal concentrations, close to the upper surface of a thin specimen film. A short-duration excitation pulse of strongly absorbed photons or electrons is normally used for this purpose. Depending upon the polarity of the electric field applied across the specimen, carriers of one sign drift across the film, inducing a signal in the series resistor R. This signal will fall to zero when all carriers have completed their transit, allowing an identification of the mean carrier transit time, and thus the calculation of the drift mobility. Note that carriers of either sign may, in principle, be examined, since the dielectric relaxation time in suitable materials is much longer than the transit time through the thin film.

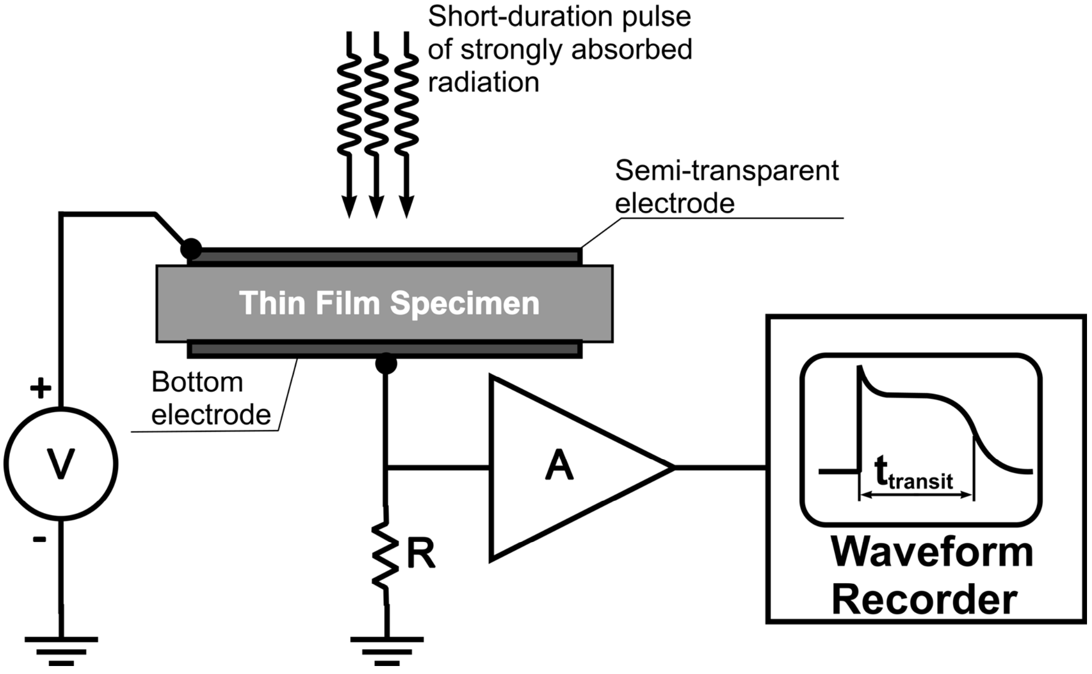

Figure 3.1 The basic principals of time of flight transient photoconductivity technique.

Under the idealized conditions of an infinitely thin sheet of excess carriers drifting through the specimen with zero dispersion, and with suitable blocking electrodes to prevent undesirable re-injection of charge, the voltage induced across the sampling resistor *R* would fall abruptly to zero at a time equal to the transit time of the carriers. In practice, of course, a spread of arrival times always occurs due to diffusion and other effects, so that a reasonably well-formed signal might be of the type shown in Figure 3.1. With such a pulse shape, it remains comparatively easy to identify a mean transit time for the excess carriers, from which average drift mobility may be computed by means of

$$\mu_{\text{average}} = \frac{L^2}{Vt_{\text{transit}}}, \tag{3.1}$$

where *L* is the sample thickness and *V* is the voltage applied across the sample.

Under certain conditions, the “TOF waveforms” observed in the study of amorphous semiconductor films can be used to determine some other characteristics of the material. These include carrier lifetimes (deep trapping times), carrier mobility-lifetime products, the trap distribution of the traps in the mobility gap, etc. The purpose of the following sections is to present a theoretical model of the TOF experiment and to explain how the above mentioned charge transport parameters can be extracted from the experimentally recorded TOF waveforms.

3.3 Theory of the Time of Flight Technique

3.3.1 Introduction

A major advance in the study of carrier transport problems in amorphous solids was achieved in 1975 with the publication of the first detailed model capable of predicting the various features of the TOF photocurrent. Scher and Montroll [97] advanced a model based upon transport by hopping between isoenergetic sites with a random positional distribution (“r hopping”). The analysis of the transport characteristics expected for this process has proved to be a daunting theoretical problem, and to date no exact solution has been achieved. All existing treatments involve the introduction of simplifying assumptions, and the validity of these has been a source of continuing controversy [98].

Around 1977, as described in [98], it became clear that many peculiarities of charge transport in amorphous films can be described in the framework of a totally different from physical point of view theory – the trap-limited band transport theory. All that was needed to achieve certain aspects of the experimental observations was to assume that localized gap states of the amorphous semiconductor are distributed over a sufficient range of energy. In 1977 Noolandi has investigated analytically the problem of trap-limited band transport [56]. The main equation, derived in this work (Eq. (3.7) in the next subsection) is identical in form to a corresponding equation derived by Scher and Montroll [97] at an equivalent stage in the analysis of continuous time random walk. This suggests the equivalence between the multiple trapping band transport formalism and the Scher and Montroll hopping approach and that correspondence was further established by both Noolandi [56,99] and Schmidlin [100].

In the next subsection only the analysis of the transient photocurrents within the framework of trap-limited band transport formalism will be presented because due to its wide application to many amorphous semiconductors including a-Se and alloys.

3.3.2 Trap-Limited Band Transport Formalism

As mentioned above, about 30 years ago Noolandi has formulated [56] the multiple trapping equations in the form

$$\begin{aligned} \frac{\partial \rho(\vec{x},t)}{\partial t} &= g(\vec{x},t) - \vec{\nabla}\cdot\vec{f}(\vec{x},t) \\ \rho(\vec{x},t) &= n(\vec{x},t) + \sum_i n_i(\vec{x},t) \quad , \\ \frac{\partial n_i(\vec{x},t)}{\partial t} &= n(\vec{x},t)c_i - n_i(\vec{x},t)r_i \end{aligned} \tag{3.2}$$

where $\vec{x} \equiv (x,y,z)$ is the position in space, t is the time, $g(\vec{x},t)$ is the local photogeneration rate, $\vec{f}(\vec{x},t)$ is the flux of mobile charge carriers, $\rho(\vec{x},t)$ is the total concentration of carriers, $n(\vec{x},t)$ is the concentration of free carriers, $n_i(\vec{x},t)$ is the concentration of carriers localized in the i-th sets in a group of different sets of trap centers, and finally, c_i and r_i are respectively the capture and release rates for this set of traps. The capture rates c_i are calculated through detailed balance as

$$c_i = C_{\mathrm{t}i}\, N_i\,, \tag{3.3}$$

where N_i is the concentration of the traps from the i-th level and $C_{\mathrm{t}i}$ is the capture coefficient for the traps in that set. The release rates r_i were calculated as

$$r_i = \nu \exp(-\frac{\Delta E_i}{kT})\,, \tag{3.4}$$

where ν is the attempt to escape frequency (the usual value assumed is 10^{12} s^{-1}), ΔE_i the depth of the i-th set of traps measured from the conduction band edge E_c for the electron traps or from the valance band edge E_v for hole traps, k is the Boltzman constant and T is the absolute temperature.

Neglecting the diffusion component of the carrier flux, assuming flash or pulse photoexcitation with highly absorbed radiation and using small signal approximation, Noolandi was able to solve the system of equations (see Eq. (3.2)) using Laplace transform technique. The first of these three assumptions implies that the carrier flux is given simply by

$$\vec{f}(\vec{x},t) = \mu_0 \vec{F} n(\vec{x},t)\,, \tag{3.5}$$

where μ_0 is the mobility of the carriers in the conduction band i.e. microscopic mobility and $\vec{F}$ is the electric field across the sample. The second assumption means that all the excess carriers having total charge Q_0 have been created at time $t = 0$ in a plane that is infinitely close to the top electrode (see Figure 3.1) which translates into the following equation

$$g(\vec{x},t) = Q_0 \delta(x)\delta(t)\,. \tag{3.6}$$

The third assumption means that Q_0 is so small that distortion in the electric field in the sample by the injected charge can be neglected together with the effects from the Coulombic interaction between the carriers in the drifting package.

Under such assumptions, the Laplace transform method, straightforwardly leads to an expression for the transform of the photocurrent in the form

$$\widetilde{I}(s) = \frac{Q_0}{t_0} \times \frac{1-\exp[-a(s)t_0]}{a(s)}, \tag{3.7}$$

where s is the variable of the Laplace transform, and t_0 is the free carrier transit time. The free carier transit time t_0 have its usual meaning

$$t_0 = \frac{L}{\mu_0 F}, \tag{3.8}$$

where L is the sample thickness.

The function *a(s)* in Eq. (3.7) is defined through the following expression

$$a(s) = s\left(1 + \sum_i \frac{c_i}{s + r_i}\right). \tag{3.9}$$

The experimentally recorded waveforms correspond to Eq. (3.7) through an inverse Laplace transform, which means that, unfortunately, for most practical cases, the waveforms have to be evaluated numerically. This is a typical ill-posed problem, which requires the application of specialized regularization techniques. The results obtained on the basis of such analysis are usually connected with significant uncertainties and have to be used with caution.

However, in the following subsections on the basis of some reasonable simplifying assumptions we will demonstrate that the TOF technique can be successfully employed to investigate the carrier transport in certain solids for which some reasonable simplifying assumptions can be made.

3.3.3 Ideal Semiconductor or Ideal Insulator

The term "ideal" in the title of this subsection implies that the concentration of traps for both types of carriers is equal to zero. For this case Eq. 3.7 simplifies to

$$\widetilde{I}(s) = \frac{Q_0}{t_0}\frac{1-\exp(-st_0)}{s}. \tag{3.10}$$

The last equation easily inverts to give the following form of the function describing the photocurrent in the sample

$$i(t) = \frac{Q_0}{t_0}\times\left[u(t)-u(t-t_0)\right] = \frac{Q_0\mu_0 F}{L}\times\left[u(t)-u(t-t_0)\right], \tag{3.11}$$

where *u(t)* is the unit step function $u(t) = \begin{cases} 0\,, t<0 \\ 1\,, t>0 \end{cases}$ and all the other symbols have the meanings defined in the previous subsection. The last equation describes a rectangular current pulse with duration t_0 and magnitude $\frac{Q_0\mu_0 F}{L}$.

The drift mobility of the charge carriers in the sample in this simple case, can be determined by virtue of Eq. (3.8) or Eq. (3.1) by experimentally measuring the width of the TOF pulse and knowing the sample thickness *L* and the voltage *V* applied across the specimen.

3.3.4 One Set of Shallow Monoenergetic Traps

Now we are considering the case when only one discrete level of shallow traps is present in the material under investigation. The term shallow implies that such traps are situated near the mobility band edges. The release rate r_{s} for such traps as defined in Eq. (3.4) will be large, so large that almost always during the experiment the Laplace transform variable *s* is much smaller than r_{s}, i.e. $r_{\mathrm{s}} >> s$.

For this case Eq. (3.9) simplifies to

$$a(s) = s(1+\frac{c_{\mathrm{s}}}{s+r_{\mathrm{s}}}) \approx s\left(1+\frac{c_{\mathrm{s}}}{r_{\mathrm{s}}}\right) = s\frac{r_{\mathrm{s}}+c_{\mathrm{s}}}{r_{\mathrm{s}}}, \tag{3.12}$$

where c_{s} is the capture rate for the shallow traps. Substituting Eq. (3.12) in Eq. (3.7) we receive

$$\tilde{I}(s) = \frac{Q_0}{\frac{r_s + c_s}{r_s} t_0} \frac{1 - \exp\left[-s\left(\frac{r_s + c_s}{r_s} t_0 \right) \right]}{s}. \tag{3.13}$$

The inversion of the last expression is straightforward and the photocurrent for this simple distribution of traps is given by

$$\begin{aligned} i(t) &= \frac{Q_0}{\frac{r_s + c_s}{r_s} t_0} \times \left[u(t) - u(t - \frac{r_s + c_s}{r_s} t_0) \right] \\ &= \frac{Q_0 \frac{r_s}{r_s + c_s} \mu_0 F}{L} \times \left[u(t) - u(t - t_{\text{transit}}) \right], \end{aligned} \tag{3.14}$$

where the observable transit time t_{transit} is given by $t_{\text{transit}} = \frac{r_s + c_s}{r_s} t_0$.

Equation (3.14) resembles the formula for the photocurrent derived for the trap-free case (see Eq. (3.11)). The difference is that drift of the carriers through the sample is now characterized by the so called effective mobility μ_{eff}. The effective mobility is connected to the free carrier mobility μ_0 through the expression given below

$$\mu_{\text{eff}} = \frac{r_s}{r_s + c_s} \mu_0 = \theta \mu_0, \tag{3.15}$$

where $\theta = \frac{r_s}{r_s + c_s}$ is the mobility reduction factor. The effective carrier drift mobility is reduced because the carriers are delayed on their drift through the solid by multiple trapping and release events. This transport mechanism is referred to as shallow trap controlled transport and the scalar θ is known as shallow trap controlled transport factor.

3.3.5 One Set of Deep Monoenergetic Traps

This case is very similar to the one presented in the previous subsection, the difference is that now the traps are deep hence the values for ΔE_d is relatively large so that. the release rate r_d for such traps is very small. This actually means that for almost all experimentally accessible times, r_d is negligibly small compared to the Laplace transform variable s, i.e. $r_d << s$.

With $r_d << s$, we can simplify Eq. (3.9) to

$$a(s) = s(1+\frac{c_\mathrm{s}}{s+r_\mathrm{s}}) \approx s\left(1+\frac{c_s}{s}\right) = s + c_\mathrm{d}\,, \tag{3.16}$$

where c_d is the capture rate for this set of deep traps. Using Eq. (3.16) we receive the following result for the Laplace transform of the photocurrent

$$\widetilde{I}(s) = \frac{Q_0}{t_0}\frac{1-\exp[-(s+c_\mathrm{d})t_0]}{s+c_\mathrm{d}}\,. \tag{3.17}$$

The inverse transform applied to Eq. (3.17) gives the relation describing the photocurrent as a function of time

$$\begin{aligned} i(t) &= \frac{Q_0}{t_0}\exp(-c_\mathrm{d}t)\left[u(t)-u(t-t_0)\right] \\ &= \frac{Q_0\mu_0 F}{L}\exp(-c_\mathrm{d}t)\times\left[u(t)-u(t-t_0)\right]. \end{aligned} \tag{3.18}$$

The photocurrent in this case has the shape of an exponential decay or a pulse with exponentially decaying top depending on the relative magnitude of free carrier transit time t_0 and the capture rate c_d. In both cases the analysis of the exponential decay of an experimentally recorded TOF waveform will result in determining the capture rate c_d and hence the deep trapping time τ_d for the set of traps

$$\tau_d = \frac{1}{c_d}\,. \tag{3.19}$$

In many practical cases, the deep trapping time τ_d can be used as rough approximation of the carrier lifetime and then analysis based on Eq.(3.18) allows the determination of both the mobility μ_0 and the lifetime τ_d of the carries. Having these values one can calculate the mobility-lifetime product $\mu\tau$ and the carrier Schubweg $\mu\tau F$ if needed.

3.3.6 Binary Trap Distribution

Following the approach in the previous two subsections, we can investigate a more realistic case when two set of traps are present; one set of shallow traps (c_s and r_s) and one set of deep traps (c_d and r_d). Again assuming that $r_\mathrm{s} >> s$ and $r_\mathrm{d} << s$ holds during the TOF experiment we can show that the following expression is valid for the photocurrent

$$i(t)=\frac{Q_0}{\frac{r_\mathrm{s}+c_\mathrm{s}}{r_\mathrm{s}}t_0}\exp(-\frac{r_\mathrm{s}}{r_\mathrm{s}+c_\mathrm{s}}c_\mathrm{d}t)\times\left[u(t)-u(t-\frac{r_\mathrm{s}+c_\mathrm{s}}{r_\mathrm{s}}t_0)\right]$$

$$=\frac{Q_0\mu_\mathrm{eff}F}{L}\exp(-\theta c_\mathrm{d}t)\times\left[u(t)-u(t-t_\mathrm{transit})\right]\ . \tag{3.20}$$

This equation describes the photocurrent that will have the same shape as in the case when only deep traps are present. As intuitively expected, the effective mobility of the carriers and hence their transit time is determined only by the kinetics of the trapping and detrapping processes connected only with the presence of shallow traps. The effect of the shallow traps on the transport is the same as in the case when only shallow traps were present in the material - the carriers drift with effective mobility defined in Eq. (3.15).

However, the exponential decay in Eq.(3.20) that is associated with the presence of deep traps is influenced by the presence of the shallow trap level. The observable trapping speed is reduced by virtue of

$$c_\mathrm{d\,eff}=\frac{r_\mathrm{s}}{r_\mathrm{s}+c_\mathrm{s}}c_\mathrm{d}=\theta c_\mathrm{d}\,, \tag{3.21}$$

which leads to an increase in the apparent trapping time i.e.

$$\tau_\mathrm{d\,eff}=\frac{r_\mathrm{s}+c_\mathrm{s}}{r_\mathrm{s}}\tau_\mathrm{d}=\frac{\tau_\mathrm{d}}{\theta}\ . \tag{3.22}$$

Such behavior is also to be expected. The carriers are available for trapping into the deep traps only when they are free. The shallow trap controlled transport factor θ actually represents the relative amount of time that the carriers spend in the shallow traps during their drift through the sample. During their time in the shallow traps, they obviously cannot be lost for the experiment through deep trapping and that explains the slower exponential decay in Eq.(3.20) compared to the case when deep traps alone are present in the sample (Eq. (3.18)).

The simplified analysis in the last four subsections was based on the assumptions that the relations $r_s >> s$ and $r_d << s$ hold over the whole experimentally accessible range of time. However, over very short times after the excitation, the Laplace transform variable has huge values and the assumption $r_\mathrm{s} >> s$ is not valid. As a result, the photocurrent at that time deviates from the one predicted by Eqs. (3.14) and (3.20). It is obvious that some time needs to pass for equilibrium to be reached between trapping and de-trapping processes associated with the shallow trap level. During the equilibration time, the number of carriers that are trapped will be greater than the number of released carriers and the photocurrent will decay with time. After the equilibrium is established, the photocurrent remains constant and the charge packed moves with an effective drift mobility μ_{eff} as predicted by Eqs. (3.14) and (3.20). That initial decrease in the photocurrent that is essentially due to the thermalization of the carriers with the shallow traps is lost for the analysis as a result of the approximations that we have made.

As a result of the same assumption that the behavior of the term $s + r_s$ in Eq.(3.12) is totally dominated by r_s, we are losing another feature of the photocurrent. The latter happens at the moment when the time is equal to the transit time of the charge packet. At that point, the free carriers are collected at the bottom electrode and the equilibrium between the traps and the carriers is disturbed. The carriers that are in the traps now have to be released before being collected at the electrode. Consequently, the photocurrent will not fall abruptly to zero as predicted in Eq.(3.14) and Eq.(3.20) but instead will exponentially decrease to zero, as more and more carriers become released from the traps and almost immediately collected at the electrode.

3.3.7 Extended Trap Distribution

3.3.7.1 Pre- and Post- Transit Approximations for the TOF Photocurrent for Extended Distribution of Traps

We will further develop the approximate analysis of Eq. (3.7) in attempt to describe the shapes of the top of TOF photocurrent pulse (the pre-transit portion of the photocurrent) and the tail of the TOF pulse (the post transit portion of the photocurrent) in the presence of extended distribution of traps. The main benefit of such an analysis is that together with the usual transport characteristics like the effective mobility and deep trapping time, one can extract reasonable information about the DOS in the band gap of the material. .

For many amorphous solids it is thought that the concentration of traps in general diminishes as the energy changes from the edges of mobility bands towards the Fermi level. A common belief is that this change can be described with a monotonically decreasing function of energy on which, if it is necessary, one or several peaks can be superimposed. In principle any continuous distribution of traps can be converted into a set of discreet trap levels if the discretization step is small enough. So, without any serious limitation, we can represent any trap distribution as a set of *m* (*m* should be sufficiently large) discreet levels of traps with capture rates c_i and release rates r_i and try to analyze the TOF waveforms in such a material using Eq.(3.7).

Since the inversion of the Laplace transformed current is not always physically intuitive we can consider two extreme cases, as it was done for example in [101]. The first one corresponds to the case when $s \to \infty$ and the behavior of the Laplace transformed current is dominated by the denominator of Eq. (3.7). Such an approximation is applicable for the region of the TOF photocurrent before the start of extraction of the carriers at the back electrode, i.e. to the pre-transit region. In this case Eq.(3.7) simplifies to

$$\tilde{I}(s) = \frac{Q_0}{t_0} \times \frac{1}{a(s)} . \tag{3.23}$$

The quantity $\frac{1}{a(s)}$ can be expanded to partial fractions [100] as follows

$$\frac{1}{a(s)} = \left[s\left(1 + \sum_{i=1}^{m} \frac{c_i}{s + r_i}\right)\right]^{-1} = \sum_{j=0}^{m} \frac{A_j}{s - \alpha_i} . \tag{3.24}$$

In the last expression the constants α_j are the m+1 nonpositive roots of the equation

$$a(s) = 0 . \tag{3.25}$$

One can define a set of positive numbers $s_j = -\alpha_j$ and look at them as a rate constant for release from a set of *characteristic* trap levels. If r_i are ordered so as $r_1 < r_2 < \ldots < r_m$, the s_j can be ordered in the same way as r_i, with each s_j being slightly bigger than the corresponding r_j. Each s_j, except the largest, is also smaller than r_{j+1}. Of course, the smallest s_j is $s_0 = 0$. Thus the characteristic trap levels with rate constant for release s_j are "located" intermediate between the real trap levels.

Using Eq. (3.24), we can straightforwardly invert Eq. (3.23) to find an approximate expression for the photocurrent in the pre-transit region in a TOF experiment as

$$i(t) = \frac{Q_0}{t_0} \sum_{i=0}^{m} A_i \exp(-s_i t) . \tag{3.26}$$

The last expression describes a current that is due to release of carriers which have been previously distributed (trapped) in these characteristic traps. The corresponding constants A_i can be found by the method of residues

$$A_i = \left[1 + \sum_{j=1}^{m} \frac{c_j r_j}{\left(r_j - s_i \right)^2} \right]^{-1}, \qquad i = 0, 1, \ldots, m \,. \tag{3.27}$$

It is helpful to think that, immediately after the photoexcitation the carriers are distributed into a set of characteristic traps with rate constants for release s_i. The corresponding A_i then define free carrier components due to release from each of the characteristic traps independently. This is consistent with the fact that, A_0 given by Eq. (3.27) is just a generalization for the familiar transport factor θ (see Eq. (3.15)) used to define the effective mobility for the steady state limit.

The other extreme $s \to 0$ is valid for the post-transit region of the TOF waveform. In the latter case the expression in the numerator in Eq.(3.7) dominates the behavior of the Laplace transform of the photocurrent. Under that assumption, Eq. (3.7) simplifies to

$$\widetilde{I}(s) = Q_0 \times \left(1 - \frac{a(s) t_0}{2} \right) \tag{3.28}$$

and, similarly to the previous case, inverts to give

$$i(t) = \frac{Q_0 t_0}{2} \sum_{i=1}^{m} c_i r_i \exp(-r_i t) \,. \tag{3.29}$$

The time span in which ether Eq. (3.26) or Eq. (3.29) should be a valid approximation can be considered by examining the movement of the first moments $\langle x(t) \rangle$ of the spatial free carrier distribution in a semi-infinite model. During the period when $0 < \langle x(t) \rangle < L$, essentially no carriers will have left the sample and Eq. (3.26) will be a good approximation to Eq. (3.7). Once $\langle x(t) \rangle > L$, most of the carriers will exit the sample at the backside electrode and Eq. (3.29) should be used in that case. The condition $\langle x(t) \rangle = L$ defines the transit time [102] provided that the spatial distribution of free carriers is fairly symmetric.

3.3.7.2 Exponential Distribution of Traps

The band theory applied to amorphous semiconductors predicts that the density of localized states in the bandgap will decrease exponentially from the band edges towards the Fermi level. This is a direct consequence from the lost of the long range order and preservation of short term order in these semiconductors. Thus the exponential distribution of traps is of great importance and it is instructive to derive the expression for the TOF photocurrent in this case.

The exponential distribution of localized states can be described by the equation

$$N(E) = N_0 \exp\left(-\frac{E}{E_0}\right), \tag{3.30}$$

where N_0 is the concentration of localized states at the band edge,

E is the energy distance from the band edge, and

E_0 is the characteristic width of the exponent that characterizes the rate of the decay of $N(E)$.

Using the relation between the release rate r and the position of the trap in the bandgap E (see Eq. (3.4)) we can express the density of the localized states as a function of r

$$N(r) = N_0\left(\frac{\nu}{r}\right)^{-\frac{kT}{E_0}}. \tag{3.31}$$

Combining the last equation with Eq. (3.3) and assuming that capture coefficients and the attempt to escape frequency are the same for all traps we receive the following expression for the capture rate c as a function of the release rate r

$$c(r) \propto r^{\frac{kT}{E_0}}. \tag{3.32}$$

As demonstrated in [100], the relation of the above type leads to the following expression for the function $a(s)$ that is valid for the pre-transit region

$$a(s) \propto s^{\frac{kT}{E_0}}. \tag{3.33}$$

Using the last expression we can show that Eq. (3.23) simplifies to

$$\widetilde{I}(s) \propto \frac{1}{s^{\frac{kT}{E_0}}}. \tag{3.34}$$

The inversion of the last expression gives an approximate expression for the TOF current in the pre-transit region for the case of exponentially distributed traps

$$i(t) \propto t^{-1+\frac{kT}{E_0}}. \tag{3.35}$$

The derivation of the post-transit asymptote is much easier compared to the analysis required to obtain the pre-transit asymptote (Eq. (3.35)). For a continuous exponential distribution of traps, we need to reformulate Eq. (3.29) replacing the summation in it with integration as it is done in the next subsection (see the derivation of Eq. (3.38) on the next page). Using the reformulated equation together with Eq. (3.32) we receive

$$i(t) \propto \int_0^\infty r^{\frac{kT}{E_0}} \exp(-rt)dr \,. \tag{3.36}$$

Evaluation of the integral in equation in Eq. (3.36) ($i(t)$and $r^{\frac{kT}{E_0}}$ are Laplace transform pair) results in the desired asymptotic expression for the current in the post-transit region

$$i(t) \propto t^{-1-\frac{kT}{E_0}} \,. \tag{3.37}$$

Equations (3.35) and (3.37) are well known and used widely when an exponential trap distribution has to be confirmed experimentally.

3.3.7.3 Theory of Post Transit Photocurrent Analysis as a Method for the Reconstruction of the Density of Localized States in the Bandgap in Amorphous Semiconductors

For times after the transit time of the charge packet, the photocurrent is increasingly dominated by the release of the carriers from the traps and not by the transport of carriers through the sample. Eq. (3.29) that applies for this case is much simpler than Eq. (3.26) and it is not very difficult to use Eq. (3.29) to extract information on the DOS distribution in the material [101]. For the case of a continuous trap distribution Eq. (3.29) is reformulated to

$$i(t) = \frac{Q_0 t_0 \nu_0}{2} \int_{r_1}^{\nu_0} \bar{g}(r) \exp(-rt)dr = \frac{Q_0 t_0 \nu_0}{2} \int_0^\infty \bar{g}(r) \exp(-rt)dr \,, \tag{3.38}$$

where r_1 is the release rate from the deepest traps in the distribution, $g(E)$ is the function describing the density of states in the gap (DOS), and $\bar{g}(E)$ is the normalized distribution defined by the ratio $\frac{g(E)}{g(0)}$ in which g(0) is the density of states at the band edge. In practice, the boundaries in the integral can be conveniently approximated by 0 and ∞. In this way the post-transit photocurrent and the normalized DOS are linked via Laplace transform

$$i(t) = \frac{Q_0 t_0 \nu_0}{2} \tilde{\bar{g}}(r) \,, \tag{3.39}$$

where $\tilde{\bar{g}}(r)$ is the Laplace transform of $\bar{g}(r)$.

The last expression allows us to calculate the density of states from *i(t)* by inverting the Laplace transform. For experimental current traces, the inversion can be done only numerically. The last difficulty can be overcame by replacing the exponential waiting-time distribution for release by a trap at energy depth *E*: $r(E)\exp(-r(E)t)$ by a delta function $\delta(rt-1)$. This means that instead of having an average release $\tau_r(E)=\dfrac{1}{r(E)}$ all carriers trapped in traps with depth *E* become free at time $\dfrac{1}{r(E)}$. We can then obtain

$$t\times i(t)=\frac{Q_0 t_0 \nu_0}{2}g(E) \quad E=kT\ln(\nu_0 t)\,, \tag{3.40}$$

where, as shown by the second relation, the energy depth of the traps and the time are related by the thermalization energy expression.

The energy range over which Eq. (3.40) is valid is limited to the post transit regime only, i.e. when the current is dominated by extraction and not by transport of carriers through the sample. Since the carriers that are captured in traps at the same energy depth but at different places in the sample, i.e. at the front electrode or just at the back electrode will have difference in the arrival times of t_{transit} at most it is instructive to use the last equation only from $2\times t_{\text{transit}}$ on.

This requirement makes the experiments on a-Se very difficult because it has very shallow trap distribution and the post-transit current rapidly decreases to the level that disappears in the noise of the measurement. However, there are other factors with which one should be careful when using post-transit technique. The derivation of the convenient and simple Eq. (3.40) became possible only after a number of approximations. That imposes additional limits to the precision with which the DOS can be recovered from experimentally measured TOF post-transit photocurrents.

The fundamental limits to the precision with which DOS function can be recovered from analysis of TOF photocurrent were described at the end of subsection 2.2 and are related to the quality of the experimental data and to the amount of noise present in it. In addition, further limitations arise from the approximations made to derive Eq. (3.40). It is difficult to systematically study all the mathematical limitations that originate from the approximations but one consequence becomes apparent from the theory of the Fredholm integral equations of the first kind. Equation (3.38) is one such equation with integration kernel $\exp(-rt)$. The original integration kernel in that equation was replaced with a Dirac delta function of the form $\delta(rt-1)$. From the point of view of an experimentalist such a simplification seems "innocent" as explained above in this subsection. For reasons explained in [103], the new equation has much lower information capacity than the original one. That means additional loss of sensitivity to the fine features in the DOS function. The result of that is loss of resolution associated with the use of the simplified Eq. (3.40). In other words, based on experimentally recorded photocurrents, one will be able to recover less information about the DOS distribution function than in the case when the original Eq. (3.38) is used. A number of researchers have done numerical simulations and have demonstrated that the replacement of the exponential function with a Dirac δ function indeed causes additional loss of resolution (see [106] for one example). This means that any sharp peaks present in the real DOS can not be recovered correctly from the analysis. Another consequence is that the calculated DOS can no`ct follow exponential distributions that are decreasing steeply, i.e. with a characteristic width of the order of *kT*.

All disadvantages mentioned here together with the fact that the post transit photocurrent analysis is not applicable to the short term photocurrent data makes the technique applicable to very slowly varying DOS distributions without any sharp features superimposed on them. This method is not very suitable for DOS analysis in a-Se. Any application of the method to this material has to be done with great caution.

3.3.7.4 Other Techniques for DOS Distribution Recovery Using the TOF Photocurrent Analysis

Equation (3.26) shows that the pre-transit portion of the TOF waveform is basically a sum of exponentials plus eventually a DC offset; that is a monotonically decreasing function of time. The exact shape of pre-transit photocurrent will depend on the trap distribution and on the field applied across the sample. It seems that it should be possible to determine the trapping rates and the release rates for the different species of traps in the material from analysis of that portion of the photocurrent. However, such analysis is not easy and results in analytical form can be obtained only for a number of fairly simple cases when only a few different species of traps are involved. For example, Blakney and Grunwald have derived equation [104] that is very similar to Eq. (3.26), considering only three different trap species: one that controls the carrier mobility (very shallow), the second one is also relatively shallow but having release time of the order of carrier packet transit time, and the third one that is deep with a release time much longer than the charge packet transit time. This technique was applied to a-Se and the results were briefly mentioned in the subsection 2.2.

There are other techniques used to recover DOS distribution from measured TOF that do not exploit the simplifying assumptions on the basis of which the asymptotes for the pre- and post- transit photocurrents were derived (Eq. (3.26) and Eq. (3.29)). Some of them utilize numerical techniques to invert the Laplace transform of the photocurrent in Eq.3.7, like Noolandi in [56] and more recently Koughia in [69,70,71]. Such techniques are not physically transparent and use other simplifying assumptions to deal with the inversion problem. The disadvantages associated, to a grater or lesser extent, with these two techniques were already discussed in subsection 2.2 .

Another method for reconstruction of the DOS distribution from measured TOF photocurrent, again based on the Laplace transform technique to solve the transport equations (Eq. (3.2)) was developed by several researchers from Japan. The authors, however, do not attempt to invert the Laplace transform of the photocurrent in Eq. (3.7) but instead try converting Eq. (3.9) to a form from which the DOS distribution can be recovered [74]. The transformed equation is a Fredholm integral equation of the first kind and the problems associated with it have already been described at the end of subsection 2.2. Two approaches have been proposed from that group of researchers. The first one is to approximate the integration kernel of the equation with a suitably weighted Dirac δ function. The integral can then be solved exactly [74] and a simple expression similar to Eq. (3.40) can be derived at the expense of additional resolution loss that appears for reasons described in the previous subsection. The second approach suggested by the authors is to use a specialized mathematically robust numerical procedure known as restricted Tikhonov regularization [74] in attempts to deal with the inversion problem. This regularization technique is general and works well in many practical cases but none of the authors has pointed out why exactly this regularization scheme has been chosen among the many other existing ones. In the specific case, a non negative solution is being sought and that restriction is imposed to the Tikhonov regularization scheme somewhat artificially. Another problem that is not addressed very accurately is the selection of the value for the regularization parameter. The authors in [74] have used automated algorithm developed to select the value of the regularization parameter "objectively" on the basis of the quality of supplied input data without justifying that the algorithm will work in their specific case. Whether this regularization technique will manage to return a DOS solution on the base of experimental photocurrents measured in a-Se film was never tested.

The multiple trapping transport equations (Eq. (3.2)) can be solved by Fourier transform techniques. Such an approach is described, for example, in [105, 106] for the case of transient photoconductivity experiments. This experimental technique is quite different than the TOF experiments in its details but as justified in [74], the equations derived for transient photoconductivity experiments can be used to process data from TOF experiments with quite good precision. The application of the Fourier transform technique again results in a Fredholm integral equation and the associated mathematical difficulties are very similar the ones that have already been discussed.

From what was said above and in subsection 2.2 we can conclude that it is extremely difficult to recover the DOS distribution function from experimentally measured photocurrent. Many limitations arise from the ill possedness of the problem. They have to be carefully considered when shallow distributions with a lot of structure are studied.

3.4 Interrupted Field Time of Flight Technique

The TOF technique has been applied successfully to many solids in the past several decades. Most of the researchers have applied the technique as it was reviewed in the previous part of this chapter. In some cases, the researchers have slightly altered the technique in order to investigate specific aspects of charge transport in certain materials. For example, the effect of delayed bias application (or advanced photo-excitation) has been investigated in attempt to study the recombination process [107]; the delayed photo-excitation has been studied to investigate the kinetics of space-charge formation [108]; excitation from both sides of the sample has been applied to study the recombination between drifting holes and electrons [109], and to complete the list we have to mention that the interrupted field time of flight (IFTOF) [110, 111, 112] has been reported as a very useful method to study the charge trapping in solids. However, in these initial reports the measured IFTOF waveforms were affected by the displacement currents during the interruption switching. This is the main reason for which the IFTOF is considered to be a very difficult for practical realization in photoconductivity experiment. The first IFTOF apparatus capable of recording displacement current free waveforms with high enough applied bias to be of practical interest for investigation of a-Se films was developed by Kasap et al. [113].

The advantages of the IFTOF technique can be easily illustrated for the case when the charge transport can be described as in subsection 3.3.6. This is the case in which the trapping process can be approximated in terms of two effective trapping levels, i.e. one set of shallow traps that control the mobility and one set of deep traps with a negligible release rate. Once the carrier is trapped in such a deep trap, it is lost for the conduction process. The trapping time for that deep level of traps will then play an important role in the conduction process, because it will be the observable carrier lifetime over the time scale of the experiment. This is a realistic case, for example, for hole transport in a-Se which can quite successfully be approximated in terms of two trapping levels as described above, and it is often of interest to measure the hole deep trapping time (lifetime). Using Eq. (3.22) we can rewrite Eq. (3.20) in the following form

$$i(t) = \frac{Q_0 \mu_{\mathrm{eff}} F}{L} \exp(-\frac{t}{\tau_{\mathrm{d\ eff}}}) \times \left[u(t) - u(t - t_{\mathrm{transit}})\right]. \tag{3.41}$$

The deep trapping time $\tau_{\mathrm{d\ eff}}$ in many cases can be determined from the analysis of the pre-transit portion of the waveform recorded in conventional TOF experiment. However, the latter procedure becomes difficult in the case when $\tau_{\mathrm{d\ eff}}$ is very long, because the top of the waveform will appear practically flat. In order to apply the conventional TOF technique one has to study thicker samples and/or to use low electric fields. Both of these measures will lead to longer transit times t_{transit}, the carriers from the drifting packet will have time to interact with the deep traps and the decay of the photocurrent will become more prominent. For amorphous selenium however there is one important further difficulty, because the photogeneration process is field dependent and at low fields the TOF waveform becomes noisy and difficult to use. Under such conditions the IFTOF technique is very suitable for a precise determination of the deep trapping time. The essence of the IFTOF technique is illustrated in Figure 3.2. Figure 3.2-a shows the conventional TOF signal as described by Eq. (3.41). Some noise is added to the photocurrent in attempt to mimic the behavior of a real TOF waveform. Instead of waiting for the charge packet to exit the sample at the back electrode, we can interrupt the motion of the packet inside sample by removing the external electric field. This is shown in Figure 3.2-b. The moment of the interruption t_1 $(0 \le t_1 \le t_{\mathrm{transit}})$ for the case shown in the figure corresponds to stopping the carrier packet close to the middle of the sample. There is no external field applied to the sample and if we neglect the diffusion and Coulombic interaction between the carriers in the packet we may think that carriers will stay close to the position where the field was removed. The number of free carriers decreases, because during the interruption the carriers are being deeply trapped with a rate c_{d}. After certain period of time t_{int} the field is reapplied and the carriers that were not deeply trapped will start to drift again until they are collected at the back electrode. The functional relation that describes the shape of the IFTOF photocurrent is

$$\begin{aligned} i(t) &= \frac{Q_0 \mu_{\mathrm{eff}} F}{L} \exp\left(-\frac{t}{\tau_{\mathrm{d\ eff}}}\right) \times \\ &\times \left\{ \left[u(t) - u(t - t_1)\right] + \left[u(t - t_1 - t_{\mathrm{int}}) - u\left(\frac{t\mu_{\mathrm{eff}} F - t_{\mathrm{int}}\mu_{\mathrm{eff}} F - L}{\mu_{\mathrm{eff}} F} \right) \right] \right\}. \end{aligned} \tag{3.42}$$

The magnitudes of the currents just before the interruption and immediately after the external field is reapplied are related by

$$\frac{i(t_1 + t_{\mathrm{int}}^{+})}{i(t_1^{-})} = \exp\left(-\frac{t_{\mathrm{int}}}{\tau_{\mathrm{d\ eff}}} \right). \tag{3.43}$$

The deep trapping time $\tau_{\mathrm{d\ eff}}$ can be easily and directly calculated from Eq. (3.43), because the interruption time t_{int} is known experimental parameter and the photocurrents just before $i(t_1^{-})$ and after ($i(t_1 + t_{\mathrm{int}}^{+})$) the interruption can be measured from experimentally recorted IFTOF photocurrent waveform (see Figure 3.2-b).

However, this is almost never done because it is difficult to determine accurately the currents before and after the interruption precisely. The difficulties arise from the noise in the waveform and, more importantly, the values of the currents before and after the interruption can be affected from the displacement currents. A better way to determine the deep trapping time is illustrated in Figure 3.2-c. The ratio of the currents before and after the interruption $\frac{i(t_1 + t_{\mathrm{int}}^{+})}{i(t_1^{-})}$ is evaluated for about 10 different interruption times t_{int}. Then the quantity $\frac{i(t_1 + t_{\mathrm{int}}^{+})}{i(t_1^{-})}$ is plotted as a function of the interruption time. As shown in Figure 3.2-c that dependence is a straight line in semi-logarithmic scale and the value of the deep trapping time $\tau_{\mathrm{d\ eff}}$ can be determined by simple regression analysis.

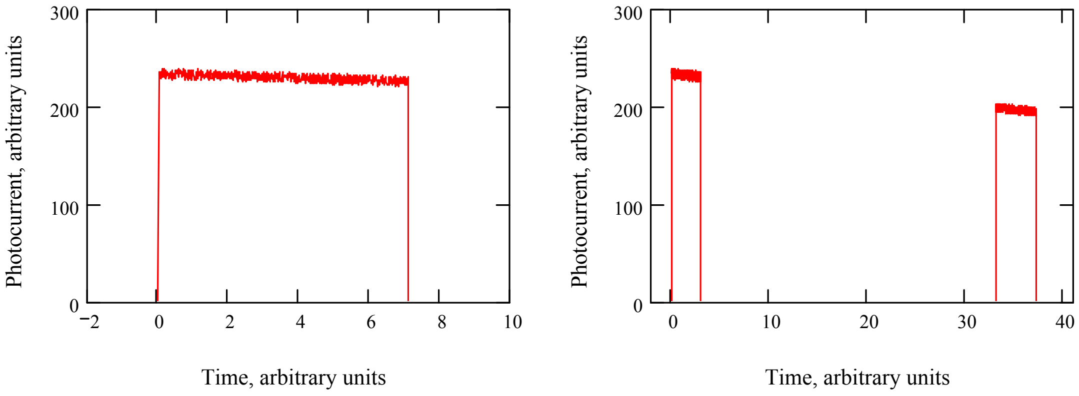

a) Conventional TOF Waveform

b) IFTOF Wavefom

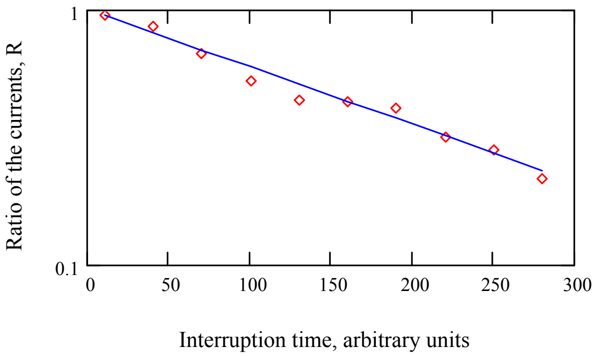

c) Deep Trapping Time Determination

Figure 3.2 Simulation of IFTOF technique based on Equations (3.41), (3.42), and (3.43):

a) Conventional TOF waveform with almost no decay in the pre-transit region (Eq. (3.41));

b) IFTOF waveform for the same applied field and the same light excitation as for the conventional TOF waveform (Eq. (3.42));

c) An experimental determination of the deep trapping time from IFTOF data.

Kasap et al. in [113] have described the important advantages of the IFTOF technique over the conventional TOF measurements:

a) The concentration of carriers involved in the conduction process can be studied over a very long time scale ($t >> t_{\text{transit}}$) until the recovered photocurrent is too small to recover or becomes dominated by the release of trapped carriers. This is possible for the materials in which the transport can be approximated in terms of two effective trapping levels; one shallow level that controls the mobility and one deep level that defines the effective lifetime of the carriers over the time scale of the experiment. Under such conditions the drift mobility is constant and the ratio between the carrier concentrations before and after the interruption is the same as the ratio between the photocurrents before and after the interruption.

b) The total trapping behavior i.e. the total trapped charge Q_t vs the interruption time t_{int} can be studied comparing the time integral over the photocurrent after the interruption (Figure 3.2-b) and that over the uninterrupted photocurrent (Figure 3.2-a). It is assumed that the photogenerated charge by the excitation light can be kept the same over the measurements.

c) The trapping process is studied under zero applied electric field conditions; there is, nonetheless, a finite internal electric field due to the charge packet injected in the sample.

d) The effects of sample in homogeneities can be eliminated by interrupting the carrier packet motion at a specific position.

e) Sample heterogeneities can be studied by interrupting the electric field when the carrier packet is at different locations inside the sample.

f) The time dependence, if any, of the drift velocity can be studied by examining the effective transit time as a function of the interruption period $t_{int.}$ The effective transit time is defined as the difference between the mean time of arrival of the packet at the back electrode and the interruption time.

g) Diffusion and dispersion of the carriers in the packet can be studied as a function of the interruption period t_{int} by examining the shape of the recovered photocurrent around the extraction point near the back electrode.

The IFTOF technique described above has some disadvantages as well. The main disadvantage is that it is difficult to implement due to the huge switching transients. The magnitude of the switching transients can be easily several hundred volts (for the case of a-Se) while the photocurrent signal is typically less than a hundred milivolts across the sampling resistor. Obviously, the detection of the photocurrent signal in this case is a very difficult technical problem. Another limitation of the IFTOF technique is that the theory described above is valid for the case when the transport can be studied in terms of two effective trapping levels; one controlling the mobility i.e. due to shallow traps, and the other defining the effective lifetime for the experimental timescale, due to deep traps. For the general case of materials having extended trap distributions, the simple analysis described in this subsection can not be applied.

More complicated analysis, based on Eq. (3.26) must be applied for extended distribution of traps. The mathematics in this case obviously leads to multi-exponential analysis which is known to be very difficult problem.

3.5 TOF Photoconductivity Technique - Summary

In this chapter the TOF transient photoconductivity technique has been described as a method to investigate charge transport in low mobility materials. The stress has been placed on describing the theory behind such experiments. The trap limited band transport formalism was used to mathematically describe the problem. We have demonstrated how basic transport parameters like effective mobility and deep trapping times can be extracted from experimentally recorded TOF photocurrent waveforms for the cases of several simple distributions of traps. It was also shown that for the case of extended trap distributions, the problem of analyzing the photocurrent becomes sufficiently more difficult. Two useful asymptotes for the photocurrent valid for the pre-transit and the post-transit parts of the TOF waveforms were introduced. A method to calculate DOS distribution on the basis of the post-transit photocurrents was outlined. Several other techniques that were proposed to solve the inverse problem were mentioned together with their advantages and disadvantages.

At the end of the chapter the theory of one important modification of the conventional TOF technique known as interrupted field time of flight (IFTOF) technique has been discussed. The advantages and disadvantages of the IFTOF techniques have also been summarized.

4. EXPERIMEMTAL PROCEDURES AND TECHNIQUES

4.1 Introduction

This chapter provides a description of the experimental procedures that were used to fabricate amorphous selenium (a-Se) photoconductor layers and characterize their properties. The first section describes the fabrication process through which the experimental samples and test detectors were produced. The second section describes the experimental setup used to perform dark measurements on amorphous selenium thick films. The following sections provide details on the experimental equipment used to perform Time of Flight (TOF) and Interrupted Field Time of Flight (ITOF) techniques. The experimental equipment is described in details and the necessary theory behind IFTOF technique is also briefly presented. The final section describes the equipment used to expose the samples to x-rays and to study the effects induced by the x-rays in the sample.

4.2 Fabrication of a-Se Films and a-Se Photoconductor Layers on CCD Chips

4.2.1 Substrates and Substrate Preparation

Production of high quality a-Se films with good long-term stability against crystallization requires that the films be deposited onto a substrate with a surface that is clean from oil, dust and other contaminants. The photoconductor layers fabricated in the course of this work were deposited on glass substrates, on Al substrates and on the surface of experimental CCD chips. The CCD chips from the production line of DALSA Inc, were sent to our lab in special packages to avoid any contamination during transport. These chips needed no cleaning or any other processing prior to the deposition of Se on their imaging areas.

In cases when glass was needed as a substrate, we have used uncoated Corning 7059 type glass (high resistivity) or Corning 1737F glass with one surface coated with ITO (indium tin oxide). The glass substrates were cut to the desired size and cleaned using the procedure described in Table 4.1 below. Metal films were deposited on the 7059 glass surface (see subsection 4.2.4) to act as bottom electrodes in future metal/a-Se/metal devices.

Table 4.1 Procedure for cleaning glass substrates.

Step #	Step Description
1	Clean the substrates ultrasonically in Extrain-MN01 bath (2-5 g Extrain-MN01 in 1 liter of deionized water) for 5-20 min.
2	Rinse using deionized water 3-4 times.
3	Clean the substrates ultrasonically in pure methanol for 3-5 min.
4	Wash the substrates ultrasonically in bath of deionized water for 1-2 min.
5	Repeat step 4 two-three times changing the water in the bath before each repetition.
6	Wash the substrates ultrasonically in hot deionized water (60 °C) for 2-3 min.
7	Blow dry purified compressed air to dry the substrates
8	Keep the substrates in dust free environment at 50 °C before further use

Table 4.2 Procedure for aluminum substrate cleaning.

Step #	Step Description
1	Remove the protective plastic film from the polished surface
2	Clean Substrates ultrasonically for 3-4 min in Trichloroethylene (C_2HCl_3) to remove remnants of glue and plastic
3	Wash substrates ultrasonically in acetone for 3-4 min.
4	Wash substrates ultrasonically in methanol for 3-4 min.
5	Wash the substrates ultrasonically in bath of deionized water for 2-3 min.
6	Repeat step 5 two-three times changing the water in the bath before each repetition.
7	Wash the substrates ultrasonically in hot deionized water (60 °C) for 2-3 min.
8	Blow dry purified compressed air to dry the substrates
9	Keep the substrates in dust free environment at 50 °C before further use

The aluminum substrates were cut to the desired size from Al sheets of thickness 1.1 mm. One of the surfaces of the Al sheets was polished by the manufacturer and protected by a thin polymer film. The amorphous selenium films were grown on the polished side of the substrate. The cleaning procedure for Al substrates is presented in Table 4.2 given on the previous page.

In some cases, in order to improve the adhesion of the Se film to the Al substrates, the surface of the aluminum substrates was etched. This was done between step 4 and step 5 in Table 4.2 following the procedure outlined in Table 4.3.

In cases where very low dark currents were required the Al substrates were oxidized in air at a temperature of about 350 °C for more than 2 hours. The oxidation process was applied on the cleaned or on cleaned and etched Al substrates.

Table 4.3 Procedure for etching the surface of Al substrates.

Step #	Step Description
1	After steps 1-4 in Table 4.2 have been performed, rinse the substrates in deionized water and keep them under deionized water before the next step
2	Prepare solution of 1.5g soda ash (Na_2CO_3) and 1.5g sodium phosphate (NaH_2PO_4) in 300 ml deionized water
3	Heat the solution prepared in step 2 to 60 °C
4	Etch the substrates immersing them in the heated solution for 20-60 s.
5	Rinse the substrates in deionized water
6	Immerse the substrates in concentrated nitric acid to remove the caustic residue.
7	Rinse the substrates with deionized water
8	Continue with step 5 in Table 4.2

4.2.2 Selenium Alloys Used in the Study

The selenium source material used in the work was provided by the ANRAD Corporation, Montreal, Canada and other suppliers, together with certificates describing their composition. The materials were pelletized by the manufacturer as shown in Figure 4.1. The pellets had the form of biconcave spheres or partial spheres. The pellet sizes were different for the different alloys. However the pellets were all typically smaller than 4 mm in diameter with masses that were less than 90 mg. All the materials were kept in glass bottles with plastic covers and placed in a dark storage cabinet at room temperature (~22 °C) and normal pressure.

Selenium materials used in the course of the study varied from high purity Se (99.999%) to differently alloyed Se with As and Cl. The alloying in most of the cases was done by the supplier with the aim to retard the crystallization of a-Se and to modify the electronic transport in Se to meet the desired application needs. The added As was in the range 0-0.7 wt % while the concentration of Cl varied in the range 0-70 ppm.

Figure 4.1 Amorphous selenium pellets.

In some cases the alloying was conducted in our laboratory. The necessary materials were sealed in a quartz ampoule evacuated to a pressure of 2-4 × 10^{-5} Torr. During the synthesis, the ampoule was heated to a temperature in the range 500-1000 °C and held at that temperature for a period of time typically 24 hours long. The mixing of the melt was achieved by the rocking action of the furnace. After the synthesis, the ampoule was quickly immersed into water to quench the alloy and preserve it in amorphous (vitreous) state. Immediately before the evaporation the ampoule was crushed and chunks of material with a maximum mass of about 10 g were loaded into Se evaporator to deposit the photoconductor films.

4.2.3 Deposition of Amorphous Selenium Thick Films

The amorphous selenium thick films were prepared by thermal evaporation of selenium pellets from molybdenum boat using a modified Norton NRC 3117 vacuum system that is shown in Figure 4.2. The vacuum chamber is 16 inches in diameter and consists of stainless steel base and a steel bell jar that is about 25 inches high. The base has 16 CF flanges (2.75 inch in diameter) to accommodate electrical and mechanical see-through, gauges, etc. The pumping part

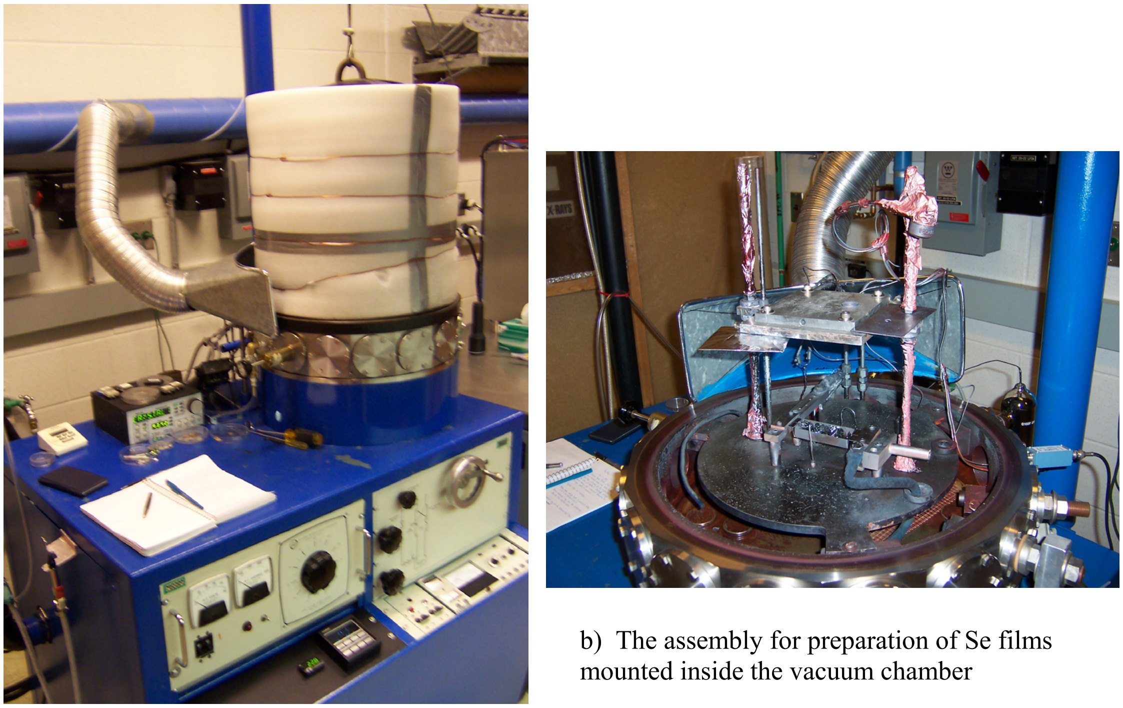

a) General view of NCR 3117 vacuum coater

b) The assembly for preparation of Se films mounted inside the vacuum chamber

Figure 4.2 Photographs of NCR 3117 vacuum coater.

of the vacuum coater is based on a two stage mechanical pump Welch 1397 (17.7 cfm) and a four stage 10 inch diffusion pump NRC VHS-10 (5300 l/s). All valves are manually operated.

The pressure in the vacuum chamber is monitored by a combination of thermocouple and a Bayard-Apert Ion gauges. The fore-line pressure of the diffusion pump is monitored by another thermocouple gauge. All gauges are connected to NRC 831 gauge controller. The ultimate vacuum in the chamber for the current configuration of the system is about 5×10^{-7} Torr. The evaporation of Se was usually performed at a pressure in the range from 8×10^{-7} Torr to 4×10^{-6} Torr depending on the evaporation conditions used (boat temperature, amount of material in the boat, etc.).

The assembly for the production of Se films mounted inside the vacuum chamber of the system is shown in Figure 4.2 (a photograph) and its most important parts are sketched in Figure 4.3 to better clarify the explanations.

The starting Se material in the form of pellets is placed inside a molybdenum boat supported by insulators on the Al base of the assembly. The boat is heated by passing a current through it. The values of the current were typically in the range 80-150 A depending on the boat construction and they were sourced from a 2 kW low voltage power supply that is a part of the

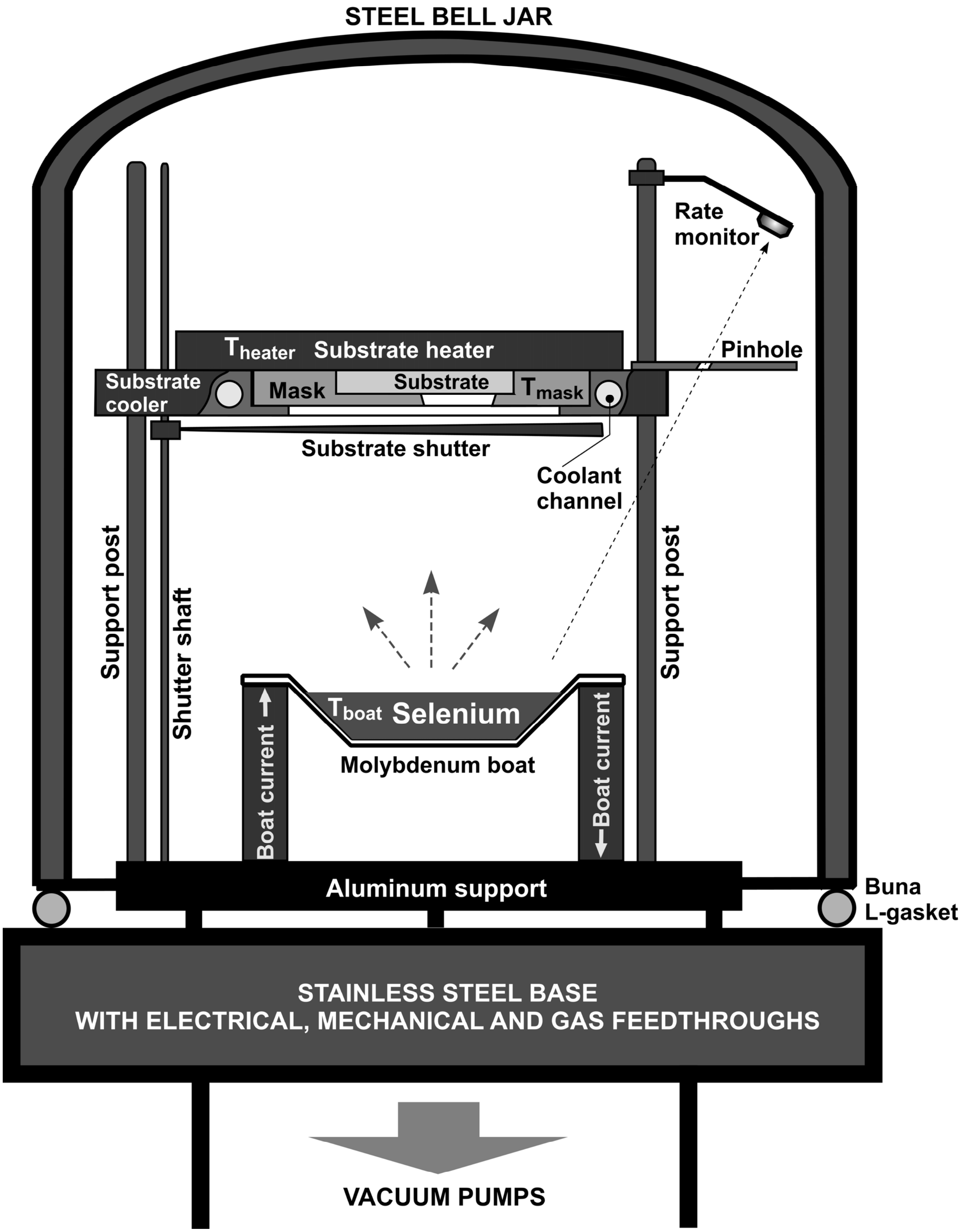

Figure 4.3 A sketch of the evaporation assembly inside the vacuum chamber.

NRC 3117 system. The temperature of the boat (T_{boat} in Figure 4.3) is measured by a thermocouple positioned into the Se melt. That temperature can be set to a desired value in the range 30-650 °C. An Omega temperature controller regulates the average current through the boat so as to keep the temperature of the molten selenium close (±1 °C) at the desired preset value. Most of the films were produced from Se evaporated from a melt with a temperature in the range 230-290 °C.

The a-Se films are grown on the desired areas of the substrates by deposition through a custom milled shadow mask (Figure 4.3). Most of the masks were machined from Al and only in some of the cases when Se was evaporated directly on a CCD chip the mask was made from Teflon to prevent scratching of the chip. A window on the bottom surface of the mask defines the area and the position of the Se film on the substrate (Figure 4.3).

The mask holder supports the mask with the substrate above the boat at a distance of 16 cm. The bottom part of the mask holder is suspended on 2 support posts and in its turn plays the role of mechanical support for the evaporation masks and for the substrate heater. The biggest mask that can be placed into the holder is 3.25" ×3.25" and that limits the area of the Se film to slightly less than 3 by 3 inch. The mask holder plays the important role of cooling the substrate as well, and that is the reason that is labeled as “substrate cooler” in Figure 4.3. Substrate cooling is accomplished by machining a channel in the Al body of the mask holder to pass a coolant.

A coolant (gas or liquid) can be run through the channel, which allows the substrate temperature to be regulated to values below the room temperature. We have used compressed air, tap water and ice-water as coolant and were able to achieve substrate temperatures as low as 2 °C during the evaporation of the film. The construction allows considerably lower substrate temperatures to be achieved if a suitable flow-through refrigerated chiller is used.

Substrate temperatures above 25 °C were achieved by operating a 150 W electrical heater in direct contact with the shadow mask and the substrate as shown in Figure 4.3. After placing the substrate with the mask into the mask holder/cooler assembly, the heater plate is bolted to the mask holder to ensure good thermal contact between all these parts. The temperature of the heater (T_{heater} in Figure 4.3) is controlled by a thermocouple connected to another Omega temperature controller. The heater operating at full power can heat the substrates to a temperature of about 350 °C. Thus the temperature of the heater/cooler assembly can be set to any value in the range the range 4-350 °C and can be controlled automatically with precision of ±1 °C. Due to the small but finite thermal resistances, the real temperature of the substrate will be somewhat different from T_{heater}. That is the reason for using an additional thermocouple in direct contact with the shadow mask (T_{mask} in Figure 4.3). The temperature T_{mask} is recorded in the evaporation logbooks as a close approximation to the real substrate temperature during the evaporation. Amorphous selenium films were deposited at different substrate temperatures in the range 2-70 °C.

A shutter (Figure 4.3) protects the substrates from Se vapors until stable evaporation conditions are reached (stable evaporation rate and pressure) and during the period after the final thickness of the film is reached and the boat with the Se melt is cooling down. The substrate shutter is manually operated.

SIGMA Instruments SQM-160 rate monitor records the deposition rate and hence indicates the thickness of the growing a-Se film. We were interested in depositing a-Se films as thick as 500 μm. Such thickness is out of the range of a quartz crystal rate monitor if the sensor is placed in the same plane with the substrates and "observes" the evaporation directly. We have solved the latter problem by placing the sensor at a greater distance from the boat and monitoring only part of the boat surface through a pinhole as shown in Figure 4.3. The disadvantage of the latter arrangement is that readings of the monitor are connected with the actual thickness of the film and with the real evaporation rate by a "tooling factor", or a scaling factor, that has to be experimentally determined by a trial run. In most cases, the tooling factor for our arrangement was about 50 and the measured evaporation rates were in the range 0.5-15 μm/min. The final thickness of the Se film was measured after the samples were taken out of the vacuum chamber by a precision micrometer Sylvac 50 with accuracy of ±1.5 μm. The majority of the films had thickness in the range 5-350 μm.

4.2.4 Fabrication of Metal Contacts

The samples for investigation of the electrical properties of a-Se films need to be equipped with metal electrodes. One the samples for TOF or IFTOF measurements require at least one of the contacts to be semi-transparent so as to allow optical excitation.

The metal contacts on the Corning 7059 glass substrates and on the surface of the a-Se films were thermally evaporated or DC sputtered.

The contacts from precious metals such as Au or Pt were typically deposited by sputtering in the Hummer VI unit shown in Figure 4.4. This production process is less expensive and less damaging for the Se films compared to the thermal evaporation process. Thus, for example, Pt evaporates at ~1800 °C which can lead to significant heating of the surface of the a-Se film. Heating of the a-Se film above the glass transition temperature of Se, which is only 40-50 °C can provoke crystallization and is not desirable. The amount of Pt needed for evaporation of one contact is much greater than the amount needed for sputtering one contact, which makes

METROVAC Coating Unit Type 12
Associated Electrical Industries LTD, SCOTLAND

General Purpose Coating Unit applicable in all branches of vacuum coating carried out on laboratory basis.

Supports:

- Filament evaporation
- Boat evaporation
- Carbon arc evaporation

HUMMER VI
Technics Inc., Alexandria, Virginia USA

Versatile D.C. Sputtering System for coating etching and cleaning of laboratory samples.

Deposits: gold, palladium, platinum, chrome, copper, nickel.

Typical thickness of the coating 75-1000 Å for 1-5 min.

Very gentle coating process, eliminating the effects of high temperature and damages from electron bombardment.

Figure 4.4 Equipment for fabrication of metal contacts.

the DC sputtering the less expensive process. The biggest samples that the chamber of Hammer VI unit can accommodate are 2.5 inch in diameter.

Contacts from other metals like Al, Cr, Mg etc. were produced by thermal evaporation in a METROVAC Coating Unit Type 12 which is shown in Figure 4.4. This small vacuum coater has an arrangement inside the vacuum chamber similar to the one for Se evaporation shown in Figure 4.3. The differences are that there is no substrate heating or cooling installed and there is no rate monitor. The metals are evaporated from a tungsten filament (Al), or a metal plated tungsten rods (Cr), or a from filament heated ceramic crucible (Mg). The thickness of the coating is controlled by the evaporation time. The biggest substrates on which metals can be evaporated in the Metrovac unit are 3 × 3 inch.

For both fabrication techniques, the area of the metal contact was defined by custom milled shadow mask. The bottom contacts (the ones produced on top of the glass slides) were rectangular in shape and area slightly less or equal to the area of the substrate. The top contacts (the ones produced on the top surface of the Se films) were circular in shape. Shadow masks for circular contacts are easier to manufacture and the contact has no sharp edges, which facilitates the measurements at high electric fields. The area of the top contact typically was 0.25 or 0.5 or 1 cm^2 to facilitate the conversion from current to current density. By carefully choosing carefully the deposition parameters and the deposition time, it was possible to produce semitransparent electrodes from Al, Pt and Au for TOF and IFTOF measurements.

4.2.5 Structure of the Fabricated Metal/a-Se/Metal Devices

Metal/a-Se/metal samples fabricated in the course of this work in most cases had one of the structures shown in Figure 4.5. Most of the samples prepared to investigate the transport in different Se alloys had the single layer structure shown in Figure 4.5-a. Such samples are best suited for TOF and IFTOF experiments and for that reason at least one of the top contacts was semi-transparent. In some cases, the film was produced on a glass substrate and the bottom contact was also transparent. In such cases photoexcitation from both sides was possible and hence using TOF experiments one can study how homogeneous the a-Se film is. The simple single layer sample structures were used also for dark current measurements. In these cases, several contacts from different metals were deposited on the top side of the sample. Thus, the influence of the metal on the metal-Se interface and on the dark currents was investigated. The samples with the structure shown in Figure 4.5-b-d are multilayer structures. The blocking layers were produced from specially doped Se or using special preparation conditions. Consequently, the transport in the blocking layer is modified. In some of these blocking layers the electrons can drift but holes become deeply trapped before crossing the layer (n-like layers). In the other type of blocking layers, the hole transport holes is good but the electrons become deeply trapped (p-like layers). The introduction of such layers aims to minimize the carrier injection from metal electrodes and hence the multilayered samples were used mainly for dark current investigations.

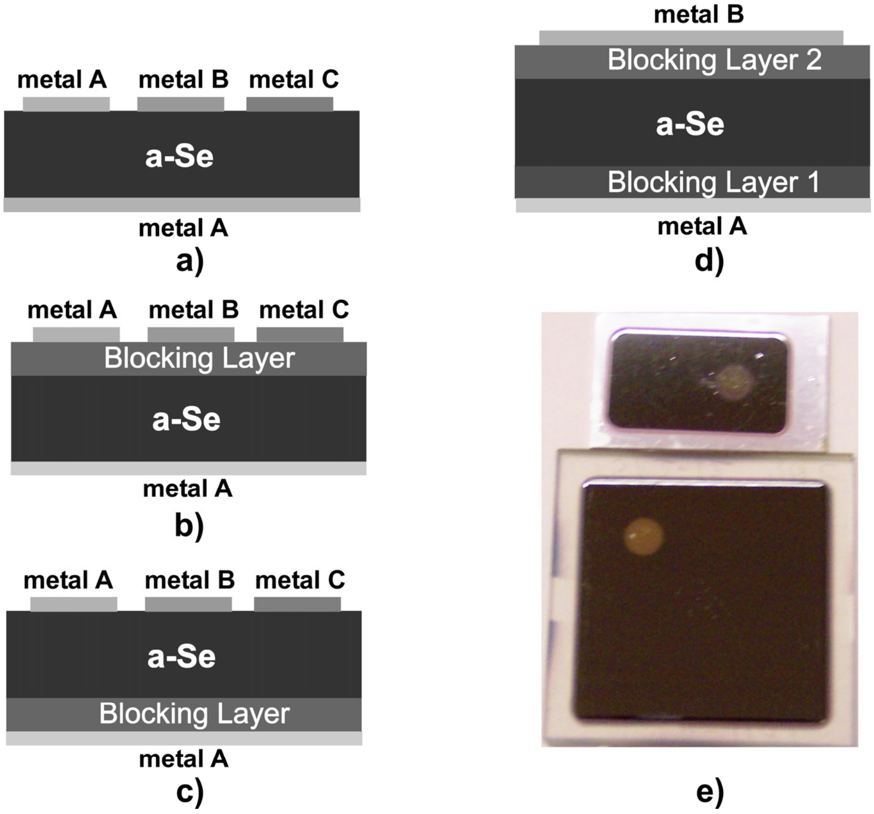

Figure 4.5 Structure of the samples used in the course of the work: a) simple single layer metal/a-Se/metal device; b) double layer metal/a-Se/metal device with blocking layer on top of the structure; c) double layer metal/a-Se/metal device with blocking layer on bottom of the structure; d) metal/a-Se/metal structure with two blocking layers; e) a photograph of two samples – the top sample is a single layer a-Se on aluminum substrate (Al/a-Se/Au) and the bottom one is again single layer Se deposited on glass coated with ITO substrate (ITO/a-Se/Pt structure).

Figure 4.5-e shows a photograph of two real single layer samples. The bottom sample is produced on top of 2.5" × 2.5" glass/ITO substrate. The thickness of Se is about 500 μm. The top

semitransparent contact is made from Au and has an area of 0.25 cm^2. The smaller sample is produced on oxidized Al substrate and has a Pt top contact with the same area.

4.3 Thermal Analysis

Differential scanning calorimetry (DSC) was routinely used for investigation, selection, comparison and performance evaluation of a-Se materials and films involved in the research. The proprties of greatest importance for us were the glass transition, the crystallization, the melting, and the material stability.

The instruments DSC 2910 and DSC Q100 (Figure 4.6) used to perform these measurements are from the product line of TA Instruments, New Castle, USA.

Figure 4.6 Model Q100, TA Instruments is a versatile research-grade DSC with capabilities to run modulated DSC experiments and built in TZERO^{TM} technology.

4.4 Dark Currents Measurements

The measurement of *I-V* characteristics is a simple experiment that requires basically two pieces of equipment. These are a power supply that acts as a source of all the voltages needed during the experiment and an ammeter capable of measuring all the currents in the range of interest. A few complications arise in the case when *I-V* measurements are performed on a-Se films. Due to the very high resistivity of a-Se, the dark currents in metal/a-Se/metal devices are very low and a sensitive electrometer should be used as an instrument for such current measurements. In the x-ray detectors, the a-Se layer is operated at very high fields – in some cases more than 10 V/μm. In order to apply such fields to the thickest samples of interest (~500 μm), the voltage source should be capable of supplying a bias in the range from 0 to ±5000 V.

The HV power supply and the electrometer, which were used for the dark current measurements in the course of this work, together with their basic technical characteristics are shown in Figure 4.7. For reasons that will be explained below, the dark current experiments on a-Se films can be very long. Computer control of the experiments is essential in this case to the measurements can be recorded accurately and also to make them more convenient for the

6512 Model Programmable Electrometer , Keithley

- Current Range: <2 fA to 20 mA
- Resistance Range: 100mohms to 200Gohms
- Voltage Range: 10μV to 200V
- Coulomb Range: 10 fC to 20 nC
- 5 fA of input bias Current
- <1mV of burden Voltage
- Built-in V-ohm Guard Switch
- Built-in IEEE-488 Interface

PS350 Model HV Power Supply, Stanford Research Systems, Inc

- Up to 5 kV with 1 V resolution, 25 Watts output power
- 0.001% Regulation, 0.05% Accuracy, low output ripple
- Dual polarity, programmable limits and trips
- Built-in IEEE-488 Interface

Figure 4.7 Photographs and the basic technical characteristics of the two major pieces of equipment in the dark current experiment.

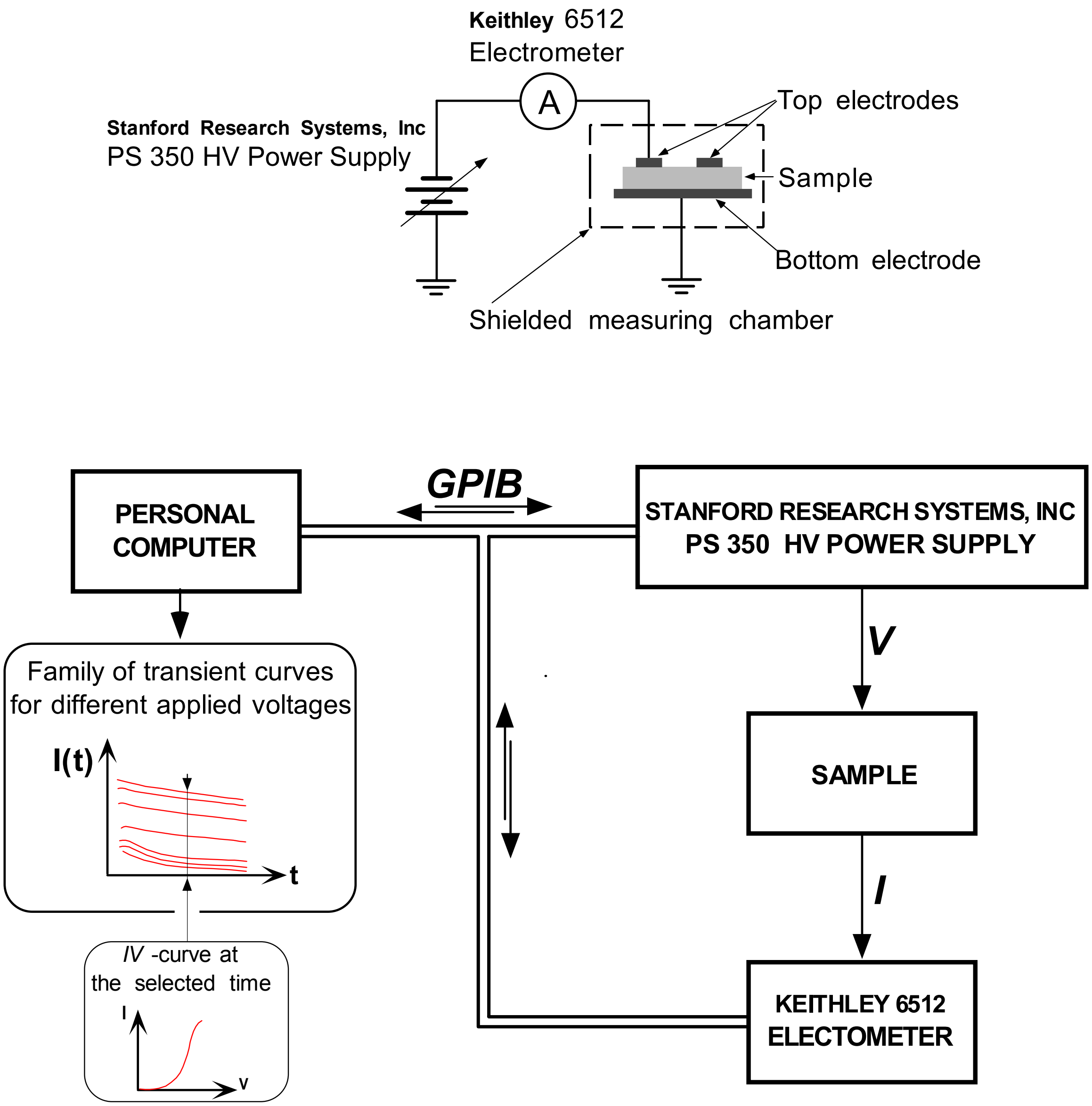

Figure 4.8 Diagram of the experimental setup for dark current I-t and I-V measurements on metal/a-Se/metal sample.

operator. For such reasons, both instruments were chosen to have built-in interfaces (IEEE-488) which ensures a relatively easy connectivity to a personal computer.

Measurements of the dark current-voltage characteristics, ordinarily a simple experiment, in the case of metal/a-Se/metal samples are complicated by long-term transients [14]. In most cases, the current would decay by several orders of magnitude over hours after application the bias voltage. Since the transient indicates that the electronic state of the sample is changing, the main difficulty is assuring the sample returns to the same state at the start of each measurement. This can be accomplished by resting the samples in short circuit for a sufficiently long period (24 hours) at the start of each experiment and at least twice the time that the previous bias was applied during the measurements.

The measurements of the dark current-voltage characteristics in this case have to be accomplished in the following order. The lowest voltage of the range of interest is applied to the sample. The current is followed for the desired time Δt (usually 20 min or more). The sample is rested for a period of time $2\times\Delta t$. The next voltage is applied, the current is followed for the same period and then the sample is rested again, and so on until the highest voltage of interest is reached.

The current-voltage characteristics can then be obtained by taking a cut at a particular time through a set of transients for a given pair of electrodes as demonstrated in Figure 4.8 which shows a block diagram of a computer controlled experiment that was built to perform dark current measurements in a-Se photoconductor structures.

Noise from the power supply capacitively coupled through the sample becomes troublesome for currents on the order of 10^{-13} A.

4.5 Experimental System for TOF Measurements

The experimental setup needed to perform TOF measurements is relatively simple in contrast to the theory of these measurement presented in section 3 . The block diagram of the equipment used in the course of this work is presented in Figure 4.9

A 60 MHz, 1 GS/s Tektronix TDS1002 oscilloscope is used to capture the TOF waveform and convert it into digital form. The built in interfaces RS-232 and IEEE-488 allow easy transfer of the data to a personal computer for storage and further processing.

The HV power supply used in our experiments is an EG&G ORTEC model 556H-P. It has been designed originally as a power source for photomultiplier tubes and for that reason it is capable of producing a relatively high current (up to 10 mA) in the whole range of the output voltages (±3000 V) with very low ripple (less than 10 mV). The unit has overload and short circuit protection and all together is very suitable for the purposes of the TOF photoconductivity measurements.

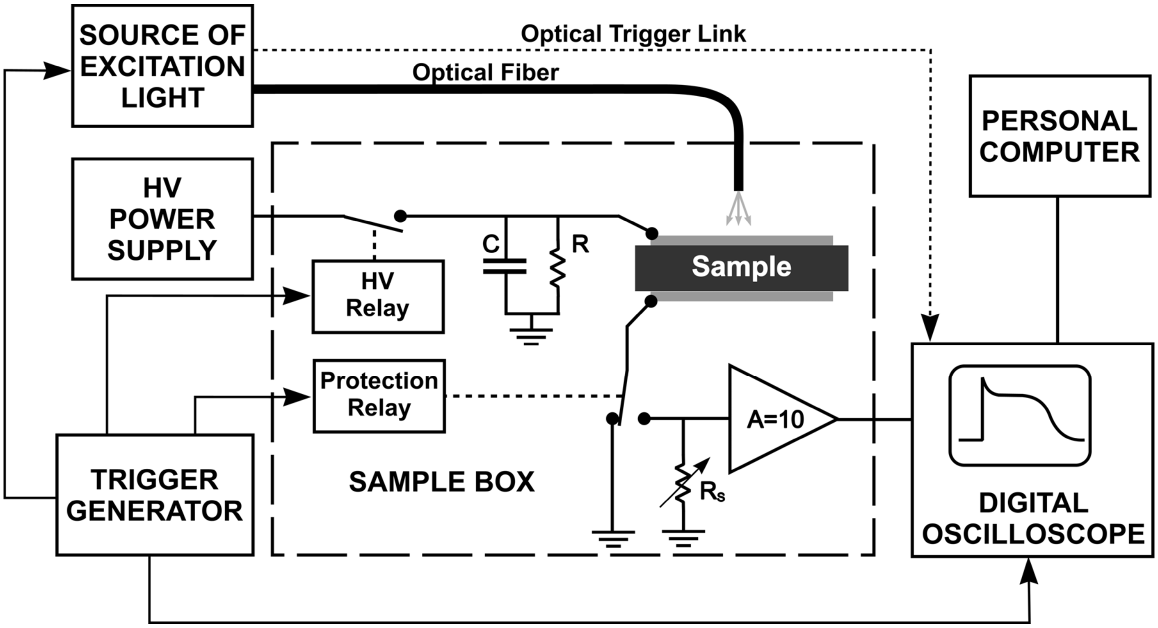

Figure 4.9 Block diagram of the experimental system for TOF transient photoconductivity measurements

The source of excitation light has to provide very short pulse of light that is strongly absorbed in the material under investigation, so that the requirements defined by Eq. (3.6) are satisfied as close as it is possible. We have used two types of light sources; guided discharge xenon flash lamp and N_2 laser. A guided discharge xenon flash lamp with modified trigger socket is capable of producing very short light pulses. In our setup the duration of the light pulse generated by the lamp is less than 200 ns. The Xe lamp produces broad spectrum light and the spectral region around 400 nm is filtered by a band pass optical filter and then coupled to an optical fiber bundle. The nitrogen laser used with the TOF system is model LN103, Laser Photonics. This is a transverse excitation N_2 laser capable of light pulses as short as 200-300 ps. The wavelength of the emitted radiation is 337.1 nm. The laser is coupled to 1mm core quartz fiber to allow easy excitation of the samples. The light intensity for both sources can be scaled down with a set of neutral density filters to meet the weak excitation requirement under all experimental conditions. Both light sources are capable of providing a synchronization signal derived from the generated light to trigger the oscilloscope at the instance of the flash (see Figure 4.9) with essentially no jitter, which is extremely important when photocurrents need to be measured over short timescales.

During the measurement, the sample is placed on an insulating platform in the sample box (Figure 4.9) and its electrodes are connected to the system by means of spring contacts. The HV relay applies the bias across the sample only when a photocurrent waveform has to be collected. Thus, the sample is under bias for a very short time and space charge built-up due to carrier injection from the contacts is minimized. The protection relay connects the sample to the amplifier with some delay after the application of the bias voltage. The delay is sufficiently long to protect the amplifier from the displacement currents when the bias is switched on, and, more importantly, from catastrophic failures associated with sample break down as a result of the application of a high voltage. The resistor R in Figure 4.9 has a value that is much smaller than the resistance of the sample and at the same time it is big enough to avoid the unnecessary loading of the HV power supply. With the HV relay opened, both contacts of the sample are grounded; one through the resistor and the other through the normally closed contact of the protection relay. The latter ensures proper conditions for resting the sample between the experiments. The capacitor C in Figure 4.9 creates an AC conduction path for the photocurrent and thus improves the signal quality significantly. In addition, it is sufficiently large to keep the voltage across the sample relatively constant during the TOF photocurrent measurements.

The sampling resistor R_S in Figure 4.9 converts the photocurrent to voltage which is then amplified about 10 times by the signal amplifier. The operator can select between 12 different logarithmically spaced values of R_S in the range 50 Ω to 200 kΩ by means of a rotary switch. The amplifier is built around OPA567; a 1.6 GHz, low-noise, FET-input operational amplifier and is configured to drive properly the 50 Ω coaxial line that feeds the amplified signal to the oscilloscope. The very high gain bandwidth product of the amplifier has been chosen to minimize the effects of the amplifier limited bandwidth on the measured signal because "paradoxically, knowledge of the short-time transient photoresponse can be vital in the estimation, via a Fourier transform, of the density of deep-lying states" [75]. The same applies when Laplace transform technique is used [74].

The sample box in Figure 4.9 shields the sample from the ambient light and from electro-magnetic interference (EMI).

The measurement of a photocurrent waveform is started and controlled by a custom built trigger generator (Figure 4.9). During a typical measuring sequence, the generator will trigger the HV relay, the protection relay, the optical source, and the oscilloscope (if not triggered optically by the light source) at appropriate instants of time so as to record a TOF waveform. All triggering signals are TTL signals, except the one that triggers the light source. A powerful electric discharge takes place in the optical source every time when it is triggered which produces strong EMI as well as high frequency feedback transients in the associated electronic circuits (e.g. the xenon trigger circuit, HV supply etc.). Their influence on the signal is minimized by triggering the light source through an optical link

4.6 Experimental Setup for Interrupted Field Time-of-Flight Measurements

In chapter 3.4 we have described the basic principles and the theory of the interrupted field time-of-flight (IFTOF) technique. As already discussed in chapter 3.4 the most significant difficulty associated with the practical application of IFTOF technique are the large displacement currents that appear in the moments of removal and reapplication of the external electric field across the sample.

In the present research we have used an IFTOF setup that relies on a grounded bridge network as a method for elimination of the displacement current signal although many other approaches are possible [113-116]. The advantage of this technique is that a grounded voltage supply may be used to bias the sample to allow for good EMI shielding. The IFTOF apparatus together with the concept of the bridge circuit is illustrated in Figure 4.10 and is described in detail in [117]. The application and removal of the high voltage bias produces a displacement current signal in both branches of the bridge. If the air variable capacitor *C* is adjusted so that it is equal to the sample capacitance, then the displacement currents in the two bridge resistors will be the same and can be eliminated by performing a differential measurement across the bridge. The differential amplifier will detect the photocurrent signal because it appears in only one branch of the bridge.

The two voltage limiting circuits built on the diodes D1-D4 protect the differential amplifier from entering saturation by limiting the displacement current signal to less than 0.8 V. The remaining common mode signal can be easily rejected by carefully matching the values of the resistors in the bridge and by using an amplifier that has CMMR better than 60dB.

The differential amplifier is build around a high CMMR video amplifierAD830 (GBP = 80MHz, CMMR = 60 dB at 60MHz), configured as unity gain differential amplifier. The output stage uses fast operational amplifier (AD827) configured as non- inverting amplifier with a gain of 16 dB. The latter stage has cable driving capability and the gain of 16 dB is sufficient to raise the signal above the noise background of the digital oscilloscope.

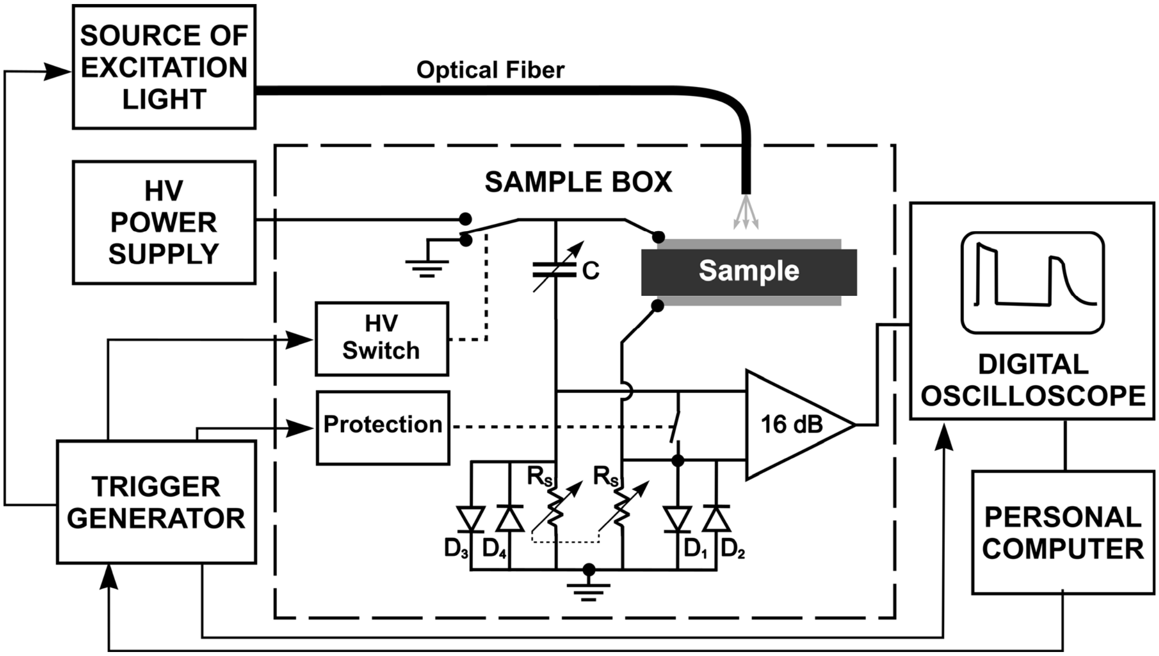

Figure 4.10 IFTOF apparatus using grounded bridge network to eliminate the displacement current signal.

A precision, normally open CMOS analog SPST switch from Maxim (MAX318) was placed across the inputs of the amplifier to protect the signal electronics from the high voltage transients during switching. The switch was selected for its low charge injection (~10 pC). The protection switch is controlled by the trigger generator through a small circuit labeled "Protection" (Figure 4.10).

The HV switch functions as a single pole double-throw (SPDT) switch with the output normally connected to ground through as shown in Figure 4.10. The switch is built using two fast switching n-channel IRFBG30 HEXFETs in a totem pole configuration [117] and is capable of switching voltages up to 1kV with rise and fall times that are less than 0.2 μs. The HEXFETs are driven by two HCPL-3120 optocouplers, which also serve to isolate the control circuitry from the high voltage output of the switch. One TTL signal supplied by the trigger generator controls the HV switch.

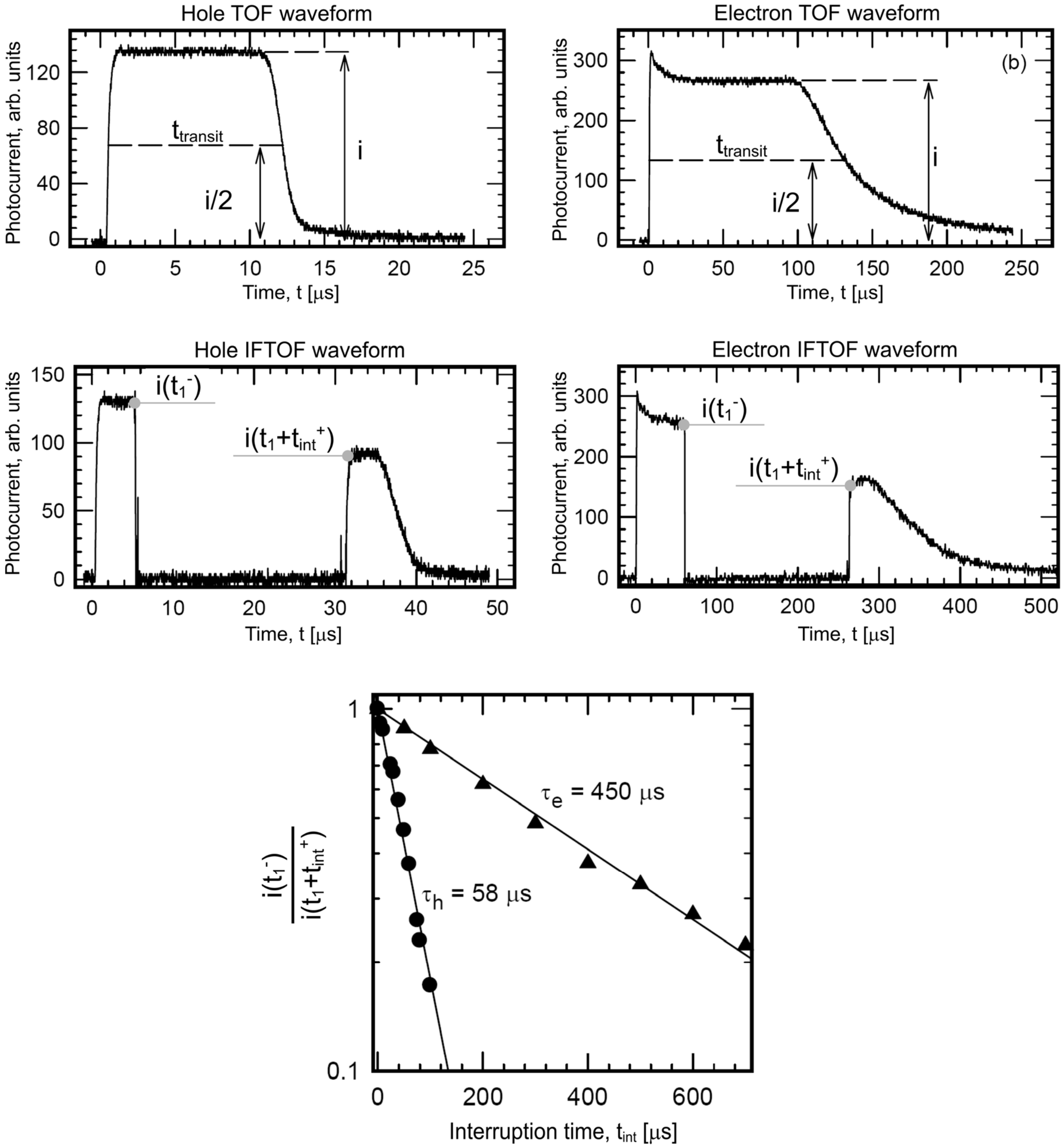

Figure 4.11 A set of typical electron and hole TOF and IFTOF waveform recorded with the IFTOF apparatus described in the subsection and example regression analysis that result in the determination of carrier lifetime. The a-Se films is 224 μm thick and is deposited from Se:0.2%As alloy. The set of graphs was taken from [117].

The trigger signals for the IFTOF system were generated using a Computer Boards PCI-CTR05 counter board installed in the PCI extension slot of the personal computer (Figure 4.10).

The heart of the counter board is an AMD 9513 counter/timer chip that contains five 16 bit up/down counters. The custom trigger generator code was written in C++ and was integrated into the TOF/IFTOF user interface software.

The high voltage power supply and the source of the optical excitation have already been described in subsection 4.5. The experiment is controlled by a personal computer through custom written software that initializes the trigger generator and starts the desired measuring sequence. Communications with the digital oscilloscope (Tektronix TDS210 in this case) use the built in that devices IEEE 488.2 interface.

A typical IFTOF experiment captures two waveforms. The moment of the interruption t_1 and the desired interruption period t_{int} are first set and the bridge is actuated without any photoexcitation but with an applied bias, to collect the baseline signal. The bridge is then automatically re-excited after a short pause, this time with photoexcitation, to capture and upload the photocurrent signal. A software routine subtracts the two signals and the resulting waveform is displayed and stored for further processing.

A set of typical electron and hole TOF and IFTOF waveform recorded the IFTOF apparatus described in this subsection are shown in Figure 4.11. In the same figure we have illustrated an example regression analysis that result in the determination of electron and hole lifetime.

4.7 X-Ray Measurements

Several types of x-ray measurements were attempted during the course of this work. Most of them were designed to measure the x-ray sensitivity of certain metal/a-Se/metal detectors and to investigate how that sensitivity changes under different experimental conditions. Other x-ray measurements were performed to study the effects that the exposure to x-rays induces in the sample; for example the effect that the x-ray exposure has on the dark current through the sample, the effect that the x-rays have on the carrier transport in a-Se films, etc.

Two intraoral dental systems were used as a source of x-ray radiation for all the measurements: Gendex, GX-1000 and Siemens, Heliodent. Each of these systems contains relatively small x-ray tube with tungsten anodes and 2.5 mm and 2 mm internal Al filtration

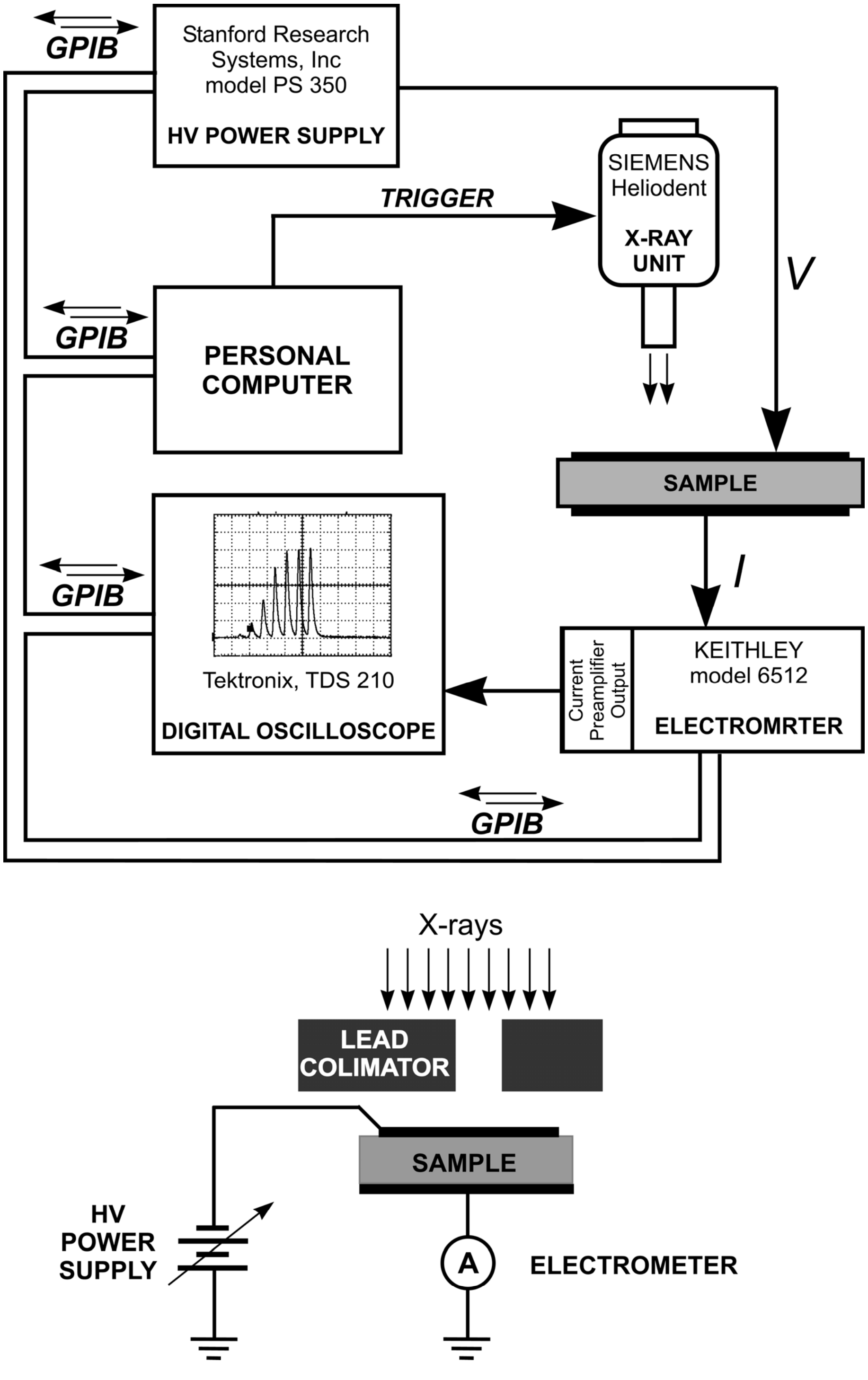

Figure 4.12 Schematic diagram of a computer controlled experiment for x-ray measurements on metal/a-Se/metal devices.

respectively. The Siemens tube operates at fixed voltage of 57 kVp and fixed tube current of 7 mA. The Gendex system is more flexible. The tube current can be set to 10 mA or to 15 mA by the operator, while the tube voltage can be varied continuously in the range 50 – 100 kVp. The exposure duration for both systems is controlled by timers and can be set to different values in the range 3/60 s to 5 s.

The magnitude of the x-ray exposure for a given set of conditions was measured using a Keithley 96035 ionization chamber connected to a Keithley 35050 dosimeter. The dosimeter produces a voltage reading that is proportional to the x-ray exposure. The proportionality factor was determined by a standard calibration procedure that was performed at the Cancer Center at the Royal University Hospital, University of Saskatchewan.

The biological protection was ensured by mounting the x-ray heads in special lead shielded (5 mm lead) cabinets. The Gendex x-ray system was used together with the IFTOF apparatus shown in Figure 4.10 while the Siemens system was used in the experimental setup shown in Figure 4.12.

The x-ray sensitivity (the charge collected per unit area per unit exposure) was measured by placing the Keithley 6512 electrometer (see Figure 4.12) into Coulomb mode. The current through the electrometer in that mode is integrated and the charge collected during the x-ray exposure is measured and then the result is transferred to the computer. The computer then calculates the sensitivity for the conditions of the experiment (x-ray exposure, electric field, etc.). The latter method is applicable if the collected charge is below 20 nC. If the collected charge was bigger than 20 nC a different technique was used. The x-ray current induced in the sample was captured on a digital oscilloscope Tektronix, TDS-210 connected to the current preamplifier output of the Keithley 6512 electrometer as shown in Figure 4.12. The current waveform was transferred to the computer after the exposure. The charge collected during the exposure was then calculated by the software running on the computer that integrates the x-ray induced photocurrent to finally yield a value for the x-ray sensitivity under the given experimental conditions. All x-ray sensitivity results were corrected for the dark current running through the sample during the measurements.

As explained above, the experimental setup shown in Figure 4.12 allows the instantaneous x-ray induced current in the sample to be directly recorded on the oscilloscope. For long exposures, the average x–ray induced current can be measured directly by the electrometer working in the current mode. That mode of operation allows the changes in the dark current in the samples after the end of the x-ray exposure to be conveniently followed and recorded on the personal computer for analysis.

The whole experiment is computer controlled, by custom written software.

4.8 Summary

This chapter provides an outline of the various experimental methods used in the course of present research. The techniques for the preparation of different metal/a-Se/metal samples and devices were described in detail in the beginning of the chapter. The apparatus and the methodology for measuring of dark current *I-t* and *I-V* characteristics on metal/a-Se/metal samples were also described. The experimental techniques take into account the long transients that follow the application of the voltage across the a-Se samples. The experimental implementation of TOF and IFTOF techniques for the investigation of carrier mobility, lifetime and mobility-lifetime products were described later in the chapter. Finally the equipment used for various x-ray measurements was briefly discussed together with the technique used to measure the x-ray sensitivity of metal/a-Se/metal samples.

5. RESULTS AND DISCUSSION

5.1 Effects of Alloying and Doping on Charge Transport in Vacuum Deposited Amorphous Selenium Films

5.1.1 Introduction

Electronic transport in a given vacuum deposited a-Se film depends on the properties of the selenium alloy used for the fabrication of the film and on the set of deposition conditions under which it was prepared. Under standard industrial conditions, the most important deposition conditions are kept constant during the film fabrication. These include the base vacuum, temperature of the molten Se, substrate to source distance, deposition rate, substrate temperature, deposition time, etc. If the fabrication conditions are kept constant, the only way to control the transport in fabricated a-Se films is by suitably alloying and doping the material used for film fabrication. Fabrication of a-Se based pin- like structures for example relies on the evaporation of at least three layers with totally different transport properties as explained in subsection 1.3. A key to control the charge transport in a-Se film under fixed preparation conditions is to suitably alloy the starting Se material by adding certain elements that will promote or suppress the transport of one or both types of carriers in the film. At the same time, the long term stability (the resistance against crystallization) of the film should not be harmed by the additive used to alter the charge transport properties. The latter, together with the huge variations in the properties of the starting pure Se material, makes the alloying process very difficult and motivates a systematic study of the effects of alloying and doping on the charge transport in vacuum deposited a-Se. Results from such experiments will be described in this subsection. The stress of the study was placed on the influence of As and Cl which are currently the most widely used additives in the industry at the moment.

In the past, the effects of different additives had been studied by either xerographic measurements or by conventional TOF experiments. Xerographic experiments involve measuring the first residual potential that results from the complete photo discharge of an electrostatically charged a-Se film. Such experiments can only provide a value for mobility-lifetime product $\mu\tau$ of the carriers. These values are strongly dependent on the actual model used to interpret first residual potential decay [118, 119], hence $\mu\tau$ values determined by this technique tend to be only estimates. In addition, for most of the films it is difficult to charge the surface of the a-Se film to high negative voltages, which makes the measuring of $\mu\tau$ for electrons difficult. In conventional TOF measurements, one relies on decreasing the electric field until the carrier transit time ($t_{\text{transit}} = \dfrac{L}{\mu F}$, see subsection 3.2) is comparable with the lifetime τ and the photocurrent decays exponentially with a time constant τ that represents the deep trapping time, i.e., the lifetime. This method was described in subsections 3.3.5 and 3.3.6, and used previously to measure μ and τ in stabilized a-Se [120, 121]. There are various problems with this technique as well. First, in a-Se alloys, photogeneration depends on the field and if we reduce the field too much we effectively extinguish the photocurrent. Long lifetimes, therefore, cannot be measured reliably. Secondly, the composition of alloyed a-Se is not completely uniform across the film, which means that the shape of the photocurrent will be influenced by this fractionation effect. Further, any net bulk space charge in the sample due to trapped carriers will result in a nonuniform field profile *F(x)* which will lead to a photocurrent shape *i(t)* that depends on this field profile rather than on trapping. Thus, the determination of τ from the shape *i(t)* of the conventional TOF photocurrent under certain conditions becomes unreliable.

In IFTOF experiments, on the other hand, the drift of photo injected carriers is suddenly halted at a time t_1 corresponding to a particular location x_1, usually near the middle of the sample, by removing the field (see section 3.4). The carriers then gradually become trapped at position x_1, and the concentration of free carriers decreases exponentially with a time constant τ equal to the lifetime (the deep trapping time). When the field is reapplied at a time t_2, the carriers begin to drift again and give rise to a photocurrent $i(t_2)$ that is less than the photocurrent $i(t_1)$ at time t_1 just before the interruption. The lifetime τ is obtained from the slope of the $\ln\left(\dfrac{i(t_2)}{i(t_1)}\right)$ vs. $(t_2 - t_1)$ plot as described in subsection 3.4. This technique has been widely used by Kasap and coworkers to obtain accurate measurements of τ for both electrons and holes in a wide range of a-Se alloys [122].

All the results from mobility and lifetime measurements that will be described further in this chapter were obtained using a combination of TOF and IFTOF techniques to achieve higher precision in lifetime determination.

5.1.2 Effects of Arsenic and Chlorine Additions on Charge Transport in Se:As:Cl Alloys

The usual way in which the influence of As and Cl additions on the charge transport in a-Se films is being investigated involves three steps. The first step is preparation set of alloys containing different amounts of As and Cl based on one and the same pure Se material. The second step is the fabrication of films from all the alloys produced in the previous step. The final third step involves charge transport measurements of the produced films and interpretation of the results. It is clear that such investigations involve a huge amount of work and are almost never complete. The published results are usually based on limited number of alloys derived in most cases from only one starting pure Se material. The starting material in most cases is chosen to have poor or modest transport properties for both electrons and holes and thus a lot of possibilities for the improvement of the transport for both types of carriers in the resulting alloys are ensured. For these reasons, the results from such studies cannot be reviewed as complete.

A set of data from the experiments conducted in the usual way described above collected in the course of this PhD study is presented in Figure 5.1 and Figure 5.3. The concentration ranges studied were from 0 to 0.7% (wt.) for As and 0-40 ppm (wt.) for Cl. Such alloys are commonly involved in the fabrication of a-Se based photoconductor layers (more precisely, i- like layers) for x-ray detector applications. The starting pure Se material (99.999% purity) was chosen to have the following transport parameters: $\mu_h = 0.135$ cm^{2}V^{-1}cm^{-1}, $\tau_h = 5$ μs, $\mu_e = 5.1\times10^{-3}$ cm^{2}V^{-1}cm^{-1}, and $\tau_e = 100$ μs. It is obvious that the starting pure Se had very modest transport for both types of carriers.

The whole set of alloys was produced by ANRAD Corp. All a-Se films were produced in our lab as described in subsection 4.2. The deposition conditions were kept as constant as possible: boat temperature of 250 °C, substrate temperature of about 60 °C. The film thickness was in the range from 80 to 200 μm.

The results for hole transport are presented in Figure 5.1. It is apparent from the latter figure that the hole lifetime and also the hole range both decrease with As addition irrespective of the Cl content. Every time the Cl content is increased, there is a corresponding increase in τ_h and $\mu_h\tau_h$. Every time the As content is increased, there is a corresponding decrease in τ_h and $\mu_h\tau_h$. It is clear that As and Cl additions have opposite effects on the hole lifetime and range. The hole

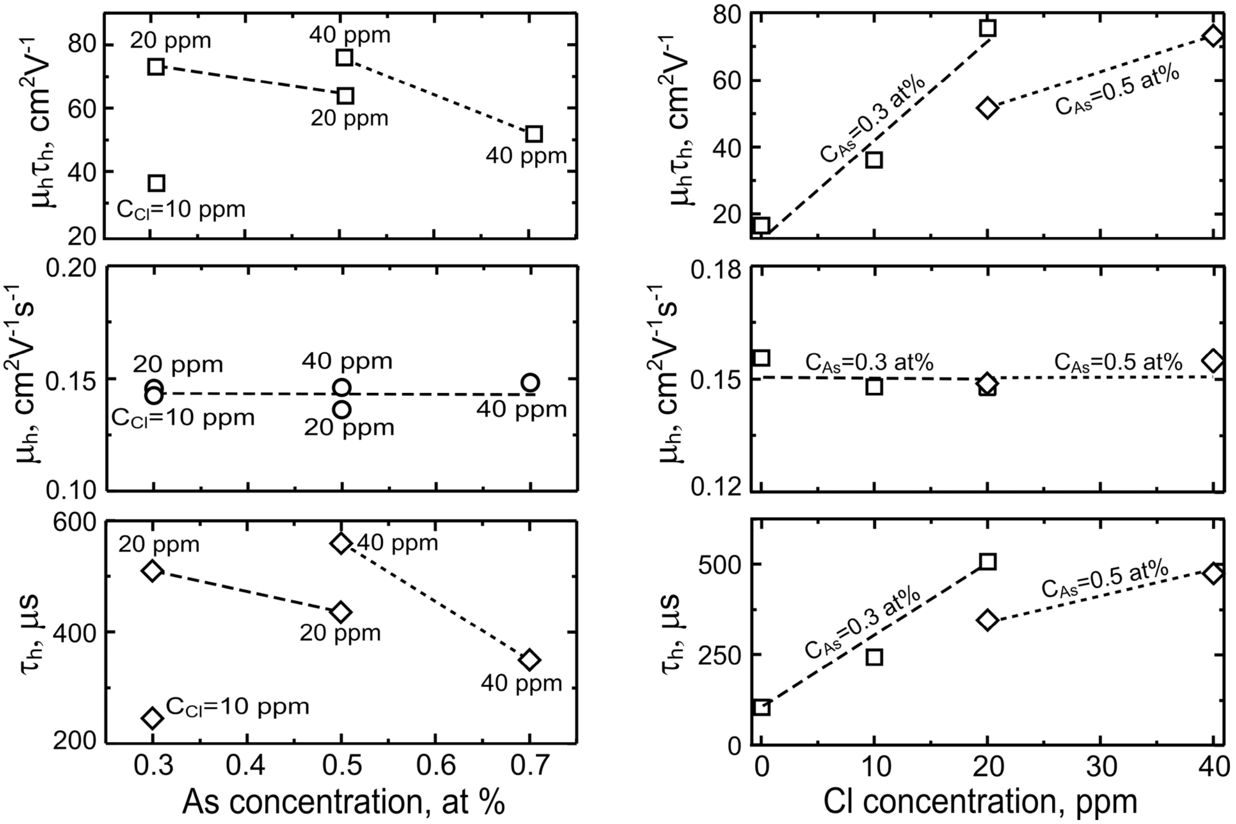

Figure 5.1 The influence of As and Cl doping on hole lifetime, hole mobility and hole mobility-lifetime products in a-Se films prepared by vacuum evaporation technique.

drift mobility is unaffected by either the addition of As or Cl. The most important technological conclusion from the data presented in Figure 5.1 is that by appropriately choosing the relative amounts of As and Cl, we can control the hole range. There is some latitude in choosing the composition of stabilized a-Se for a given $\mu_h\tau_h$ product. For example, the hole range for 20 ppm of doped a-Se:0.3% As is about the same as that for 40 ppm of doped Se:0.5% As. Approximately 20 ppm Cl is needed to compensate for the addition of 0.2% As.

The influence of As and Cl additions on the electron transport have also been studied. It is well known that the electron mobility μ_e in a-Se depends on the applied electric field [123]. The results from our measurements of μ_e confirm the latter dependence as illustrated in Figure 5.2. In order to get comparable values for different samples, we have measured μ_e at the same electric field (4 V/μm) for all the samples. Figure 5.3 shows the effects of As and Cl on electron transport parameters. It is apparent that the behavior of the electron lifetime τ_e is opposite to that of holes. Increasing the concentration of As increases the electron lifetime, whereas increasing the Cl content decreases the lifetime. The electron mobility tends to decrease as the As content is increased (Figure 5.2 and Figure 5.3), but the increase in the lifetime is greater and thus the electron range $\mu_e\tau_e$ increases by adding As (Figure 5.3), which is a distinct technological advantage. The electron mobility is not affected by Cl doping, which is apparent from Figure 5.3. The results are qualitatively summarized in the Table 5.1. It is interesting that only small amounts of Cl (only a few ppm) are needed to observe large changes in the properties compared with the amount of As (typically 0.1–1%) needed for similar changes. For example, the reduction in hole lifetime induced by a 0.2% increase in the As concentration from 0.3 to 0.5 at. % may be compensated by the addition of only 20 ppm of Cl (see Figure 5.1).

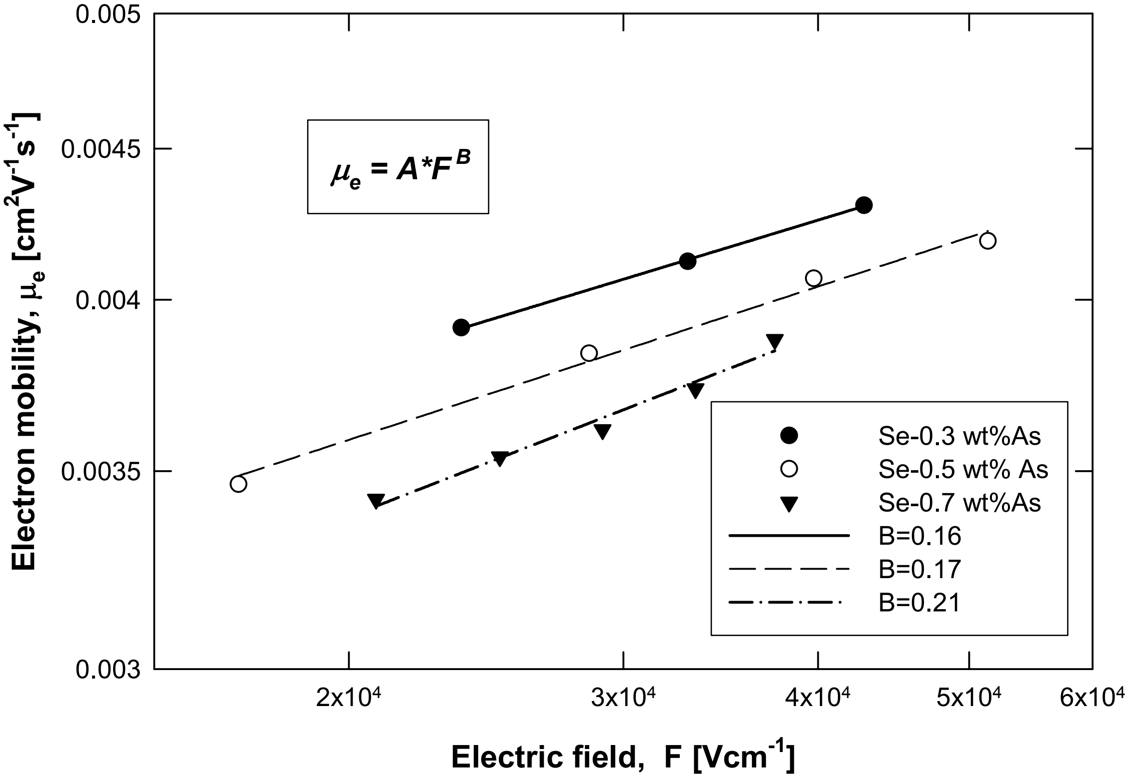

Figure 5.2 A log-log plot of the electron mobility vs. the applied electric field in vacuum deposited films from Se:As:Cl alloys.

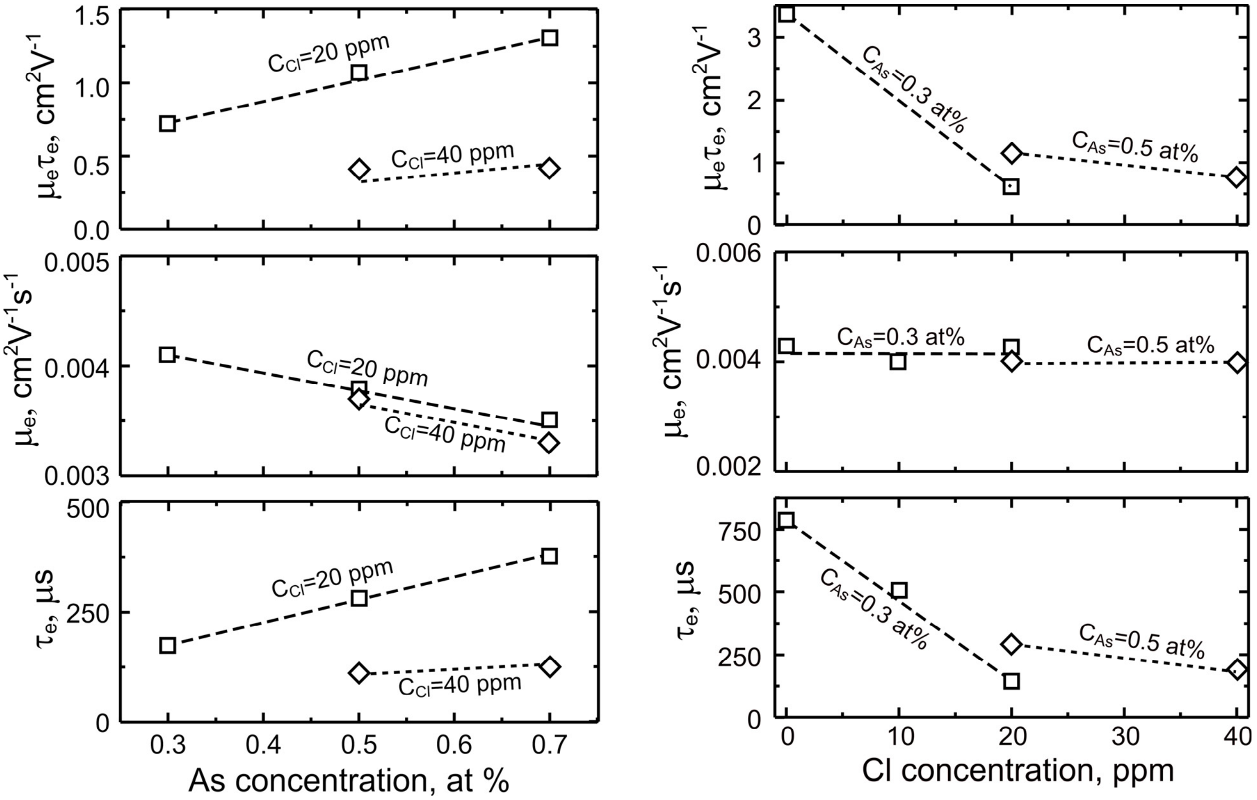

Figure 5.3 The influence of As and Cl doping on electron lifetime, electron mobility and electron ranges in a-Se films prepared by vacuum deposition technique.

Table 5.1 The influence of As and Cl doping on charge transport in vacuum deposited a-Se films.

ADDITIVE	EFFECTS ON HOLE TRANSPORT			EFFECTS ON ELECTRON TRANSPORT		
	Mobility	Lifetime	Mobility-lifetime product	Mobility	Lifetime	Mobility-lifetime product
As	no or very small change	decrease	decrease	decrease	increase	increase
Cl	no or very small change	strong increase	strong increase	no or very small change	strong decrease	strong decrease

The results described above have been published in [124,125] and are in good agreement with the data from previous studies. However, widely accepted explanation of the influence of As and Cl on the charge transport in vacuum deposited a-Se films is still missing in the scientific literature because the structure of a-Se and nature of the structural defects in it are not fully understood even today.

Most authors will try to explain the effects of As and Cl within the framework of the band transport formalism for amorphous semiconductors, in terms of changing the populations of traps that control the mobility and lifetime of the carriers. This approach was adopted in [124] and can be summarized as follows. Some authors believe [126] that over (Se_3^+) and under (Se_1^-) coordinated charged defects in a-Se act as deep electron and hole traps respectively. Then the action of As and Cl can be explained in terms of defect forming reactions which alter the population of such deep electron and hole traps. Indeed Cl is highly electronegative and for that reason it is believed that it can cause the following reactions to occur:

$$\begin{aligned} \mathrm{Se}_2^0 + \mathrm{Cl}_1^0 &\longrightarrow \mathrm{Se}_3^+ + \mathrm{Cl}_0^- \\ \mathrm{Se}_1^- + \mathrm{Cl}_1^0 &\longrightarrow \mathrm{Se}_2^0 + \mathrm{Cl}_0^- . \end{aligned} \tag{5.1}$$

The first reaction describes the formation of a deep electron trap at the expense of one neutral normally coordinated Se atom under the influence of Cl. The second reaction shows how Cl can neutralize a deep hole trap and turn it in a normally coordinated Se atom. Thus Cl increases the population of deep electron traps (Se_3^+) and decreases the population of deep hole traps (Se_1^-) which translates into increasing hole lifetime and decreasing electron lifetime. At the same time, one can assume that the population of shallow traps that control the mobility of the carriers remains unaffected by Cl and so neither electron nor hole mobility is affected by the addition of Cl. The above is true, only if we assume that Cl_1^- does not act as deep or shallow hole trap.

It is more difficult to explain the effects of As in terms of simple defect-forming reactions. The electronegativity of As differs only slightly from that of Se, which implies the formation of both As_2^- and As_4^+ charged defects. Normally bonded As_3^0 atoms can react with Se_3^+ defects to create As_4^+ by the structural reaction

$$\mathrm{Se}_3^+ + \mathrm{As}_3^0 \longrightarrow \mathrm{Se}_2^0 + \mathrm{As}_4^+ \ . \tag{5.2}$$

The above reaction explains the effect of As on the electron transport if we assume that As_4^+ acts as shallow electron trap. The reaction demonstrates the conversion of one deep electron trap (Se_3^+) into a shallow electron trap As_4^+. Thus the population of deep electron traps decreases and the population of shallow electron traps increases due to the addition of As. This results in an increase in the electron lifetime and a decrease in the electron mobility, or exactly the trends that are experimentally observed as As is added to Se.

The effects on hole transport induced by As can be explained by the reaction below

$$\mathrm{Se}_2^0 + \mathrm{As}_3^0 \longrightarrow \mathrm{Se}_1^- + \mathrm{As}_4^+ . \tag{5.3}$$

The reaction explains the formation of deep hole traps and a shallow electron traps at the expense of normally coordinated Se and As atoms. Due to the above reaction, the population of deep hole traps increases and the hole lifetime decreases.

One would expect that As_2^- type centers will also be formed within the a-Se:As structure. Such centers can also trap holes. Thus, it is difficult to unambiguously explain the role of As. On an intuitive level, the formation of As_4^+ should require somewhat greater energy than the formation of As_2^- because As_4^+ must spatially connect with four neighbors (more lattice distortion will be needed to find four neighbors), whereas As_2^- simply fits into a chain. Although we do not yet have a complete model for the compensation effects of As and Cl in the a-Se structure, we can nonetheless speculate that under- and over- coordinated charged defects play an important role. There have been other discussions in the literature on the compensation mechanism between As and Cl in stabilized a-Se [95] though, to date, there is no accepted final model that can explain all the observations.

The explanation in terms of defect forming reactions presented above are speculative and do not exclude other possible explanations. Finding an universal explanation of the effects induced in charge transport in a-Se by different additives is extremely complicated, or even impossible. Each pure Se material comes with a unique cocktail of trace impurities which can have significant impact on the charge transport in that material. The added As or Cl can with great probability form compounds with some of the impurities present in the pure Se material. Thus certain impurities can be eliminated from the structure of a-Se as a result of As or Cl addition and that "purification" can be the reason for the observed changes in the transport properties. Further, the newly formed compounds can act as crystallization centers in a-Se film. Thus, nanocrystals from different types with concentrations 10^{15} cm^{-3} can easily be formed [29]. Trapping at the phase boundaries can alter the charge transport in a-Se significantly. The net effect of a given dopant on the charge transport in a-Se is probably a combination of all the channels of influence mentioned so far. Universal and quantitative explanation of charge transport effects is a-Se induced by different additives is an extremely difficult task.

The results from the next set of experiments seem to confirm further the above flow of thoughts. In the following experiments, we have examined the reproducibility of charge transport parameters in vacuum deposited a-Se films produced from different alloys that have one and the same composition – Se-0.2%As no Cl. That composition is often used for the production of i- like s in x-ray image detectors that collect electrons at the pixel electrodes. In this case, the electron transport is more important for the detector performance than the hole transport. This is the reason why only As is added to the pure Se – to retard crystallization and to improve electron transport. All alloys studied in this set of experiments were produced under industrial conditions by one of ANRAD Corp. Se suppliers. This means that several crude Se source materials were purified using the same equipment and methods to 99.999% purity. Further, thus purified Se materials were alloyed with 0.2% As using the same reactor and the same conditions. All the materials were pelletized under the same conditions. All packing, transport and storage conditions were the same for all alloys involved in the study. The description above shows that only the properties and the origin of the crude Se material were different for the alloys under study.

The a-Se films for studying the electron transport were produced in our laboratory. The deposition conditions were kept as constant as possible. The temperature of the molten Se was 250 °C and the substrate temperature was 60 °C for all the depositions. The thickness of the produced films was in the range 80-200 μm.

The results from the charge transport investigations of these films are summarized in Figure 5.4 and Figure 5.5 above. As can be seen from Figure 5.4 the electron transport is “good” for all alloys which can be seen from the values of mobility-lifetime products for all investigated alloys. These values are in the range from 1×10^{-6} to 3×10^{-6} cm^2V^{-1}. This is a great improvement over the electron transport in the pure (99.999%) source Se materials from which these alloys were prepared (see for one example Pure Se #1 in Figure 5.6). However, alloys #1, #2 and #3 are considered to have poor to mediocre electron transport for production of thick (700 μm or more) a-Se based i- like layers.

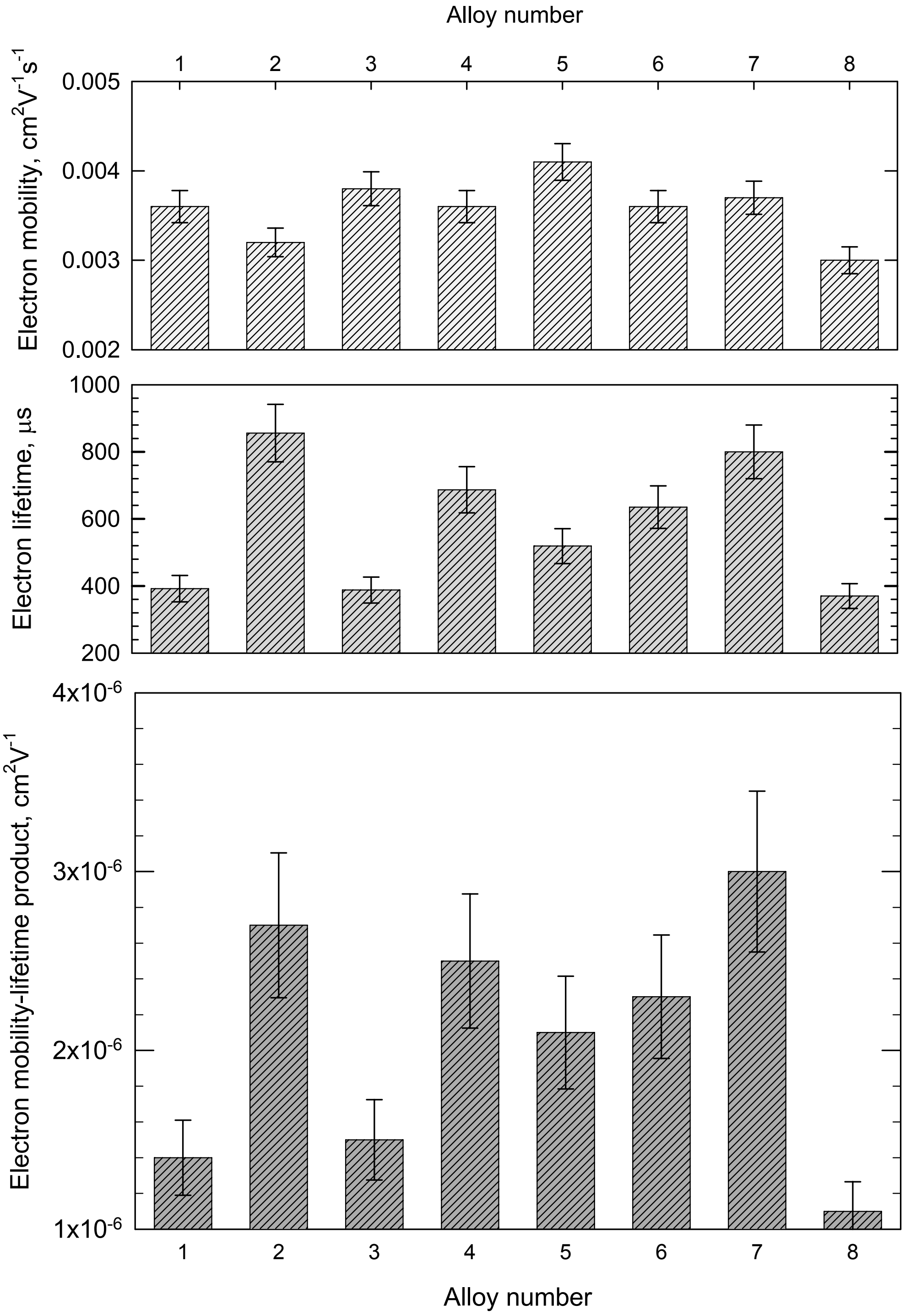

Figure 5.4 Electron transport in vacuum deposited a-Se films from different alloys having the same composition Se:0.2%As. The alloys are based on crude source Se materials with different origins. The purification of the crude Se and the alloying with As was done in the same way under industrial conditions for all alloys involved in the study.

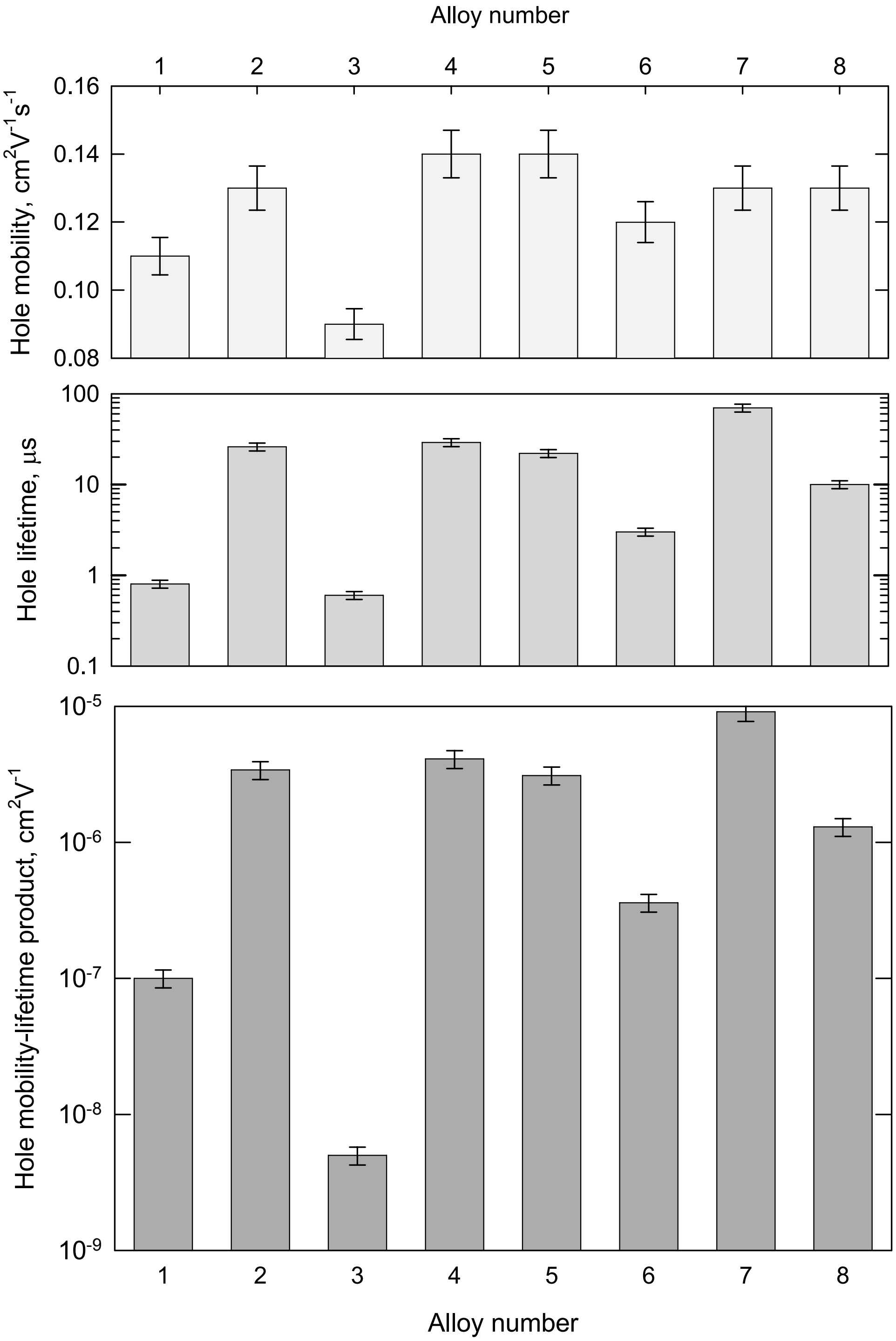

Figure 5.5 Hole transport in vacuum deposited a-Se films from different alloys having the same composition Se:0.2%As. The alloys are based on crude source Se materials with different origins. The purification of the crude Se and the alloying with As was done in the same way under industrial conditions for all alloys involved in the study.

The variations in the hole transport are much greater. As can be seen from Figure 5.5 hole mobility-lifetime product varies over 3 orders of magnitude and that is mainly due to variations in hole lifetime.

Why did the addition of one and the same amount of As have such different effects on the charge transport in these eight alloys?

The first thing that comes to mind is to question the success of the alloying procedure. Probably something went wrong during the production of alloys #1, #3 and #8 and less As entered the structure of Se. This is not the case because the presence of 0.2% As in these alloys was confirmed by elemental analysis.

The only explanation that remains is that something in the structure of the crude source Se like average chain lengths, number of rings, cis- to trans- linkage ratios in a-Se molecules, presence of certain impurities is preserved after the purification process. Thus the purified materials remain different in that sense and the net effect of alloying with 0.2% As is very different for the different pure Se materials.

Another very interesting question is “why do alloys that contain 0.2% As and no Cl produce films that have such good hole transport?”. Usually Se is purified to 99.999% by several vacuum distillations. Films produced from vacuum distilled pure Se materials will extremely rarely demonstrate hole lifetime above 10-20 μs. As apparent from Figure 5.5, five out of eight alloys (Se:0.2%As no Cl) have hole lifetime that is bigger than 10 μs in spite of the 0.2 % As addition that is supposed to introduce deep hole traps and significantly suppress the hole transport. Such observation raises the question about the charge transport in the starting purified Se materials from which the alloys investigated in Figure 5.4 and Figure 5.5 were produced.

We have obtained several different purified Se materials from the same supplier that produced the Se:0.2%As alloys discussed above. These pure (99.999%) Se materials were result of the same purification process but were produced from crude Se materials with different origins. The technique that was used to purify these materials was the same as the one used to produce the pure Se materials from which all Se-0.2%As alloys discussed above were produced. We have produced and investigated films from these pure Se materials under the same conditions: 250 °C boat temperature and 60 °C substrate temperature. All films without any exception demonstrated excellent hole transport and extremely poor electron transport. A typical representation of the type hole transport is shown in Figure 5.6 . The pure Se #1 in that figure is typical representative for that set of pure Se materials. As can be seen from the figure the electron transport in that film is almost immeasurable. This means that for films about 100 μm thick the electron TOF waveform represents only decay; no extraction point can be found to fields up to 10 V/μm. Under such conditions only the electron lifetime can be estimated and the value extracted from the initial decay is about 10 μs. The hole transport on the contrary is excellent. Hole mobility is about 0.14 $cm^2V^{-1}s^{-1}$, hole lifetime is well above 100 μs and that results in mobility-lifetime product in the 10^{-5} cm^2V^{-1} range. This clearly comes to show that the type of purification technique can have significant impact on the charge transport in the vacuum deposited films.

The elemental analysis on the pure Se material, have clearly shown that the materials do not contain halogen elements in significant quantities. Thus, the good hole transport and the absence of electron transport can not be contributed to the presence of halogens. The "unusual" charge transport properties characteristic for that set of pure Se materials were traced to be due to the presence of oxygen, which will be explained in more detail in subsection 5.1.3.

Another interesting question related to the effects induced by As addition on the charge transport in vacuum deposited a-Se films is related to the magnitude and the direction of the effects: how big the observed changes can be, and are they always in the same direction, etc? The basis for these questions is that in almost all the papers on the subject the researchers chose to investigate changes triggered by the As in pure a-Se that has , moderate electron transport, i.e. lifetime in the range 100-200 μs and hole lifetime 5-10 μs. There is no data published on the extreme cases. For example from the published work it is not clear what will happen if one tries to improve the electron transport by adding As to a pure Se that already has very good electron transport, i.e. electron lifetime of say 600 μs and more.

Two types of pure selenium materials with properties suitable for investigation in the direction described above were available for experiments. In Figure 5.6 they are labeled as Pure Se #1 and Pure Se #2. As can be seen from the figure and described previously in the chapter, Pure Se #1 has no electron transport (τ_e =10 μs) and very good hole transport (τ_h =150 μs). Pure Se #2 has very good electron transport (τ_e=600 μs) and moderate hole transport (τ_h =15 μs). Both materials were alloyed with 0.2 wt % As at our laboratory. The synthesis was done in evacuated quartz ampoule as described subsection 4.2.2. The synthesis temperature of 800 °C and the process duration of 24 h were used. At the end of the synthesis, the temperature of the ampoule was decreased to 600 °C for 30 min, and the ampoule was quenched into tap water (7-18 °C).

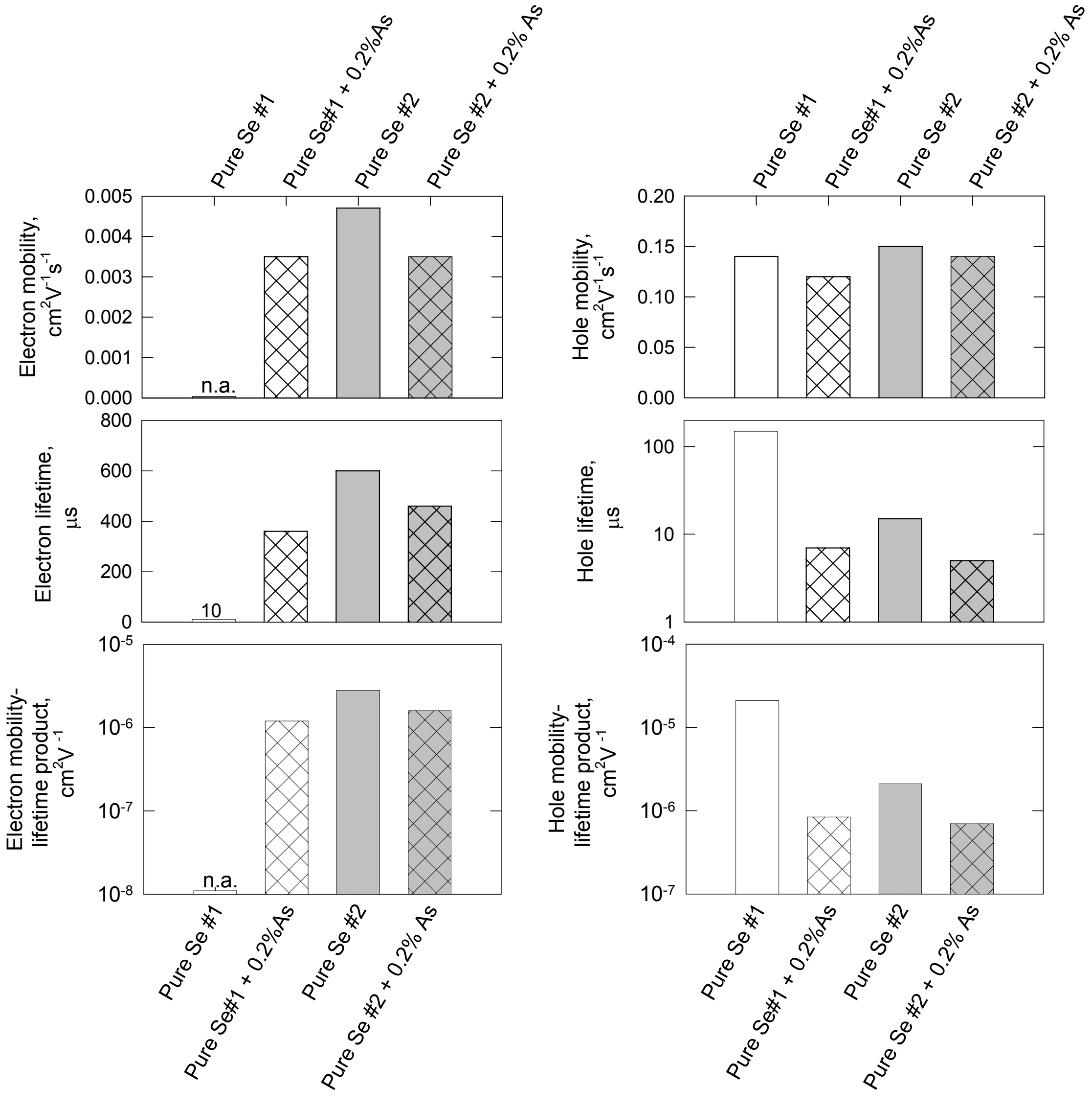

Figure 5.6 Charge transport changes caused by the addition of 0.2% As to two different pure selenium materials with very different initial charge transport properties.

The films were vacuum evaporated from the synthesized alloys under standard conditions: boat temperature 250 °C and substrate temperature 60 °C. The results from the charge transport measurements on these films are shown also in Figure 5.6. The addition of 0.2% As to Pure Se #1 has improved the electron lifetime 30-40 times. At the same time, the hole lifetime has decreased more than 20 times. The alloy produced by us has almost identical properties to alloy #8 in Figure 5.4 and Figure 5.5. This was expected because alloy #8 was produced from Pure Se #1 as a base material under industrial conditions. The fact clearly shows that the introduction of 0.2% As has very similar effects in spite of the differences in the alloy preparation procedures.

The charge transport changes observed in the other alloy are different. First, as expected the hole lifetime decreases, but the magnitude of that decrease is only 3 times. Second and more interestingly, the introduction of 0.2% As in Pure Se #2 has actually decreased the electron lifetime by 25% instead of increasing it. At the same time the electron mobility has decreased, so the effect of As on the electron mobility is in the expected direction.

This observation can not be explained in terms of defect forming reactions. For some reason (5.2) does not work for that alloy, or if it works there is at least one other mechanism that leads to an overall decrease in the electron lifetime with the addition of As.

This subsection can be concluded by saying that the effect of As and Cl on charge transport has now been studied for many years. The general believe, that As improves electron transport at the expense of deteriorated hole transport has been verified for many alloys and, in most cases, it holds. In the opposite fashion, Cl is believed to improve the hole transport in a-Se, at the same time inducing a deterioration of the electron transport. That has also been checked, and holds for most of the cases. The effects of Cl are stronger than those of As in the sense that Cl addition in the ppm range is needed to achieve measurable effects on the charge transport, while the As addition has to be of the order of 0.1wt % to induce effects of the same magnitude on charge transport.

The exact explanation of the effects of As and Cl on charge transport in a-Se is still unknown. Many authors tend to explain the effects in terms of defect forming reactions. Our results however, show that charge transport in the alloy also depends on the properties of the pure Se starting material. We have shown that the same amount of As can have very different effects on charge transport, if the starting pure Se materials are different. We have also shown that the addition of As can cause a decrease of the electron lifetime and electron mobility-lifetime products, while causing changes in the expected direction (decrease) for the electron mobility and hole transport.

These effects cannot be explained totally in terms of defect forming reactions. They generally show that additives can affect the charge transport through some other channels. These other mechanisms are probably related to the molecular structure and the unique cocktail of impurities present in each pure Se material. Addition of As and Cl can then "purify" Se by bonding with some of these impurities. The latter itself can cause changes in the charge transport of the resulting alloy. The newly formed compounds can also act as crystallization nuclei, and thus lead to formation of high number of micro- and nano- crystal in the a-Se matrix. The trapping at the phase boundaries can then cause changes in the charge transport in the material. Alternatively, As and Cl can cause changes in the molecular structure of a-Se. For example, they can change the ratio cis to trans linkages in Se molecules, or they can alter the concentration of Se_8 and Se_6 ring molecules that are present in a-Se. Thus intuitively one can expect changes in the charge transport due to mechanisms other than defect forming reactions.

The exact mechanisms of the changes induced by As and Cl will have to be explained in the future. However, our experiments have confirmed that the alloying process is very sensitive to the starting Se material. A very interesting direction for future experiments will be to produce and investigate alloys from Se of much higher purity than 99.999% purity. In this way one can investigate the significance of the trace impurities that are inevitably present in the purified Se material. The presence of such trace impurities can be making the current alloying process not very well reproducible with respect to the charge transport in the final alloys.

5.1.3 Effects of Oxygen

In late 1960s the general belief was that impurities in range below 1 % can not have significant effect on the electrical properties of amorphous semiconductors such as selenium [127]. However, Twaddell et al. [128, 129] have demonstrated that chlorine and oxygen in amounts 100 ppm or even in much lower amounts can cause drastic changes (several orders of magnitude) in the resistivity of a-Se. Effects of oxygen impurities on carrier ranges in Se were investigated in [130]. Takasaki and coworkers have found that mainly the electron ranges were affected by the addition of oxygen. A much bigger study on the effects of oxygen on the electrophotographic properties of selenium [131] was conducted by Oda and coworkers in 1985. Using TOF techniques these researchers have found that oxygen impurities ranging from 1 to 1800 ppm do not affect hole and electron mobilities. However according to their results both electron and hole lifetimes decrease when the concentration of oxygen impurities is higher than 100 ppm. In addition, the authors have found that the residual potential in the positive charge mode decreases with increasing amounts of oxygen while the residual potential in the negative charge mode decreases. Further, Frank Jansen [132] has shown that trace amounts of oxygen can cause significant increase in the crystallization rate at the substrate-Se interface in films deposited from pure Se. Several years later Jeffrey Szabo and coworkers [133] have demonstrated that the presence in oxygen in the vacuum chamber during the film deposition process alters the photoconductivity of the produced pure Se films.

In the recent years, when the interest in a-Se was renewed as a result of its application as a photoconductor in digital detectors for medical imaging, the question for the influence of oxygen on the properties of vacuum deposited a-Se films has received little or nor attention. This is quite surprising, considering the magnitude of the effects related to the presence of oxygen [128,129], the fact that the published data are highly controversial [131], and negative impact that oxygen can have on the long term stability of a-Se based x-ray photoconductor layers [132].

From a technological point of view, oxygen is an impurity that can be present in pure Se with a great probability. The recovery of the crude selenium and later its purification involves many oxidations of selenium as different steps at the technological process. Thus the presence of trace amounts of oxygen in the pure Se material is almost inevitable. When oxygen free selenium is needed, the production process includes special steps to remove the oxygen impurities. Selenium is considered to be oxygen free when the content of oxygen is 5 ppm or below (specification of RETORTE, Germany, taken from company's website).

However, in view of the published data on the magnitude of oxygen effects on the properties of a-Se films, there are significant doubts that even such small quantities of oxygen can have significant impact on the electronic transport properties of the produced films. For example, the films produced from Pure Se #1 have shown very poor electron transport and unusually good hole transport as can be seen in Figure 5.6 . That can not be contributed to the presence of halogens because the elemental analysis has confirmed their absence. The question that arises is whether such transport can be related to the presence of oxygen impurities in the range 10 ppm or below, which in many cases are difficult to prove analytically.

In order to answer the above question, we have planed and conducted a series of experiments on the influence of oxygen on the electronic transport in vacuum deposited films from pure Se. We have chosen to work with pure Se material that has reasonable holes and very good electrons (Pure Se #2 in Figure 5.6). Such transport properties suggest that the amount of oxygen impurities in this material, if any, is indeed small, and give us a good base for the examination of the changes in carrier transport as oxygen is introduced. We have chosen to introduce oxygen in the form of SeO_2 because this substance was used in the past research [128, 129 and 131] for that very purpose. Obviously, such a choice makes the fair comparison of our results with the ones published in [131] possible and, in addition, selenium dioxide is a solid substance, that can be conveniently handled during alloy preparation process. Alloys were prepared in evacuated quartz ampoules as described in section 4.2.2. Both, the synthesis temperature (800 °C) and synthesis duration (24 hours) were bigger than the ones used in [131] which eventually can ensure better homogenization. The films from the thus produced oxygen containing alloys were fabricated in the way described in section 4.2 using boat temperature of 250 °C and substrate temperature of 60 °C.

The results from charge transport measurements on a set of freshly (24-48 hours after the evaporation) produced oxygen containing films are shown in Figure 5.7. The films were then aged naturally at room temperature (23 °C) and in dark for several months. The charge transport was then re-measured. The effects of ageing on the charge transport in the films are summarized in Figure 5.8.

Figure 5.7 clearly shows that oxygen even in amounts less than 50 ppm has a very strong effect on the charge transport in vacuum deposited Se films. Oxygen in amounts of only 47 ppm has almost completely eliminated the electron transport. Even at highest voltages and hence field accessible in the TOF equipment the electron photocurrent waveforms represented only a decay, so that no mobility and mobility-lifetime products can be extracted from such TOF measurements. The lifetime estimated from the decay of the TOF waveforms was indeed very small - only ~ 4 μs. This lifetime is about 150 times less than the lifetime in the starting undoped Se material (0ppm of intentionally added oxygen). The effect of oxygen on the hole lifetime is just the opposite. The films containing oxygen have shown considerable increase in the hole lifetime. The films with 47 ppm added oxygen have a hole lifetime of about 385 μs which is about 26 times longer than in the starting material. The addition of only 7 ppm oxygen has significantly changed both electron and hole lifetimes, leaving the mobility of both type of carriers unchanged. The addition of 47 ppm of oxygen seem to have decreased the hole mobility. The effect in Figure 5.7 is larger than the experimental error.

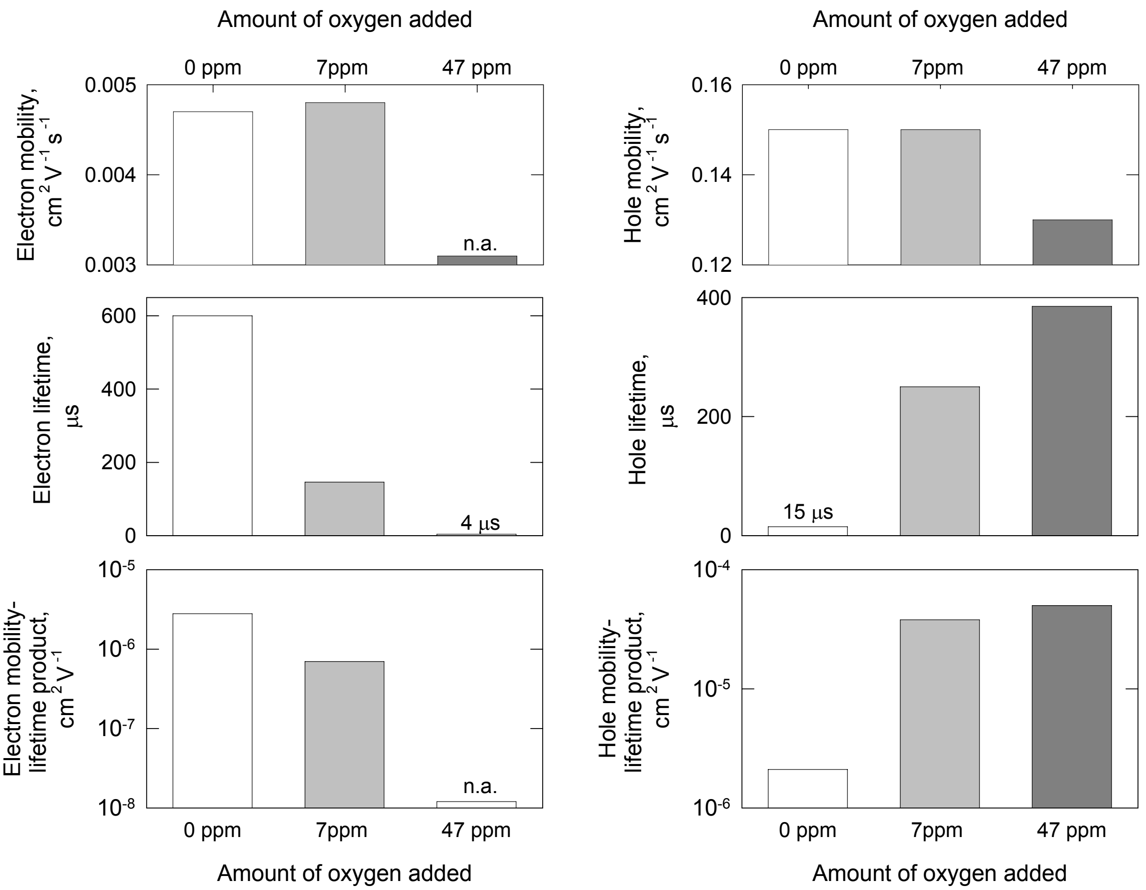

Figure 5.7 Influence of small amounts of oxygen on charge transport in vacuum deposited a-Se films. Oxygen was introduced as SeO_2. The measurements were done 24 to 48 hours after the evaporation of the film.

These results do not agree with the data published in [130] and mainly in [131]. According to the data published in [130, 131], oxygen affects the carrier transport only if added in amounts bigger than 100 ppm causing the lifetime of both type of carrier to decrease.

In an attempt to resolve that disagreement we have added oxygen to several other pure Se source materials with completely different origins (geographical and technological). The magnitude of the results was indeed material dependent but the direction was always the same. The addition of oxygen in ppm range to pure Se always caused hole transport to improve, increasing significantly the hole lifetime. In all cases the electron transport was deteriorated by the addition of oxygen, the main effect being the decrease of the electron lifetime.

The effects of ageing of oxygen containing films are also quite unusual as can be seen from Figure 5.8. Our observations in agreement with previous works [134] show that usually films produced from pure Se or stabilized Se (Se:As:Cl) demonstrate an improvement in the charge transport for both type of carriers as the films are ageing. However, in Figure 5.8 we are observing a deviation of that behavior if the films contain oxygen. Electron transport indeed improves with ageing of the samples but hole transport deteriorates. We observe that for films produced from other pure Se materials as well.

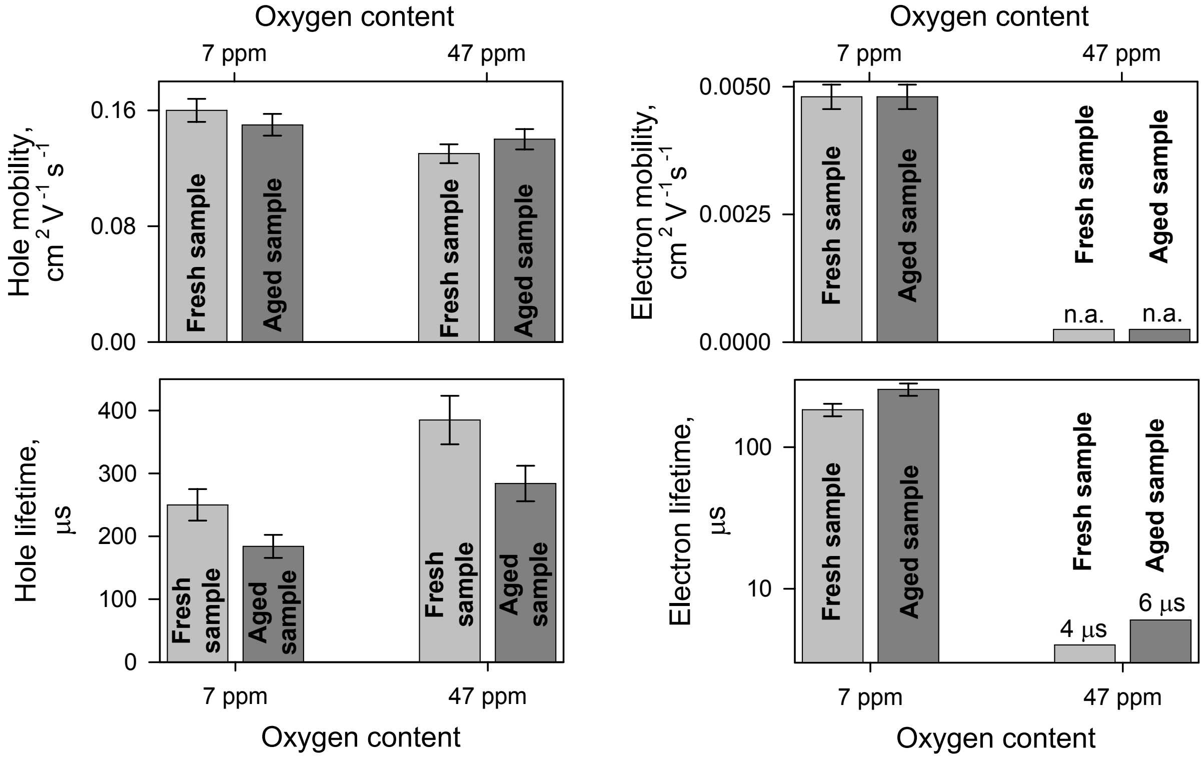

Figure 5.8 Effects of ageing on the charge transport in oxygen containing films. The oxygen was introduced as SeO_2. The films were aged for several months at room temperature (23 °C) and in dark.

Our results can be explained on the basis of the hypothesis that oxygen changes the concentration of the charged over- (Se_3^+) and under- (Se_1^-) coordinated defects in a-Se as it was already done in [131]. In addition, we need to assume, as we did in subsection 5.1.2 when explaining the influence of Cl on the transport in a-Se, that Se_3^+ centers act as deep electron traps while the Se_1^- centers act as deep hole traps and that the concentrations of these two type of traps determine carrier lifetime in a-Se.

The way in which oxygen affects the concentration of charged defects was explained [131]. Following the ideas introduced in the latter work, we can express the neutral condition of the structural defects in a-Se by the mass-action law as follows

$$2Se_2^0 = Se_3^+ + Se_1^-, \qquad K = \frac{\left(Se_3^+\right)\times\left(Se_1^-\right)}{\left(Se_2^0\right)^2}, \tag{5.4}$$

where K is a constant and the symbols of a charge defects in brackets stand for the concentration of that type of defect in a-Se structure.

Further, the authors of [131] have suggested that all of the oxygen impurities will become negatively charged defects by substituting Se atoms most of which are bonded in the chain-like molecules. The latter assumption is based on the fact that oxygen has higher electronegativity (3.4) than Se (2.4).

Thus the presence of oxygen will affect the neutrality condition because the oxygen atoms will compete with the chain ends (Se_1^0) to receive an electron from the Se_3^0 defects

$$\left(\mathrm{Se}_3^+\right) = \left(\mathrm{Se}_1^-\right) + \left(\mathrm{O}^-\right). \tag{5.5}$$

We can solve Equations (5.4) and (5.5) together to express the concentrations of the structural defects as follows

$$\begin{aligned} \left(\mathrm{Se}_3^+\right) &= \frac{\sqrt{\left(\mathrm{O}^-\right)^2 + 4\mathrm{K}} + \left(\mathrm{O}^-\right)}{2} \\ \left(\mathrm{Se}_1^-\right) &= \frac{\sqrt{\left(\mathrm{O}^-\right)^2 + 4\mathrm{K}} - \left(\mathrm{O}^-\right)}{2}. \end{aligned} \tag{5.6}$$

The last set of equations is plotted in Figure 5.9. As can be clearly seen from the latter figure, if the concentration of oxygen impurities is bigger than a certain threshold value, the concentration of deep electron traps Se_3^+ increases with the concentration of oxygen impurities, while the concentration of deep hole traps Se_1^- decreases.

The latter change in the defect concentrations can qualitatively explain our results. Indeed the carrier lifetime is inversely proportional to the concentration of deep traps

$$\tau = \frac{1}{C_t N_t}, \tag{5.7}$$

where N_t is the concentration of deep traps and C_t is the capture coefficients of these traps in the absence of shallower traps. Equation (5.6) shows that the concentration of deep electron traps increases almost linearly with increasing oxygen content and indeed the electron lifetime (see Figure 5.7) decreases in an almost hyperbolic fashion as required by Eq. (5.7). The data in Figure 5.7 are insufficient for precise analysis; however they give us some basis to think that the agreement is not only qualitative but semiquantitative as well. The same is not true for the hole lifetime. The concentration of deep hole traps decreases linearly with oxygen content (Eq. (5.6)).

The hole lifetime increases as a consequence of that, but the experimentally observed increase is quite different than the one predicted by Eq. (5.7). This fact comes to show that oxygen might

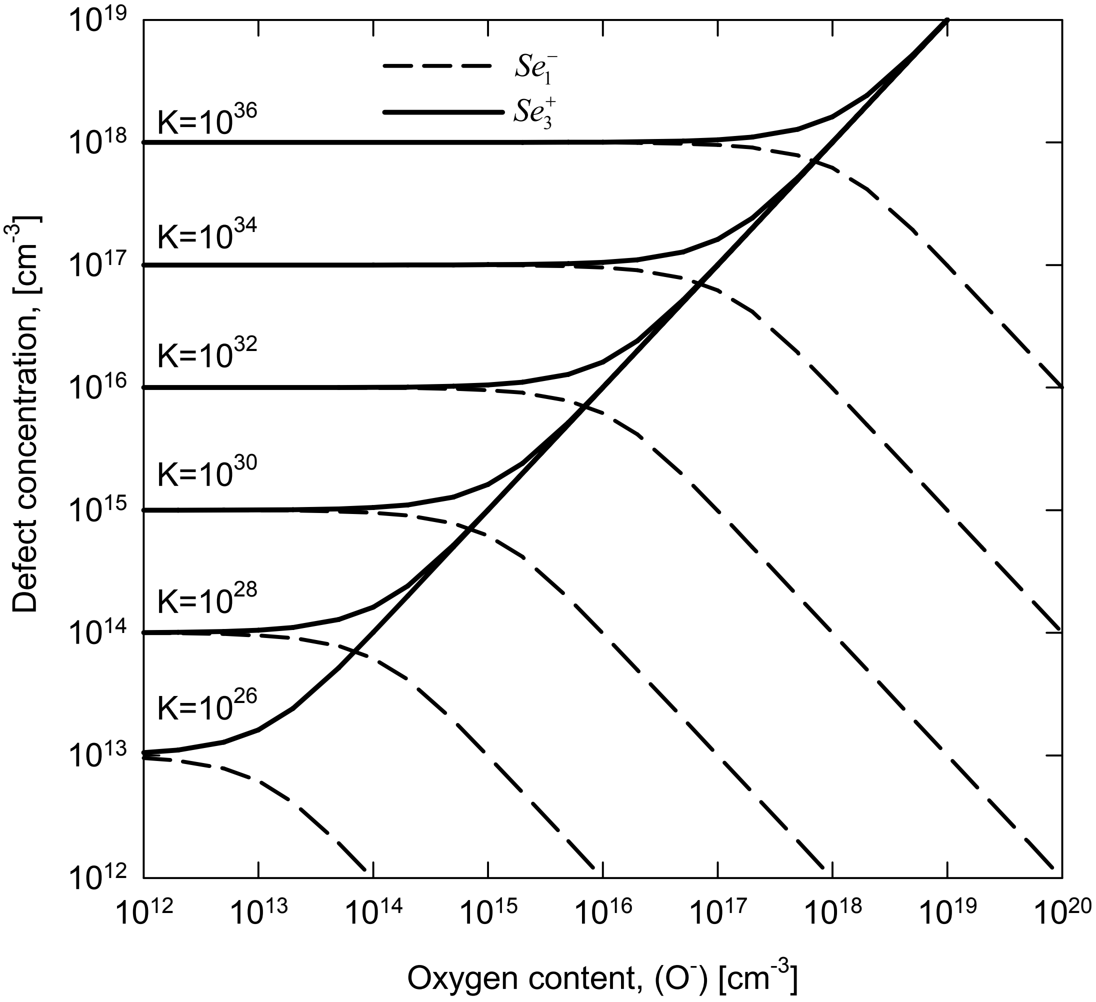

Figure 5.9 Influence of oxygen on the concentration of Se_3^+ over- and Se_1^- defects in a-Se as described by Eqs. (5.6). After [131].

have other channels for influence on the lifetime of carriers in a-Se. One such influence might bedue to the formation of other types of deep electron and deep hole traps that are normally not present in an oxygen free a-Se films such as the hypervalent defects discussed in chapter 2.1.2.4. For example, in the presence of oxygen the appearance of threefold coordinated Se atoms of valency 4 seems quite possible 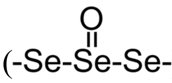 $(\text{-Se-}\overset{\overset{\text{O}}{\|}}{\text{Se}}\text{-Se-})$ [42]. Other possibility is that oxygen forms crystallites of SeO_2 [128] and/or aids in the formation and the growth of nano- and micro- Se crystals of different polymorphic modifications [21, 132, 143]. Trapping at the interface between such crystals and the amorphous phase can have significant impact on charge transport in these Se films; such a complicated situation is obviously very difficult to analyze quantitatively.

The ideas used above can be applied to explain the change in the charge transport observed with the ageing of oxygen containing films. Lacourse and coworkers [128] have shown that as oxygen containing Se samples age their infrared spectra change. These changes are illustrated in Figure 5.10. The nature of the changes in the spectra suggests that oxygen changes its bonding configuration in the samples. The spectrum of the fresh sample does not show distinct absorption bands that are characteristic for a double bond between oxygen and selenium (as in SeO_2). This is in agreement with our earlier assumption that the oxygen atoms initially simply substitute for Se atoms in selenium chain molecules in the vast majority of the cases. In the IR spectrum of the aged sample the absorption bands of $Se = O$ bonds are clearly present and the authors of [128] have concluded that this is due to the formation of SeO_2 crystallites in the oxygen containing Se samples with time. We can not infer that this is necessary the case,

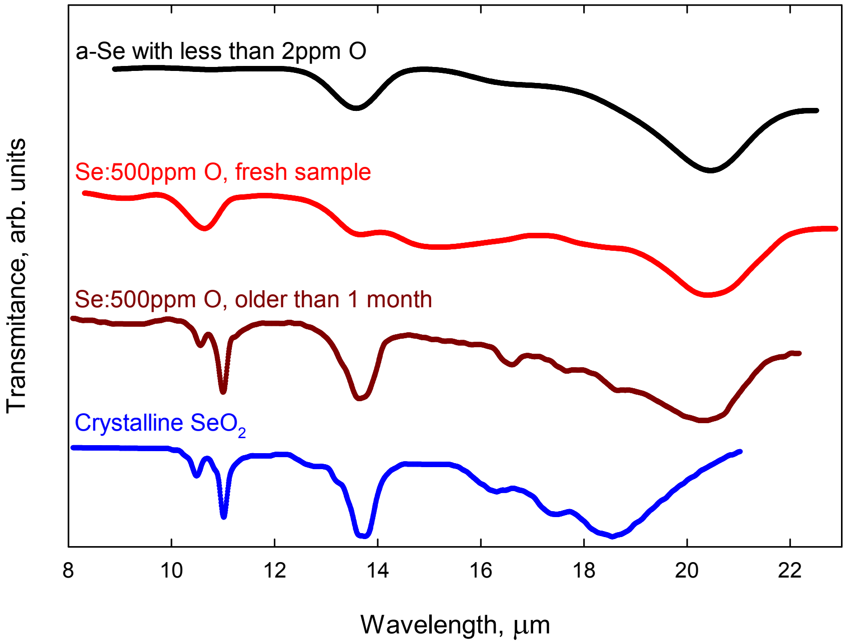

Figure 5.10 The IR spectra of fresh and aged oxygen containing samples together with the spectra of oxygen free Se and crystalline SeO_2. Data were selectively extracted from [128].

however the spectrum of the aged sample clearly shows that with time oxygen atoms start to form double bonds with the Se atoms. Thus as oxygen containing films age it is quite possible that the concentration of threefold coordinated Se atoms of valancy 4 increaces.

We can further assume that the defects of type 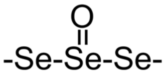 $\mathrm{-Se-\overset{\overset{O}{\|}}{Se}-Se-}$ act as deep hole traps. Then the observed decrease in the hole lifetime as the oxygen containing films age becomes a simple consequence of the increasing concentration of 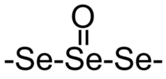 $\mathrm{-Se-\overset{\overset{O}{\|}}{Se}-Se-}$ defects which act as deep hole traps. An alternative explanation can be given assuming that nano- and micro- crystals form in the sample as a result of its ageing, and trapping at the boundaries of these crystals decreases the hole lifetime in the observed way. One can also assume a combination of the mechanisms specified above which probably is closer to the reality.

In conclusion, we would like to summarize the technological importance of the set of experiments described above. Unlike the previously published data [129, 131], we have shown that small amounts of oxygen have a very strong effect on electronic transport in pure a-Se films. The effects of oxygen on pure Se resemble those of Cl in stabilized a-Se alloys. When introduced into pure Se, oxygen increases greatly the hole lifetime and decreases the electron lifetime. The effect is very strong. Less than 10 ppm of oxygen can a have very strong impact on the lifetime of both types of carriers, leaving the carrier mobilities unchanged. With time, the oxygen changes its bonding configuration in a-Se with the dominant tendency of forming double bonds with the Se atoms. As a result of changes in bonding, the hole transport slightly deteriorates as the samples age, while the electron transport remains the same or improves slightly.

5.1.4 Effects of Chlorine Doping on Charge Transport: Comparison with Oxygen

In section 5.1.2 we have discussed the effects of small amounts of Cl on charge transport in Se:As:Cl alloys. Our data clearly demonstrate that when added in such alloys, Cl suppresses the electron transport and improves hole transport. The effect is very strong and only a few ppm Cl are needed to observe significant changes.

This behavior makes Cl a very useful dopant when a p- like (good hole transport and poor electron transport) has to be produced. Following the general logic, in such situation only Cl has to be added to pure Se since As has exactly the opposite effect on charge transport in Se. However, some evidence exists in the scientific literature that when added to pure Se, chlorine has somewhat different effect on the charge transport. For such cases, in 1971 it was found [135] that Cl indeed suppresses very effectively the electron transport in a-Se films, leaving the hole transport relatively unchanged (small deviations in both directions are observed). Later in 1983, this finding was confirmed independently by Takasaki et al. in [130]. In 1982-1984, the effects of Cl on carrier drift mobilities in Se:Cl materials have been investigated thoroughly by Kasap and Juhasz [136, 121] and some data about the effects of Cl on hole lifetime in pure Se ware presented in [121]. The latter two works report that the addition of Cl to pure Se act to decrease hole mobility and to improve hole lifetime, and in the same time the electron lifetime is greatly deteriorated by the addition of Cl.

All literature sources mentioned above agree that effect of Cl on electron transport in pure Se is negative. In most cases addition of more than 10 ppm Cl will result in deep traps limited electron transport in the resulting films. However, there is no such good agreement about chlorine induced effects on hole transport in pure Se. Every thing from slight improvement to slight deterioration of hole transport as a result of Cl addition was reported in the above 4 works.

In the last 5-6 years, the effects of Cl on the thermal properties of a-Se were investigated [136] and quantum modeling study on the effects of Cl on different structural defects in a-Se was published [137]. Both works suggests that Cl acts as chain terminator and can lead to bond switching in the rearrangement of network fragments. The net effect on charge transport was not studied but the reader remains with the feeling that such action of Cl should improve the hole transport in a-Se.

Led by lack of recent information on the influence of Cl on charge transport in pure a-Se films and by the unexpected results from the experiments on the oxygen doping experiments (see the previous subsection) we have conducted a limited in number experiments on the influence of Cl on the charge transport in vacuum deposited films from pure Se.

Several Se:Cl alloys supplied by ANRAD Corp., Montreal, Quebec were involved in the study. The Cl content ranged from 0 to 67 ppm. This range was selected because in [136], it was shown that the introduction of Cl in this concentration range does not have significant effects on the crystallization stability of the films.

The a-Se films were prepared as described in section 4.2. Boat temperature was 250 °C and substrate temperature was 60 °C.

The results from TOF and IFTOF measurements on the charge transport in these films are in good agreement with the results present in the scientific literature [130, 135].

The typical influence of Cl on electron and hole transport in pure Se films is presented in Figure 5.11 and compared with the typical influence of similar amounts of oxygen. Small amounts of Cl have almost no effect on the hole mobility-lifetime product. When the concentration of Cl is higher there is a tendency towards a slight decrease in the hole lifetime and hole mobility. In all cases the introduction of Cl has a drastic effect on the electron lifetime. In almost all samples the electron transport is deep trap limited, i.e. the TOF waveforms represent only decays. Under such conditions, only the electron lifetime can be estimated from the decay rate of the photocurrent and the values are almost never better than 10-20 μs. Thus, in contrast to the cases when added to Se:As alloys, Cl seems to have no positive effect on hole transport in pure Se.

It is interesting that the addition of both oxygen and chlorine to pure Se cause a huge decrease in the resistivity [128, 129], however our experiments show that only oxygen actually causes similar in magnitude improvement in the hole transport in a-Se and it is known that there is a positive correlation between hole transport and the conductivity of a-Se. The effect of both dopants on the electron lifetime is in the same direction – decrease of electron lifetime and electron mobility-lifetime product. The effect of both additives is very strong. Only a few ppm are needed to significantly suppress the electron transport in Se. Our data are limited but indicates that Cl is more effective than oxygen in suppressing electron lifetime in pure a-Se.

The experiments with pure Se have revealed interesting aspects of the influence of Cl on the charge transport in that material. The net effect induced by Cl on hole transport, unlike the effect on the electron transport, is dependent on the presence of other impurities such as arsenic. As described earlier (subsection 5.1.2), in the presence of sufficient amounts of arsenic (<0.1%), the introduction of Cl increases the hole lifetime in the films, while when introduced into pure selenium, Cl has no significant effect on hole transport. This observation clearly shows that the action of Cl can not be completely described in terms of Eq. (5.1). Indeed, the first reaction describes the creation of deep electron traps under the influence of Cl. That process seems to take place equally successfully in both pure Se and in Se:As alloys. In this way the action of Cl on the electron transport is always the same – the electron transport is always strongly suppressed by the introduction of Cl in both pure Se and Se:As. The effect of the second reaction in Eq. (5.1) (neutralization of deep hole trap under the influence of Cl) is different in Se:As and

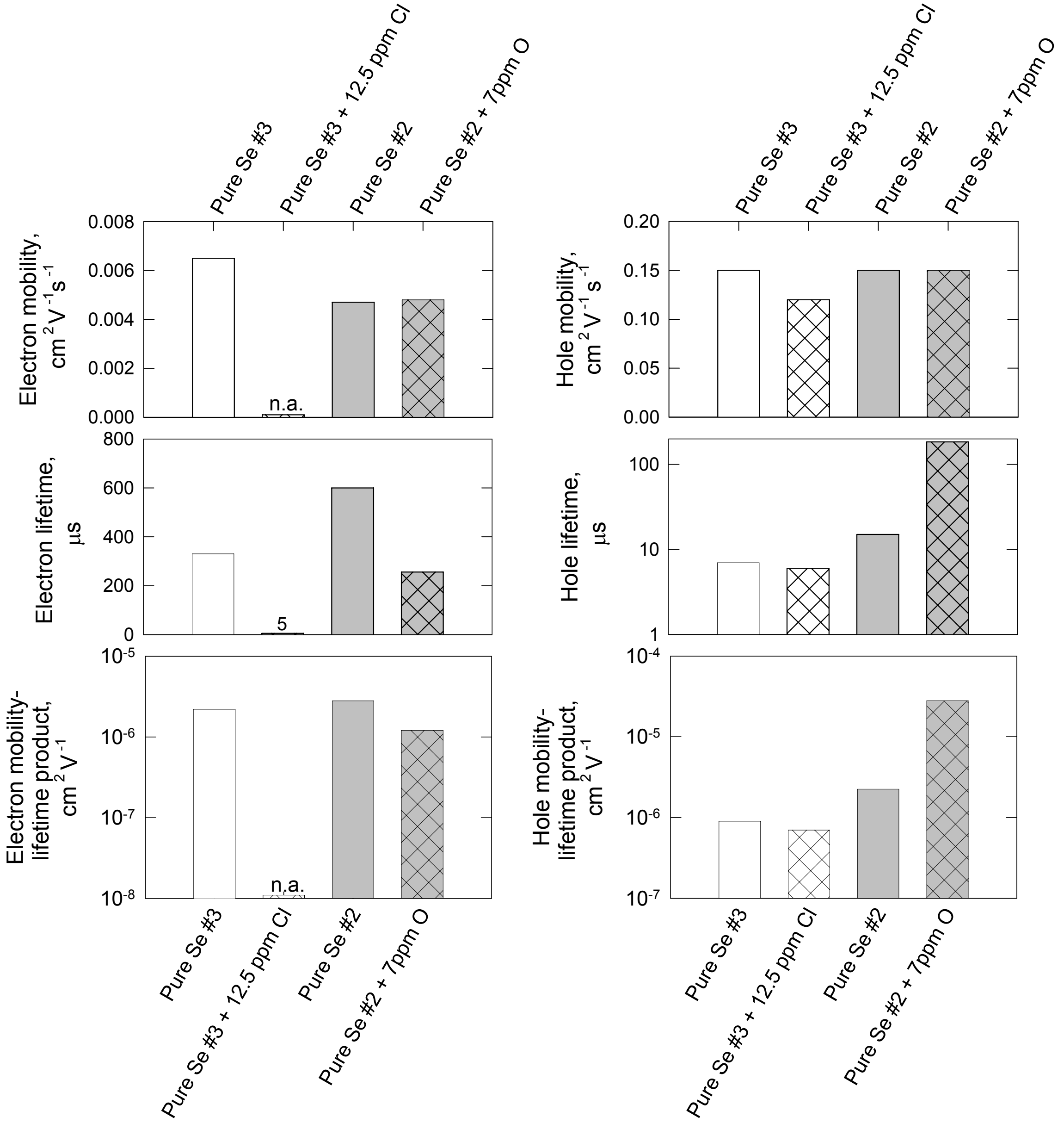

Figure 5.11 Comparison between effects of chlorine and oxygen additives on the charge transport in vacuum deposited films from pure Se. The measurements were done on well aged films and hence represent the relaxed charge transport in them.

in pure Se. In pure Se, the effect of the neutralization of deep hole traps under the action of Cl seems to be partly compensated by some other effect of Cl which was not discussed so far. We may speculate that Cl can not only neutralize but also create deep hole traps in Se. Indeed the results published in [136, 137] suggest that the most probable action Cl atoms is to terminate existing Se chain ends or to instill into Se-Se bonds. This results, in most cases, in the formation of two Se chains that are shorter than the starting one or into the opening of a Se ring molecule. In all cases one of the newly formed chain ends is terminated by the Cl atom and the net result is the formation of one new chain end that according to the VAP theory will finally be turned either into a deep electron trap Se_3^+ or a deep hole trap Se_1^-. Thus the transformations caused by Cl, depending on the circumstances can lead both to the formation and to the neutralization of deep hole traps. If the amount of added Cl is small compared to the number of Se_1^- sites existing in pure Se, the net effect on the hole lifetime will be relatively small because the two channels of interaction compensate for each other. No effect on hole lifetime will be observed at all or small changes in both directions are possible. However, if the amount of Cl added is large, say 100ppm or more, Cl in majority of the cases will lead to the formation of new deep hole traps and the hole lifetime will be shortened as the concentration Cl impurities in pure Se increases.

In the case of Se:As alloys, the bond breaking action of Cl is compensated for by the action of As which tends to link the Se chains in a star like configuration. The newly created shorter chains due to the bond breaking action of Cl in the vast majority of the case will be linked together by As because the concentration of As is typically one or two orders of magnitude higher than that of Cl. Thus, in the presence of sufficient amounts of arsenic, Cl can no longer form deep hole traps through bond breaking and the effect of its presence will be to increase the hole lifetime in the resulting Se:As:Cl alloy.

The explanation of the action of Cl on charge transport in a-Se presented above is quite speculative. At present time it is impossible to predict the exact effect of Cl on all known and unknown structural defects in a-Se. Due to its bond breaking and chain terminating action, Cl can cause significant changes in the polymerization and crystallization properties of Se in the process of film growth and that can lead to the formation of deep carrier traps of other nature [29, 132, 143].

5.1.5 Electronic Transport in Commercial N-like and P-like a-Se Layers

In this subsection we will summarize the results from TOF measurements on commercial pin- like structures and n- likelayers. Most of the measurements were done on samples supplied by ANRAD Corp., Montreal, Quebec. Semitransparent Au TOF contacts were produced on the top surface of the samples in our laboratory by DC sputtering (subsection 4.2.4). The resulting sample structure allows illumination from both top and bottom side, i.e. through the n- like and through the p- like layer which was very important for our measurements. Most measurements were done on pin- like structures although we have also done small number of measurements on single n- like layers. The thickness of the pin- like structures was in the range 500-1000 μm while the thickness of the n- like layers was 10-15 μm. Such thickness ranges and the structure of the samples, as it will be described below, led to certain difficulties with the TOF measurements. At relatively low voltages the waveforms represent only an initial spike in the current which then quickly decays almost exponentially and represents carrier trapping in the blocking layer. The carrier lifetimes were extracted from the parameters of the decay. The measured lifetimes for holes and electrons in the n- like s were then compared against the results of limited number of control measurements on single n- like s with a thickness 10-20 μm produced on the same type of ITO coated glass substrates. The results were in reasonable agreement which confirms that the measurements on pin- like structures can be used to estimate the lifetimes in the trapping layers.

The results from the lifetime measurements on a-Se based pin- like structures are summarized in Table 5.2. Since the carrier mobilities in most of the measurements could not be determined together with the lifetimes we have entered only estimates in the table. The mobility of the electrons in the n- like layer is represented by a value that is typical for a-Se that has good electron transport while the mobility of holes is represented by the lowest hole mobility measured in stabilized a-Se films (the n- like layer must have poor hole transport). A similar approach was used to enter estimates for electron and hole mobilities in the p- like layer.

The values in Table 5.2 illustrate important features of the transport in the n- and p- like layers. In the p- like layer, the mobility-lifetime product for the holes is more than two orders of magnitude bigger than the one for electrons. In the n- like layer the electron mobility-lifetime product is only about and order of magnitude better than the one for the holes. This illustrates that n- like layers are more difficult to manufacture than the p- like layers and that the thickness of an efficient n- like layer is much bigger than the thickness of an efficient p- like layer.

In an average quality i- like layer, the hole lifetime is ~20 μs or longer while electron lifetime is greater than 300 μs. From Table 5.2 we find that the hole lifetime in the p- like layer is only 5 μs while the electron lifetime in the n- like layer is typically below 50 μs. So the suppression of the electron transport in the p- like layer is achieved at the expense of significant deterioration of hole transport. A similar trend is evident for the n- like layer; the hole transport is suppressed but the quality of the electron transport is well bellow the quality in the electron transport in an i- like layer. Such characteristics will lead to trapping of holes in the p- like layer and trapping of electrons in the n- like layer which eventually can lead to deteriorated detector performance.

Table 5.2 Electronic transport in a-Se based n- and p- like layers.

Layer Type	Electron Transport			Hole Transport		
	Lifetime τ_e, μs	Mobility μ_e, $cm^2V^{-1}s^{-1}$	Range $\mu_\varepsilon\tau_e$, $\times10^{-6}cm^2V^{-1}$	Lifetime τ_h, μs	Mobility μ_h, $cm^2V^{-1}s^{-1}$	Range $\mu_h\tau_h$, $\times10^{-6}$,cm^2V^{-1}
n- like (hole trapping layer)	30-50	0.003*	0.09-0.15	0.2-0.5	0.1*	0.02-0.05
p- like (electron trapping layer)	5	0.0014*	0.007	10	0.13*	1.3

*** The value is a rough estimate, since no transit time can be derived from the TOF signal performed on pin- like structure.**

The situation is actually worse than the one presented above because carrier mobilities in the n- and p- like layers are expected to be much lower then the estimates given in Table 5.2. Typically an n- like layer is produced by doping Se with an alkali metal (Na being the most common example). Alkali doping tends to encourage crystallization in a-Se films [138] and to suppress that tendency the manufacturers use heavy arsenic doping (up to 10% As). Such levels of As lead to dispersive electron and hole transport in the films evaporated from these alloys. The charge carriers move more slowly and their motion can be described with a distribution of drift mobilities, and not by a single mobility as in the case of films produced from stabilized a-Se. The p- like layers are produced from As_2Se_3 or heavily doped Se:Cl and the same type of dispersive charge transport is observed in films produced from the later two materials. The exact structure, doping and other details about the n- and the p- like layers involved in our study were not supplied.

However, we were able to design and conduct a TOF experiment that clearly demonstrates that the hole mobility and/or the hole lifetime in the p- like layer is much worse than those in the i- like layer, and that the electron mobility in the n- like layers is worse than the one in the i- like layers. A typical TOF hole waveform recorded with high voltage applied to the pin- like structure and some measures to prevent the field in the structure from entire collapse is shown in Figure 5.12. The illumination was done through the p- like . The p- like was positively biased and thus a packet of holes was injected through that layer into the sample. Note that in this case a foreword bias is applied across the pin- like structure and that the dark current is significant. The main consequence is that the electrons injected from the negative electrode will pass through the n- like layer, then through the i- like layer and will be trapped in the p- like layer. Similarly, the holes injected from the positive electrode will pass through the p- and i- like layers and will be trapped in the n- like layer. If the bias across the sample is left for long enough time, the field in the i- like layer will collapse due to the trapped charge accumulated in the p- and n- like layers. For the latter reason many researchers fail to observe TOF waveforms even in foreword biased pin- like structures. However, the result shown in Figure 5.12 is not

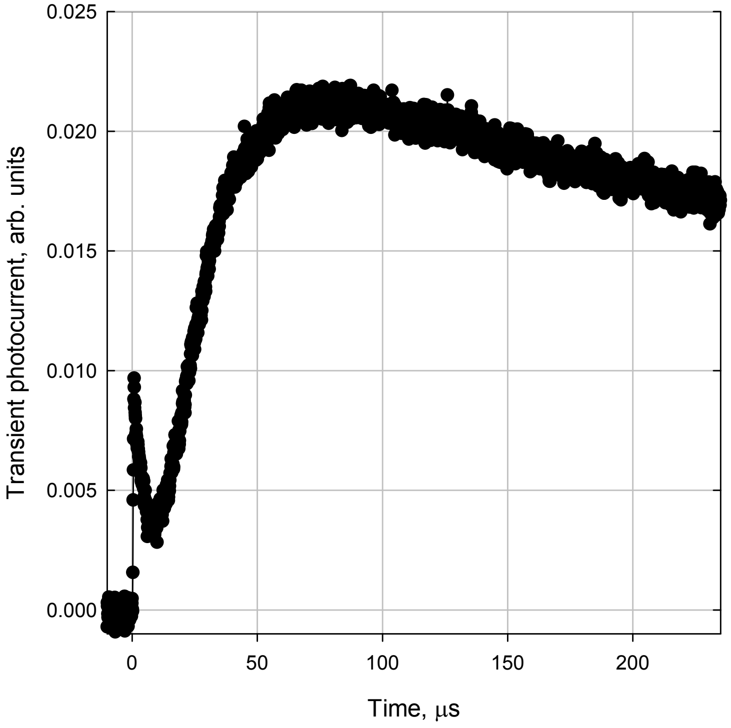

Figure 5.12 A hole TOF waveform measured on a commercial a-Se based pin- like structure with total thickness of 860 μm. The sample was illuminated through the contact on the p- like layer. The applied bias during the measurements was 3500V.

what is intuitively expected to be observed in a good quality pin- like structure that should have comparable hole transport in the p- and i- like layers. Indeed, if the hole transport was comparable for the p- and the i- like layers, the thin p- like layer should be "invisible" for holes and one should observe a normal TOF waveform due to the motionof the holes through the thick i- like layer. When the packet enters the n- like layer all the holes will be almost immediately trapped and that will appear as the "extraction" point in a normal TOF waveform on a single layer when the packet has reached the backside electrode. However, as demonstrated in Figure 5.12 the hole waveform in the pin-like structure is very different from the waveforms reported for single a-Se layers but has a shape that is very similar to the shapes of the TOF waveforms reported by Vaezi-Nejad and Juhasz for much thinner heterojunction multilayer a-Se based photoreceptor structures [139]. Example of a typical hole TOF waveform measured on triple layer photoconductor structure (Se:Te-Se-Se:Te) and reported in [139] is shown in Figure 5.13. The authors of the latter work have pointed out that the reasons for the observed shape are the differences in charge carrier mobilities and differences in the charge trapping kinetics in the different layers of a multilayer structure.

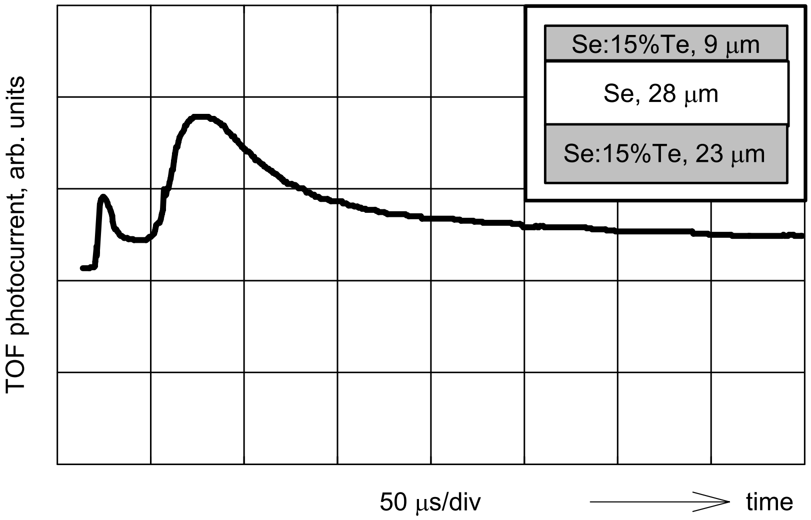

Figure 5.13 Hole TOF waveform measured on triple layer Se:15%Te-Se-Se:15%Te photoreceptor. The thickness of the layers from the substrate to the top of the structure is 23, 28 and 9 μm respectively. The applied bias across the structure was 20V. The transit of the charge packet through the bottom layer was undetectable. Data were selectively extracted from [139].

The waveform shape in Figure 5.12 is due in particular to the fact that hole mobility and/or the hole lifetime in the p- like layer are much lower than those in the thick i- like layer. According to the authors of [139] the part of the waveform from the initial spike of the photocurrent to the lowest point of the "saddle" is due to the motion of the holes through the p- like layer. The motion of the holes in the i- like layer corresponds to the fraction of the waveform between the lowest points of the "saddle" to the maximum of the photocurrent. The motion of the holes in the n- like layer can not be resolved since the hole lifetime there is about two orders of magnitude lower than in the i- like layer and practically all holes entering the n- like layer are almost immediately immobilized (trapped). The slow decay of the waveform after the maximum in the photocurrent is due to the slow de-trapping of holes that were initially trapped in the n- like layer. The shape of the waveform in Figure 5.12 directly confirms the fact that the hole transport in the p- like layer is much worse than the one in the i- like layer. The effect is even stronger than intuitively thought because of the uneven field distribution in the sample. As explained earlier, the dark current causes the field in the i- like layer to decrease. Let us estimate how significant is that decrease. The time needed by the holes to traverse the i- like layer (from the lowest point of the "saddle" to the maximum in the photocurrent) is about 60 μs. Hole mobility in the i- like layer is 0.13 cm^2 V^{-1} s^{-1} (as measured on single i- like layers) and the i- layer in the structure is about 830 μm thick. Based on this data set we can calculate that the average field in the i- like layer of the pin- like structure during the measurement was about 1 V μm^{-1}. A total of 3500 V was applied across the pin- like structure to record the waveform and only about 830 V of them were dropped across the i- like layer. The rest of the voltage was dropped across the much thinner trapping layers and if we assume that the voltage was dropped uniformly across both the n-, and the p- like layers we can estimate that the field in these layers was around 9 V μm^{-1}. Even at such high fields, the holes in the p- like layer move much more slowly and with considerable trapping than in the i- like layer, and thus we can safely conclude that indeed the hole transport in the p- like layer is much worse than the hole transport in the i- like layer.

The observation of electron TOF waveform in pin- like structures of such thickness (~800 μm) is more difficult due to the much lower mobility of the electrons and will require the application of much higher voltage across the sample. We have not been able to attempt such measurements due to equipment limitations but we believe that similar measurements for electrons are possible..

We can finalize this subsection by concluding that indeed by suitable doping it is possible to produce effective a-Se based n- and p- like layers. However, the doping or the fabrication technique, or both of them affect in undesirable direction the electron transport in the n- like layer as well as the hole transport in the p- like layer and they both are much inferior compared to the electron and hole transport in the i- like layer. This undesired “side effect” of the doping and the preparation techniques used to produce efficient electron and hole trapping layers can have negative impact on the imaging performance of the x-ray detector.

5.1.6 Effects of Alloying and Doping on Charge Transport in Vacuum Deposited a-Se Films – Summary

In this subsection we have described the most important results from experiments investigating the influence of some dopants on the charge transport in vacuum deposited a-Se films.

It was found that arsenic in amounts 0.1-0.7 wt % increases electron lifetime and decreases electron mobility when added both to pure and stabilized (Se:As:Cl) selenium. Overall, As increases the electron mobility-lifetime products (ranges) because the increase in the electron lifetime compensates for the observed decrease in the electron mobility. In very limited cases, when As is added to pure Se with extremely good starting electron transport, there can be deviations from the tendencies described above. In such cases, the electron transport can remain unaffected or can even slightly deteriorate. The effect of As addition on the hole transport is opposite. Arsenic leaves the hole mobility relatively unchanged but causes hole lifetime to decrease, as a result hole mobility-lifetime product also decrease as the amount of added As increases.

The effects of Cl addition on charge transport in selenium films are somewhat opposite to those of As. Chlorine in the amounts 2-70 ppm sharply deteriorates electron transport in selenium whether it is pure or stabilized. The effect is dominated by the decrease in the electron lifetime, since Cl in the amounts specified above does not strongly affect the electron mobility especially in the cases when it is added to stabilized a-Se material. When Cl is added to stabilized selenium, it forces a significant increase in the hole lifetime, leaving the hole mobility unchanged. The total effect in such cases is an increase in the hole range. However, when Cl is added to pure Se, the effect on the hole transport is not clear. In such cases, Cl tends to decrease hole mobility slightly, while the effect on the hole lifetime shows significant variations with the starting pure Se material and the alloying conditions. Anything between a slight increase to a slight decrease in hole lifetime can be observed. The magnitude of the effect is much smaller compared to the case when Cl is added to stabilized a-Se.

These results are in good qualitative agreement with those published earlier in the scientific literature and confirm that the combined alloying-doping with As (0.1-0.7 wt % and Cl (2-60 ppm) is an effective way to control carrier ranges in vacuum deposited films of a-Se. The main difficulty accompanying the alloying process is the very strong dependence on the properties of the starting pure Se material which makes the exact determination of the right amounts of As and Cl additions needed a very difficult task.

Our experiments indicate that when added in large amounts both As (above 1 wt %) and Cl (above 100 ppm) force changes in a-Se which result in dispersive transport in the films for both type of charge carriers.

The effects of oxygen on pure Se were also investigated, since oxygen impurities are very likely to be present in the material as a result of the nature of the technological processes used for recovery and purification of Se. Unlike previously published works in the scientific literature [130, 131], it was found that oxygen in amounts below 50 ppm can have very strong impact on both electron and hole transport in a-Se films. Oxygen deteriorates electron transport and improves hole transport when added to pure Se. Both effects are caused mainly by changes in carrier lifetimes.

Charge transport in n- and p- like layers in commercial a-Se based pin- like structures was also investigated. The n- like layers were produced from Se:As material with alkali doping, while the p- like layers were produced with heavy Cl doping or by evaporation of As_2Se_3. Details on layer structures and concentration of dopants were not supplied for the investigated pin- like structures. As expected, it was found that electron range in the p- like layer is 2-3 orders of magnitude smaller than the hole range. At the same time, the hole range in the n- like layer is only one order of magnitude or less smaller than the electron range in that layer and thus we can conclude that a-Se based n- like layers are more difficult to fabricate than a-Se p- like layers. Our TOF measurements on the pin- like structures have also shown that the hole transport in the p- like layer is much worse that the hole transport in the i- like layer.

The observed effects on charge transport in a-Se films caused by different dopants can be qualitatively explained in terms of relatively simple defect forming reactions if we assume that charged over- and under- coordinated defects in a-Se act as deep traps for charge carriers. Such reactions cause changes in the concentrations of deep hole and electron traps and/or the creation of new shallow ones. This explanation cannot be made quantitative due to the complexity of the bonding in a-Se and to the lack of complete knowledge on defect properties and the structure. The presented explanation does not exclude the existence of other mechanisms for inducing charge transport changes in a-Se due to the presence of certain impurities.

5.2 Effects of Preparation Conditions on Charge Transport in a-Se Films

5.2.1 Introduction

There are a number of deposition parameters that can potentially influence the structure and electronic properties of a-Se prepared by thermal evaporation. The most important these parameters are the boat (source) temperature, evaporation rate, and the substrate temperature. Post-deposition treatments such as annealing can also modify the charge transport in vacuum deposited a-Se films.

In addition, the a-Se that is used in actual x-ray photoconductor applications is not simply pure (99.999%) a-Se but stabilized a-Se (Se:As:Cl) alloys. The small amounts of As are added to retard crystallization of the a-Se films by forming cross-links between Se chains [126, 135]. We have shown in the previous section that suitably choosing the amounts of As and Cl in the Se alloy, one can achieve both good electron and good hole transport in thick films prepared by vacuum deposition. However, the preparation of films by vacuum deposition from stabilized a-Se is much more difficult than preparation of films from pure Se. Due to a number of different reasons, when stabilized Se is used for film preparation by vacuum deposition, the distribution of the impurity (mainly As) in the resulting film is non uniform across the thickness of the film. This is shortly described with the term "fractionation". Under certain evaporation conditions, the fractionation can be really severe. For example, the evaporation of an a-Se:0.3%As alloy, can lead to a film having almost no As near the substrate and around 10% As close to the top surface. This will lead to huge variations of charge transport across the thickness of the film which is unacceptable.

We have examined the influence of the deposition conditions and sample post-treatment on electronic transport in films produced from pure Se and stabilized a-Se alloys. Planning experiments we have focused on those factors that can eventually provide an efficient way to control carrier ranges in the produced films. The investigations were limited only to those sets of deposition parameters which resulted in films with acceptable quality for applications in a-Se based x-ray photoconductors in digital medical image detectors. The results from these experiments are described in this subsection.

5.2.2 Influence of Boat Temperature and Deposition Rate on Charge Transport in Vacuum Deposited Films form Pure Selenium

Evaporation selenium alloys can lead to fractionation, resulting in unacceptably non-uniform composition across the thickness of the sample as described in the introduction to this subsection (5.2). The amount of fractionation that occurs depends very strongly on the boat (source) temperature and when alloys are being evaporated that parameter can not be freely varied. Evaporation of pure Se avoids the fractionation issues and alloys experiments in which the boat temperature can be varied in relatively wide range.

In the deposition experiments with pure Se we have fixed the substrate temperature to 60-65 °C just above the glass transition temperature, which is known to lead to electronic quality a-Se films [130] and have varied the boat temperature in the range 190-250 °C. In our vacuum coater, the source to substrate distance was set to 16 cm (see subsection 4.2.3) and the variation of the boat temperature led to variations in the deposition speed as well. At boat temperatures below 190 °C, the deposition rate became impractically low, while boat temperatures over 250 °C led to a vigorous evaporation with a lot of splashes (spitting) and produced films with poor surface quality.

However, the boat temperature controls more than the grow rate of the films. When the temperature of the boat changes the composition of the Se vapor also changes [140]. Increasing the boat temperature from 190 °C to 250 °C, causes Se_5 molecular species to increase and become predominant instead Se_6 species.

We have investigated pure a-Se films deposited by using various boat temperatures in the range 190-250 °C. Figure 5.14 summarizes the mobility and lifetime values as a function of boat temperature and shows that the lifetimes and mobilities of both electrons and holes are relatively independent of the boat temperature, even though the deposition rate varied by nearly two orders of magnitude. The lack of any change in the electronic properties despite the change in the vapor-phase composition implies that all arriving species are incorporated into the growing film in a uniform way regardless of the particular vapor phase composition. Such results are actually expected. The growth of the Se film on the surface of the substrate is a result of complicated and simultaneously appearing processes such as polymerization and de-polymerization of Se molecules, formation of nanocrystals followed by their growth or by their dissociation, etc. The kinetics of all these processes in the absence of additives (impurities) is governed by the substrate temperature and thus the properties of the films are mainly determined by the substrate temperature. Maintaining the substrate temperature above the glass transition temperature of the material during the film deposition enhances the surface mobility of deposited molecular species and allows them to find their optimal positions in a-Se network. This results in films that have good visual appearance and very similar electronic transport properties independent of the source temperature during the deposition.

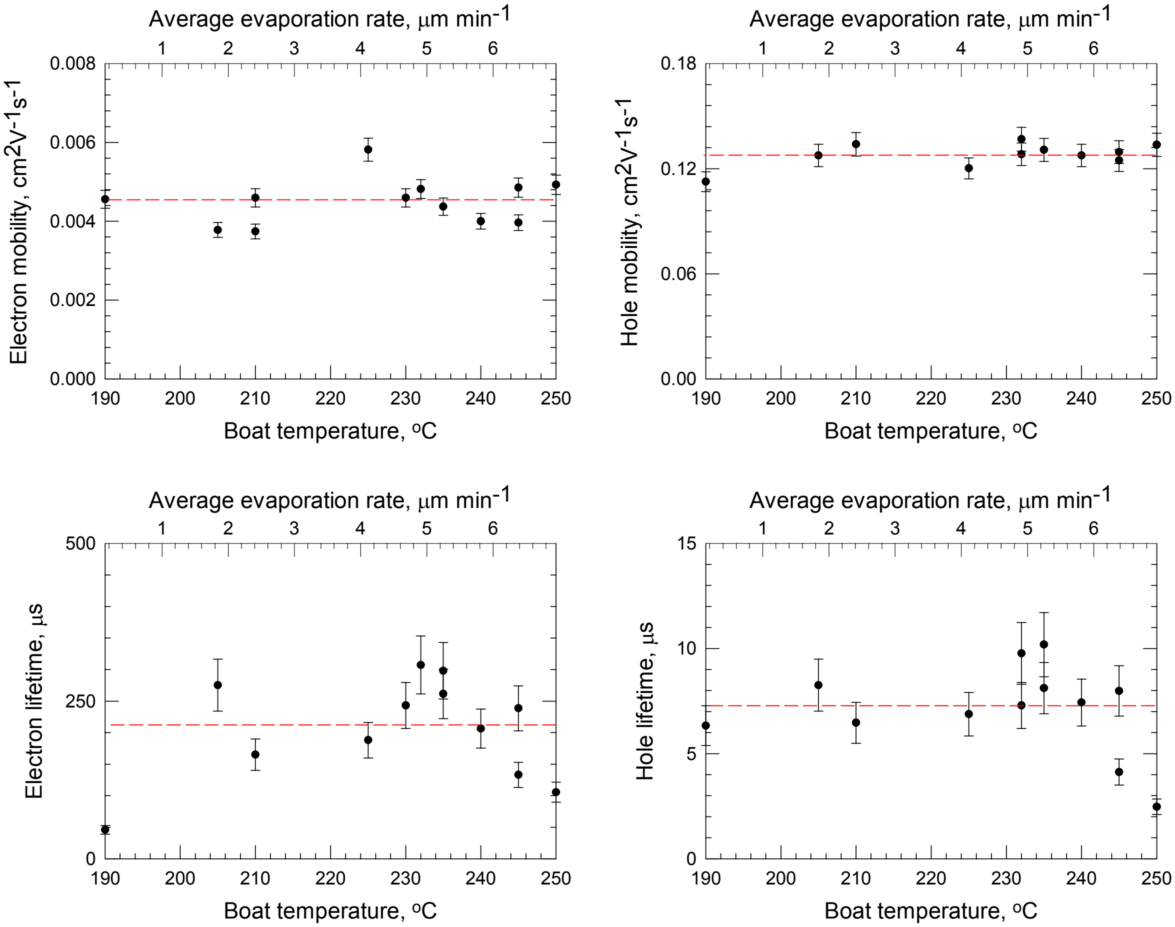

Figure 5.14 The influence of the boat temperature and deposition rate on electronic transport in vacuum deposited films of pure (99.999%) Se. The lines are drawn just as guide for the eyes.

The data in Figure 5.14 demonstrate significant scatter which is well above the errors of the mobility and lifetime measurements. This scatter is due to the fact that the electronic properties of the vacuum deposited films from pure Se are extremely sensitive to coater residual gas atmosphere, impurities present in the coater from previous evaporations, amount of high vacuum silicone grease on the gaskets, etc. Such high sensitivity of film properties to the coater history is not unique to our vacuum system only and has been previously reported by other researchers [133]. The films with the properties reported in Figure 5.14 have not been produced in a continuous series of depositions. This means that between the depositions of the films involved in the study, the coater has been used for the production of films of other differently doped Se materials. In addition, the pauses between the depositions have been of different length, the vacuum grease to the L-gasket (see Figure 4.3) has been reapplied and the walls of the bell jar have been cleaned from time to time as part of the short term maintenance of the vacuum system. All these and other factors that are difficult to take into account can affect the properties of the films produced from pure Se and cause the scatter in the data observed in Figure 5.14.

Strong dependence of electronic transport in a-Se films on the residual atmosphere in the vacuum chamber is typical for the case in which the films are produced from pure Se. We observe that the properties of the films produced from stabilized a-Se are much less sensitive to the residual gas atmosphere in the vacuum chamber.

The results from the experiments described above in this subsection can be summarized as follows. Boat temperature variations in the range 190-250 °C that cause changes in the deposition rate of almost two orders of magnitude does not have significant effects on charge transport in films deposited onto substrates kept at a temperature in the range 60-65 °C. The scatter in the data can be attributed to the differences in the residual gas atmosphere in the coater from evaporation to the evaporation. The insensitivity of the electronic properties of the films produced from pure Se to the deposition rate and boat temperature suggests that the properties of the films are determined from processes of polymerization, de-polymerization, crystallization, etc, that take place during the film growth and which are controlled primarily by the substrate temperature during the deposition.

5.2.3 Influence of Substrate Temperature on Charge Transport in Vacuum Deposited a-Se Films

5.2.3.1 Introduction

The production of films from stabilized a-Se as described in subsection 5.2.1 can be quite complicated due to the fractionation that can appear in the film. Many efforts have been devoted to solving the fractionation problem. All suggested methods involve suitable mechanical and thermal treatments of the Se pellets prior to the deposition of the films and optimization of the deposition conditions. Among all deposition parameters, the boat temperature is the one that influences most strongly the fractionation in the produced a-Se films. The issues of fractionation can be almost fully avoided if the boat temperature during the deposition of the film is kept sufficiently high for the given a-Se alloy (the exact temperature depends on the amount of As in the alloy). By simply protecting the substrates with a shutter during the heating of the boat in the beginning of the evaporation and at the end when very little material is left in the boat allows the production of films that are practically free from fractionation. Thus when films are to be fabricated from stabilized a-Se, the boat temperature cannot be freely varied and the substrate temperature remains the only parameter of practical importance that can be easily changed during the production of a thick Se film.

The results from the experiments in the previous subsection (5.2.2) suggest that the substrate temperature plays decisive role in the determination the charge transport in films produced from pure Se. The data published in literature in relation to the substrate temperature is limited. There exists some evidence that, as early as 1971, it was known that the substrate temperature can have a huge impact on the hole ranges in films produced in a-Se. According to [135], Regensburger has found that the hole mobility-lifetime products are strongly dependent on the substrate temperature during the deposition of the film and that the hole range decreased two orders of magnitude when the substrate temperature was decreased from +80 °C to -80 °C. Compared to the latter, the electron range demonstrated little sensitivity to that wide change in the substrate temperature. Two years later in 1973 Montrimas and Petretis have investigated the influence of the substrate temperature on the crystallization processes in vacuum deposited a-Se films and the formation of deep electron and hole traps in these films [29]. The a-Se films produced in Kasap's laboratories at University of Saskatchewan in the period 1980-2000 were typically grown on substrates kept a temperature in the range 40-80 °C, because such condition is known to produce electronic quality a-Se films [130]. Initial and fractional data collected on such films suggests that the hole transport indeed deteriorates with the decrease of the substrate temperature while the electron transport remains relatively unaffected. This short discussion can be finished by mentioning that the deposition on cold substrates was successfully exploited to produce a-Se based diode devices from Se:3at%As described in [141, 142].

As briefly demonstrated above for almost 40 years it has been known that substrate temperature during the deposition has some impact on the charge transport in a-Se films produced by vacuum deposition. However, the knowledge on the subject was very fragmental. The latter together with the fact that the substrate temperature is a parameter that can be changed without significant technological difficulties have motivated us to study the influence of the substrate temperature on charge transport in the vacuum deposited a-Se film.

We have experimented with pure Se, Se:As and Se:As:Cl alloys and have varied the substrate temperature in the range from 2 to 80 °C keeping the rest of the deposition conditions as constant as possible. From each alloy, a set of films was produced by using constant boat temperature in the range 250-280°C and changing the substrate temperature from deposition to deposition to cover the range specified above. It turned out that it is possible to produce good quality a-Se films if the substrate temperature is kept below the glass transition temperature of the Se material during the deposition. The film production process involves two steps: first the deposition of the film and second, a mild annealing of the film at a temperature around the glass transition temperature of the Se material for a duration from one to several hours. The charge transport in all films was then investigated and the results from the study will be reported in the following subsections.

5.2.3.2 Properties of a-Se Films Deposited on Cold Substrate

Before continuing with the description of the results from the investigation of the influence of the substrate temperature on charge transport in the produced films, it is instructive to discuss the basic observations related to deposition of a-Se films on cold substrates. The term “cold substrate” implies that during the deposition substrate temperature $T_{\text{substrate}}$ was kept below the glass transition temperature T_g of the selenium material used for the production of the films. Films produced at such substrate temperatures sometimes had matt and grayish surface, unlike the films produced at $T_{\text{substarte}} > T_g$ which always have a dark and mirror like surface. The magnitude of the substrate temperature effect depends on the Se material, the value of the substrate temperature and the deposition rate. For example, this effect has greatest influence at about 25-35 °C for films prepared from Se with 0.2-0.5% As and no Cl. We have observed that the latter samples were prone to surface crystallization. The crystallization process can be significantly accelerated by touching the surface of the sample, by prolonged exposure to light, etc. and our initial feeling was that such samples might not be suitable for the purposes of our project due to the lack of stability. However, we have found out that mild annealing of such samples at temperature around the glass transition temperature of the sample material transforms quickly the sample surface to a dark and mirror like state. Careful examination under low magnification microscope of the surface of the cold deposited samples after the annealing has shown that there are no appreciable visual differences between the surface of a cold deposited and annealed samples and the surface of the samples deposited at $T_{\mathrm{substarte}} > T_g$.

Further evidence that the cold deposited and post annealed samples should have similar crystallization resistance as the ones prepared using the traditional substrate temperature range ($T_{\mathrm{substarte}} > T_g$) comes from the results of differential scanning calorimetry (DSC) studies on films prepared in both ways. Figure 5.15 shows the thermograms of three a-Se samples prepared in different way from Se:0.2%As (no Cl) alloy. The first sample (top curve in the figure) is a piece of a pellet of as received material and it essentially is a melt quench a-Se sample that has been well aged. The other two samples were peeled off from a-Se films prepared by vacuum deposition. The first of those samples (the middle curve in Figure 5.15) was peeled of from film prepared under standard conditions (65 °C substrate temperature), while the second one was peeled off from a film deposited at 8 °C and annealed after the end of the deposition for one hour at temperature of 50 °C. All other deposition parameters were the same for both films.

The two films have aged at the same conditions but for different time intervals before the DSC samples were prepared from them. Thus the different ageing history and the slight differences in the DSC sample preparation can explain the differences in the T_g regions of the curves corresponding to hot and cold deposited films. The crystallization peaks are similar in shape for the two film samples. The maxima of the crystallization peaks are at different temperatures which might suggest that the average length of the chains is different in the two films i.e. different viscosity. Remarkably, the onset of the crystallization process is almost the same (~104 °C) for all the three samples which suggests that all the three samples should have similar resistance to crystallization at room temperature. Indeed, our observations over a period

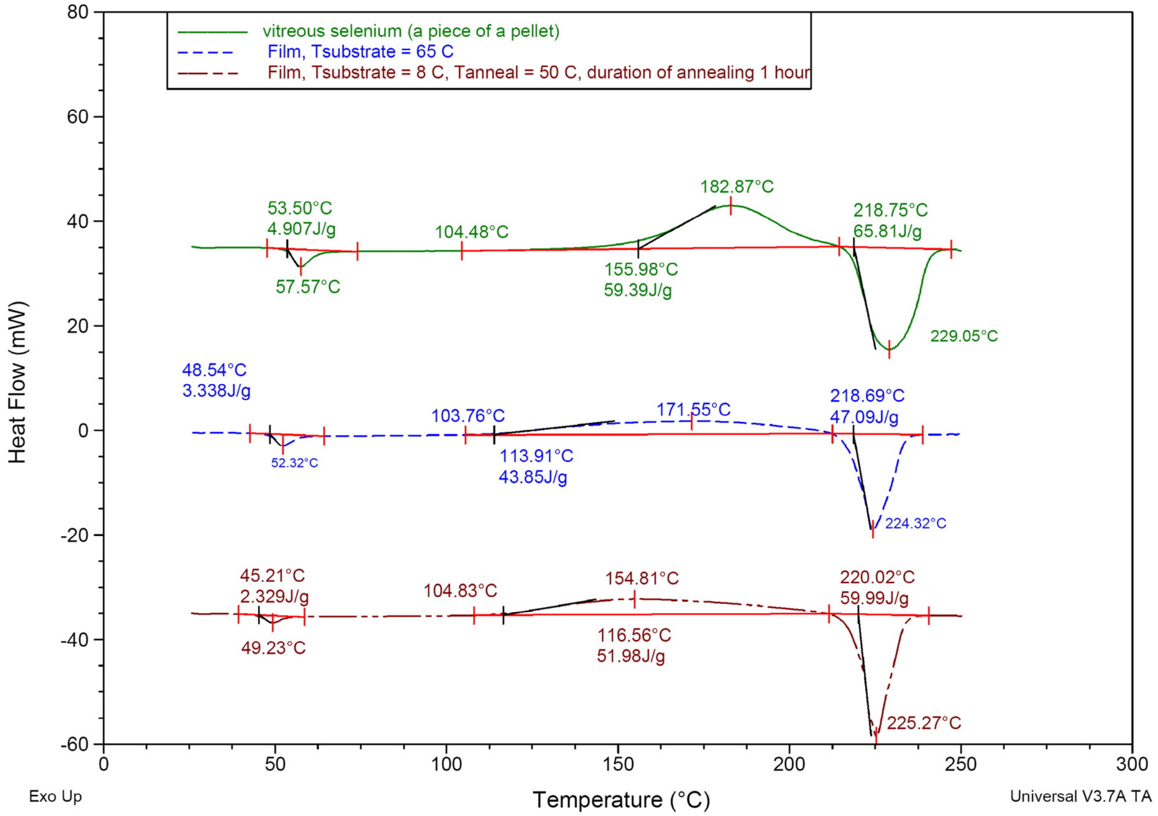

Figure 5.15 Comparison between the thermograms (heating 10 °C/min) of three differently prepared a-Se samples from the same material (Se:0.2%As no Cl). The onset of the crystallization of the film deposited at $T_{substrate} = 65$ °C is the same as for the film produced by cold deposition ($T_{substrate} = 65$ °C) and mild post annealing (1 hour at $T_{anneal} = 50$ °C) which suggests that the films should have similar resistance to crystallization. The small differences in the T_g region can be explained in terms of different sample history and do not necessarily reflect different material properties.

of 4-5 years have confirmed that the cold deposited and post annealed samples have very similar crystallization properties to the films prepared under the standard conditions ($T_{\text{substarte}} > T_g$). From the discussions in the subsection so far it is evident that the annealing has beneficial effects on cold deposited films with respect to their mechanical properties and their resistance to crystallization. It is interesting to know what happens to the charge transport after the annealing. Results from a typical experiment that was designed to answer the above question are presented in Figure 5.16. The charge transport was measured before the annealing of the samples and 24

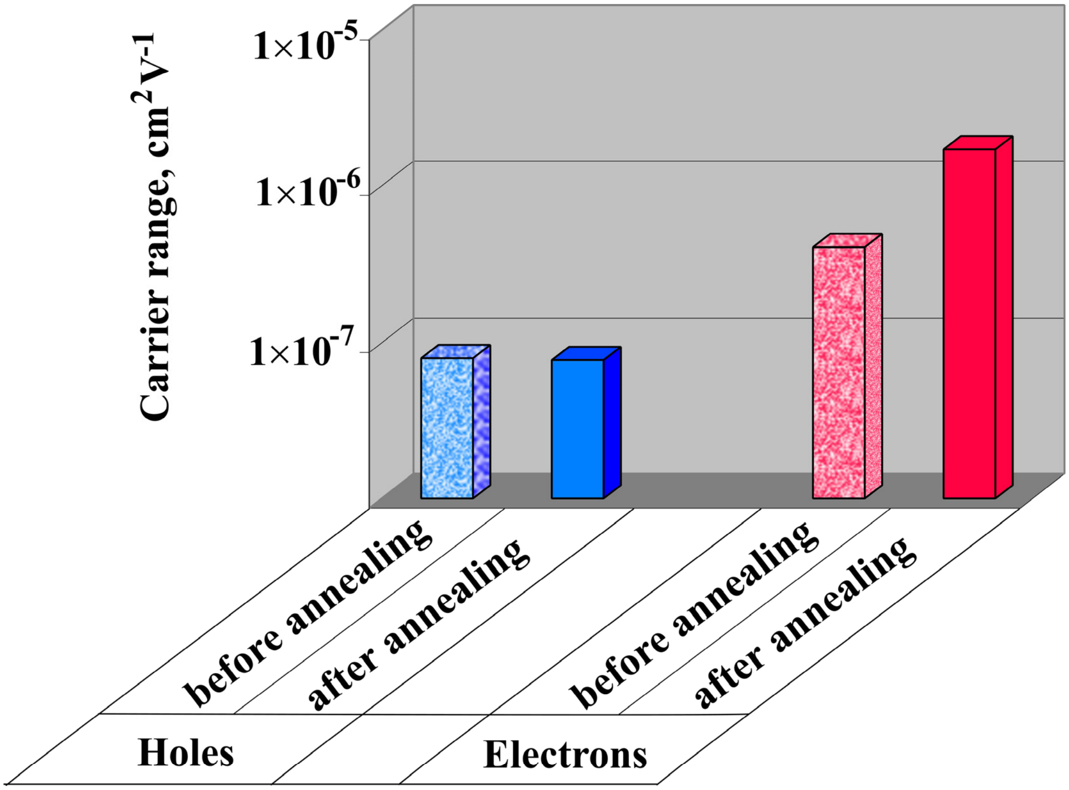

Figure 5.16 Effect of a mild post annealing (T = 50 °C ≈ T$_g$) with duration of about one hour on carrier mobility-lifetime products in films produced from Se:0.5wt%As (no Cl) films.

hours or more after the end of the annealing. Immediately after the annealing, the transport of both types of carriers is suppressed compared to the state before the annealing. However, 24-48 hours after the annealing, the relaxation processes in the sample cause the transport to change most often in the direction illustrated in Figure 5.16. As can be seen from the figure, the hole transport does not change much, while the electron transport shows tendencies towards improvement. For the films in the figure, the electron range has improved about 2-3 times. Similar changes in the transport are observed if the cold deposited films are aged without annealing in dark at room temperature for a period of 1-4 months.

In cases when the cold deposited film has preserved significant hole transport, we observe that the mild annealing of the samples causes hole ranges to decrease.

We can summarize the effects as follows. The mild post annealing ($T_{\mathrm{annealing}} \sim T_g$) with a duration from one to several hours does not improve the hole range and does not deteriorate the electron range in cold ($T_{\mathrm{substarte}} > T_{\mathrm{g}}$) deposited a-Se films. This result is important because as it will be explained later in subsection 5.2.3.3, the cold deposition followed by subsequent annealing has demonstrated significant potential for production of a-Se based n- like layers ($\mu_h\tau_h << \mu_e\tau_e$).

5.2.3.3 Dependence of the Charge transport in a-Se Films on Substrate Temperature during the Vacuum Deposition Process

The dependence of charge transport in vacuum deposited a-Se samples on the substrate temperature during the film deposition process was investigated for 3 different groups of materials. These include Se:As no Cl alloys, Se:As:Cl alloys and pure Se materials. Typical results for each group of materials are illustrated in Figure 5.17, Figure 5.18 and Figure 5.19 respectively. The films deposited at $T_{\text{substrate}} < T_{\text{g}}$ were annealed typically for 1 hour at 50 °C before any charge transport measurements on them. All the films were rested for at least 24 hours prior to the TOF and IFTOF measurements.

As can be seen from Figure 5.17 the substrate temperature has huge impact on the hole transport in the films. As the substrate temperature decreases the hole mobility and hole lifetime are also decreasing. The decrease in the hole lifetime is huge - more than two orders of magnitude as the substrate temperatures decreases from 75 to 25 °C. At the same time the electron transport is not so strongly affected. The tendency shown in the figure is towards a slight decrease in electron mobility and more pronounced decrease in the electron lifetime. However, the decrease in the electron lifetime that corresponds to substrate temperature decrease from 75 to 25 °C is only about 3 times, which is much less than the corresponding decrease in the hole lifetime. Experimenting with different Se:As alloys we have observed that the hole lifetime always decreases significantly as the substrate temperature is decreased while electron lifetime might decrease, might remain the same of might demonstrate a slight increase. The magnitude of the change in all cases is much smaller compared to the observed changes in the hole lifetime. Figure 5.17 demonstrates that the transport in the films clearly switches from p- like type ($\mu_h\tau_h > \mu_e\tau_e$) to n- like type ($\mu_h\tau_h < \mu_e\tau_e$) as the substrate temperature decreases. The substrate temperature around which the latter transition occurs is in the range 30-40 °C as can be seen from Figure 5.17. The transition from p- like type to n- like type transport is quite sharp – almost step like and most of that effect is due to a change in the hole lifetime.demonstrates that the transport in the films clearly switches from p- like type ($\mu_h\tau_h > \mu_e\tau_e$) to n- like type

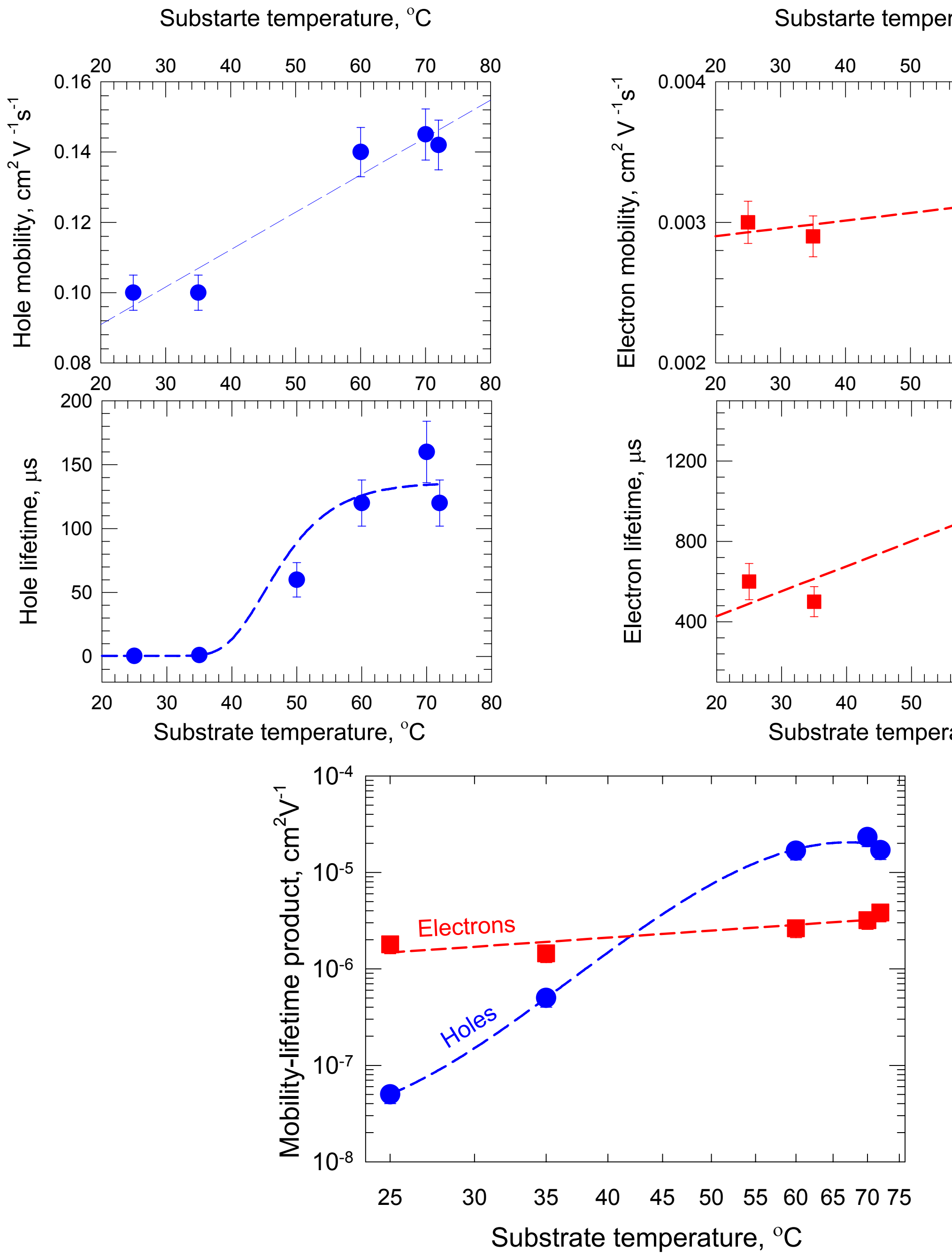

Figure 5.17 Influence of the substrate temperature on the charge transport in vacuum deposited films from Se:0.5%As no Cl alloy. The lines are plotted as guide for the eyes only.

($\mu_h \tau_h < \mu_e \tau_e$) as the substrate temperature decreases. The substrate temperature around which the latter transition occurs is in the range 30-40 °C as can be seen from Figure 5.17. The transition from p- like type to n- like type transport is quite sharp – almost step like and most of that effect is due to a change in the hole lifetime.

This result has a very significant technological importance. The layer produced at 25 °C has electron range that is 40 times bigger than the hole range and in many cases can act as hole trapping (n- like layer) in a-Se based pin- like structures for x-ray image detector applications. The two step process (cold deposition and annealing) is quite simple and does not require the production of alloys accurately doped with alkali elements to suppress the hole transport and which in the same time have to be heavily doped with As to ensure the long term resistance of the films against crystallization.

The practical importance of this result motivated us to investigate the influence of the substrate temperature on charge transport in vacuum deposited films further for films produced from Se:As:Cl alloys. One set of results from such investigations for Se:0.3%As:10ppm Cl alloy are presented in Figure 5.18. The results are very similar to the ones we have already described for the Se:As no Cl alloys. The decrease of the substrate temperature forces a significant decrease in the hole mobility-lifetime products leaving the electron mobility-lifetime products relatively unchanged. The step like change from p- like type transport to n- like type transport when the substrate temperature is decreasing is observed again and effect is again almost totally due to the decrease in the hole lifetime. The exact substrate temperature at which the transport in the films switch from p- like type to n- like type for this type of alloys lays somewhere in the range between from 6-7 to 20 °C (Figure 5.18). This is 15-20 degrees lower than in the case when Se:0.2%As no Cl alloys (Figure 5.17) and this difference must be due purely to the presence of Cl because both alloys have very similar hole transport when the films are deposited at a high substrate temperature (say 60 °C). Thus, it is clear that Cl somehow affects the changes in the structure of the films that appear as a result of deposition on a cold substrates and lead to the changes in the charge transport that we have described above.

If only 10 ppm Cl can observably affect the changes in the transport related to the deposition on cold substrate, a question arises about the influence of the arsenic. Arsenic impurities are present in much higher concentration and one might think that the changes in the charge transport observed in the cold deposited a-Se films are mainly due to the presence of arsenic impurities in selenium.

The data presented in Figure 5.19 demonstrate that is not the case. Films deposited from pure Se source material exhibit the same dependence of the charge transport on the substrate temperature as the films produced from Se:As or Se:As:Cl alloys. Figure 5.19 clearly demonstrates that the pure Se #2 has similar ranges for both types of carriers when deposited on a hot substrate. The deposition on cold substrate (4 °C) has produced from the same Se material

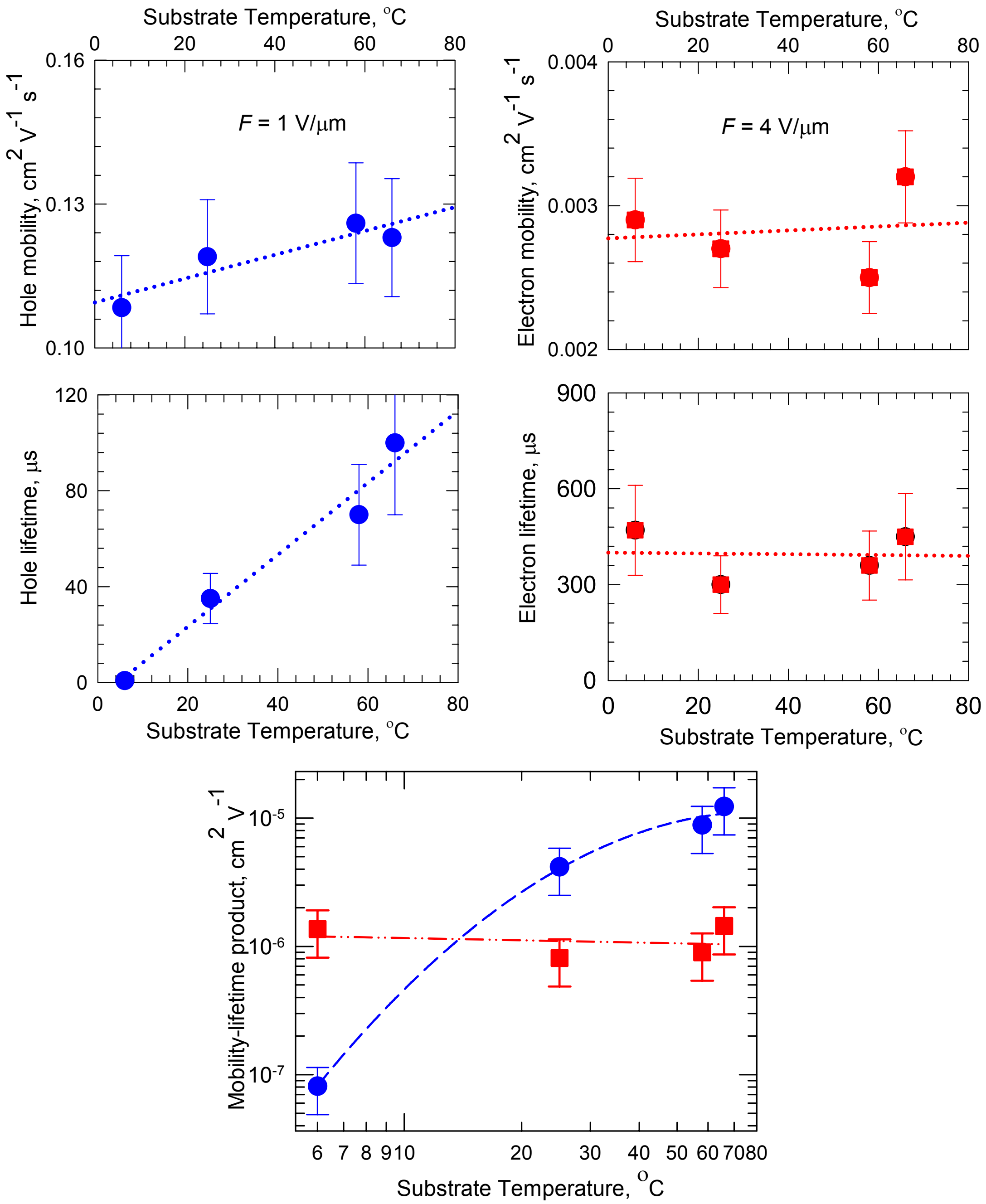

Figure 5.18 Influence of the substrate temperature on charge transport in vacuum deposited films from Se:0.3%As:10ppm Cl alloy. The lines are shown as guides for the eyes only.

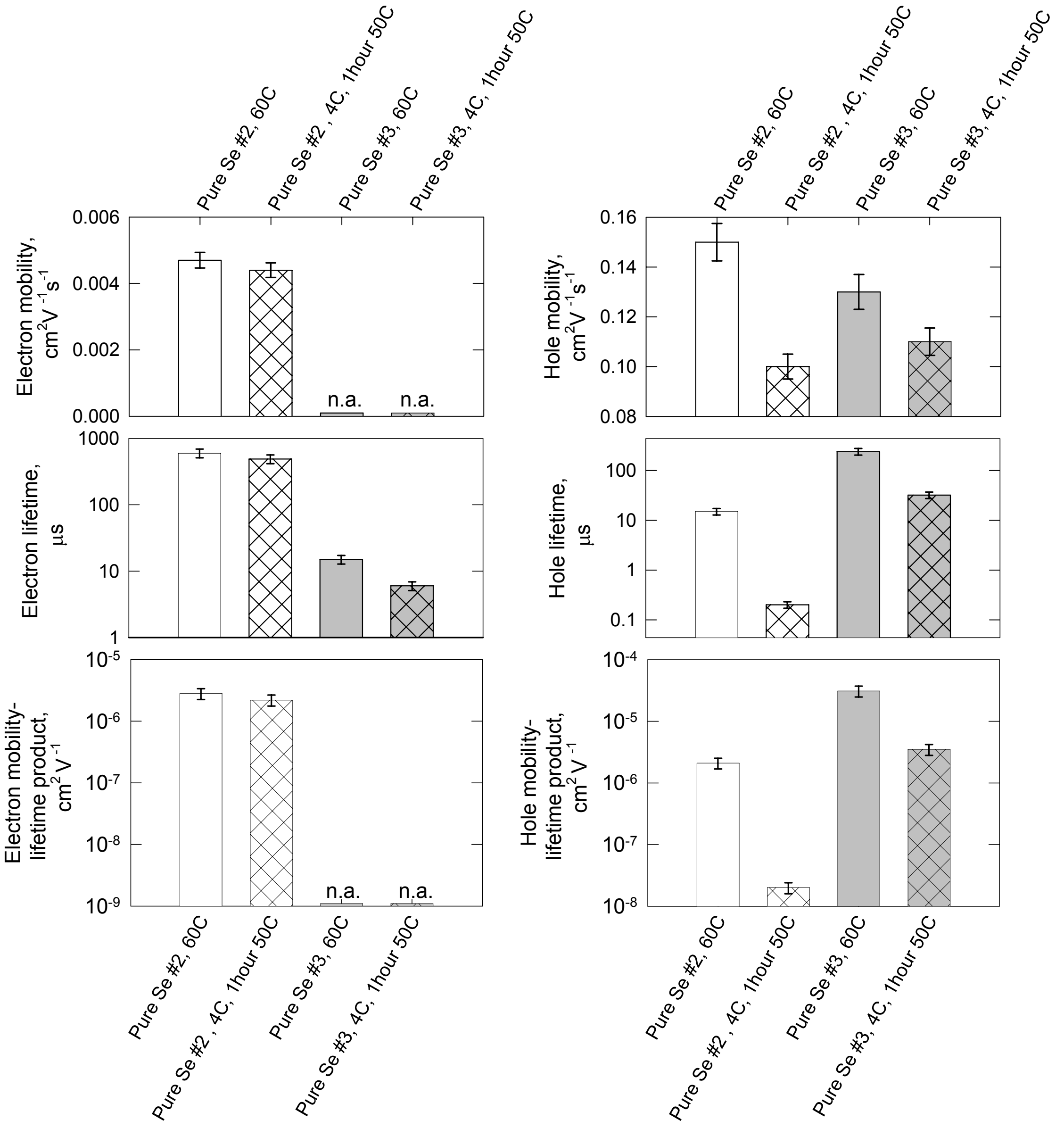

Figure 5.19 Influence of the substrate temperature on the charge transport in vacuum deposited films from pure Se (99.999%).

a film possessing clearly n- like type of transport. The observed change in the hole range is almost two orders of magnitude and the film deposited at 4 °C has trap limited hole transport. Hot deposited films from pure Se #3 have holes with very long lifetimes and deep trap limited electron transport. As discussed in subsection 5.1.3 such charge transport properties are probably due to oxygen impurities in the ppm range that are present in the material. The same change in the substrate temperature (from 60 °C to 4 °C) has left the electron lifetime practically unchanged and has decreased the hole range about one order of magnitude. Similar to the case of Cl containing alloys, we might expect that further decrease in the substrate temperature is required and/or longer annealing to produce films from pure Se #3 that have trap limited hole transport.

The results described in this subsection so far indicate that the deposition on cold substrate induces changes in the structure of the a-Se films which, in their turn, alter the charge transport in the films. If the substrate temperature is sufficiently low the transport in the cold deposited layers becomes n- like ($\mu_h\tau_h < \mu_e\tau_e$). The mild post annealing ($T_{\text{annealing}} \sim T_{\text{g}}$) with duration from 30 min to several hours obviously affects the structure of the films but the changes in the structure induced by the annealing usually amplify the effects of on the charge transport that resulted from deposition on a cold substrate. The question that logically arises is how permanent are the changes in the a-Se structure that result from deposition on cold substrate and what does it take to "reset" the structure of a-Se material to the state prior to cold deposition. We carried out the initial research towards answering the latter question by performing the experiments described below.

We have selected several Se:0.2%As materials and have produced films from them at a high substrate temperature (60 °C) and on a cold substrate (4 °C). The cold deposited films were then annealed for 1 hour. Additionally, we have evaporated films from each material on Al foil with a sufficiently large area kept at 4-10 °C. We have then reclaimed the cold evaporated material from the foil. From the cold reclaimed material we have produced films onto a substrate kept at 60 °C. All other deposition parameters were the same for all the films. The charge transport was measured in all the films and a typical set of results is presented in Figure 5.20.

It is well known that the temperature of the melt determines key parameters in the structure of the molten Se like chain length, average distance between the chains etc. According to the data published in the literature [28] it takes less than 15 mins for the melt to reach its equilibrium state. For our coater, it takes about 5-10 min after the boat has reached its nominal temperature (250 °C) for the evaporation rate to stabilize. The shutter is then opened and the films begin to grow on the substrate for a period of time that is more than 40-50 min longs. Our intuitive expectations were that the films deposited from the starting material at 60 °C substrates and the films produced from the cold reclaimed material on substrates kept at the same temperature (60 °C) will have very similar transport properties. In spite of our expectations,

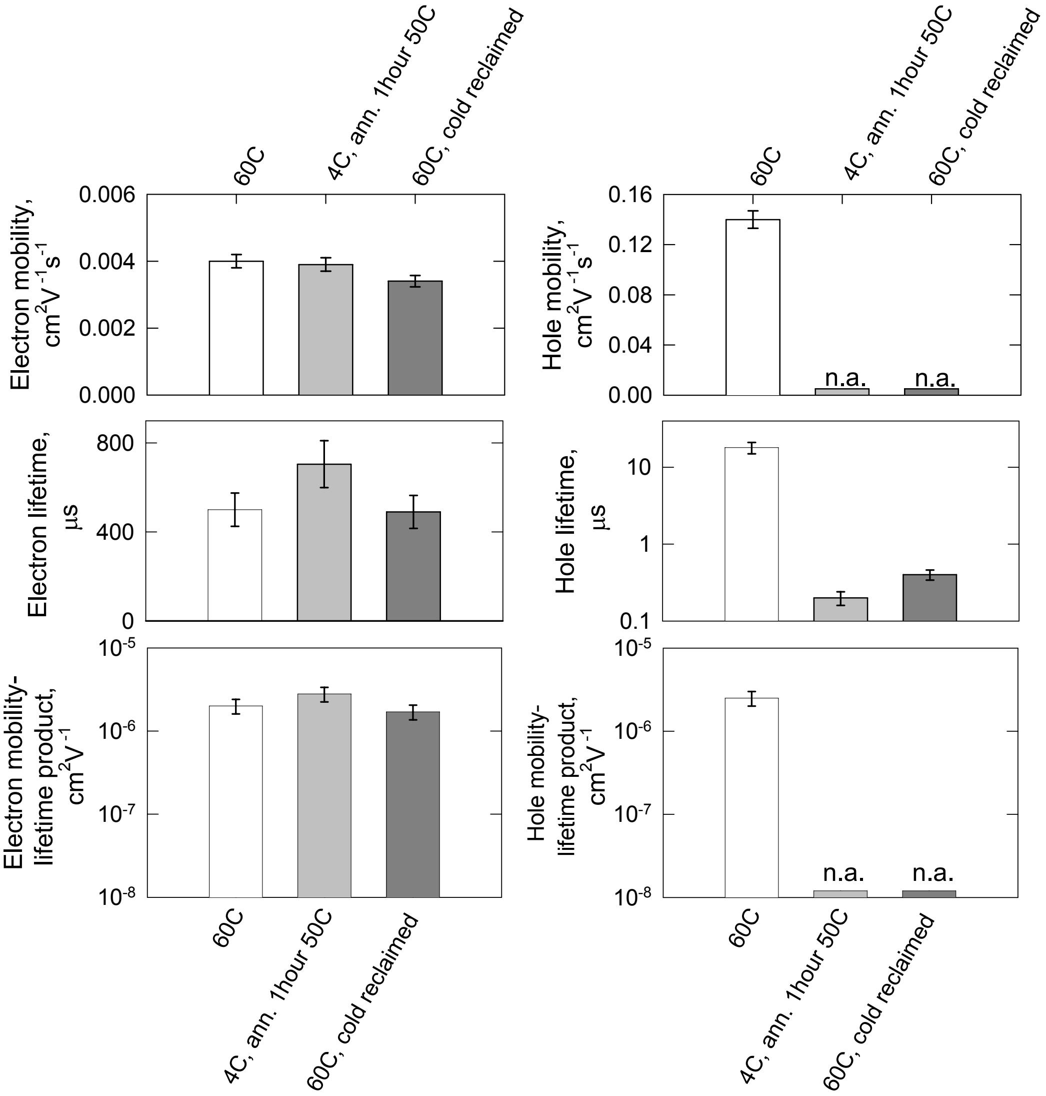

Figure 5.20 Charge transport in vacuum deposited films from cold reclaimed Se:0.2%As material produced at 60 °C substrate temperature. Cold reclaimed means that the alloy was first evaporated on a cold (4-10 °C) Al foil. The material from the foil was then reclaimed and from the reclaimed material we evaporated films onto substrates kept at 60 °C. The transport in such films is compared with the transport in films produced directly from the starting alloy on hot (60 °C) and cold (4 °C) substrates. The cold deposited films were annealed at 50 °C for one hour. The samples were rested in dark for at least 24 hours prior to the charge transport measurements.

Figure 5.20 clearly shows that the transport in the films produced from the cold reclaimed material on hot substrates have almost the same charge transport properties as the films deposited from the starting material on cold (4 °C) substrates. The result is a clear manifestation of a "memory" effect associated with the structure of the cold deposited material. The changes in the structure of a-Se induced by the deposition on cold substrate are very strong and persistent, at least re-evaporation of the cold reclaimed material on a hot substrate cannot “reset” the structure and charge transport properties of the material.

5.2.3.4 Discussion on the Influence of the Substrate Temperature on Charge Transport

It is difficult to explain all experimental findings related to the charge transport changes in a-Se films induced by deposition onto a cold substrate in the frame of a simple model. The reduction in the hole range with decreasing $T_{\text{substrate}}$ is due almost totally to the reduction in the hole lifetime τ_h. The observed decrease in the hole lifetime related to the deposition on a cold substrate can be two and a half orders of magnitude. Thus evaporation of films on a substrate kept at sufficiently low temperature must result in concentration of deep hole traps that is two and half orders of magnitude higher than the one in hot deposited films. The mild ($T_{\text{annealing}} \sim T_g$) post-annealing up to a few hours seems to have negligible effect on on the concentration of deep hole traps. At the same time, the concentration of deep electron traps is much less sensitive to the substrate temperature because the observed changes in the electron lifetime are much smaller in magnitude compared to the changes observed for the hole lifetime.The drift mobilities of both type of carriers show tendencies towards decreasing as the substrate temperature is decreased, the effect associated with hole mobility being much more pronounced.

Many attempts have been made to relate the electron and hole traps to various structural defects in the a-Se films. Such defects can be under- (Se_1^-) and over- (Se_3^+) coordinated charged centers that can be found in the structure of a-Se. In section 5.1 we have assumed that Se_1^- acts as deep hole trap while Se_3^+ acts as deep electron trap. Such assumption enabled us like many researchers to qualitatively explain the effects of different dopants on the charge transport in a-Se films.

Such assumption alone can not explain our results related to the deposition of a-Se on a cold substrate. Obviously, when Se molecules arrive at the substrate kept at low enough temperature, they are immediately “frozen” on the surface of the film. In contrast, deposition on a hot substrate ($T_{\text{substrate}} > T_g$) allows Se molecules arriving at the substrate to move for a while on the surface of the film and thus to polymerize and form longer Se chains and bigger and more stable Se aggregates. Thus the films produced on cold substrates will be built by shorter Se chains and will be more disordered which will result in a bigger distance between the chains. Such changes in the structure will indeed result in higher concentration of chain ends which can act as hole traps and thus, at first view, explain the observed decrease in the hole lifetime resulting from the deposition on a cold substrate. However, during the post annealing or as the sample ages over the time at room temperature the shorter chains will tend to organize forming long chains and decreasing the average distance between them. This should lead to an observable increase in the hole lifetime. Further, according to the VAP theory, the chain ends (Se_1^0) are unstable defects in a-Se and they gradually will be transferred into pairs of Se_1^- and Se_3^+ which will lead to changes in both hole and electron lifetimes. In contrast, our observations are that, as a result of annealing or ageing, the hole lifetime stays the same or gets worse, while the electron lifetime stays the same or increases.

The research of Montrimas et al. published in [29, 143] suggests that deep carrier traps of totally different origin can additionally exist in a-Se layers. According to the transmission electron microscope studies published in the latter works, in each a-Se layer can be found numerous nano-crystalline inclusions. Some of them have the structure of trigonal selenium while the others have the structure of monoclinic Se. In [29] have been suggested that the trapping at the interface between the crystalline inclusions and the amorphous phase can have significant impact on charge transport in a-Se films. The hypothesis raised in that work is that the interface surrounding the crystalline inclusions of trigonal allotrope modification of Se can trap deeply holes while the interface around the inclusions of monoclinic Se allotrope deeply traps electrons. The authors have investigated the concentration of the microcrystalline inclusions as a function of the substrate temperature and that dependence is reproduced below in Figure 5.21.

The results of Montrimas and Petrètis (Figure 5.21), clearly show that the concentration of microcrystalline inclusions changes over more than 4 orders of magnitude as the substrate temperature is decreased from 60-70 °C to about 8 °C. It is worth noting that the substrate temperature according to their results has effect on the size and the morphological structure of the crystalline inclusions. The authors have found that the average size of the of the crystalline inclusions produced at $T_{substrate}$ = 8-30 °C is about 50 nm while the inclusions in the films produced at higher substrate temperatures are bigger in size reaching 200 nm for $T_{substrate}$ = 80-90 °C. Crystalline inclusions of trigonal type are predominant in layers produced at substrate temperatures above 50 °C while both monoclinic (mainly β) and trigonal inclusions exist in the layers produced at substrate temperatures lower than 30 °C. The authors have also pointed out

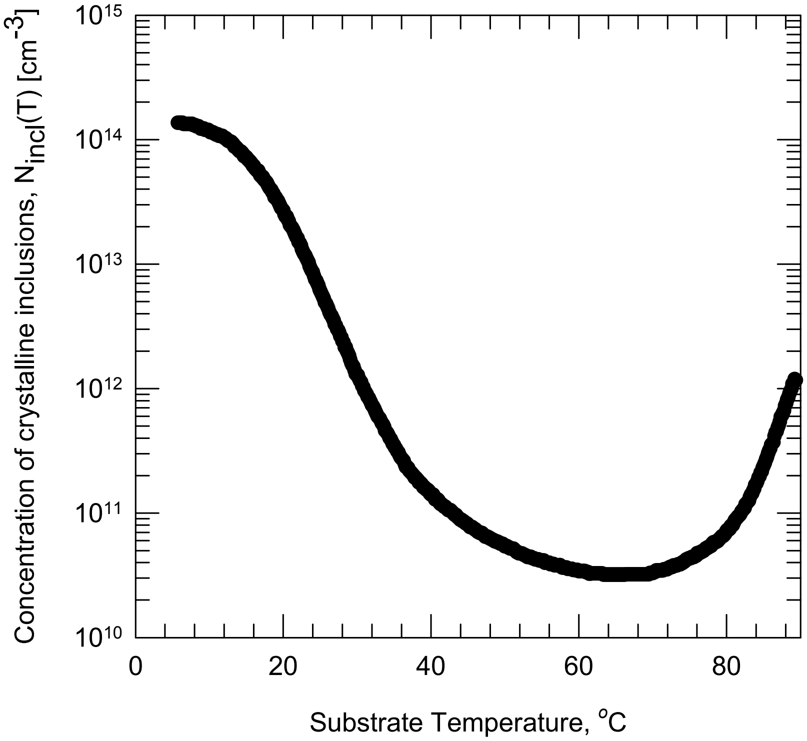

Figure 5.21 Concentration of crystalline inclusions in a-Se films as a function of substrate temperature. Data were taken from [29].

that the existence of the nano-crystals in the a-Se films is not the only reason for the formation of deep charge carrier traps in them. They have argued that deep traps with concentrations below 10^{13} cm^{-3} can easily form by structural fluctuations in the amorphous phase.

Based on the findings of Montrimas and Petrètis [29] we can explain quite consistently the results from the charge transport measurements on films produced at different substrate temperatures. Films produced at substrate temperatures 50-70 °C have very low concentration of nanocrystalline inclusions. In these films the deep traps due to structural fluctuations (these very well might be the over- and under- coordinated charged defects) in the amorphous phase dominate the lifetimes and the ranges of the carriers.

As the substrate temperature decreases the number of crystalline inclusions in the amorphous matrix increases. In films produced at lower substrate temperatures the amorphous phase itself has two different components and when crystallizing it produces crystallites of both trigonal and monoclinic type [29]. At very low temperatures the concentration of crystalline inclusions is very high (see Figure 5.21) and the deep traps that exist due to the presence of these nanocrystals dominate the hole lifetime and hole ranges. Most of the crystalline inclusions are of trigonal type. That is the reason for which the hole transport is more sensitive to the substrate temperature during the growth of the film. During post annealing and ageing of the samples, several processes take place. First, some of the inclusions that are very small will disappear forming amorphous phase. Second, some new crystal inclusions of trigonal and monoclinic type are formed. Third, the crystal inclusions that have a size bigger than certain critical radius grow at the expense of the amorphous phase or of the smaller crystals around them. Fourth, the inclusions from monoclinic type are transformed into crystal inclusions of trigonal type which is the more stable crystal form of Se. Fifth, the amorphous part of the film homogenizes because the phase that tends to crystallize in monoclinic form gradually transforms into the phase that crystallizes in the trigonal Se crystal form.

As a result of all these processes, depending on the exact conditions (substrate temperature, annealing temperature, annealing time, ageing time, starting material, etc.) the concentration of trigonal nano-crystal is not likely to be decreased while the concentration of the monoclinic crystalline inclusions is not likely to be increased. Such trends qualitatively explain the reasons for the hole lifetimes and ranges that tend to decrease with annealing and ageing while electron lifetimes and ranges tend to improve with annealing and ageing.

The crystalline inclusions can also act as scatter centers for the charge carriers and in this way we can explain why both hole and electron mobilities tend to decrease for films produced at lower substrate temperatures.

The exact substrate temperature which will force the Se molecules arriving at the substrate to freeze immediately and efficiently form numerous crystalline inclusions depends on the starting Se material and from dopants like As and Cl. It is well known that Cl tends to make Se chains shorter and a-Se network structure more flexible [136, 137] while As tends to link several Se chains together and has exactly the opposite effect. For that reason, the exact substrate temperatures at which the charge transport in the film will switch from p- to n-type and the hole transport will become deep trap limited depend on the starting Se material and impurities (see Figure 5.17 and Figure 5.18). In light of the above discussions, Cl will cause these changes to happen at lower substrate temperature while As will have the opposite effect and that is exactly what is observed in Figure 5.17 and Figure 5.18.

Further we can roughly check whether the experimentally obtained in [29] and presented in Figure 5.21 function $N_{\text{incl}}(T)$ describing the concentration of crystalline inclusions in a-Se layers vs. substrate temperature is consistent with our results presented in Figure 5.17 and Figure 5.18. Assuming that almost all inclusions after the annealing of the samples are of trigonal crystal modification of Se we can use the function $N_{\text{incl}}(T)$ to calculate hole lifetime in the a-Se films using the following relation

$$\tau_h(T) = \frac{1}{C_1\,N_{\text{incl}}(T+T_0)+C_2}\,. \tag{5.8}$$

In the last expression C_1 is a constant that, multiplied by the concentration of crystalline inclusions, gives the deep hole trapping rate that is due to deep trapping related to the crystalline inclusions alone. The other constant C_2 has the meaning of deep hole trapping rate, that is due to the hole traps present in the material in the absence of any crystalline inclusions. The last constant T_0 describes the shifts to the left and to right on the temperature scale of the function $N_{\text{incl}}(T)$ due to the properties of the staring material, the presence of impurities like As and Cl, etc. Equation (5.8) can be fitted to the hole lifetime data presented in Figure 5.17 and Figure 5.18 and the results from one such attempt are presented in Figure 5.22. As can be seen from the figure, the data on the concentration of crystalline inclusions [29] in a-Se layers prepared at different substrate temperatures agrees quite well with both set of our own experimental data having in mind that $N_{\text{incl}}(T)$ and hole lifetimes were measured on films produced from materials with totally different origin and are separated in time by more than 30 years. However, the number of hole lifetime data points in each of the data sets is limitted and the agreement can not be characterized quantitatively.

If the nano-crystalline inclusions really exist in the vacuum evaporated a-Se films in such high concentrations and play such significant role in shaping the charge transport properties of such films a lot of data published about a-Se have to be re-examined. For example almost all experimental results are processed on the base of the assumption that the film has uniform properties across its thickness. As one intuitively expects and as it was actually experimentally found, the concentration of the nano-crystalline inclusions in vacuum deposited films is not uniform across the film thickness. The concentration of such inclusions is much bigger near the

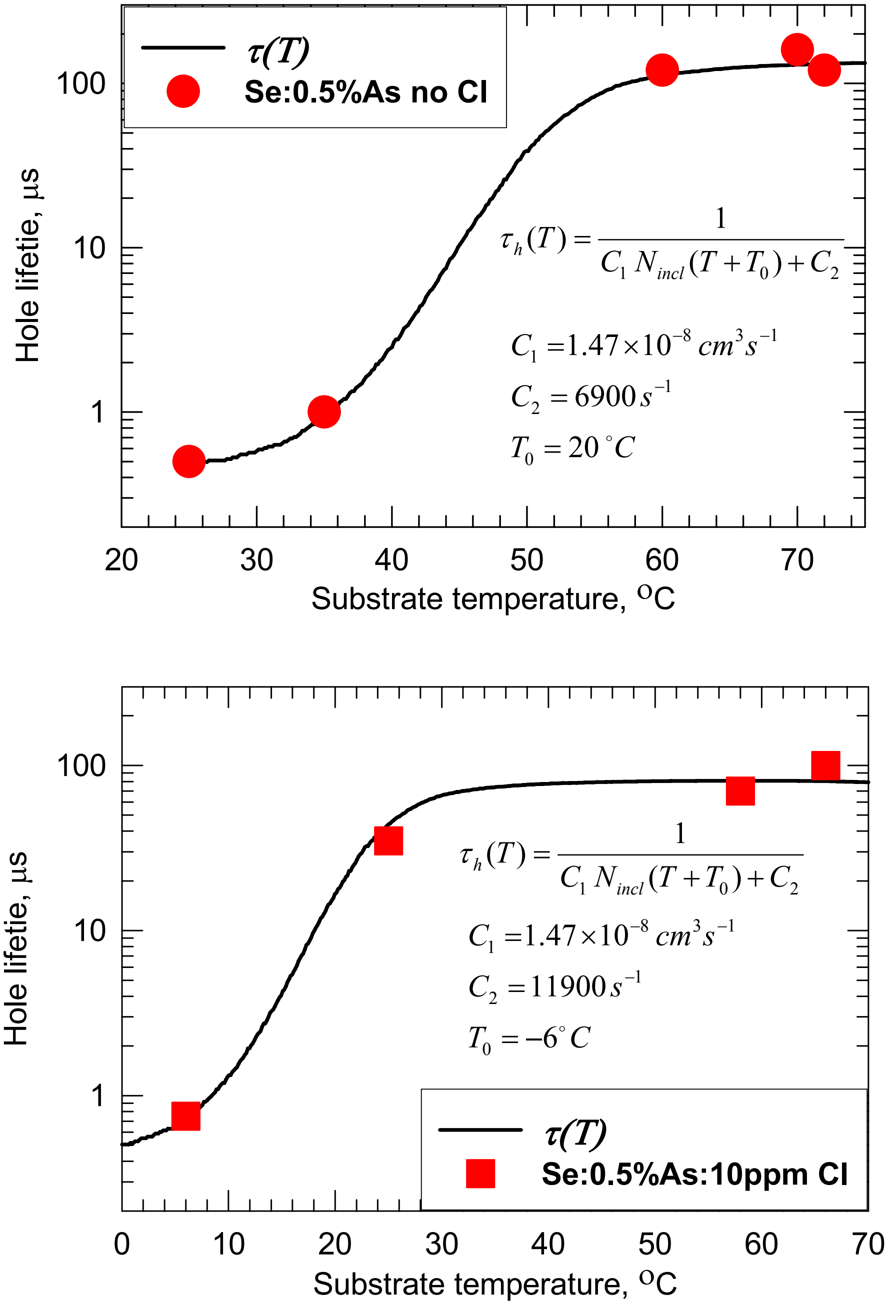

Figure 5.22 Comparison between experimentally measured hole lifetimes in a-Se films produced at different substrate temperature in our laboratory with the ones estimated on the basis of experimentally measured concentration [29] of nanocrystalline inclusions in a-Se films produced at different substrate temperatures.

substrate and near the top surface of the film and the observed variation can be several orders of magnitude [29] thus the films are far from having uniform properties across its thickness.

Unfortunately, we cannot explain in a consistent way the data from our experiments with Se that was reclaimed after the evaporation on cold substrate (see Figure 5.20) with the hypothesis based on the formation of nanocrystalline inclusions with different concentrations for different substrate temperatures. The only idea that can be used is that the deposition on a cold substrate results in the formation of highly

distorted Se structure that is preserved after melting. Then the evaporation of the material with highly dispersive structure results in a vapour phase consisting of predominantly smaller Se molecules which cannot rearrange efficiently and form bigger and more stable Se aggregates on the substrates even at high (60 °C) substrate temperatures. We can then speculate that a metastable form of Se is formed even at high substrate temperatures that later results in the formatin of nanocrystalline inclusions.

The lack of fundamental understanding of the a-Se structure and hence on the exact nature of the deep carrier traps in a-Se films makes it particularly difficult to formulate an exact physical model that can explain all experimental observations related to alloying and to cold deposition of a-Se.

5.2.4 Effects of the Preparation Conditions on the Charge Transport in a-Se Films - Summary

The influence of preparation conditions on charge transport in vacuum evaporated a-Se films was investigated in this subsection. The emphasis was placed on the two parameters that can be easily changed in every vacuum deposition system – the boat temperature and the substrate temperature. Due to fractionation issues, it is not possible to freely vary the boat temperature when films from stabilized a-Se are to be prepared and we therefore studiedthe the dependence of charge transport parameters on the boat temperature for films produced from pure Se material only. In our coater, for a boat to substrate distance of 16 cm, variation of boat temperature in the range 190-250 °C changes the evaporation rate in the range 0.1-10 μm/min and the composition of the Se vapor as well. For films deposited at high substrate temperatures ($T_{\text{substarte}} > T_g$), the variation of the boat temperature and hence the evaporation rate in above ranges did not cause any systematic change in the charge transport properties of the deposited films. We observe a big scatter in the data which can be attributed to the huge sensitivity of the properties of the pure a-Se to the residual atmosphere in the chamber and hence to the coater history.

The observed lack of dependence of charge transport on the boat temperature, deposition rate and on the accompanying small changes in the composition of the Se vapor suggests that after the arrival of the Se molecules at the substrate held at $T_{\text{substarte}} > T_{\text{g}}$ they can travel a small distance on the surface and take part in the processes of polymerization (and possibly of crystallization) taking place at the surface of the growing film. In the absence of As and Cl atoms, the processes of rearrangement mentioned above will depend mainly on the substrate temperature, which is the parameter that determines the charge transport properties under such conditions.

Charge transport in vacuum deposited films produced from stabilized a-Se and from pure Se was investigated as a function of substrate temperature in the range 0-80 °C.
It was found that good quality a-Se films can be produced by evaporating Se on cold substrates ($T_{\text{substrate}} < T_{\text{g}}$). The production process involves two steps: first evaporation of the film onto a cold substrate and second mild ($T_{\text{annealing}} \sim T_{\text{g}}$) annealing with duration from one to several hours. Films produced by using the procedure described above have resistance to crystallization similar to that observed for films produced on hot substrates as estimated with DSC measurements. It has been demonstrated that the mild post annealing process does not improve the hole transport while the electron transport does not deteriorates due to the annealing.

The decrease in the substrate temperature has a huge impact on the hole transport decreasing the hole range about two and more orders of magnitude in the same time the electron transport remains relatively unaffected. Films produced at low substrate temperature demonstrate clearly n-type transport ($\mu_h \tau_h < \mu_e \tau_e$) and if the substrate temperature is low enough the hole transport becomes deep trap limited. Such behavior of charge transport has been observed for films produced from Se:As, Se:As:Cl and pure Se materials. The temperatures at which the transport switches from p-type to n-type and the temperature at which the hole transport becomes deep trap limited depend on the material. Films evaporated on substrates kept at temperatures 20-30 °C from alloys that contain only As have, in most cases, deep trap limited hole transport, while the films produced from Cl containing alloys demonstrate deep trap limited hole transport only if produced on substrates kept at temperatures that are at least 20 °C lower than the range specified above.

It was found that the changes in the Se structure related to the deposition onto a cold substrate are quite persistent. For example, if Se:As alloy is evaporated onto a cold substrate (4-

10 °C), and then the material is reclaimed and re-evaporated onto hot substrates (60°C) the resulting films demonstrate hole transport that bares no resemblance to that observed in films produced directly from the starting Se:As material on substrates kept at 60°C. In the same time the charge transport in films produced from cold reclaimed material on hot substrates is very close to the one observed in films produced directly from the starting material on a cold substrate (4°C).

The changes in the transport related to the deposition on cold substrate can be quite consistently explained if we assume that nanocrystalline (50 nm typical dimensions) inclusions with different concentrations are formed in the a-Se matrix during the evaporation. The concentration of such inclusions is several orders of magnitude higher in films produced at lower substrate temperatures and the trapping at the interface between the crystalline and the amorphous phases modifies the charge transport in the films.

The above explanation however is speculative and does not rule out other possibilities until carefully re-examined.

The lack of fundamental understanding of the a-Se structure and the exact nature of the deep carrier traps in a-Se films makes it particularly difficult to formulate an exact physical model that can explain all experimental observations related to to cold deposition of a-Se.

On the positive side, the finding that films produced on cold substrates can have deep trap limited hole transport and good electron transport has a significant technological impact. This finding enabled us to produce n- like s from almost any Se:As material by simply changing the substrate temperature during the deposition. The method avoids the necessity of alkali doping and all complications related to the latter. For further details see subsection 5.4.

5.3 Dark Currents in Single Layer Metal/a-Se/Metal Samples

5.3.1 Introduction

Dark currents in a-Se have not been well studied and fully understood. This is partly due to the fact that a-Se was mostly studied under the free surface geometry used in xerography [130]. It is quite strange that the use of this material as a photoconductor in medical x-ray image detectors over the last 20 years has produced very little work on the dark currents in metal/a-Se/metal devices.

Most of the published works in sixties and seventies are related to studies of space-charge-limited currents (SCLC) in a-Se as a tool obtain information about different properties of the material [144,145, 146]. In several cases the I-V curves were found to be proportional to $\exp\left(V^{\frac{1}{2}}\right)$ which suggest that the currents were limited by Schotky or Poole-Frenkel mechanisms [148]. The authors of [141, 142] claim that the contact Au/a-Se is ohmic and that the interface between Al/Al_2O_3 and a-Se (Se with 3-10% As) possess rectifying properties.

Careful study of these initial works reveals several interesting issues. First, most of the authors have mentioned that they have measured the steady state current in their samples, or that they have waited long enough for the current to stabilize. This suggests that the measurements are complicated due to the presence of non-steady state (transient) currents although that the authors have not mentioned them explicitly. Second, in many of the works, the presence of contact “formation” process is described [141, 142, 145]. By contact “formation” the authors mean that application of high electric field for the first time, or annealing at temperature around 50 °C lead to permanent changes in the metal/a-Se contact properties. In some cases the changes lead to the appearance of an ohmic region in the I-V curves at low voltages [145] and, in other cases, to the formation of a rectifying device [141, 142]. Third, in [146] the authors have observed that films produced in one and the same run of the vacuum coater can have dark currents that can differ more than two orders of magnitude which suggests that the surface of the Se films has very important role for the properties of metal/a-Se/metal samples.

In 1998 Johanson and coworkers [14] have investigated contacts between many metals and a-Se films. The existence of long transients after the application of the bias across the a-Se film has been acknowledged for the first time in this work. The authors do not observe any correlation between the dark currents through the samples and the work function of the metal and have concluded that the current is controlled by complex details of the metal to a-Se junction. The authors did not found presence of significant amounts of space charge using TOF measurements and concluded that the dark currents in a-Se are not space charge limited currents (at least according to the definition of space charge limited currents used in [14]) over the time scale of their experiments. The study however is not a complete one, because the experiments were limited only to the top surface of the a-Se films produced in industrial coaters on standard glass/ITO substrates. Obviously the bottom interface of a-Se films can not be studied under such experimental conditions.

The lack of sufficient experimental data on the dark currents in metal/a-Se/metal devices and the importance of the problem have motivated us to collect experimental data on the subject. The purpose of this subsection is to describe the main experimental results from that study.

5.3.2 Dark Currents in Symmetrical Metal/a-Se/Metal Devices

The term symmetrical meta/a-Se/metal devices imply that these devices were produced to be as symmetrical as possible. The evaporation conditions were selected to have as little fractionation as possible and both bottom and top contacts were produced from the same metal. The produced samples can be divided in three main groups:samples produced from pure Se, sample produced from Se:As no Cl alloys, and samples produced from Se:As:Cl alloys. The measured dark currents demonstrate complicated behavior as can be seen in Figure 5.23 Figure 5.24 and Figure 5.25.

In all cases the current decayed over the time after the bias was applied to the sample. In some cases the decay was greater than 2-3 orders of magnitude. For certain applied voltages and certain samples, the dark current demonstrates a tendency towards reaching a steady state or quasi-steady state but for the vast majority of the measured the I-t curves represent a decay with time for the whole duration of the measurement. The shape of the I-t curve depends on the material and on the applied bias across the sample. In contrast to our expectations, the I-t and I-V curves are not fully symmetrical with respect to the polarity of the applied bias even when the samples are produced from pure Se, that is no inhomogeneity due to the fractionation exists.

The I-V curves have two regions: low field one and high field one which is in good agreement with the data in [14] and in [146]. For both regions the current is a power law function of the applied bias

$$I \propto V^n \quad , \tag{5.9}$$

where n is a constant. As can be seen from figures Figure 5.23-Figure 5.25 the values of n for the low field region are in the range 1.1-1.9 while for the high field region n takes values in the interval 3.1-4.4. These values are somewhat different from those published in previous works [14, 146] which is not unexpected because the sample thickness is quite different, the Se alloys are different, and electrodes are different.

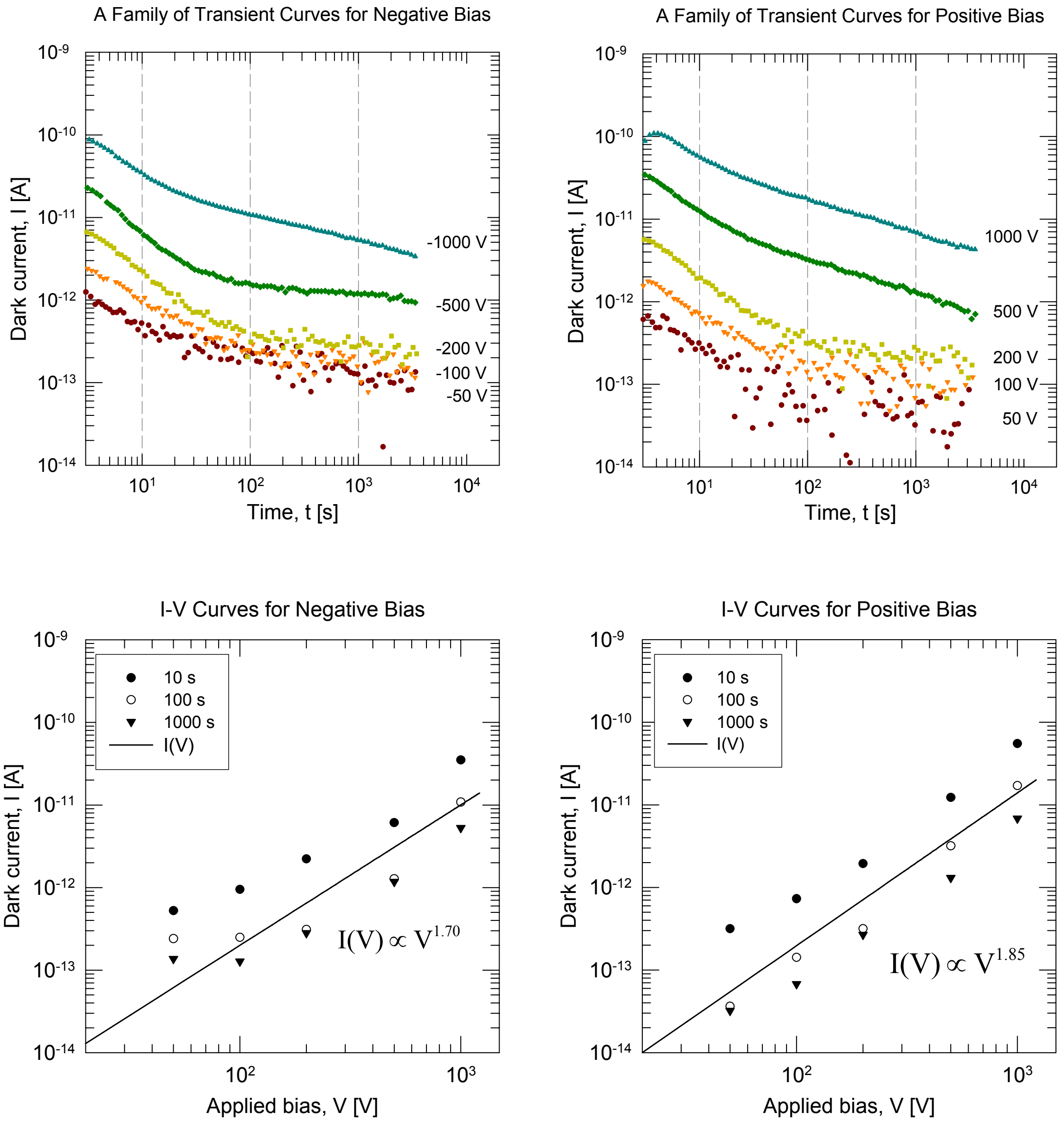

Figure 5.23 Dark current I-t and I-V curves for a-Se film produced at 70 °C substrate temperature from photoreceptor grade pure (99.999%) selenium material. The sample has a thickness of 105 µm and both bottom and top contacts are made from gold. Hole lifetime is about 2 µs and the electron lifetime is in the range 250 µs.

The authors of [14], based on their data, have explained the decay in the dark current curves with a gradual decrease of the electric field close to the electrode/s due to small amounts of trapped charge, undetectable with TOF measurements.

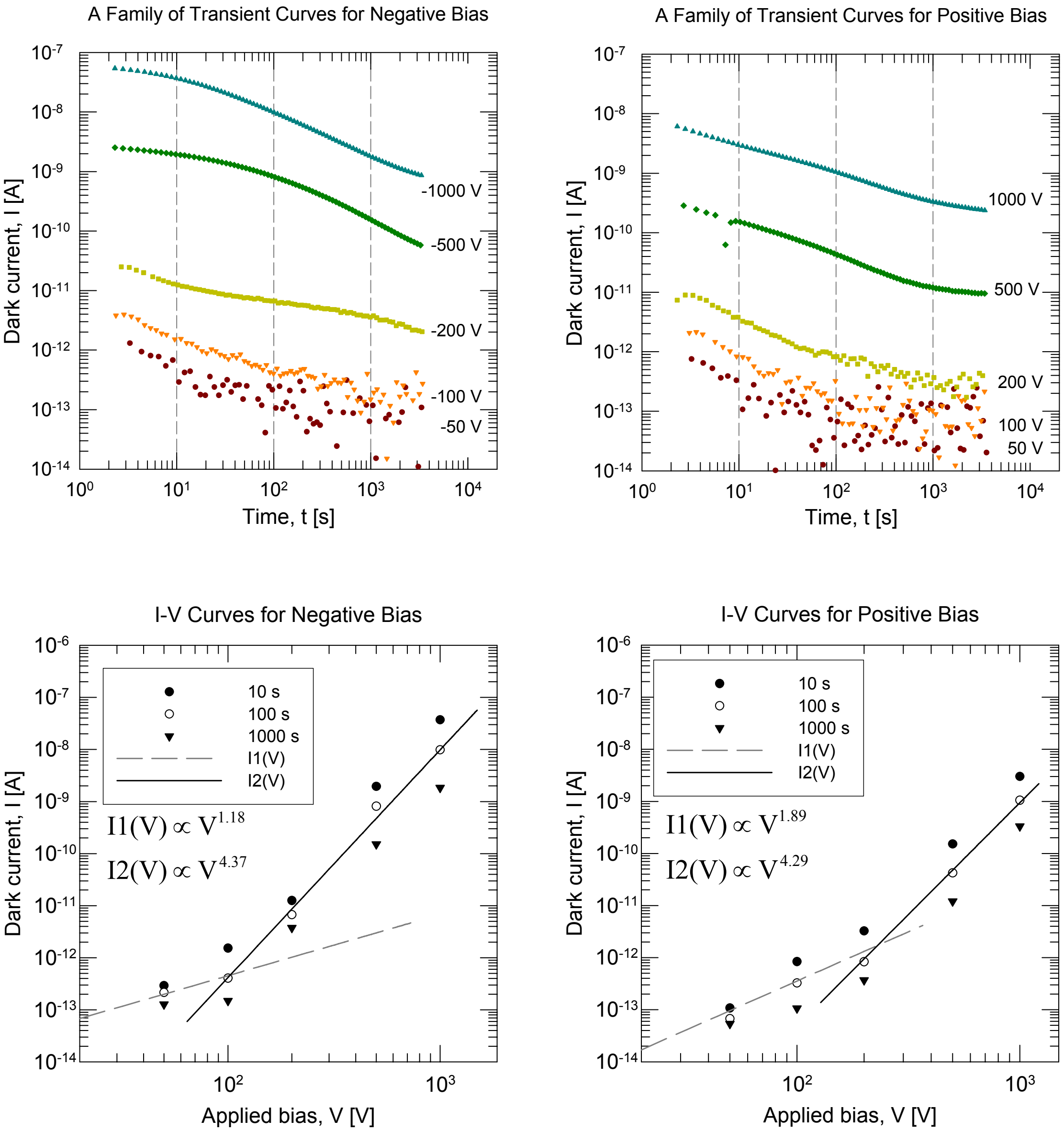

Figure 5.24 Dark current I-t and I-V curves for a-Se film produced at 70 °C substrate temperature from Se/0.3%As no Cl alloy. The sample has a thickness of 130 μm and both bottom and top contacts are made from gold. Hole lifetime is about 15 μs and the electron lifetime is in the range 400 μs.

Our data suggest that the conclusion that the dark currents in a-Se being not space charge limited might be premature. In the I-V characteristics we observe a low field superlinear region ($I \propto V^n, 1 < n < 2$) and a high field region in which the exponent n is bigger than two ($I \propto V^n,\ n > 2$). For thin samples and low applied voltages, an ohmic region ($I \propto V$) has been reported by several researchers. At very high fields, and hence high injection rate at the electrodes, the observed dark currents will most probably follow the usual relation for space

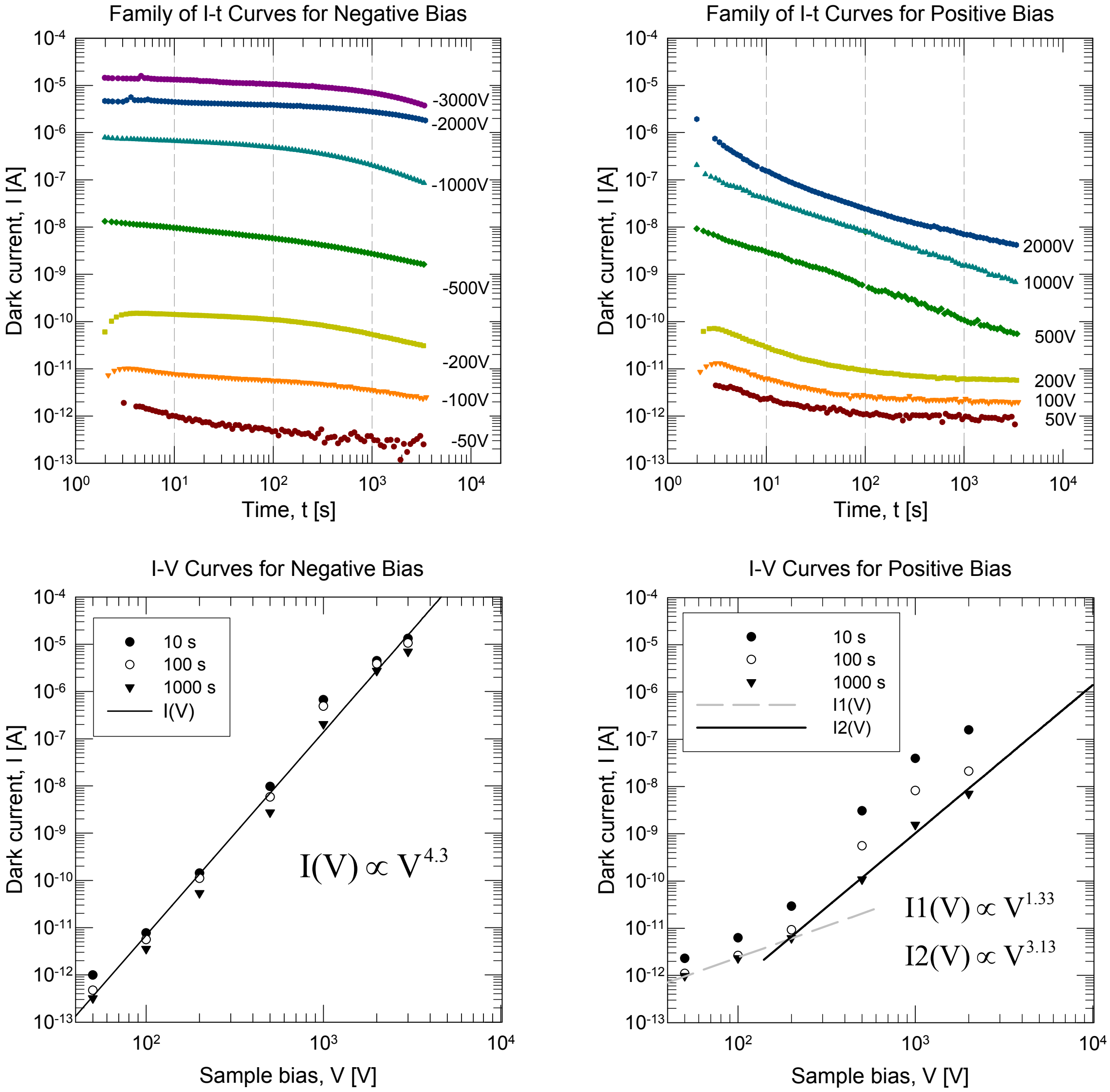

Figure 5.25 Dark current I-t and I-V curves for a-Se film produced at 70 °C substrate temperature from Se:0.5%As:10ppmCl alloy. The sample has a thickness of 114 μm and both bottom and top contacts are made from gold. Measured hole lifetime is about 100 μs and the electron lifetime is in the range 350 μs.

charge limited currents ($I \propto V^2$). Thus the I-V curve measured for the dark currents over wide range of applied voltages will most probably contain all the four regions described above. Similar I-V curves have been proven to exist theoretically and experimentally for insulators having two different sets of traps distributed in energy [147]. For the latter distribution of traps and single carrier conduction, the application of the regional approximation theory leads to I-V curves that can contain four regions with different values of the exponent for increasing applied voltage across the sample (n=1, 1<n<2, n>2 and n=2). In a-Se, the conduction is not of single carrier type (both electrons and holes can move). The situation is further complicated by the fact that exact distribution of traps is unknown for both electrons and holes. However, the ideas behind the regional approximation analysis should still be applicable and, as it will be described in subsection 5.3.7, there is evidence that significant space charge regions do form in metal/a-Se/metal devices left under bias.

Films produced from pure Se (Figure 5.23) have lower dark currents than films produced from stabilized Se (Figure 5.24 and Figure 5.25). This is expected because As and Cl are known to produce states in the band gap of Se. Thermal generation of carriers associated with the band gap states is one of the reasons for the above observation. The second reason is that the electron and hole transport in layers produced from stabilized Se is better that the one in the films produced from pure Se. If electron and hole transport is similar in films produced from Se:As and Se:As:Cl alloys, then the films produced from the alloys that contain Cl typically demonstrate higher dark currents.

The most unexpected observation associated with the data presented in Figure 5.23-Figure 5.25 is that the dark currents are not symmetrical with respect to the polarity of the applied bias. The currents when the top electrode is positive with respect to the bottom (substrate) electrode seem to be a little higher compared to the case when the top electrode is negatively biased in the films produced from pure Se (Figure 5.23). Films produced from Se:As or Se:As:Cl (Figure 5.24 and Figure 5.25), on other hand, exhibit exactly the opposite behavior and the negatively biased top electrodes produce higher dark currents. Since all electrodes, are produced from Au, this asymmetry suggests that Se films are not homogeneous across their thickness and/or that the top and the bottom surface of the films do not have the same properties. Consequently, the charge injection from the top and bottom contacts must be different and this must have added to different trapping profiles across the film thickness to produce the observed asymmetry in the dark currents for negatively and positively biased samples (see Figure 5.26). The authors of [29] have shown that the concentration of deep hole and electron traps can be up to several orders of magnitude higher near the bottom and top surface of the film than in the bulk of the film. The exact trap concentration profile depends on the material and on the substrate temperature during the deposition of the Se film and strictly it is almost never fully symmetric (Figure 5.26-a). Further the investigation in [132] and in [143] have shown that in many cases a continuous polycrystalline Se sub-layer forms between the substrate and the a-Se film (Figure 5.26-b and Figure 5.26-c). Arsenic and Cl additives, together with the oxygen impurities and the

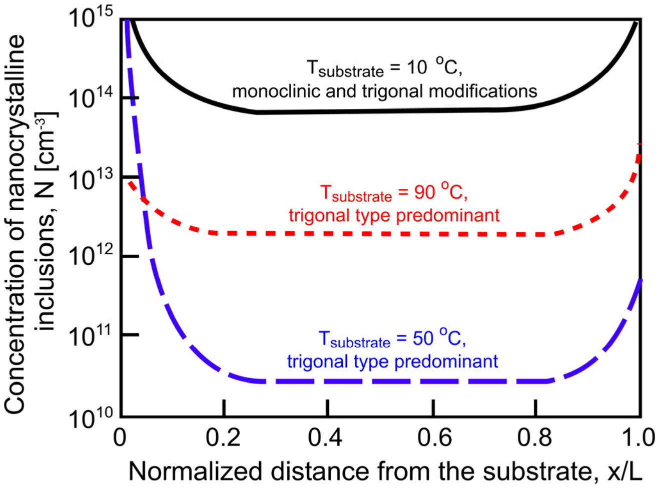

a) Distribution of nanocrystalline inclusions across the thickness of a-Se films for several different substrate temperatures. Data were taken from [29].

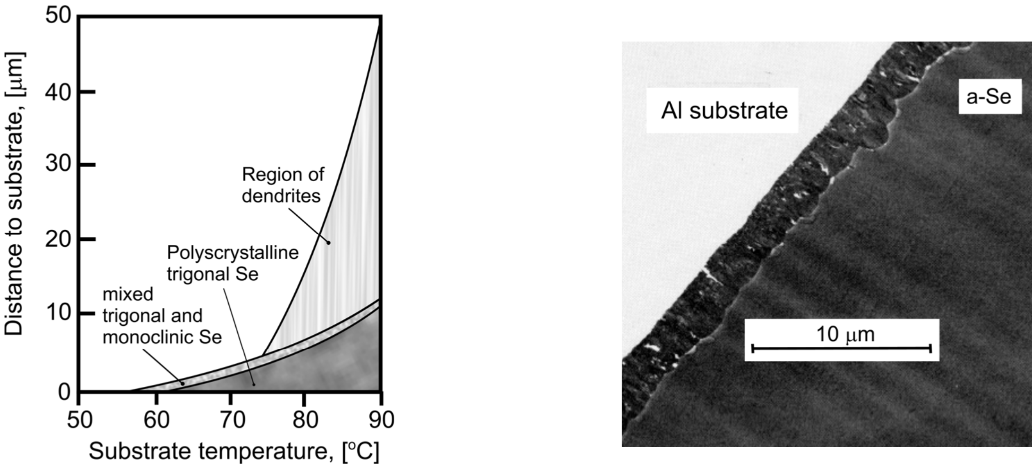

b) Distribution of the crystalline phase near the substrate in thick vacuum evaporated a-Se films as a function of substrate temperature. After from [143].

c) A transmission electron microscopy cross section of high purity a-Se film deposited on Al substrate kept at 80 °C during the evaporation of the film. The photo is taken from [132].

Figure 5.26 Factors that can potentially contribute to the observed asymmetry in the dark current I-t and I-V curves with respect to the polarity of the applied bias.

substrate temperature during the deposition of the film play a significant role in altering the nucleation rate and thus in the formation of microcrystalline sub-layer between the substrate and the bulk a-Se film. As the substrate temperature is increased above 60 °C the density of the microcrystalline inclusions at the substrate interface increases. When the substrate temperature is 70 °C or higher, the microcrystalline sub-layer becomes continuous (Figure 5.26-b and Figure 5.26-c). The charge injection from the metal electrode into such a microcrystalline layer and then into bulk a-Se will obviously be different compared to the injection from the top metal electrode directly into the a-Se film. Such difference can easily contribute to the observed asymmetry in the dark currents. When the top electrode is negatively biased, theenhanced hole injection from the metal contact into the sub-layer of microcrystalline Se is probably one of the reasons for the observed higher dark currents compared to the case when the top electrode is positively biased (Figure 5.25). This, by the way, is one of the probable reasons for which the free surface of Se can only very rarely be charged to high negative potentials in the case of a-Se photoconductor layers for xerographic applications.

In conclusion, we have to mention that it is possible to produce samples that have higher dark currents in cases when the top contact is positively biased. A way to achieve this for a-Se:As without Cl is to deposit the films on a substrate kept at a temperature of 50 °C or lower from Se:As no Cl alloys. Under such conditions the continuous microcrystalline sub-layer does not form. The distribution of deep carrier traps across the sample thickness also changes significantly which results in higher currents for positively biased top electrodes. One example is shown Figure 5.27. The dark currents in that sample are higher for positive bias. Such asymmetry is probably due to the reasons explained above and not to the fact that this particular sample has top and bottom electrodes produced from different metals. If the electrodes were the same only the relative magnitude of the asymmetry will be affected.

5.3.3 Experimental Observation of Contact “Formation” Process

As described in subsection 5.3.3 several authors have observed in their experiments changes in the properties of the electrical contacts to a-Se films involved in their studies. The changes were associated with application of sufficiently high electric fields across the sample for a time interval of sufficient length [145] or with thermal annealing of the samples for 1 hour at 50 °C [141, 142]. The first treatment of the sample leads to significant changes in the electrical properties of the contact, following which the properties of the contacts are stable in time.

In our dark current experiments we observe similar behavior for the cases of some metallic contacts to Se. One example is presented in Figure 5.27 below. The transient curves in the figure are numbered in the order of which they are measured. After the recording of each transient the sample is rested under short circuit conditions for a period of 2 hours during the first set of measurements and of 4 hours during the second set of measurements. Direct comparison between I-t curves #1 and #13 for negative bias (top contact is negative) and transient curves #5 and #9 for positive bias across the sample demonstrates the effect of the contact "formation" process. As demonstrated in Figure 5.27, the contact formation process affects the low field region of the I-V characteristics of the samples. The asymmetry in the conduction process for positive and negative bias becomes stronger and (thin samples up to 15 μm) with high content of As (3%-10%) can have rectification properties as strong as 10^6 for low applied voltages [141]. We have typically worked with much thicker samples produced from alloys containing up to 0.7% As. This makes the measurement in the low field region difficult but we observe asymmetry in the conduction for positive and negative bias that can be different

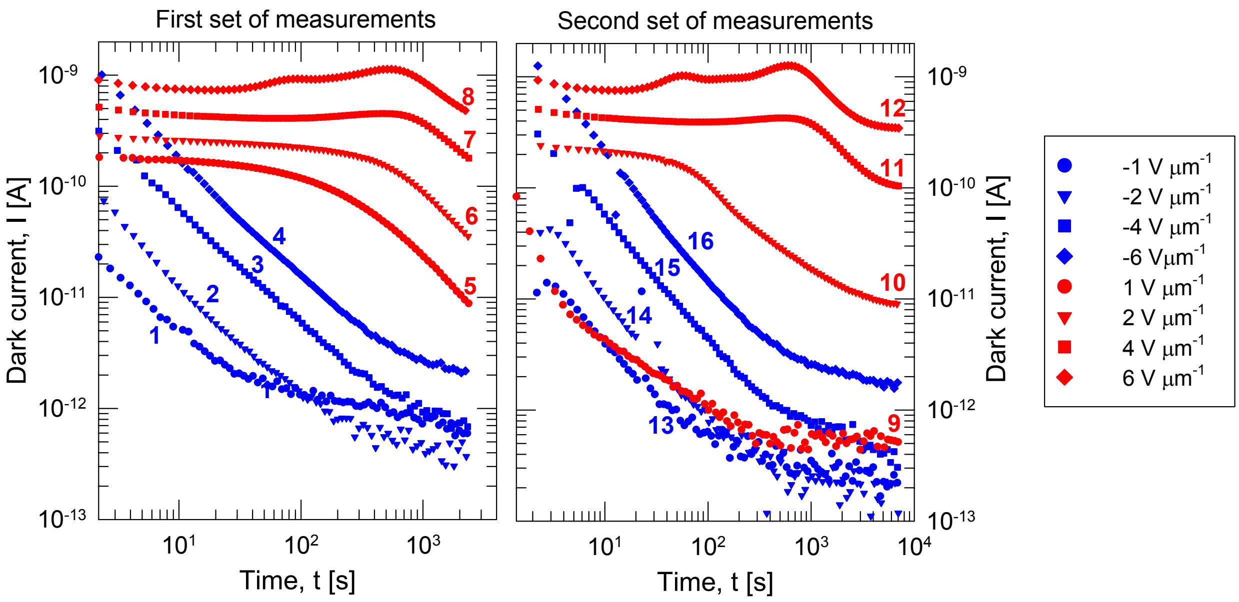

Figure 5.27 An example for contact "formation" process under the influence of high electric fields applied for a sufficient time across the sample. The results of the contact formation process are easily seen if we compare transient curve #1 with transient curve #13 and I-t curve #5 with I-t curve #9. The number associated with each transient curve reflects the order in which the measurements were taken. Third and subsequent set of measurements resulted in I-t curves that are very similar to the ones obtained in the second set of measurements. The sample structure is glass/Al-a-Se-Au. The film thickness is 110 μm. The film was evaporated on a substrate kept at 60 °C from Se:0.2%As no Cl alloy. The asymmetry of the sample with respect to the polarity of the applied bias is not a result from the difference in the metal electrodes. The maxima in the I-t curves #7, #8, #11, and #12 are not an artifact of the measurement. The reason for their appearance will be explained in subsection 5.3.4.

by 2-3 orders of magnitude. The rectification properties are better expressed when a bottom Al contact is involved.

Very similar contact “formation” process can be observed if the sample is annealed under mild conditions (50°C for 1 hour). Our experiments show that the decrease in the conduction at low electric field is related mostly to changes at the bottom contact. Most probably processes of inter-diffusion and/or crystallization are taking place at the bottom interface of the samples (see Figure 5.26-b). In addition, the crystalline inclusions of monoclinic type are transformed to those of trigonal modification. All these changes are facilitated by the applied high electric field or by the elevated temperature during the annealing of the samples but the crystallization process is most probably responsible to greatest extent to the observed changes.

The described above formation process bares striking similarities with the technique used to fabricate standard polycrystalline Se rectifiers. The fabrication process of such devices begins with roughened Al plate which is coated with a layer of Bi on top of which the Se layer is placed. Cadmium top electrode is then applied and the whole structure is annealed to transform the Se into polycrystalline trigonal form. In this process, the diffusion of Bi into Se and of Cd into Se is very important. It is known that Bi cause Se to crystallize very quickly due to the difference in the size between Bi and Se atoms. In addition, at the top interface a thin layer of CdSe is formed and the actual diode is formed between the insulating CdSe thin n- like and the p-type Se polycrystals [149].

The process of contact “formation” in our films must have a very close origin to the processes that are taking place during the high temperature fabrication step in polycrystalline Se rectifier production technology. In any case, the formation of metal selenides, the crystallization of Se at the interface, and the formation of metal contacts to the Se crystalline inclusions present at the interface must be the most important factors that lead to the observed contact “formation” process in our films.

5.3.4 “Abnormal” Dark Current I-t Curves

The data that will be described below illustrates the extreme complexity of the dark currents in a-Se samples. The current that flows in any sample after application of a constant voltage is usually constant or monotonically decreasing in time. In the vast majority of cases, the dark currents in thick a-Se films are no exception of that behavior. However, as shown in Figure

5.28, there are cases in which the a-Se thick films demonstrate I-t curves that exhibit maximum in spite of the constant bias across the sample. Very often the films produced in our lab that have an Al bottom electrodes demonstrate I-t curves as the ones shown in the left graph of Figure 5.28. These I-t curves exhibit a maximum or maxima (Figure 5.27, transients #8 and #12) for certain applied voltages. The maxima in the curves shift towards shorter times after the application of the bias, as the applied voltage across the samples increases. At the same time, the I-t curves when the top electrode is negative are of the normal monotonically decreasing type. Such behavior in a-Se films to our knowledge has never been reported in the scientific literature before. Our initial understanding was that this strange behavior is related to the properties of the bottom electrode. It is known that Al is very reactive and the exposure to air almost immediately leads to the formation of Al_2O_3 on the surface of the Al electrode. The oxide layer formed in this way is highly disordered and the Al-Se interface would consist of Se, Al_2O_3, $Al_2(OH)_3$, and Al [141]. Obviously such an interface can have very complicated properties and it was thought this specific interface had the decisive role for the appearance of the "abnormal" I-t curves.

However, later we have recorded similar "abnormal" I-t curves on a foreword biased commercial a-Se based pin- like structure as shown in Figure 5.28. In this pin- like structure the n- like is grown on a glass/ITO substrate and thus the bottom electrode is ITO while the top one is made from Au. The "abnormal" I-t curves appear again only when the top electrode is positively biased, but this time the bottom contact interface is totally different.

Current transients displaying a peak whose time position depends on the applied voltage have been observed in many thin films produced from other materials. In the vast majority of the cases, the results have been interpreted on the basis of the theory of space-charge-limited currents, reference [150] being one recent example. The time position of the peaks in the I-t curves observed by us will lead to mobilities of the order $10^{-8} – 10^{-10}$ $cm^2V^{-1}s^{-1}$ if the space charge limited current theory [151] is applied to our experimental data. Such values are for example compatible with negative ions (O^{2-} or OH^-) moving through the sample. However, careful examination shows that the shape of the transients observed by us does not agree with the one described in [151] and that the currents do not scale appropriately with the square of the applied voltage, and thus no grounds exist for the interpretation of our results in terms of space charge limited currents.

It seems that in both cases presented in Figure 5.28 the appearance of the “abnormal” I-t curves is related to the presence of layers through which the electrons can move with difficulties. For the sample produced in our lab this is an Al_2O_3 layer while for the pin- like structure this is n- like , because as described in subsection 5.1.5 the electron mobility and lifetime in the n- like are much worse than the ones in the i- like . At the very beginning after the application of the bias the current through the sample is due to drifting holes injected from the positive top electrode (we are neglecting the thermal generation of carriers in the film). Let us assume that the applied bias is such that the centroid of the positive charge due to trapped holes is situated closer to the bottom surface of the film. As a result, the field near the top electrode decreases while near the bottom electrode it increases and the increase of the field near the bottom electrode is bigger in magnitude. This will lead to a decrease in the hole injection and generally to decrease in the current through the sample. This process will continue for sometime until the field at the back electrode increases to the point when the Al_2O_3 layer or the n- like will become permeable for some of the electrons. Some electrons will start moving in the sample and some of them will be trapped in the bulk of the film. Because the field between the bottom electrode and

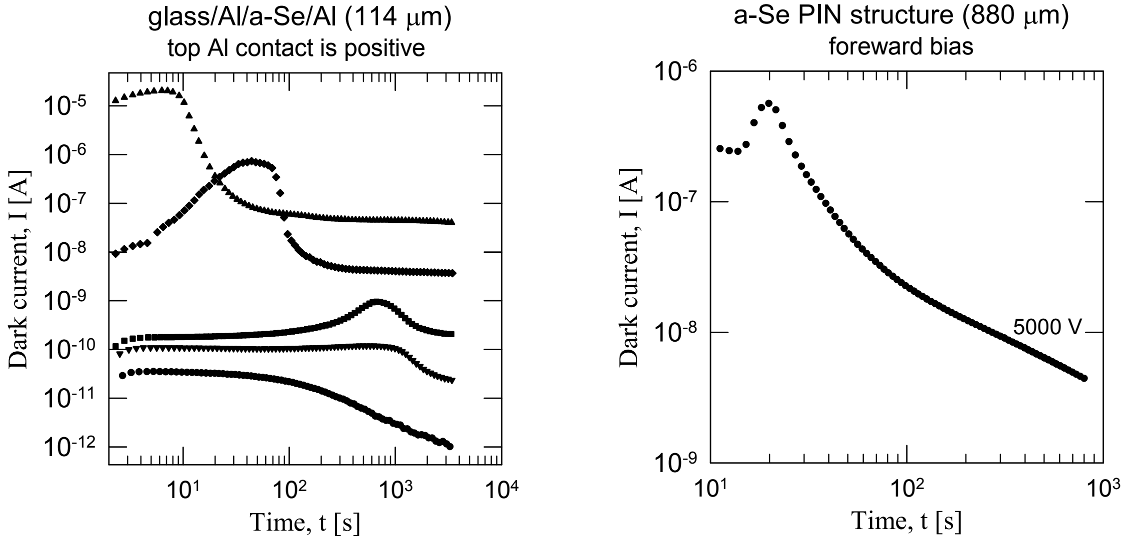

Figure 5.28 The dark current in the samples is intuitively expected to monotonically decrease with time after the application of a constant bias. In contrast to that some a-Se samples exhibit clear maximum in the I-t curves measured on them under certain conditions. Two “abnormal” I-t curves measured on single a-Se layer produced in our laboratory (Se:0.3%As no Cl, $T_{substrate}$ = 70 °C) and on commercially produced multilayer pin- like structure are shown above.

the centroid of the positive space charge due to trapped holes in the film is high it is more likely the portion of the trapped electrons to be bigger in the space between the centroid of the positive space charge and the top electrode of the sample than in the other part of the film. Thus the centroid of the space charge due to trapped electrons will be positioned somewhere in the region between the electrode and the centroid of the trapped holes. Under such conditions the negative space charge that is forming due to the trapped electrons will affect mostly the field near the top electrode leaving the field near the bottom one without significant changes. Thus the field at the top contact will increase due to the electrons trapped in the sample which will cause the hole injection also to increase. More holes will be trapped close to the bottom surface of the sample, the field at the bottom electrode will increase and thus the injection of electrons through the oxide layer or the n- like will increase. The trapped negative space charge will grow and the field at the top electrode will increase even further causing further increase of the hole injection. Thus a positive feed back is established and the current in the film starts to grow. This process does not continue indefinitely because as the amount of positive and negative, free and trapped charge in the sample increases some other processes become important. Two of them are the recombination of the drifting electrons with trapped holes and recombination of drifting holes with trapped electrons. As these processes become intensive the region of negative space charge near the positive top electrode and the region of positive space charge near the bottom negative electrode can not grow further. Thus the positive feed back is destroyed and the current in the sample will seize to grow. In selenium the electron traps are some what deeper than the hole traps, the average release times are different for holes and for electrons and a tendency exist more negative space charge to be accumulating in the sample as the time progresses. As the time flows the amount of trapped negative charge increases and will tend to spread more uniformly across the sample. The profile of the accumulated trapped charge in the film will gradually change and as the amount of the trapped charge in the sample increases the amount of the free charge that can be injected in the sample decreases because the total charge that can be accommodated in the sample is limited by its geometric capacitance. These processes limit the injection and force the current in the sample to decrease in time as in the usual dark current I-t curves measured on a-Se thick films (see subsection 5.3.2).

Note that the possible qualitative explanation presented above is valid also for the case when no layer with poor electron transport is present between the negative electrode and the a-Se film. The most significant difference is that the peak in the current will be observed at much shorter times which are inaccessible for our current experimental setup ($t > 3s$). Thus the function of the electron trapping layer is only to introduce delay before the electron current in the a-Se film become significant and thus to shift the peak in the current to longer times after the application of the bias that can be accessed with the measuring setup we are currently using.

Obviously a careful experimental verification for shorter times after the application of the bias is needed in order to arrive at more rigorous explanation of the nature of the observed "abnormal" dark current I-t curves. This is a nice direction for continuation of the experimental work but was beyond the scope of our research.

5.3.5 Time Needed for the Dark Current in a-Se Films to Reach Steady State

As discussed in the previous subsection, trapping in a-Se can play significant role in controlling the dark currents in thick films produced from that material. If that is the case the question arises on the length of time needed for the dark currents in a-Se films to reach steady state. The time needed for the dark currents in a-Se to stabilize should be related to the average release time of carriers from deep electron and hole traps in the material. Since the carrier concentration in the sample can reach steady state only for times that are basically longer than the release time for the deepest carrier traps. The discussion in subsection 2.2 has shown that in a-Se a significant amount of deep traps for both holes and electrons is present around the Fermi level. The deep hole traps are located 0.87 eV from the valence band edge, while the electron traps are located 1.22 eV below the conduction band edge (see Figure 2.5). Assuming that the traps are charged when empty their effective depth can appear somewhat lower due to Poole-Frenkel effect. Thus, for example the barrier height for the traps in a-Se will appear with 0.09 eV lower at an applied field of 10 V/μm. Even with this lowering the trap depth remains significant and thus leads to huge average release time especially for the trapped electrons. The average release times at room temperature (295 K) for trapped holes calculated with trap depth of 0.8 eV and 10^{12} s^{-1} for the attempt to escape frequency is ~48 s. The average release time for electrons under the same conditions and with a trap depth of 1.1 eV is about 6,427,302 s or ~1, 785 hours (about two months!).

Almost all dark current transients shown in the figures so far demonstrate that the dark currents in the samples are hardly steady state currents after one hour. Some curves give a hint that eventually a steady state or quasi-steady state is about to be reached. The latter motivated us to perform experiments in which we followed the current transients after the application of the voltage step for extremely long times from experimental point of view (as long as 100,000s).

Typical results are shown in Figure 5.29. For the particular sample in the figure 7200s are not enough for the current to reach even quasi-steady state under a negative bias of approximately 10 V/μm (top electrode negative). For a positive bias of 10 V/μm and times of the order of 20,000 s, the dark current seems to stabilize. However, this state lasts for 10,000-20,000 s and then the current starts to change again; this time it increases. That might be the beginning of the behavior we have described in the previous subsection that will cause a peak to appear in the dark current. Another possibility is that the field due to trapped charge in the sample becomes to high and leakage current cause the rise in the curve. The exact reason for such a behavior is unknown; however the fact is that the dark currents in a-Se are not strictly constant for even impractically long times after the application of the bias.

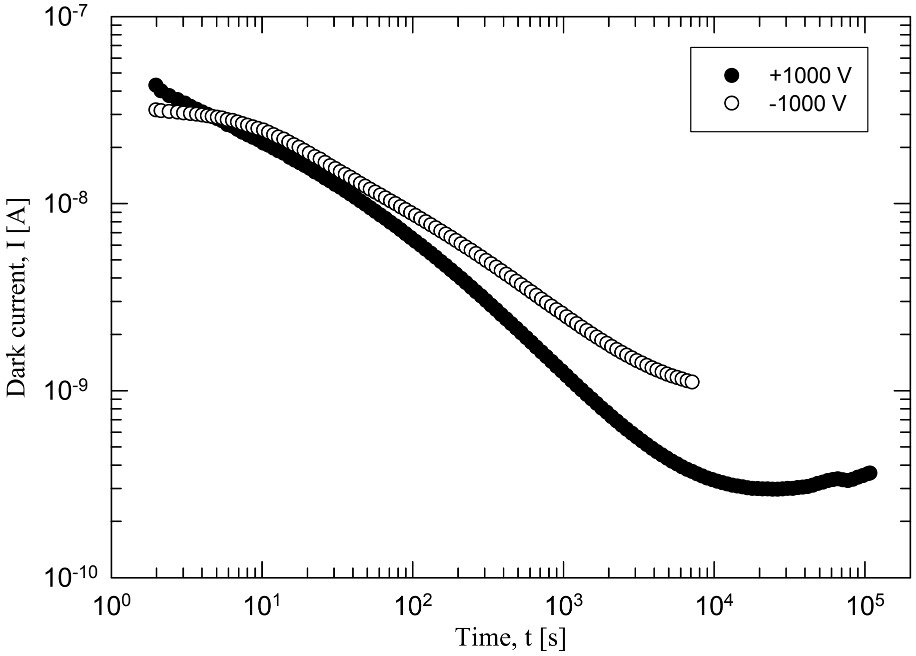

Figure 5.29 I-t dark current curves recorded on 105 mm thick a-Se film with Au top and bottom contacts. The currents were followed for time of up to 28 hours after the application of the bias. The film was produced from Se:0.5%As no Cl on substrate kept at 70 °C. It is difficult to say that for that time the dark current has reached steady state.

We have also found a very similar behavior for the photoinduced currents in a-Se films under constant bias when one of the contacts is under a steady illumination with blue light. The fact that the currents in a-Se films are complicated by such long transients makes the application of some typical DC conductivity experimental techniques to a-Se very difficult. Most of these techniques require the steady state DC current to be measured.

5.3.6 Reproducibility of the Dark Current I-t Curves in a-Se Films

In the previous subsection we have discussed some data that give us an idea on how long it will take for the dark current in a-Se device to reach its steady state. The waiting time has been proven to be long for almost all cases of practical importance. This means that an experimentalist is forced to work with slowly time-varying dark currents. In many experiments it is necessary to make corrections for the dark current. Such experiments can be related to measuring the x-ray sensitivity of a-Se devices, the actual imaging with some detectors, correction for the dark current in post transit time-of-flight experiments, etc. The question that arises in relation to such situations is how reproducible the dark in a-Se devices are. The change in the dark current with time in a-Se films after the application of the bias indicates that the electronic state of the sample is changing. There are number of experiments in which it is important to make sure that the sample has been restored to its original state before the next measurement can begin. A factor of importance for such experiments is what resting period will ensure that the sample has been restored to its initial state. Both of these questions have not been properly addressed in the scientific literature. The only criterion found is due to Johanson et al. [14]. The approach adopted in that work is that the sample has to be rested for a period of time that is at least twice as long as the period for which the sample has been kept under bias. Since we have used this approach in part of our measurements it will be interesting to know how well this criterion works.

The following experiments have been designed to partially give an answer to the questions described above. We have recorded the dark current in the samples after the application of a high enough electric field. Each I-t curve was followed for 1200 s. The samples were rested prior to the next measurement for a period of time that was 2400 s or longer and thus the criterion described in [14] was met. After the rest period, the same field was applied to the sample and the dark current was followed for another 1200 s. Several I-t curves collected in this way were compared to get an idea of how reproducible is the dark current under such conditions.

A set of typical results from such experiments is shown in Figure 5.30. Two things are almost immediately evident. For negative bias (Figure 5.30-a), a rest period of 2400 s seem to be sufficiently long to roughly restore the sample to its initial state. The graph shows that the I-t curves overlap quite well and no particular relation can be bound to the order in which the measurements were taken. The reproducibility seems to be good. The curves coincide to within ±20% - ±30% and that is the best reproducibility for the dark currents that can be achieved by simply resting the samples.

However the reversal of the polarity of the sample bias changes the reproducibility of the dark currents significantly as illustrated in Figure 5.30-b. In each subsequent measurement the dark current I-t curve systematically sinks towards lower currents and that is not affected significantly by the duration of the rest period before the measurement. Although the change is systematic, the average reproducibility of the dark current I-t curves 1000 s after the application of the bias remains about ±20%. For shorter times the reproducibility can be as much as a factor of 2 worse.

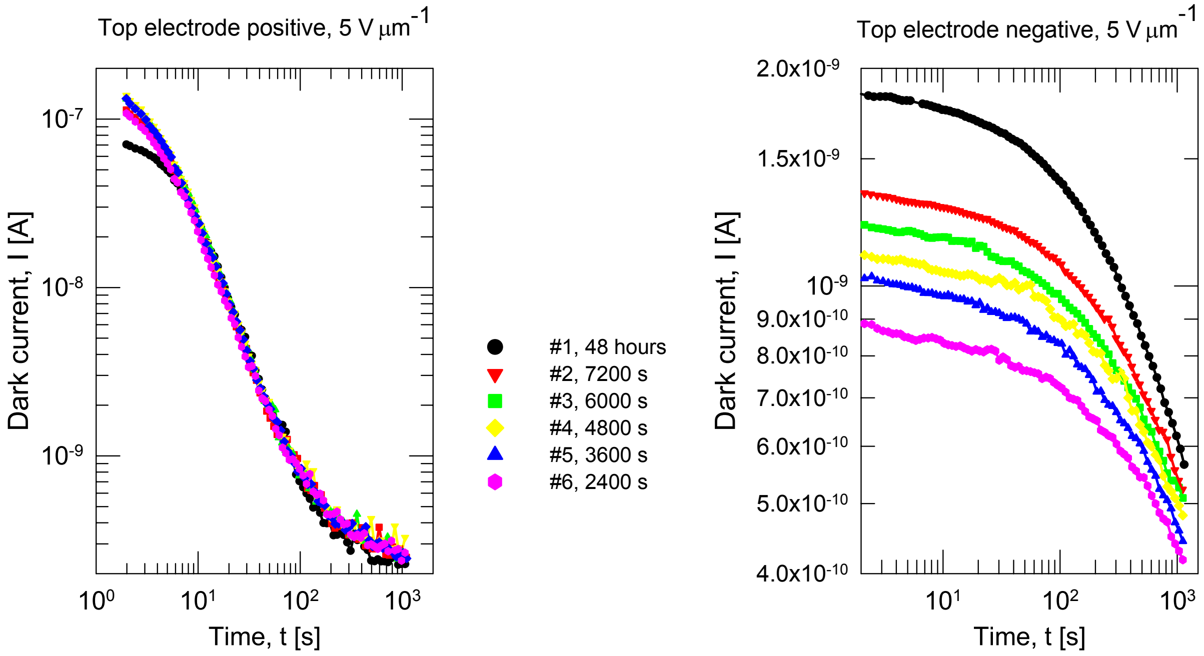

Figure 5.30 Reproducibility of the dark current I-t curves in a-Se film recorded in subsequent measurements after different rest periods. During the rest period the sample was kept under short circuit conditions and in dark. The sample was evaporated on polished Al substrate kept at 70 °C from Se:0.5%As:10ppm Cl material. The film thickness is 100 μm and the top contact is sputtered Pt with area of 0.25 cm^2. The data illustrate that after a reasonable in duration rest periods the dark current is reproducible to within ±20 % at best. This fact makes the corrections for the dark current in a-Se films that are required in many experiments an extremely complicated task.

The most probable explanation for such behavior is based on deep trapping of electrons in the a-Se film and/or in the case of Figure 5.30 in the Al_2O_3 layer that is present between the bottom electrode and the film. The release time of the trapped electrons in a-Se as explained in subsection 5.3.5 can be very long compared with the rest period involved in these measurements (max 7200 s). The difference for negative and positive bias is probably due to the fact that the sample is not symmetrical; presence of a thin insulating oxide layer at the bottom electrode, a nonuniform distribution of traps across the thickness of the a-Se film, etc. The speculative explanation presented so far does not rule out other possibilities.

The most important practical implication of this result is that the correction for the dark current becomes quite a complicated task, and that the precision with which such correction can be applied is unsatisfactory for many cases; not better than ±20 % if only resting of the sample in dark is used to restore the sample to its original state.

5.3.7 Experimental Evidence for Formation and Relaxation of Regions of Immobile Charge in Single Layer a-Se Films Left under Bias

As explained earlier in subsections 5.3.2-5.3.6 the dark currents in a-Se are very complicated and not fully understood. After the application of a voltage step to a metal/a-Se/metal structure, the dark current is not constant but changes with time. In many cases we observe that the dark current decreases monotonically with time over several orders of magnitude as reported in [14, 163]. A quasi steady state current is reached in some of the samples after 10-30 minutes but in other samples many hours are needed to a reach similar quasi steady state. The magnitude of the dark current and its temporal behavior depend on the a-Se material, on the preparation conditions, on the metal from which the electrodes are produced, on the sample history (irradiation with x-rays or visible light, application of bias etc) on the polarity of the applied bias. The fact that there are so many different factors that can alter the dark current in a-Se shows that there are probably several different processes that are controlling the dark current in a-Se and the latter makes a simple explanation impossible.

Amorphous Se is a semiconductor with a relatively wide bandgap (~2.2 eV) and as shown in subsection 2.2, various localized states that can act as electron and hole traps are located in the bandgap. At room temperature and in dark, the electronic properties of the material should be very close to those of an insulator with defects. It has been known for more than one century that the dark currents in insulators with defects have temporal behavior similar to those we observe in a-Se. The temporal behavior has been related to the presence of defects in the band gap of the insulator and it was found that two empirical laws in many cases correctly describe the temporal behavior of the dark currents in such systems. These are the Curie – von Schweidler Law and the Kolrausch-Wiliams-Wats Law

$$I(t) = I(\infty) + I_0 t^{-n}, \quad 0 < n < 2 \qquad \textbf{Curie – von Schweidler Law}$$

$$I(t) = I_0 \exp\left(-\left(\frac{t}{\tau}\right)^{\beta}\right) + I(\infty), \qquad \textbf{Kolrausch-Wiliams-Wats (KWW) Law} \tag{5.10}$$

where I(∞), I_0, n, τ, and β are suitable constants that enable the equations to best describe the data.

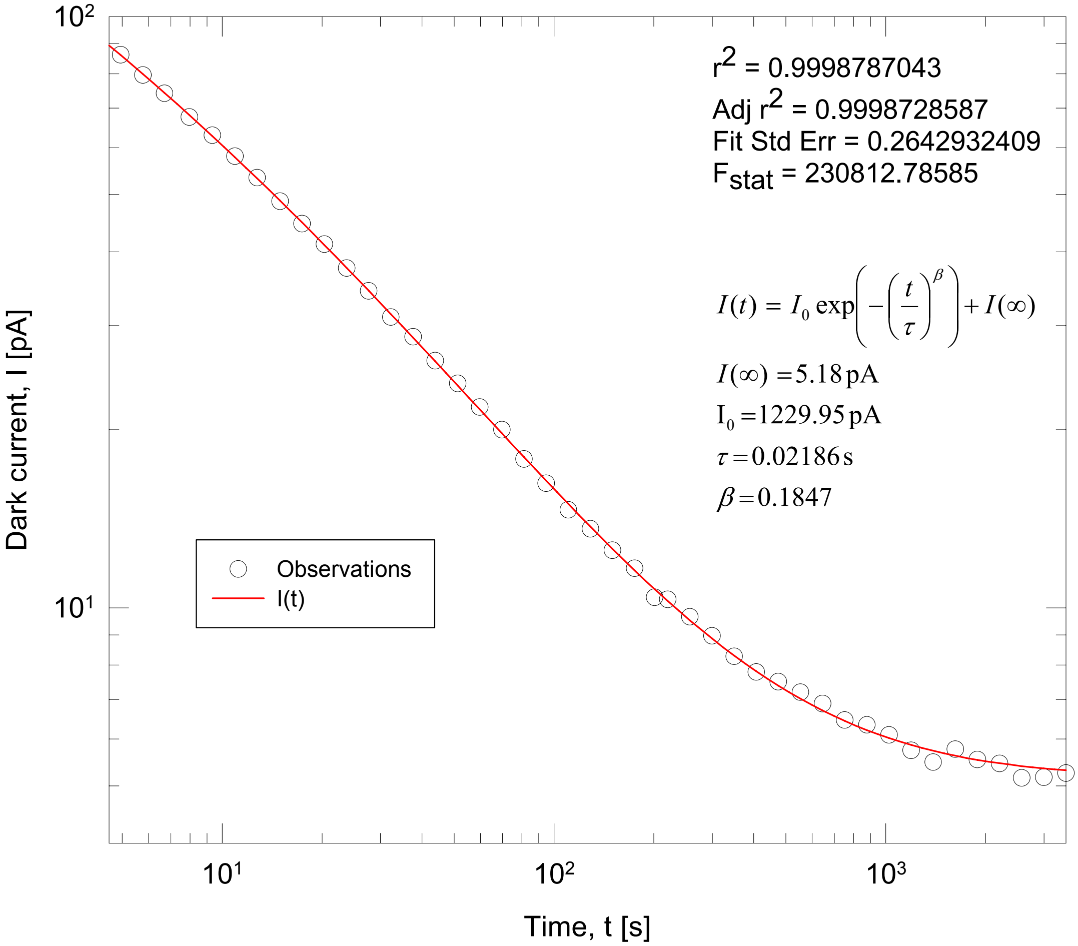

Figure 5.31 A fit of KWW law to experimentally measured dark current transient curve in a-Se thick film with thickness 90 μm. The film was deposited Se:0.5%As:10ppm Cl alloy on substrate kept at 70 °C. The sample has Pt bottom electrode and Au top electrode. The applied voltage was 200 V. The Au electrode was positively biased.

Figure 5.31 and Figure 5.32 illustrate that these two emperical relations can be fitted really well to some of the experimentally recorded transient I-t curves in a-Se films.

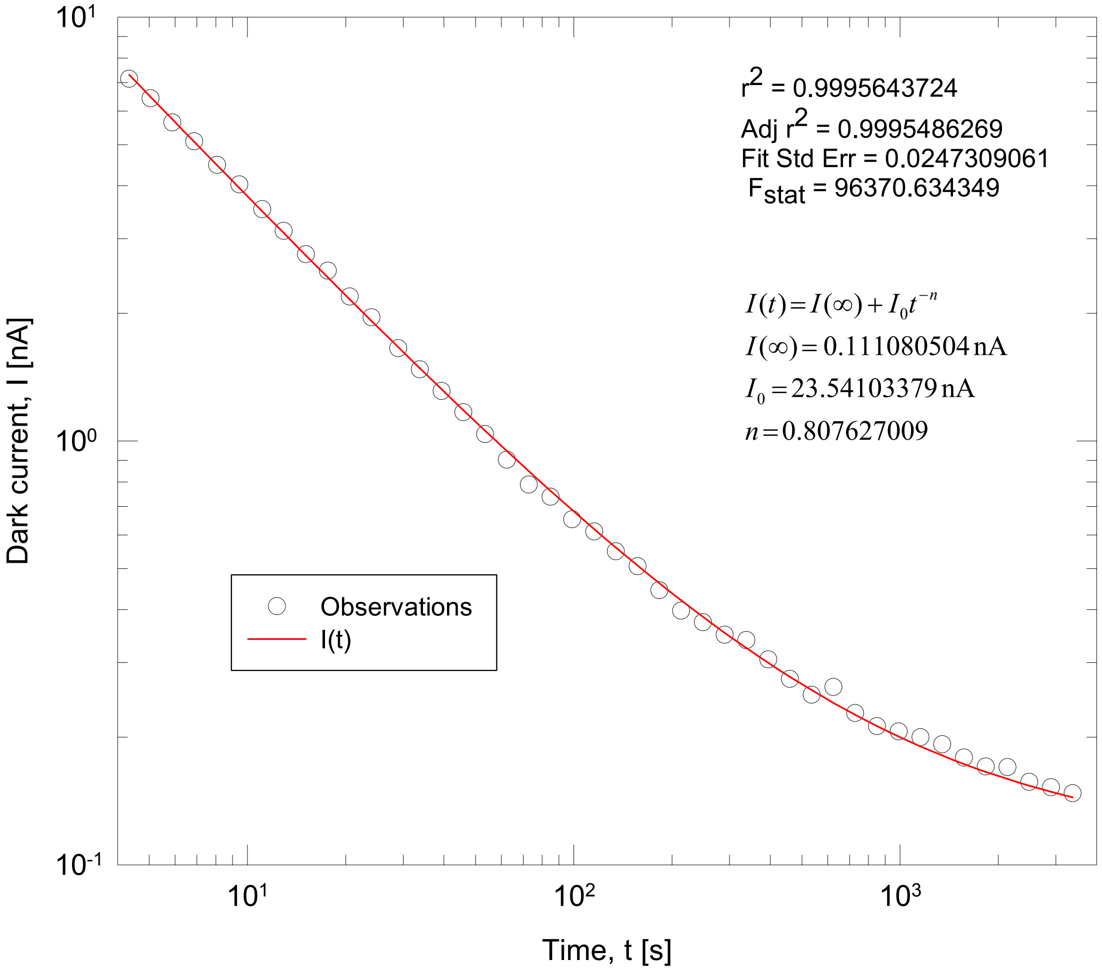

Figure 5.32 A fit of Curie's law to experimentally measured dark current transient curve in a-Se thick film with thickness 70 μm. The film was deposited Se:0.5%As:10ppm Cl alloy on substrate kept at 70 °C. The sample has Au top and bottom electrodes. The applied voltage was 500 V. The top electrode was positively biased.

The possible mechanisms for the occurrence of a temporal behavior of the type described by Eq. (5.10) in a wide range of different materials have already been discussed in the scientific literature. There are numerous mechanisms that can lead to the manifestation of the equations (5.10). In many cases, these mechanisms are of totally different physical nature. For example, the most popular mechanisms for the appearance of Curie – von Schweidler behavior in various materials are:

a. Distribution of relaxation times [152]
b. Distribution of hoping probabilities [100]
c. Space charge due to trapping [153, 154]
d. Maxwell-Wagner relaxation [155]
e. Energetically inequivalent, self-similar multi-well potentials [156].

From the above list the second and the third mechanisms seem to be of particular relevance to a-Se. Formation of space charge region or regions due to carrier trapping is a highly likely mechanism that may be responsible for the temporal behavior of the dark currents in a-Se films. Quantitative explanation of many effects related to the dark currents observed in a-Se have been qualitatively explained in [14] on the basis of the modification of the internal electric field in the sample especially in the regions near the electrodes. The authors of that work did not report any evidence for a considerable amount of trapped charge in their samples.

If the trapped charge in the films is a key factor for the observed dark current temporal behavior in metal/a-Se/metal devices, one should be able to design an experiment through which the space charge in a-Se will reveal its existence. In this subsection we are presenting experimental evidence for the formation of regions of space charge in a-Se films left under bias that significantly alter the electronic state of the samples in particular the internal electric field in the films.

The idea for the first set of experiments that provide some evidence for the existence of significant amounts of space charge in a-Se films left under bias was taken from reference [154]. The authors of the latter work have proven that development of space charge regions due to immobile carriers in defect insulators can lead to the manifestation of Curie-von Schweidler Law (see Figure 5.32) and force the appearance of different "memory" effects related to the current flow in thin film samples when the applied bias changes in a step-wise manner.

We have studied the changes in the current in an a-Se sample as a result of changes in the applied bias that occur step-wise. Figure 5.33 presents the most commonly observed results from such studies. Before discussing the results we would like to remind the reader that we can get reliable readings from the electrometer only 2-3 s after the bias has been changed. Thus the currents that we observe reflect the real behavior of the sample. They are not related to the

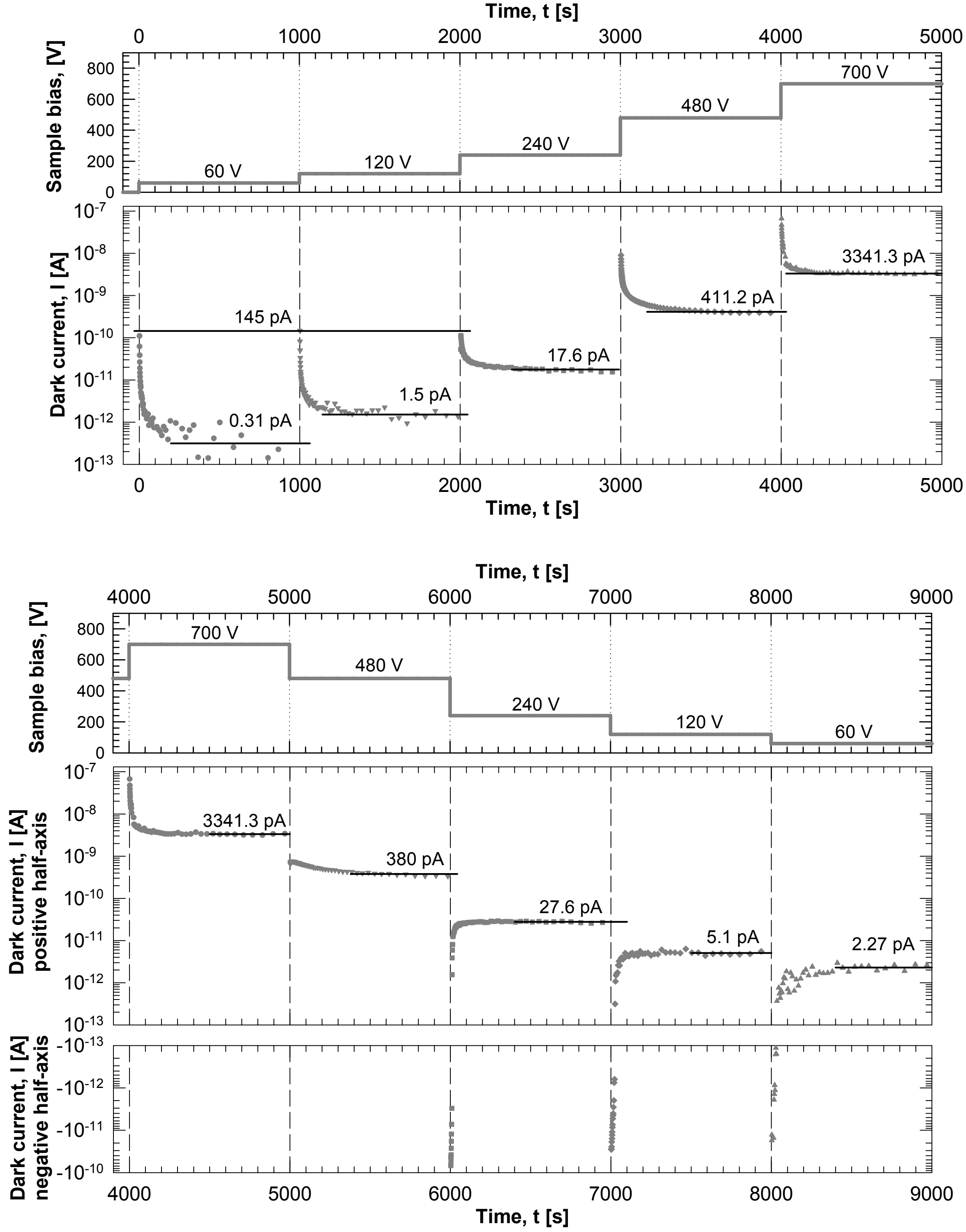

Figure 5.33 A typical reaction of metal/a-Se/metal structure to stepwise changes in the applied bias. The nature of the changes in the currents indicates the existence of strong internal fields due to space charge regions. The space charge is due to trapped carriers as evident from the long time that it takes for the space charge region to relax to its new equilibrium state when the bias changes.

response time of the HV power supply, or to transients that appear due to the finite RC- constant of the sample.

When a voltage bias of 60 V is applied across the sample (top pair of graphs in Figure 5.33) a non-steady state time dependent current starts flowing in the system as space charge develops in it. The system then approaches its quasi-equilibrium state and the current eventually relaxes to a more stable value at a level of about 0.31 pA. Then we increase the applied voltage to 120 V and a time dependent current again begins to flow and eventually stabilizes at about 1.5 pA as the system relaxes from the quasi-steady state defined by the first applied bias to the quasi-steady state defined by the second applied bias. Note that the current that corresponds to the initial portion of the decay at a bias of 120 V is not bigger than the initial portion of the current in the sample when 60 V are applied across it. The latter behavior is different than the one shown in Figure 5.23 and Figure 5.25. In the case of those measurements, the samples were rested for a long time before the application of the new bias. We can see that the effect of the space charge on the internal electric field in the sample is significant and that the electric field defined by the 60V applied bias is almost completely absorbed across the space charge region. In such a situation, the current corresponding to the initial portion of the decay will be greater than that for the initial bias voltage only if the new bias voltage is more than two times bigger than the initial bias voltage what is observed in Figure 5.33. Identical relaxations process is observed when the applied bias increases from 120 V to 240 V. The latter voltage step appears 2000 s after the beginning of the experiment and the behavior of the current through the film demonstrates that the amount of charge stored in the sample is capable of completely absorbing the field defined by application of 120 V across it.

The amount of immobile charge that can develop in the sample is usually limited. As the applied bias increases, the space charge region will not be able to completely absorb the electric field, and deviations from the behavior described above will be observed. Such deviations are clearly observed 3000 s and 4000 s after the beginning of the experiment when the voltage across the sample is increased to 480 V and to 700 V respectively. Even at such high applied biases the influence of the space charge region in the sample is significant which is demonstrated in the bottom set of graphs in Figure 5.33, which illustrate the changes in the current in the cases when the applied bias across the sample is decreased step-wise.

After time interval of 5000 s from the beginning of the experiment, the applied bias is decreased from 700 V to 480 V. The current in the sample decreases from 3341.3 pA to a new quasi-steady state value of 380 pA. The initial part of the relaxation is very interesting. The current jumps down to a value that in many cases is smaller than the quasi-steady state value of the current at the new applied voltage (in our case 380 pA). Then the current increases, passes through a maximum, and then decreases again to reach the quasi-steady state value for the new applied bias (380 pA). This manifestation of the relaxation of the space charge region inside the sample to its new quasi-equilibrium state defined by the new applied voltage is much better elucidated at low applied voltages across the sample when the changes in the internal electric field caused by the immobile space charge are of relatively larger importance. Thus, the change in the current 6000 s after the beginning of the experiment is much more impressive. At that time, the voltage is decreased from 480 V to 240 V, and an initial reverse current flows in the sample (i.e. one which flows in the opposite direction to the conventional current that normally flows for the given applied bias) as the system relaxes to the new quasi-steady state defined by the new applied bias. The current crosses the time axis (is zero) at the moment when the internal relaxation current is equal to the current injected at the electrodes. Thereafter, since the injection current exceeds the relaxation current, the net current in the system flows in the positive direction as in Figure 5.33. Relaxation processes with the reversal of the current direction are clearly observed 7000 s and 8000 s after the beginning of the experiment.

The observed difference in the quasi-steady state currents that are established for increasing voltages (upper set of graphs in Figure 5.33) and for decreasing voltages (lower set of graphs in Figure 5.33) are different. This is another indication that the electronic state of the sample changes continuously during the measurements. Such changes are most likely due to very slow relaxations of the regions of immobile space charge inside the sample. The relaxation times are relatively long, in any case, much longer than the duration of practical measurements.

The accumulation of charge in a-Se films left under bias was further investigated by TOF technique as proposed in [14, 157]. Hole TOF waveforms were used to probe the space charge distribution in the samples [157] because in a-Se the holes move with higher drift mobility and exhibit less dispersion than electrons. Thus, the packet of injected charge remains with small width from injection to extraction, which makes the experiments more sensitive to the shape of

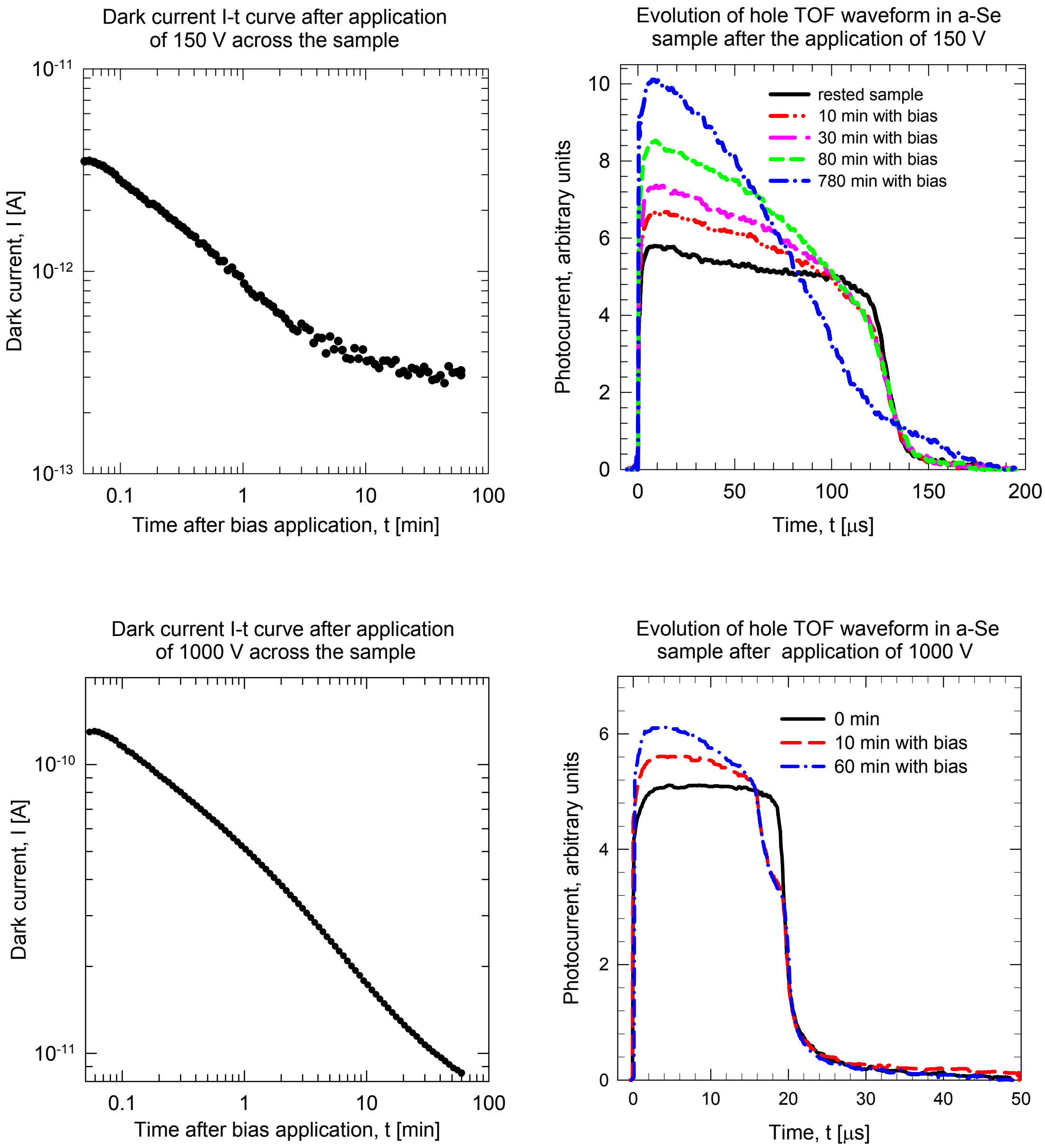

Figure 5.34 The dark current transient curve following the application of bias across the sample are shown together with the changes in the shape of the hole TOF waveform recorded on the same sample left under the same bias. The sample is a single a-Se layer with thickness *L* = 500 μm deposited on glass/ITO substrate. The top contact is produced by sputtering of Au and has area of 0.5 cm^2. The I-t curve and the evolution of the hole TOF waveforms were studied in two separate experiments. The sample was rested in dark for several days prior and between the measurements.

the space charge accumulated in the sample. The results from the experiments for two different applied voltages across the sample are summarized in Figure 5.34.

For both applied voltages across the sample, the dark current decays in a monotonic manner over the period of the measurement (Figure 5.34-a and Figure 5.34-c). The magnitude of the decay is about one order of magnitude in both cases. The current for a bias of 150 V (Figure 5.34-a), unlike the current for 1000V (Figure 5.34-c), shows a tendency towards reaching a quasi-steady state values close to the end of the measurement. As expected, the shape of hole TOF waveform changes as the time after the application of the bias progresses. The magnitude of the changes for higher bias (Figure 5.34-d) is "at most a few percent" as previously described in [14], however the changes observed for lower bias (Figure 5.34-b) are much stronger than a few percent. In our view, in both cases, these changes are significant and reflect significant amount of charge accumulated in the sample. The increase in TOF photocurrent after the excitation indicates that the electric field near the top electrode is increasing as the time after the application of the bias progresses.

The increased electric field can cause more efficient photogeneration process close to the top electrode. Thus, a charge packet that eventually contains more holes travels at higher speed through the sample and for such reasons we can observe initial increase in the photocurrent as in Figure 5.34. A pronounced decay in the current is observed for all TOF waveform recorded on samples that have been under bias for 10 or more minutes. Such decay of the photocurrent near the extraction point can mean that the electric field decreases as the charge packet approaches the bottom side of the sample, and/or loss of carriers due to trapping and recombination.

The analysis of the TOF waveforms shown in Figure 5.34 can be developed further and made quantitative. For example, one can easily calculate the changes in the electric field near the excitation electrode as the time after the application of the bias across the sample progresses. Such calculation can be easily done on the basis of the observed changes in the photogeneration efficiency. It is possible to go even further and calculate the time evolution of the trapped charge profile in the sample using, for example, the method proposed in [157] with some minor modifications. Such quantitative analysis was beyond the scope of our research program and would require data that have been collected more systematically. However, the data presented in Figure 5.34 clearly demonstrates that the internal electric field in the sample is changing after the application of the bias. The change is is significant for applied external electric fields as high as 2 V/μm and indicates that significant space charge develops in the a-Se film that is left under bias for sufficiently long time.

Neglecting the thermal generation of carriers in the bulk of the sample, we can say that the dark currents in a-Se films depend on the applied external field, on the rate of carrier injection at the electrodes and on the transport properties of the a-Se film. The rate of carrier injection depends, in a complicated way, on the metal/a-Se interface. The type of metal used for the electrode and the presence of crystalline inclusions at the interface can have an extremely important role in determining the injection efficiency at the electrodes. The bandgap of a-Se contains sets of deep electron and hole traps with significant concentrations and space charge will build up in the sample after the application of the bias. The situation is even more complicated because the deep traps most probably are never uniformly distributed across the thickness of the a-Se films (see Figure 5.26). The rate at which the space charge will grow depends mainly on carrier injection rates, and the on carrier Schubweg ($\mu\tau F$). However, the presence of the immobile charge in the sample affects both the carrier injection rate at the electrodes and the carrier Schubweg. The injection rate is affected because the immobile space charge, merely by its presence, limits the amount of charge that can move in the sample (the total amount of charge free or trapped that the sample can hold at a given bias is limited by the geometric capacitance of the sample). Further, even very small amounts of immobile charge can change the electric field near the electrodes, and thus significantly alter the carrier injection process. Carrier transport properties are also affected by the presence of space charge. Since the space charge is not uniformly distributed across the sample, the electrons and holes will have different deep trapping times (τ) at different spots in the sample, simply because the deep trap occupancy is different across the sample. In addition, since the electron mobility in a-Se is field dependent, the electron mobilities in the sample will be position dependent, because the electric field in the sample is not uniform. At high densities, the immobile space charge (we assume that the space charge forms due to trapped carriers) can make the recombination process in the sample of particular significance and this also affects the transport of carriers through the sample.

The temporal behavior of dark currents is a result of a complicated interplay of these processes. Under different circumstances, totally different scenarios are possible which explains at least qualitatively the great variety of characteristics in the observed I-t curves. The results from the experiments, described in this subsection, have demonstrated that in many cases of practical importance the build up of space charge regions in a-Se films and their relaxation to a new state when the conditions change, play a very important role in determining the magnitude and the temporal behavior of the dark currents in a-Se devices.

5.3.8 Effects of X-ray Irradiation on the Dark Currents

Some changes in the dark currents similar to the ones described in reference [158] are almost always observed in single layer a-Se films after they have been irradiated x-rays. The main purpose of this subsection is to briefly describe the observed x-ray induced changes in the dark currents after a relatively small exposure of an a-Se film to x-rays.

The samples used for the purpose of these experiments were produced on Al substrates from Se:0.5%As:10ppm Cl alloys. The a-Se layers had a thickness in the range 50-150 μm and were grown on substrates that were kept at 70 °C during the film deposition process. Fabrication of the test metal/a-Se/metal devices was completed by the fabrication of a top electrode with area 0.25 cm^2 by sputtering Au or Pt.

The dark current in the sample decreases about two orders of magnitude (from $\sim 10^{-7}$ to $\sim 10^{-9}$ A) after applying positive voltage (top contact positive) with most of the decay occurring in the first 300 s as shown in Figure 5.35. The same figure also shows that for the first 100 s after applying negative bias to the sample the current is almost constant at $\sim 10^{-9}$ A. The dark current decreases by only a factor of two after applying a negative voltage to the samples over the period of the measurements.

The samples were rested for a period of 2400 s between the measurements. As described previously (subsection 5.3.6) this rest period in not long enough to restore the initial state of the sample before the measurements and, as a result, the reproducibility in the dark currents from measurement to measurement is similar to the one shown in Figure 5.30. The dark currents for positive bias overlap within 30% in the subsequent cyclic measurements (1200s with bias-2400s rest) implying that the rest period is long enough to restore the initial state of the sample if the measurement involves the application of positive bias across the sample. However, the I–t curves measured under a negative bias in subsequent cycles shift to lower currents; thus, the 2400 s rest period is not long enough for negative bias (complete restoration requires between 30 and 100 h of zero bias). Quantitatively, the dark current I-t curve during the 6-th measuring cycle is shifted down towards lower currents by about 60% compared to the I-t curve measured in the first cycle on a well rested sample.

Exposure to X-rays immediately before applying positive bias has no effect on the dark current decay curves. Exposure immediately before applying negative bias results in I–t curves similar to those without exposure but the observed shift downwards from cycle to cycle is some what bigger. After six measuring cycles, the dark current is 25% smaller when pre-exposing to x-rays before each cycle compared to the same procedure without exposure.

The expose of the sample to x-rays while the bias is applied results in a different behavior as shown in Figure 5.35. The biased samples were irradiated 10 s after applying the negative voltage. The x-ray exposure induced current was ~100 times greater than the dark current in the sample. The current after the exposure decreases quickly to a value that is 1.6 times higher than the dark current at the same time after the application of the bias as measured on an unexposed sample. Figure 5.35 clearly shows that after the x-ray exposure, the current for negative bias is bigger than the dark current in an unexposed sample until the end of the measurement (for more than 1100 s). The difference $\Delta I_{\mathrm{dark}}(t)$ ranges from 60% of I_{dark} immediately after the end of the exposure to about 20% of I_{dark} close to the end of the measurement.

For positive bias, irradiation of the sample 10 s after application of the voltage induces a totally different behavior. During the exposure the x-ray induced current is only 2.7 times bigger than the dark current in the unexposed sample. However, the absolute value of the x-ray induced current is about the same as that recorded with negative bias (89nA:85 nA, see Figure 5.35). The difference between the two dark currents in exposed and unexposed samples measured after the end of the exposure, $\Delta I_{\mathrm{dark}}(t)$, is negative for the first 10-15 s after the exposure, then becomes positive for the next 500-600 s and then settles to zero (Figure 5.35, lower left graph). Thus, in the case of positive bias it takes about 10 min for the dark current to return to the values measured in unexposed sample.

The irradiation of the same sample carrying the same positive bias 100 s after the voltage application, when the dark current has completed most of the decay, results in a photoconductivity that is about 100 times larger than the dark current (Figure 5.35, lower right graph). The absolute magnitude of the x-ray induced photocurrent is this case is about 1.2 (106nA:89nA) times bigger than that when the irradiation is done 10 s after the bias application (see Figure 5.35). However, the persistent photocurrent in this case requires 300-400 s to return to the I–t curve measured without exposure (lower right graph in Figure 5.35). The difference between the dark currents for exposed and non exposed sample, $\Delta I_{\mathrm{dark}}(t)$, in this case is always positive and starts its monotonous decay to zero from about 400% of I_{dark} immediately after the end of x-ray exposure.

The experiments involving x-ray irradiation give good grounds to think that the formation and relaxation of space charge regions in the films might be responsible for the temporal behavior of the dark currents themselves and for the observed changes in the currents when the samples are irradiated with x-rays. Under the conditions given in Figure 5.35, assuming that the electric field in the sample is constant, x-ray exposure (1.6 R, 30 kV average energy, 2.8s)

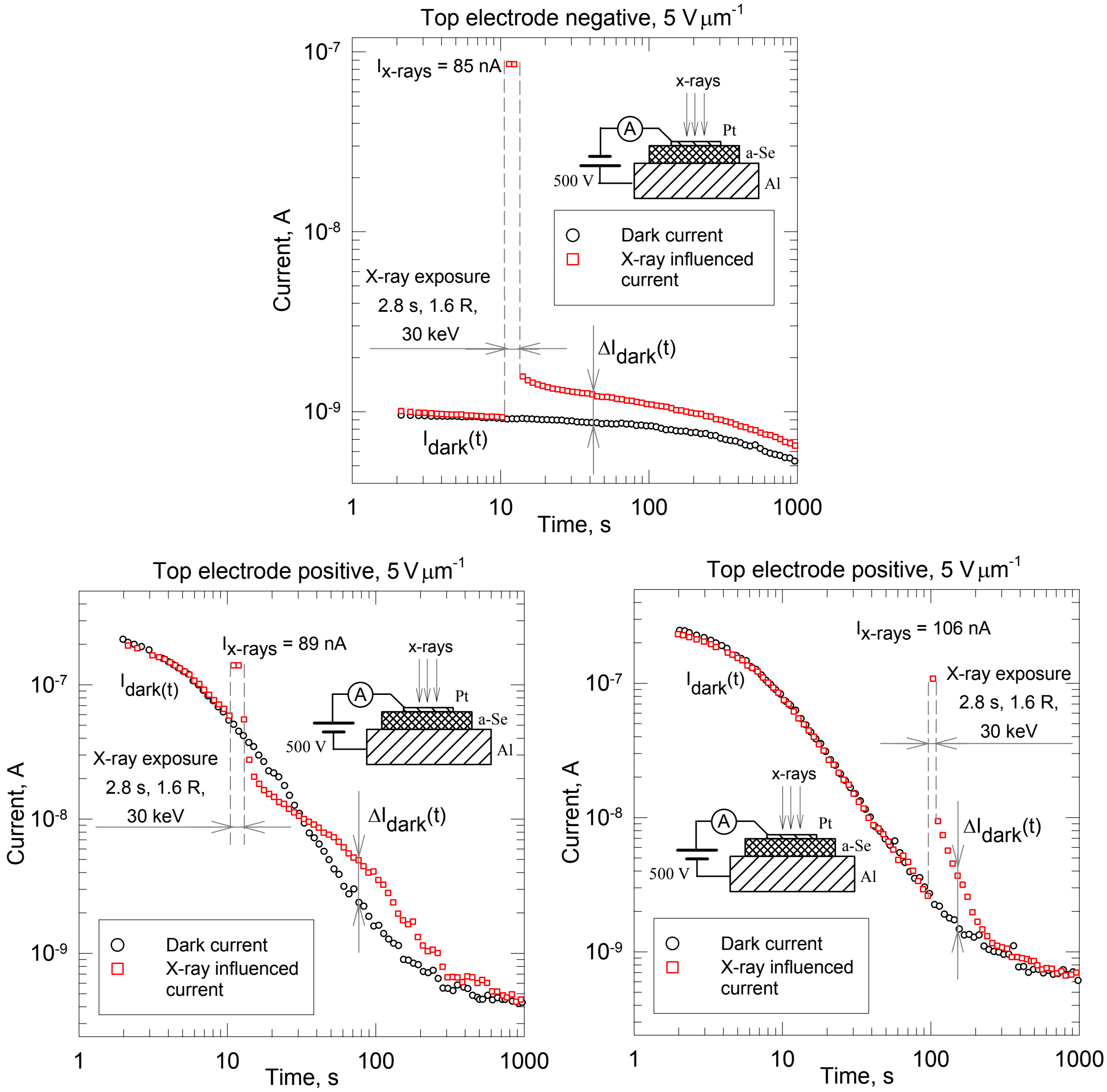

Figure 5.35 Effects of x-ray irradiation on the dark currents in single layer a-Se samples. The films had a thickness of 100 μm and were evaporated on Al substrates kept at 70 °C during the deposition process from a Se:0.5%As:10ppm Cl alloy. The top contact is produced by sputtering of Pt and has an area of 0.25 cm^2. Films produced under the same conditions from the same material usually demonstrate hole lifetime of about 100 μs and electron lifetime of approximately 300-350 μs.

generates about 2×10^{14} electron-holes pairs in the sample. This amount of charge can interfere significantly with the space charge regions in the sample through the processes of trapping and recombination. Consequently, the space charge regions in the sample after the end of the exposure are different than they were before that and naturally different currents will flow in the sample. The samples involved in these experiments are not symmetric. The bottom and the top metal/a-Se interfaces are different. The bottom interface is complicated by the presence of thin (several nm) insulating Al_2O_3 that is known to block the traffic of electrons between the metal electrode and the a-Se film and possibly by a continuous layer of polycrystalline trigonal Se as shown in Figure 5.26 due to a relatively high substrate temperature during the deposition of the film ($T_{\text{substarte}}$ = 70 °C). The sample recovery after the end of the x-ray exposure to the state of unexposed sample will take different times for the cases of negative and positive bias (see Figure 5.35) due to the asymmetry of the samples.

Additional support for the space charge region hypothesis can be found in the x-ray induced photocurrents in the sample. The net x-ray currents (corrected for the dark current) are given in the three graphs in Figure 5.35. The samples, irradiated 10 s after bias application, have produced almost the same x-ray currents for both polarities of the applied bias; the current for positive bias being ~5% bigger. The reasons for the latter can be a difference in the internal electric field in the sample, different x-ray sensitivity of a-Se film sample for positive and negative bias due to a non-uniform x-ray photogeneration across sample thickness and difference in the electron and hole Schubwegs as described in [159]. The analysis in [159] applied to the experimental conditions shown in Figure 5.35 gives difference in the sensitivity for the cases of negative and positive bias of about 1% assuming that the internal electric field in the sample is constant and equal 5 $V\mu m^{-1}$. That 1% sensitivity difference and an experimental error of a few percent can explain our experimental results for the case of x-ray irradiation with 10s delay after the bias application but can not explain the measured value of the x-ray induced current when the sample was irradiated 100s after bias application which is close to being 25% bigger. Such big difference strongly suggests that the internal electric field in the sample changes as the time after application of positive bias progresses. The results presented in Figure 5.35 are consistent with internal electric field that is becoming bigger than the nominal field (applied bias divided by the sample thickness) in the region of the sample that is close to the positive (radiation receiving) electrode. The increased electric field makes the x-ray photogeneration efficiency bigger in the top portion of the sample and that explains the observed increase in the x-ray induced photocurrent. The changes in the internal electric field profile under a constant applied bias across the sample must be related to the formation of regions of immobile space charge in the a-Se film and to their relaxation when the experimental conditions are changed. (the onset and the end of x-ray exposure).

In conclusion, it should be mentioned that we do not have ready explanations for the changes in the dark currents observed after irradiation with x-rays since the dark current I-t curves themselves are not fully understood. However, one result of practical importance following from our experimental observations is that precise correction for the dark in the sample in experiments involving x-ray irradiation is a complicated task. The magnitude of the x-ray currents depend on the time of the irradiation with respect to the application of the bias and on the polarity of the applied bias. The persistent current after the end of the x-ray exposure can be quite different than the dark current in unexposed samples both in magnitude and in shape, depending on the polarity of the bias, the time after the application of the bias, the magnitude of the previous exposure to x-rays, the time after the previous exposure to x-ray, etc. It is almost impossible to take into account all these factors quantitatively and obviously fine corrections for the dark current in the sample will be extremely difficult and close to impossible in many practical cases.

5.3.9 Effects of Substrate Temperature during Film Fabrication Process on the Magnitude of the Dark Currents in Metal/a-Se/Metal Devices

In subsection 5.2.3 we have discussed the influence of the substrate temperature during the deposition process on charge transport in a-Se films. It was found that by lowering the substrate temperature, the hole mobility-lifetime products can be reduced by two and more orders of magnitude while the electron lifetimes remain relatively unaffected. This can be understood if we assume that the cold deposited films have a concentration of deep hole traps that is greater (sometimes more than 2 orders of magnitude) than the one in the films deposited on hot substrate ($T_{\text{substrate}}>T_g$). If the additional deep hole traps formed as a result of the cold deposition do not act as centers for thermal generation of carriers as well one would expect that the dark currents in the cold deposited films will be lower than the currents in the hot deposited ones simply because they can hold more trapped charge. The experiments that will be summarized in this subsection were devoted to studying the dark currents in cold deposited a-Se films towards the fabrication of metal/a-Se/metal devices having tolerable dark currents for applications in digital x-ray image detectors.

The a-Se alloys chosen for the experiments contained only As (0.2-0.5%) because Cl is known to create centers in a-Se that act to improve thermal generation of carriers and hence to increase the dark conductivity of the films which was not desired. Most of the films were produced on Al or Al coated glass substrates since the final goal was depositing of a-Se structures on CCD chips that had Al metal bus on top of them to interface the x-ray photoconductor. Further, because the CCD readout circuit was designed to collect electrons we were interested mostly in creating a-Se based photoconductor structures that have low dark currents when the top electrode is negatively biased.

Figure 5.36 shows the dependence of the dark current density on the applied electric field (J-F curves) for the case of two devices; Pt/a-Se/Pt and Al/a-Se/Au. Both samples contain single cold deposited and post-annealed a-Se layer. The top contacts were sputtered on the films after the annealing. A direct comparison between Figure 5.24 and Figure 5.36 reveals that the dark currents are significantly suppressed as a result of the cold fabrication technique of the film. Additional and beneficial difference is that the dark currents in the cold deposited sample unlike in the hot deposited ones (Figure 5.24) are lower for a negatively biased

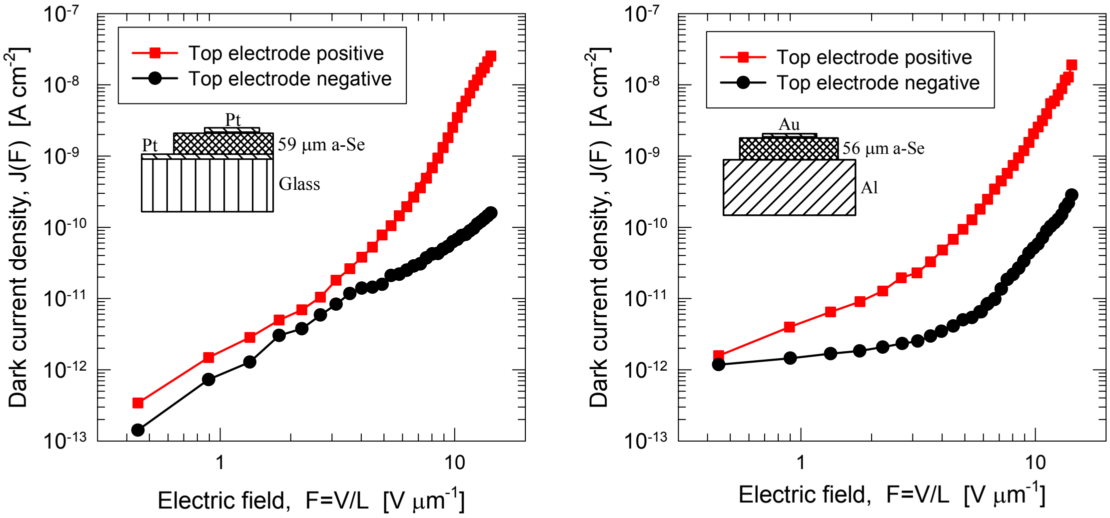

Figure 5.36 Dependence of dark current density on the applied electric field in a-Se films produced by deposition on cold substrates ($T_{\text{substrate}}$ = 25 °C) from Se:0.5%As alloy on glass/Pt and Al substrates. Both films were annealed after the deposition (1 hour, at ~50°C). The top electrodes (Pt and Au) were produced on the annealed films by sputtering.

top electrode. The dark currents in cold deposited films like those in hot deposited films are not symmetrical with respect to the polarity of the applied bias even when the sample is fabricated to be symmetrical (Pt/a-Se/Pt sample in Figure 5.36).

The observed changes are related to the preparation technique and not to the specific Se alloy used to produce the film. Amorphous Se films produced on a hot substrate from the same alloys as the samples in Figure 5.36 do not exhibit the same behavior and demonstrate much higher dark currents in Figure 5.37.

In subsection 5.2.3.3 we have discussed our experimental findings that a two step fabrication process consisting of the deposition of an a-Se film on a cold substrate followed by mild annealing leads to significant suppression of the hole transport (hole lifetime decreases more than two orders of magnitude) in the resulting films leaving the electron transport relatively

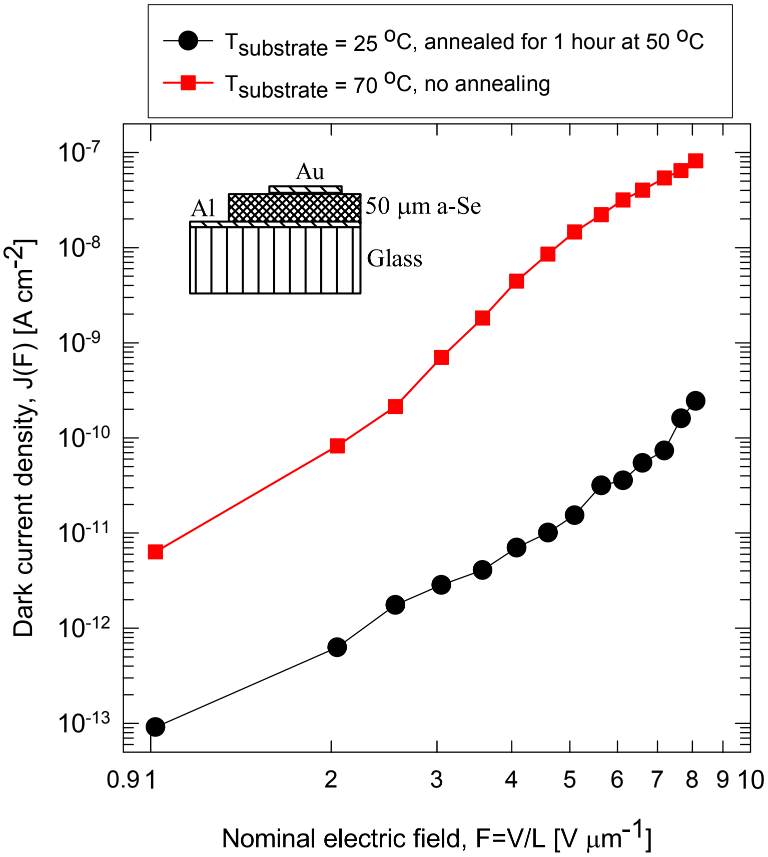

Figure 5.37 Comparison between the dark current J-F curves for negative bias in samples produced on hot and cold substrates. The samples were produced from the same Se:0.5%As material used to fabricated the samples shown in Figure 5.36.

unaffected. The decrease in the hole lifetime and the relatively unchanged electron lifetime can be explained assuming that the cold deposition technique leads to a significant increase in the concentration of deep hole traps while the concentration of deep electron traps remains relatively unaffected.

We can speculate that the dark currents in the cold deposited a-Se films are low because the films having a higher concentration of deep hole traps can hold more immobile positive charge. If more immobile charge is present in the sample, the amount of free charge that can be injected in the sample decreases because the total amount of charge (free + immobile) that the sample can accommodate is limited by the geometric capacitance of the sample and the applied bias. The bulk immobile charge will decrease the amount of charge that can be transported through the sample per unit time or in other words will cause the dark current to decrease.

Alternatively, we can explain the observed decrease in the dark currents in a-Se films deposited onto a cold substrate as follows. The concentration of deep hole traps is most likely not constant across the thickness of the sample. The exact distribution of traps is substrate temperature dependent as Figure 5.26 shows. The cold deposition leads to changes in the distribution of deep hole traps in the bulk of the sample and especially in the regions near the electrodes. That change will affect the profile of immobile space charge developing in the sample after the application of bias. The modification of internal field in the sample due to the presence of the immobile space charge might act to decrease the charge injection from the electrodes (due to decreased electric field near the contacts).

It is also possible that the deposition on a cold substrate simply prevents the formation of a continuous layer of trigonal Se between the bottom electrode and the a-Se film as illustrated in Figure 5.26. If that layer is absent, hole injection from the bottom electrode will be significantly modified and possibly decreased. That can explain the observation that in the cold deposited films, unlike the case for hot deposited films, the dark currents for negative bias are lower than those flowing under a positive bias across the sample.

We observed a strong correlation between hole lifetime and the dark currents for the cases of cold deposited a-Se films ($T_{\text{substrate}}<T_g$). The decrease of the hole lifetime is almost always accompanied by the decrease in the dark currents in the films. This means that the formation of deep hole traps resulting from the deposition on cold substrate seems to control both quantities.

There are a few exceptions. Films produced on an Al surface (Al or glass/Al substrates) by cold deposition and annealing from Se:As alloys (0.2-0.5 %As) and having a hole lifetime in the range 0.3-10 μs can have very similar dark currents for negative bias especially if the applied bias is not very high (less than 10 $V\mu m^{-1}$). This observation suggests that in these samples there exists an additional mechanism that acts to reduce the dark current. A hint of the latter behavior can be seen if we compare the two graphs presented in Figure 5.36. The sample with the Al bottom electrode seems to have additionally suppressed dark currents for negative bias if the field is below 8 V/μm.

The additional blocking of the dark current can be due to the insulating properties of the Al_2O_3 layer present on the bottom Al electrode. Alternatively, following the ideas published in [141,142], we can contribute these additional blocking properties to the modification of the interface Al-Al_2O_3-Se as a result of inter-diffusion between Al_2O_3 and Se facilitated by the combination of the cold deposition with the subsequent annealing process. However, our experimental results do not support the findings that a p-n junction is formed between a modified n-type Al_2O_3 and p-type Se. The difference is probably due to the fact that the films in [141,142] we produced from Se heavily doped with As (3%) and were much thinner (typically less than 10 μm). Since Al_2O_3 that is naturally present on the Al substrate is a highly disordered system and since that disorder can be amplified due to inter diffusion between Al_2O_3 and Se ith Se phase one can expect some improvement of the blocking properties of the interface.

The reduction of the dark current in a-Se films related to the deposition on a cold substrate is a significant finding with important technological consequences. It can be used as a very suitable technique to minimize the dark currents in single layer a-Se based photoconductors or to create multilayered photoconductor structures (pin-, ni and- in- like structures) in which the n- like layer can be produced by the cold deposition process. For further details see subsection 5.4.

5.3.10 Influence of the Electrode Metal on the Dark Currents in Metal/a-Se/Metal Devices

When a metal contact is formed on a semiconductor, one will normally expect formation of either an ohmic or an Schotky contact depending on the difference between the work functions of the materials. Since the work function of a-Se is larger than that for all metals [14] that are practically used for electrodes one will expect a Schotky barrier to holes to form at the metal/a-Se interface. Although the formation of both Schotky and ohmic contacts to a-Se has been reported in the scientific literature (see subsection 5.3.1) it is not very likely that the complicated metal/a-Se interface can result in a contact that can be fully described within the framework of such a simple theory. Early indications that the metal/a-Se interface will be neither ohmic nor Schotky can be found in the works of Paul Nielsen [48] who investigated Au/a-Se and (Al-Al_2O_3)/Se interfaces. More recently Johanson et all. [14] found no correlation between the work function of the metal and the current flowing through the metal/a-Se junction and based on that and the complicated nature of the interface (formation of metal selenides, etc.) have suggested that no simple theory (Schotky or ohmic) can explain the electrical behavior of metal contacts to a-Se. However, they have suggested that the dark currents in metal/a-Se/metal devices can be minimized by proper selection of the metal for contact fabrication and found that an ITO/a-Se/Mg structure resulted in exceptionally low dark currents when the Mg contact that was deposited on the top surface of the film was biased negatively.

In the case of x-ray image detector applications the bottom electrode is predetermined by the technology used in the production of the readout circuit. Thus, when polysilicon AMA array is used as a readout circuit the bottom electrode is most often ITO. Our research was primarily related to a CCD readout technique. The CCD chips were manufactured at DALSA Inc. and had an Al bus on them, i.e. the bottom electrode was fixed - always Al. In addition, the CCDs were designed to collect the electrons created by the x-rays in the photoconductor. Thus, by necessity, most interesting case for us became Al/a-Se/metal structures biased negatively (radiation receiving electrode is negative). Following the ideas expressed in [14] we have decided to study the possibility for dark current minimization in Al/a-Se/metal structures by a proper selection of the metal for the radiation receiving electrode.

Under a negative bias, the top electrode will inject electrons into a-Se film. Thus, changes in the electron component of the dark current through different Al/a-Se/metal structures have to be observed. Typical a-Se films have much better hole transport than electron transport, especially if deposited on a hot substrate ($T_{\text{substrate}}>T_{\text{g}}$). In such films, the dark current at room temperature is dominated by hole injection from the positive contact as it was found in [14]; and any observation of small changes due to the electron component of the current might not be possible. Our experiments were conducted on cold deposited and annealed films because in such films the hole transport is strongly suppressed which means that the hole component of the dark currents is smaller in magnitude. We also needed to study the potential of the cold deposited films for application in x-ray image detectors.

The metals investigated as top electrode were chosen to be stable and to allow the convenient fabrication of the contact without risking damage to the CCD chip with the equipment that was available in our laboratory. For these reasons, the experiments were conducted using Pt, Au, and Al as top electrodes. The Pt and Au contacts were produced by DC sputtering, while the Al ones were fabricated by thermal evaporation.

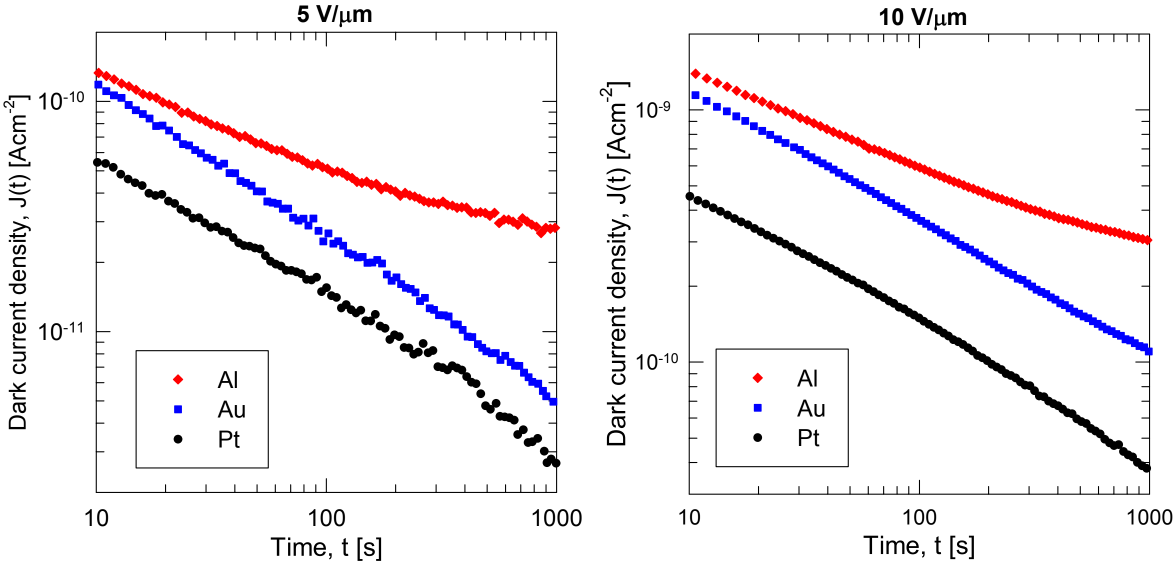

Figure 5.38 The influence of the top electrode metal on the dark current J-t curves in Al/a-Se/metal structures under negative bias. The a-Se film was produced on glass/Al substrate. The film was deposited on a substrate kept at 25 °C from Se:0.5%As no Cl alloy. After a mild annealing (50 °C, one hour), contact from Pt, Au and Al were fabricated on the top surface of the sample. The area of the contacts was 0.25 cm^2.

As demonstrated in Figure 5.38, the dark currents for electrodes were decaying with time after the bias is applied over the whole period of the measurement (20 min). For the period 10 to 1000 s after application of the voltage, the dark current measured with Pt is the smallest one while the dark current measured with Al is the highest.

There is a clear negative correlation between the work function of the metal from which the top electrode was fabricated and the dark currents measured in the film as summarized in Table 5.3.

Assuming that the observed dependence in the dark currents is due only to different electron injection rates at the top electrodes our results can be explained as follows. We can think that the injection is a two step process. At first stage, the electron is injected into a localized state in the bandgap of a-Se near the interface and in the second stage; the electron is thermally released into the conduction band in which it starts its drift. The rate of the first stage will depend on the density of available unoccupied localized states in the bandgap of a-Se that are accessible for an electron occupying a state around the Fermi level in the metal. As the work function of the metal increases the electrons in the metal that can be potentially injected into a-Se will be seeing a decreasing density of localized states in the bandgap of a-Se because its work function is large (5.9eV according to reference [14]) and, as a result, the injection rate will decrease. Such ideas can explain the observed correlation between the dark currents in the film and the work function of the metal for the top electrode but is highly speculative since there might be significant contributions from bulk processes that alter the injection of carriers as well.

Table 5.3 The electron work function, J(100s), and the ratio of current densities at t=1000s and t=10s for each metal studied. Work function data were taken from [160].

Metal	**Work Function, Φ [eV]**	**5 V/μm**		**10 V/μm**	
		J(100s), [A cm^{-2}]	**$\frac{J(1000s)}{J(10s)}$**	**J(100s), [A cm^{-2}]**	**$\frac{J(1000s)}{J(10s)}$**
Al	4.25	5.11×10^{-11}	0.21	4.94×10^{-10}	0.22
Au	5.1	2.67×10^{-11}	0.05	3.63×10^{-10}	0.10
Pt	5.65	$1.55e\times10^{-11}$	0.05	1.50×10^{-10}	0.08

Form a practical point of view, our data show that by manufacturing the top electrode from Pt one can obtain 2-5 times lower dark currents compared to those cases when the top electrode is produced from Al or Au.

5.3.11 Dark Currents in Metal/a-Se/Metal Devices - Summary

In above subsections we have presented results from different experiments on dark currents in single layer metal/a-Se/metal devices.

As observed in previous studies [14] the dark current after the application of a constant voltage decreases as the time after the bias application progresses, in some cases over 2-3 and more orders of magnitude. We have observed decays as long as 20000 s and even after this long, it is difficult to say that the dark currents become constant. The magnitude of the decay and the shape of the *I-t* curves depend on the applied bias, on the Se material, and on the metals from which the top and the bottom electrodes are produced.

In many cases Currie von Schweidler Law ($I(t) \propto t^{-n}$) or Kolrausch-Wiliams-Wats Law ($I(t) \propto \exp\left(-\left(\frac{t}{\tau}\right)^{\beta}\right)$) can be used to describe the shapes of the dark current transient curves.

We observe that the dark current *I-t* curves for negative and positive bias are never fully symmetrical even when the metal/a-Se/metal device was fabricated to be symmetrical. For some materials and preparation conditions, the dark currents are larger when the top electrode is positive; for other materials and preparation conditions, the dark currents are bigger when the top electrode is negative. For all deposition conditions and materials the substrate temperature seems to play an important role. Films produced at sufficiently high substrate temperatures have higher dark currents when the top electrode is negatively biased, while the opposite is generally true if the films are produced at low enough substrate temperatures. The asymmetric dark currents for negative and positive bias can be explained with the asymmetric properties of the top and bottom metal/a-Se interface and/or with asymmetric non-uniform distribution of various microcrystalline inclusions that act as carrier traps across the thickness of the a-Se film. The major factor that contributes to the asymmetry between the top and bottom metal/a-Se interface is probably the formation of a continuous layer of polycrystalline trigonal Se between the bottom electrode and the bulk of a-Se film for films produced at high substrate temperatures.

In our samples we observe a process of “contact formation” which basically is a permanent change in the electrical properties of the contacts after application of high electric field to the sample for the first time, or after mild annealing ($T_{\text{annealing}} \sim T_g$) of the sample. We observe a decrease in the dark currents at low fields when the voltage is applied after the contact has been “formed”.

The process of contact “formation” in our films must have very close origin to the processes that are taking place during the high temperature fabrication step in the polycrystalline Se rectifier production technology. In any case, the formation of metal selenides, the crystallization of Se at the interface, and the Se crystalline inclusions present at the interface must be important factors that lead to the observed contact "formation" process in our films.

In most of the cases the dark current *I-t* curves are monotonically decreasing. However, in certain cases we observe deviations form the latter behavior and the *I-t* curve passes through a distinct maximum. Such "abnormal" behavior was observed for samples that have Al-Al_2O_3-Se bottom interface or for multilayer pin- like structures. In the scientific literature, the presence of a peak in the *I-t* curves for some ceramics have been explained on the basis of space-charge-limited currents and mobile ion species. We think that the observed peak in the *I-t* curves for our samples most likely reflects the dynamics of the developing space charge regions in the sample after the bias application. By growing and changing their shape, the space charge regions in the sample can alter the electric field at the electrodes, which would lead to changes in the injection of carriers from the electrodes. The altered carrier injection in turn affects the kinetics of space charge region formation in the sample. For certain periods of time, a positive feed back can exists between these two processes and that can result in the observed maximum in the *I-t* curves for constant applied bias.

We observe that the dark current *I-V* curves are strongly non-linear. Our data suggest that the *I-V* curves measured on single layer metal/a-Se/metal devices contain several regions for which $I(V) \propto V^n$. The value of the exponent n is different in the different regions. Over the range of film thicknesses and over the range of electric fields covered in our experiments we observe two distinct regions with different values of n in the measured *I-V* curves; $1.1 \leq n \leq 1.9$ for the lower field region and $3.1 \leq n \leq 4.4$ for higher field region. Several authors have claimed that they observe an ohmic region ($I(V) \propto V$) in thinner samples. It has also been proven that $I(V) \propto V^2$ for the cases when the contacts are made more injective by application of high fields or illumination with strongly absorbed light.

The theory of SCLC (the method of regional approximation) applied to an insulator having two sets of traps well separated in energy can theoretically account for the observation of *I-V* curves having up to four distinct regions for which $I(V) \propto V^n$. The ohmic region is observed for the lowest fields and the usual dependence for SCLC $I(V) \propto V^2$ is observed at highest fields. The two other regions occur due to the presence of the two distinct sets of traps. The value of the exponent *n* can be related under certain experimental conditions to the exact shape of the trap distribution in energy and values for *n* well above 2 can easily be observed.

The application of the regional approximation theory to a-Se is difficult because the two types of carriers are mobile and can contribute to the conduction and because the exact distribution of the traps in the bandgap is still unknown. However, our data show that the space charge regions do form in a-Se and that these regions alter significantly the conduction process is a-Se.

Based on two different groups of experiments we have demonstrated that significant amount of space charge builds up in a-Se films left under bias at least for nominal applied fields below 2 V/μm.

The space charge can cause significant changes in the internal electric field in the sample and that was illustrated by monitoring the changes in the dark current as a result of stepwise change in the bias across the sample. The internal electric fields in some cases can become stronger than the externally applied ones, for example after stepwise decrease in the voltage, which can cause negative currents to flow in the samples for positive applied biases as the space charge regions in the films are relaxing to their new equilibrium state.

The changes is the internal electric field in samples left under bias were also probed with hole TOF experiments. The changes in the shape of the recorded TOF waveforms at different times after bias application clearly indicate changes in the internal electric filed profile, which in turn indicates build up of space charge in the samples.

These results suggest that the space charge has significant contribution to the observed behavior of the dark currents in metal/a-Se/metals devices. The amount of charge that can move in the sample gets smaller as the regions of trapped charge grow in the sample because the total amount of charge free or trapped that the sample can hold at a given bias is limited by the geometric capacitance of the sample. Carrier transport properties are also affected by the presence of space charge. Since the space charge is not uniformly distributed across the sample the electrons and holes will have different deep trapping times (τ) in different regions in the sample, simply because the deep trap occupancy is different across the sample. In addition, since the electron mobility in a-Se is field dependent, the electron mobilities in the sample will be position dependent, because the electric field in the sample is not uniform. At high densities the immobile space charge (we assume that the space charge forms mostly due to trapped carriers) can make the recombination process in the sample of particular significance and this also affects the transport of carriers through the sample.

The accumulation of trapped charge in the sample changes the field near the electrodes and thus affects carrier injection form the electrodes in the sample as well.

The temporal behavior of the dark currents is a result of a complicated interplay of the processes described above. Under different circumstances totally different scenarios are possible which explains at least qualitatively the great variety in the observed *I-t* curves. Because very deep traps exist for both electrons and holes in a-Se, the process of relaxation of the space charge regions to their new equilibrium state after abrupt change in the experimental conditions will be very long. For that reason, the dark current in a-Se will be a strong function of the history of the sample and precise corrections for them might be very difficult.

The effects of x-ray radiation on the dark currents in single layer metal/a-Se/metal devices were studied. It was found that x-ray irradiation (about 2 R) of a sample prior to application of the voltage across it has no effect on the dark currents within the precision of our measurements. Irradiation of biased samples however leads to changes in the dark current. The effect depends on the polarity of the applied bias, as well as on the time interval between the application of the bias and the irradiation with x-rays. The dark current after the end of the irradiation is generally bigger that the dark current in unexposed sample measured at the same time after the application of the bias. This effect is known as the "persistent x-ray current" and has been previously described in the literature [157]. The time needed for the persistent dark current to decay to zero depends on the polarity of the applied bias. For the case of our samples and positive polarity of the applied bias, the dark current after the irradiation returns to the level of the dark current in unexposed sample after 300-700 s depending on the time interval between the application of the bias and the exposure to x-rays. The persistent current decays to zero faster when the sample is exposed to irradiation when the dark current I-t curve has almost completed its decay.

For the case of negative applied bias, the dark current in our samples after the irradiation with x-rays was bigger then the dark current in unexposed samples for the whole duration of the experiment (~20 min).

The observed behavior of the persistent current in our sample agrees well with the idea that space charge regions develop in the sample after the application of the bias. The x-ray generated carriers in the bulk of the sample, as a result of the profile of the space charge regions after the irradiation, is different than that established in an unexposed sample. That is the reason for the observed persistent currents. It can take quite a long time for the space charge regions after the irradiation with x-rays to return to their unperturbed state (the state in the unexposed sample). During that time a different current will flow compared to the one in unperturbed samples

Effects of the substrate temperature during the film fabrication process on the magnitude of the dark currents in metal/a-Se/metal structures were studied. We have found that the magnitude of the dark currents in films produced by deposition on cold substrates and subsequent post annealing have much lower dark currents than the films produced on hot substrates. Our measurements indicate that films produced by cold deposition and annealing have lower hole lifetimes and hence bigger concentration of deep hole traps, most significant part of which have appeared as a result of the cold fabrication process. Dark current measurements on cold deposited films have, however, confirmed that the deep hole traps that appear as a result of the deposition on cold substrate do not act as centers for thermal generation of carriers in the film. Thus we can assume that the thermal generation component of dark currents is the same for the cold and hot deposited films. The observed decrease in the dark current is most probably due to the fact that the cold deposited films can deeply trap much bigger amount of holes then the films deposited on hot substrates. The observed decrease in the dark current can be then explained in terms of space charge limited currents. Another possible explanation is that the region of positive space charge that develops due to trapped holes near the positively biased electrode acts to decrease the electric field near that electrode and thus the rate of hole injection from the electrode decreases. These results have big technological importance because they prove that the cold deposition process is very suitable for the production of n- like layers.

The influence of the metal from which the top electrode has been produced on the dark current in metal/a-Se/metal devices in which the top electrode is carrying the negative bias was investigated. Several metals were investigated as top electrodes: Al, Au and Pt. It was found that Pt top electrode results in the lowest dark current densities under all other conditions being the same. We observe a negative correlation between the work function of the metal used to produce the top electrode and the dark current in the metal/a-Se/metal structure. The metals with higher work function lead to lower dark currents in the samples under allother conditions being the same.

We do not have a complete explanation for the observations described above. However, the results do have a significant technological importance giving a way to decrease the dark current in a-Se photoconductor layers operating a under negative bias up to 5 times by simply fabricating the top contact from Pt.

5.4 Reduction of Dark Currents in a-Se Photoconductor Devices for X-ray Detector Applications

Based on the results from experiments described in subsections 5.1 through 5.3, we have been able to propose a new technology for dark current reduction in a-Se based photoconductor layers. In this subsection we will describe this newly proposed technology and compare it with the existing methods for dark current reduction in a-Se based photoconductor layers.

5.4.1 Description of the New Technology for Dark Current Reduction in a-Se Photoconductor Layers

The existing methods for dark current minimization in a-Se photoconductor layers for application in x-ray image detectors are based on the use of multilayered structures [161, 162]. United States patent [161] is directed to reducing the dark current in a-Se x-ray detectors by the inclusion of buffer layers, or blocking layers as shown in Figure 5.39. These are specially alloyed and doped layers, or layers from different material placed on the top and bottom surfaces of the a-Se x-ray detection layer, between the a-Se and the bias electrodes. The buffer layer between the a-Se x-ray photoconductor and the negative electrode is called the p- like layer. This p- like layer, is a buffer layer, which is normally As_2Se_3 or a-Se heavily doped with Cl (more than 100 ppm). The buffer layer between the positive bias electrode and a-Se is called the n- like layer, and it is an a-Se layer that has been doped by an alkali metal dopant, and has been alloyed with a few per cent As to achieve stability against crystallization. The buffer layers are much thinner than the a-Se photoconductor layer so that the x-rays are absorbed mainly in the a-Se layer. This multilayer structure with buffer or blocking layers between a-Se and the bias electrodes, normally metals, reduces the injection component of the dark current. The holes injected from the positive electrode will be trapped in the n- like layer. The electrons injected by

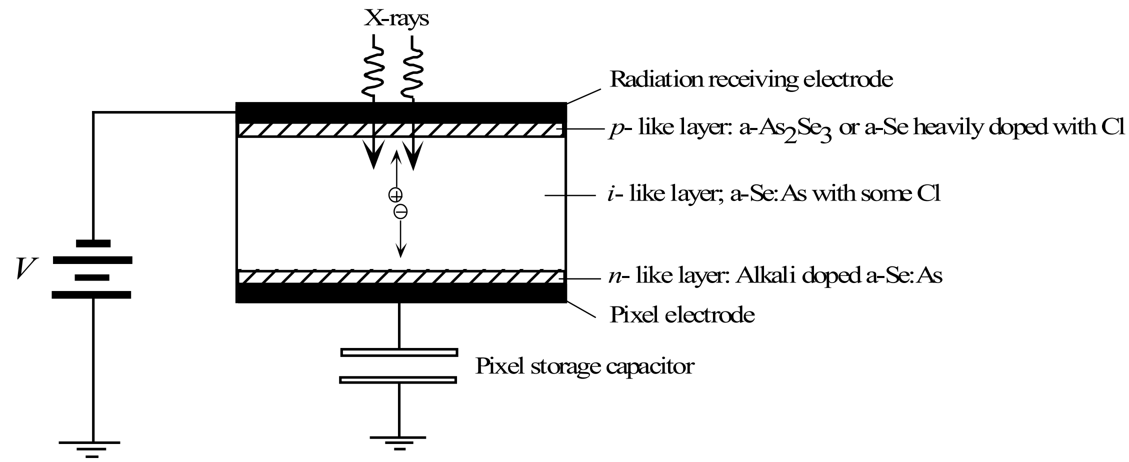

a) Reversed bias a-Se based pin- like structure as an x-ray image detector for collecting electrons.

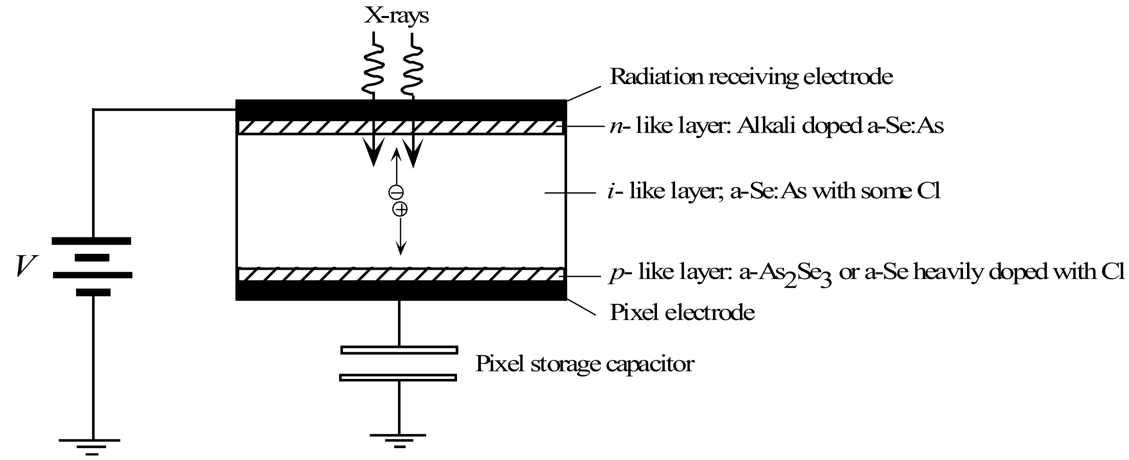

b) Reversed bias a-Se based pin- like structure as an x-ray image detector for collecting holes.

Figure 5.39 Method of producing multilayer metal/a-Se/metal pin- like structures for digital x-ray image detectors as proposed in [161].

the negative electrode will be trapped in the p- like layer. The electric field near the electrodes will collapse due to the presence of the trapped holes and electrons, and thus the carrier injection rate that is proportional to the electric field at the electrodes will decrease which leads to the reduction of the dark current in the pin- like structure.

An United States patent [162] directed to the reduction of the dark current in an a-Se x-ray detector by using a double layer structure, containing a transport (buffer) layer based on di-antimony three-trisulfide (Sb_2S_3) is shown in Figure 5.40. The authors claim that a diode whose cathode is the charge transport layer is formed at the interface between the x-ray detection layer and the charge transport layer so that no holes are injected from the positive electrode into the x-ray detection layer. Thus, the hole component of the injection current is minimized and the structure has tolerable dark currents for applications in digital x-ray image detectors.

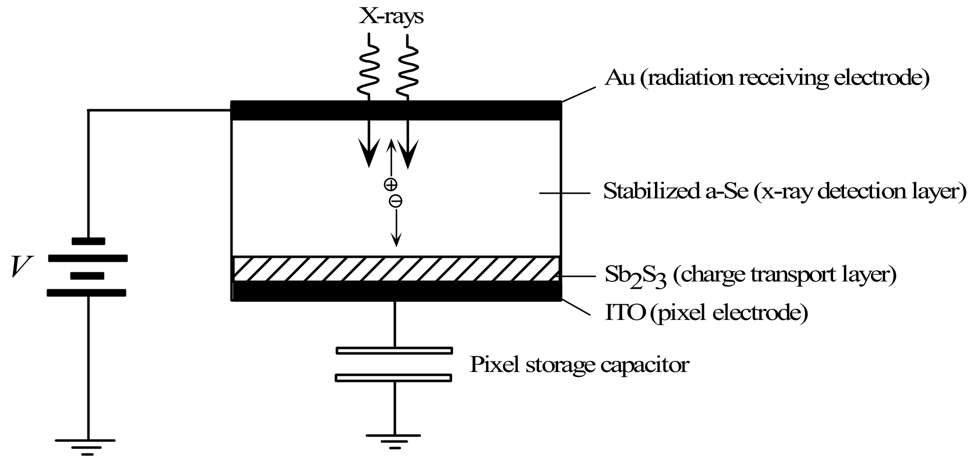

a) Double layer detector structure with low dark currents for collecting electrons.

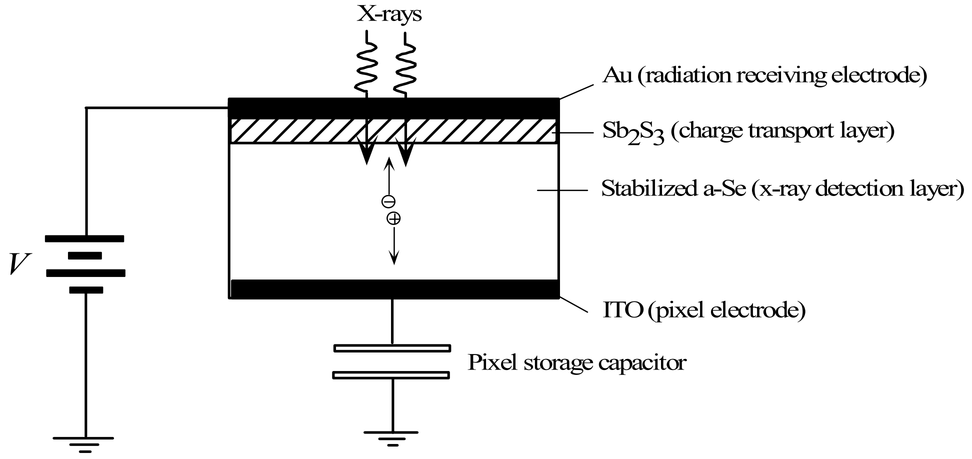

b) Double layer detector structure with low dark currents for collecting holes.

Figure 5.40 X-ray Detection Plate based on double layer structure proposed in [162].

The only fundamental difference between the two patents [161] and [162] is that the dark current reduction is achieved by using different chemical compositions in the buffer layers. Both cases involve using a blocking layer of particular composition that is different than the actual x-ray detection layer (i- like layer) which absorbs the x-rays and generates the charges. The latter differance leads to certain difficulties that will be described below.

The technology for the dark current reduction that we are proposing is based on the same rational as the techniques described above that use a trapping layer to block carrier injection from the electrodes. The novelty is that we have found a convenient way to produce hole trapping layers (n- like layers) by the combined use of two technological processes – cold deposition and annealing that were described in subsection 5.2.3.2. The term "cold deposition" refers to the deposition of a-Se from its vapor in a vacuum system

on a substrate whose temperature is kept bellow the glass transition temperature of the particular a-Se alloy used. The annealing process basically corresponds to heating the a-Se layer to a temperature that is close to its glass transition temperature for time period from one to several hours. The films produced on substrates kept at sufficiently low temperatures during the deposition process have very poor hole transport, good electron transport and low dark current (see subsections 5.2.3.3 and 5.3.9) which essentially makes them good quality n- like layers. Such cold deposited layers can obviously directly replace the alkali metal doped n- like layers in the structures shown in Figure 5.39 and the Ss_2S_3 charge transport layers in Figure 5.40. However, the full potential of the technology we are proposing is best understood by examining the structures shown in Figure 5.41. When a double layer structure is used (Figure 5.41-a and Figure 5.41-b), both layers can be produced from one and the same a-Se alloy (Se:0.2-0.5 at. % As:very little (≤2ppm) or no Cl). The n- like layer is produced using a low substrate temperature (in some cases around 4 ^{o}C). The i- like layer is deposited at a higher substrate temperature that will ensure reasonable hole transport in this layer. The exact substrate temperatures are found by several trial and error experiments for a given a-Se alloy.

In some cases, the new technology enables x-ray imaging with a single a-Se layer when the readout electronic circuit requires a negative bias across the photoconductor layer (Figure 5.41 c)). In this case the hole injection from the bottom metal/a-Se interface is to some extend suppressed for the cold deposited a-Se layer. In some practical cases, this suppression is sufficient to reduce the dark current to tolerable levels. The application of a single photoconductor for x-ray imaging is a big advantage in the case of high-resolution detectors because the buffer layer (n- like layer) has undesirable effects on the imaging performance of the detector.

When the n- like layer is at the bottom of the structure (Figure 5.41-a) the observed reduction in the dark current is somewhat greater than the case when the cold deposited n- like

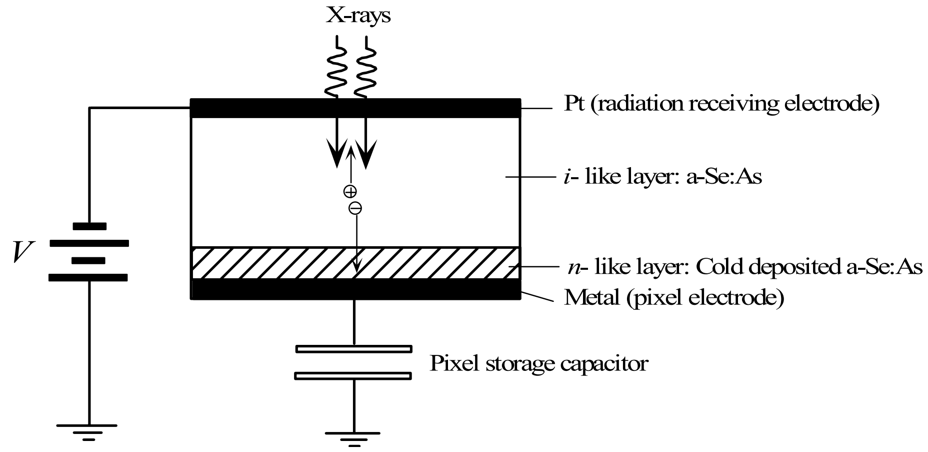

a) Amorphous Se based in detector structure for collecting electrons.

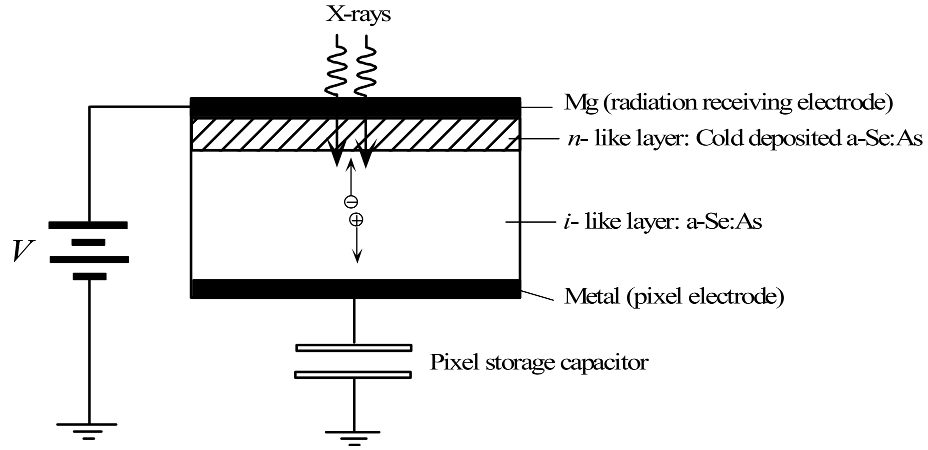

b) Amorphous Se based ni detector structure for collecting holes.

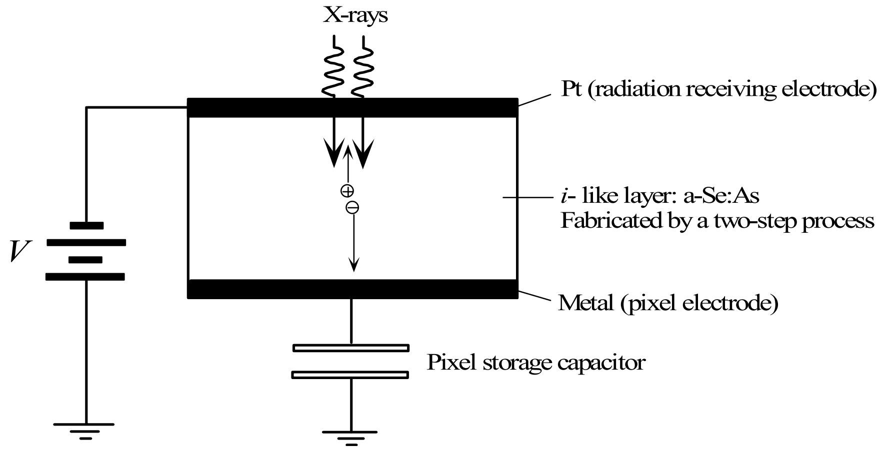

c) Single layer a-Se detector structure for collecting electrons.

Figure 5.41 The most suitable detector structures for fabrication by the cold deposition technology.

layer is at the top side of the structure (Figure 5.41-b). This might be due to changes at the bottom surface of the films related to cold deposited that act additionally to reduce the hole injection from the bottom electrode. The latter enables the use of thinner n- like layers for the case of negative bias, and hence the buffer layer at the pixilated electrode is thinner with very little negative impact on the imaging performance of the detector.

It was experimentally found (subsection 5.3.10) that top electrode fabricated from Pt results in the smallest dark current when the structure is negatively biased and all other conditions are the same. When positive bias is needed, the top electrode can be fabricated from Mg. Such a choice as suggested in reference [14] will minimize the dark currents for the case of positively biased radiation receiving electrode.

The main difference between the technology for dark current reduction in a-Se photoconductor layers and those that previously existed [161, 162] is that the hole blocking properties of the n- like layer have been achieved by changing the deposition conditions instead of changing the actual chemical composition of the layer. This simplifies the production process because single a boat deposition system cab be used, and there is no need to produce specially doped alloys for production of n- like layers, which by its self is a difficult task; and avoids some other issues that will be described in the following subsection.

5.4.2 Levels of Dark Currents in Single and Double layer a-Se X-ray Detector Structures Achievable with the Cold Deposition Technology

In this subsection we provide experimental results from initial tests of the cold deposition technology for dark current reduction in a-Se photoconductor structures described in the previous subsection.

As discussed in subsection 5.3, the dark current *I* in a simple single layer metal/a-Se/metal structures depends not only on the applied field but also on time from the instant of application of the bias; $I = I(t)$. In detector applications, usually the bias is applied and kept on the detector for long times e.g. at least longer than 300 s. Figure 5.42 shows typical *J-F* (current density vs. field) curves obtained from a cut through a family of *I-t* curves 300 s after the application of the bias voltage (see subsection 4.4 for more details) for several Al/a-Se/Pt structures produced from selenium alloys that contained no Cl. The single i- like was deposited on a heated substrate ($T_{substrate}$ = 60 °C) from Se-0.5%As alloy, which resulted in $\tau_h \sim 80$ μs and $\tau_e \sim 400$ μs. This single layer exhibits dark currents that are 2-3 orders of magnitude greater than

~10^{-10} A cm^{-2} that are needed in detector applications over operating fields greater than 5 V/μm. Figure 5.42 also shows the *J-F* data points for an single n- like layer produced from the same alloy (Se-0.5%As) as the single i- like layer by cold deposition; in this case $T_{substrate} = 25$ °C. The hole and electron lifetimes in this layer were measured to be $\tau_h \sim 0.8$ μs and $\tau_e \sim 300$ μs respectively. The *J-F* data for a double layer ni- like detector structure are also shown in Figure 5.42. This particular detector structure was recently used in prototype detectors for slot scanning x-ray imaging [11]. Both layers in the latter structure were produced from the Se-0.2%As alloy. The n- like layer was deposited at a substrate temperature of $T_{substrate} = 7$ °C and is 20 μm thick.

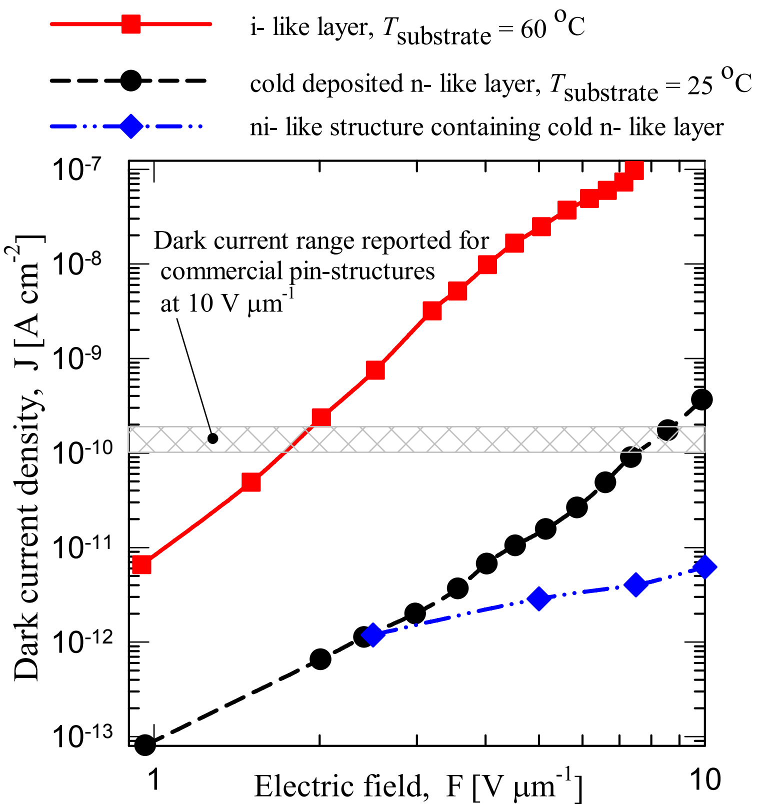

Figure 5.42 Current density vs electric field characteristics of thee different a-Se based detector structures, all fabricated from Se:As no Cl alloys. ■ - Simple Al/a-Se/Pt structure produced from Se-0.5%As no Cl alloy at $T_{substrate} = 60$ °C, which is an i- like layer ● - An n- like layer produced from the same alloy (Se-0.5%As no Cl) by cold deposition in which $T_{substrate} = 25$ °C. ♦ - An ni- like structure produced as a sister sample for one of the x-ray detectors described in [11]. Both layers are produced from the same alloy (Se-0.2%As no Cl). The n- like layer was deposited at $T_{substrate} = 7$ °C and is 20 μm thick. The i- like layer was deposited with $T_{substrate} = 40$ °C and is 110 μm thick. The dark currents measured and reported for commercial selenium based pin- like structures at 10 V μm^{-1} typically lay in the hatched area. The smallest x-ray exposures of interest for mammography will produce currents that are slightly bigger than those corresponding to the upper end of the hatched area if the thickness of the a-Se photoconductor is about 200 μm and the applied bias is greater than 5 V μm^{-1}.

The i- like layer was deposited at a substrate temperature $T_{substrate}$ = 40 °C and is 110 μm thick. The n- like layer in this structure has a hole lifetime $\tau_h \sim 0.6$ μs and $\tau_e \sim 300$ μs. The lifetimes measured in the i- like layer were $\tau_h \sim 6$ μs and $\tau_e \sim 400$ μs. It is worth mentioning that the electron transport in the cold deposited n- like layer is much better than the electron transport measured in commercial alkali metal doped n- like layers (see Table 5.2). This can potentially be a big advantage for the case of high resolution image detectors with fast dynamic pixel readout such as CCDs working in TDI mode.

It is clear from Figure 5.42 that the dark current in the double layer ni- like structure at 10 V/μm is almost an order magnitude lower than that in the simple cold deposited n- like layer. The dark current in the ni- like layer produced in the described manner is somewhat lower than the typical values reported for pin- like structures at the same field (hatched area in Figure 5.42). The smallest x-ray exposures of interest for mammography will produce currents that are slightly bigger than those corresponding to the upper end of the hatched area in Figure 5.42 if the thickness of the Se photoconductor is about 200 μm and the applied field is larger than 5 V/μm.

However, we have to admit that the direct comparison between the dark current densities for the commercial pin- like structures and the ni- like layer based on the results presented in Figure 5.42 is not fair. The buffer layer approach for dark current reduction addresses only the injection component of the currents and can not suppress currents that are due to thermal generation of carriers in the bulk of the sample. The dark current density due to thermal generation of carriers in the photoconductor is proportional to the thickness of the sample. The ni- like structure in Figure 5.42 is only 130 μm thick while a typical commercial pin- like structure for general radiography can be more than 700 μm. That difference in the thickness accounts almost in total for the observed difference in the dark current densities at 10 $V\mu m^{-1}$ between the commercial pin- like strucures and the ni- like structure based on the cold deposition technique. The small difference that still remains after taking into account the difference in the thickness between the samples can be attributed to the differences in the bottom electrode interface. A commercial pin- like structure is typically grown on ITO layer that serves as the bottom electrodes. The cold deposited ni- like structures were grown on an Al film, to imitate the metal bus on top of the CCD readout chip. As described in subsection 5.3.9, the interface Al/Al_2O_3/a-Se might have additional hole blocking properties.

Taking into account of all the differences, we have to conclude that the cold deposition technique for dark current reduction gives very similar results with respect to the observed magnitude of the dark current densities as the commercial pin- like structures [161] and the double layer structures containing Sb_2S_3 charge transport layer [162].

The success of all methods for dark current minimization proposed so far [161, 162, 163] is attributed mainly to the successful reduction of the hole injection rate from the positive electrode. It is difficult to explain all experimental findings connected to the reduction of the dark current in cold deposited a-Se photoconductor structures within the frame of a simple model since the charge transport through a-Se multilayer structures is generally not well understood. Theoretically, two separate mechanisms, or a combination of them, can lead to reduced hole injection and hence to the observed dark current reduction in cold deposited Se layers. The first is related to the modification of the properties of the metal/n- like Se interface in a way that suppresses the hole injection from the metal electrode. Phenomena that can lead to such a modification resulting from the cold deposition have been proposed in the literature [29, 141] and we have already discussed these in subsection 5.3. Their relative contribution to the observed dark current reduction will be investigated in the future.

The second mechanism for the reduction in the current must be related to the modification of the electric field at the interface between the positively biased metal electrode and n- like Se. Due to the poor hole transport in the n- like layer, most of the holes injected from the positive electrode become deeply trapped in this layer and form a positive bulk space charge region near the metal electrode. By virtue of Poisson's equation, the field at the metal interface becomes reduced from its original value, which decreases the hole injection, and hence the dark current. Similar things probably happen in the single cold deposited layers due to increased concentration of hole traps near the bottom interface.

The reduction in the hole range, as we have already discussed in subsections 5.2.3.3 and 5.2.3.4 with decreasing $T_{\mathrm{substrate}}$ is due almost totally to the reduction in the hole lifetime τ_h. Thus, lower substrate temperatures must result in a higher concentration of deep hole traps N_t and mild ($T_{\mathrm{annealing}} \sim T_g$) annealing for approximately 1 hour seems to have a negligible effect on N_t. At the same time, cold deposition does not increase the concentration of deep electron traps. Many attempts have been made to relate the electron and hole traps to various structural defects in a-Se films, the disorder in the amorphous structure including chain ends and the generation of monoclinic nanocrytal inclusions at low substrate temperatures; but the exact nature of these traps still remains unknown and published work is sometimes highly controversial. The latter makes it particularly difficult to formulate an exact physical model that can explain all experimental observations related to the proposed in this work technology for dark current reduction in a-Se photoconductor layers.

5.4.3 Potential Advantages of the Cold Deposition Method for Dark Current Reduction over the Previously Used Multilayer Structures

As described in the previous subsection, the newly proposed technology for dark current reduction limits the dark currents densities in a-Se multilayered structures to approximately the same levels as achieved by the previously existing methods. In addition, the new technology has certain potential advantages that will be briefly discussed below:

- It enables x-ray imaging with a single layer a-Se photoconductors at electric fields 5 V μm^{-1} and slightly higher, which is a distinct advantage for applications in very high resolution x-ray image detectors one example being mamography.
- The new technology is simpler for implementation than the previously existing ones. All the layers can be produced from one and the same starting a-Se alloy and thus a simple single boat evaporation process can be used. The other technologies use two or more materials with different chemical compositions and require evaporation from two or more boats and or co-evaporation to produce a multilayer structure. The cold deposition technology avoids the necessity to produce materials required for the production of n- and p- like layers by previous structures for dark current reduction. Synthesis of such materials on itself is quite complicated, challenging and time consuming process.
- The n- like layers produced with the cold deposition method have some potential advantages compared to the layers produced from alkali metal doped a-Se (as practiced by ANRAD). Both types of n- like layers have similar hole transport (similar hole trapping properties) but electron transport in cold deposited n- like layers is better (the electron $\mu\tau$-product is at least 4 times bigger) than in alkali metal doped n- like layers, which minimizes the unwanted effects due to electron trapping in such layers. The absence of big amounts of As in the cold

deposited n- like layers ensures higher mobility for electrons in such layers which is a distinct advantage when fast readout of the pixels is required, and the readout circuit collects electrons.

- Long-term stability of the cold deposited n- like layers will probably be better compared to those produced from alkali metal doped Se, because the latter material tends to crystallize and, further, positive ions like Na^+ ones can diffuse in the structure, aided by the large applied field.

In subsections 5.4.1 and 5.4.2 we have explained that advantages offered by the new technology are much better pronounced when the radiation-receiving electrode is negatively biased. This is the case for many detector applications because the image readout electronic circuit offers distinct advantages in simplicity and price when designed to collect electrons and hence requiring the use of negatively biased photoconductor structures (radiation receiving electrode negative).

5.4.4 Dark Current Reduction - Summary

The experimental research during this work has enabled us to propose and test a novel method for dark current reduction in a-Se photoconductor structures. The method as well as the previously existing techniques for dark current minimization, reduces the injection component of the dark current through the use of a thin buffer (trapping) layer that is inserted between the x-ray generation layer and the electrodes on its sides. We have proven that efficient hole trapping layer (n- like layer) can be fabricated in two steps: the deposition of a-Se on cold substrate and mild post annealing. Such cold deposited n- like layers can replace the alkali metal doped Se:As n- like layers in commercially used multilayer a-Se photoconductor structures. The new method leads to x-ray imaging with simple single, ni-, and in- like structures. The electron injection by the negative electrode is minimized by proper selection of the electrode metal. Thus the simple cold deposited single and double layer structures can be produced by the evaporation of only one suitably chosen Se:As alloy. We achieve different charge transport properties of i- like layer and n- like layer by changing the deposition conditions during fabrication. In particular we can change the substrate temperature to switch from n- like layer production to i- like layer production and vice versa. Thus a simple single boat evaporation system can be used for the production of the photoconductor structure. In all previous methods, materials with completely different chemical composition are used for the production of different layers and that requires the use of multi-boat evaporation. In addition, materials suitable for fabrication of buffer layers have to be synthesized and produced which on its own is a complicated task.

The simple ni- like structures proposed by us reduce the dark currents to approximately the same levels that can be achieved with commercial pin- like structures based on alkali metal doped n- like layers or double layer structures containing Sb_2S_3 as charge transport layers.

The cold deposited n- like layers have potential advantages over alkali metal doped n- like s that are related to the absence of alkali metal ions. The advantages include better electron mobilities and lifetimes in the cold deposited n- like layers and potentially better long term stability to crystallization and drift.

5.5 Image Characteristics of Pilot X-ray Detectors

5.5.1 Introduction

The cold deposition based technology described in subsection 5.4 was developed and tested as a part of a bigger project aiming at the development of high resolution (20 lp/mm) digital momographic detectors for use with slot scanning digital x-ray machines.

Currently existing detectors for slot scanning imaging are of indirect type. They utilize CCD readout circuits working in Time Delayed Integration (TDI) mode coupled to phosphors that makes them sensitive to the x-rays. The lateral scatter of light produced in the scintillation events limits the resolution of such indirect detectors to about 8 lp/mm in spite of the fact that the size of the pixel on the CCD in some cases allows imaging with much higher resolution.

The goal of the project was to develop a direct conversion detector for slot scanning imaging based on a CCD readout circuit coupled directly to an a-Se photoconductor. The charge created in the photoconductor by the x-rays is collected and injected in the CCD wells by the applied electric filed with almost no lateral scatter and such detectors have the potential of achieving very high resolution. After some preliminary research [13], a-Se was selected as the photoconductor because of its high intrinsic resolution and due to the fact that it can be conveniently coated onto the CCD by vacuum deposition which is a distinct technological advantage.

More details on the slot scanning technique for x-ray imaging, TDI readout technique, and the pixel structures of direct conversion x-ray detectors with CCD readout are provided in APPENDIX A.

Several different CCD chips fabricated at DALSA Inc., Waterloo, Ontario, Canada were used as image readout circuits in the different stages of the project. In this subsection we will present results from tests with two prototype CCDs. The first of these two types of CCD chips was basicaly a line detector known under the code name SELMA. The used version of the chip contained 400 detector elements with size 20×1000 μm arranged in one line. The pixel electrodes in the line were parallel along their long side and the gap between them was 5 μm. Further details and pixel structure (see Figure A.5 in APPENDIX A) for this type of CCD chips are given in [11]. The second type of prototype CCD chips was known under the code name SALLY. These chips are array detectors with an image area of 5×10 mm. Pixel size in SALLY CCDs was 20×20 μm and the pixel pitch was 25 μm. Both SELMA and SALLY CCD chips had an aluminium metal bus to interface the a-Se photoconductor layer. Both types of chips were designed to collect the electrons generated by the absorbed x-rays in the photoconductor layer. Thus, the a-Se layers on top of the CCDs had to be optimized for operation under a negative bias. The chips were functionally tested at NOVA R&D Inc, Riversdale, California, USA. The a-Se based photoconductor was fabricated on top of the CCD chips in our laboratory using the cold deposition technology for dark current reduction after which a radiation receiving Pt top electrode was sputtered on top of the a-Se layer to complete the detector structure. The Se coated detectors were shipped back to NOVA R&D Inc for functional testing, mounting in carrier packages and wire bonding.

The performance of the detectors was studied by our partners at Sunnybrook Hospital, Toronto, Ontario, Canada. Figure 5.43 shows a photograph of a SALLY detector PCB card and the data acquisition system PCB board used to evaluate the performance these detectors.

The x-ray detector imaging performance is most often quantitatively characterized in terms of its Detective Quantum Efficiency (DQE) and Modulation Transfer Function (MTF). MTF is a measure for the spatial resolution, while DQE is a measure of the signal-to-noise ratio, contrast resolution and dose efficiency. An imaging system is best characterized by examining the corresponding MTF and DQE curves over a range of spatial frequencies, because one number at a single spatial frequency cannot adequately describe the imaging performance of a

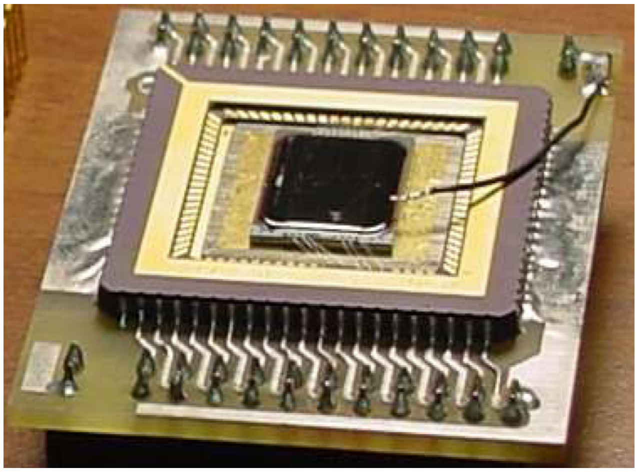

a) A pilot x-ray detector based on SALLY CCD and an a-Se photoconductor layer produced by the cold deposition technology described in this work. The detector is mounted in a ceramic chip carrier and wire bonded. The PCB card on which the chip carrier is mounted provides a means to conveniently connect the x-ray detector to the data acquisition and cooling systems. The thick wire supplies the HV bias to the radiation receiving electrode which is not visible in the picture. The actual connection between the electrode and the HV wire is accomplished by the use of a small diameter wire that can not be seen in the photo. The latter wire is glued to the radiation receiving electrode of the detector. The spot of glue holding the wire to the electrode can barely be seen in the picture close to the bottom edge of the Se area. However, both the tiny wire and the spot of glue connecting it to the top electrode are clearly seen in the x-ray images.

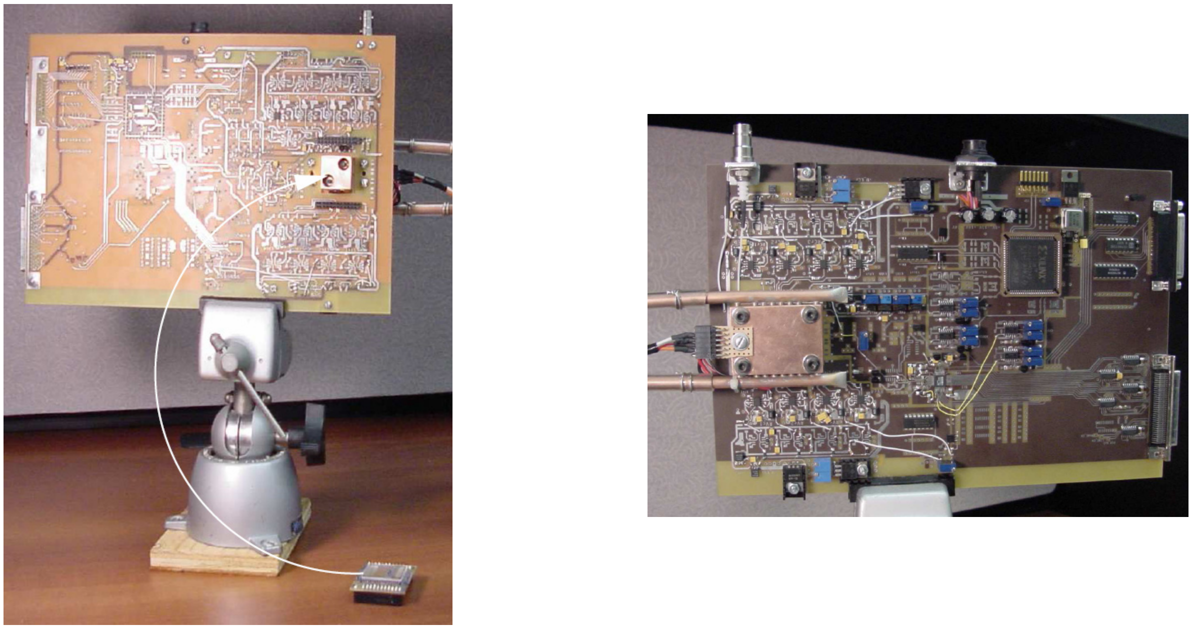

b) SALLY detector data acquisition system. The picture on the left is shows the cooling finger that keeps the chip at about 20 C. The photo on the right shows the component side of the PCB board.

Figure 5.43 SALLY x-ray detector and data acquisition systems. All photographs courtesy of David Hunter, Sunnybrook and Women's Hospital, Toronto.

detector system. Thus the measurements of the DQE and MTF as a function of the spatial frequency are routinely used to determine how well the imaging system captures information over that range of spatial frequencies of interest.

The a-Se layers produced in our lab on top of SELMA and SALLY CCD were about 200 μm thick. The a-Se layer with such a thickness absorbs about 95% of the incident radiation in the mammographic energy range. That value is higher than screen-film cassettes and indirect conversion detectors and the DQE is not expected to be adversely affected, so the first image performance measurements with SELMA and SALLY detectors were focused on measurements of their MTFs, rather than their DQEs. The measurements were performed at the Sunnybrook Hospital, University of Toronto by the method of tantalum edge as described in [11].

Some results of the resolution performance testing of SELMA and SALLY chips will be reported in this subsection together with some results related to the dark current minimization problem.

5.5.2 Dark Current Measurements

The first set of experiments was aimed at the evaluation of the dark current performance of a-Se layers produced by the newly proposed fabrication technology based on the cold deposition technique. The photoconductor layers were deposited on silicon wafer pieces with Al deposited on one of their surfaces to imitate closely the interface between the metal bus of the chips and the photoconductor layer. The dark currents, as well as the x-ray induced currents were measured on these Al/a-Se/Pt structures under negative bias (see Figure 5.41) to evaluate the performance of the photoconductor layer under conditions close to the ones present in a real detector. The investigated conditions have covered a range of applied fields up to 10 $V\mu m^{-1}$. The x-ray induced currents were measured at the lowest exposure rates of interest used in mammography. The results have demonstrated that the dark currents are sufficiently low and that the ratios between the x-ray induced current and dark currents are very reasonable. For example, we have measured ratios better than 200:1 at a bias of 5 $V\mu m^{-1}$.

In a second set of experiments, the influence of the dark current on the performance of the x-ray detectors containing SELMA readout CCD and cold deposited photoconductor structure was studied. A selection of important results is shown in Figure 5.44. The expected

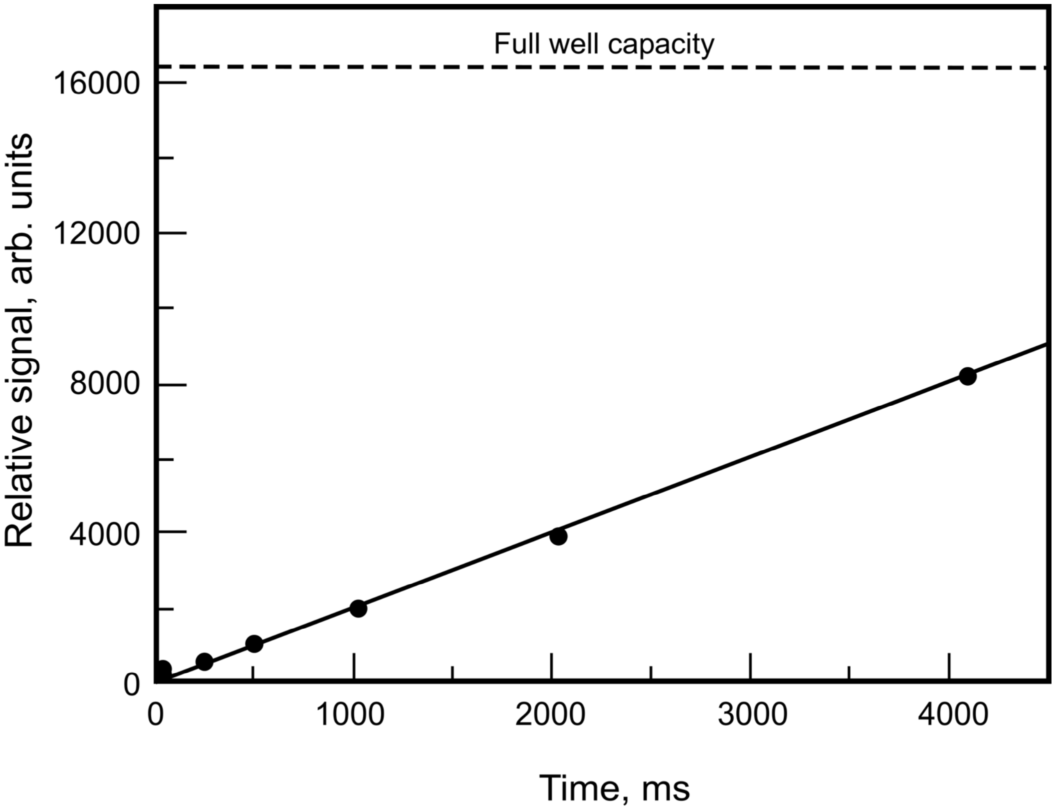

Figure 5.44 The total dark signal in Se coated SELMA CCDs biased at 3.5 V/μm in shown in this figure. The photoconductor utilizes the dark current reduction technology based on the cold deposition technique and has a double layer ni-structure. The n- like layer is 30 μm thick while the thickness of the i- like is about 180 μm. The dark signal represented in the graph has two components. One of them is the dark current trough the Se photoconductor caused by the applied HV bias. The second one is due to the dark current of the CCD chip. The measurements have shown that the dark signal is dominated by the dark current of the CCD chip, due mainly to surface generation of carriers in Si. The typical dwell time of the electric charge in the quantum well of the CCD is expected to be 200 ms or less. Thus the dark signal does not pose a serious problem for the SELMA detector operation. The figure is based on experimental data obtained by our partners at Sunnybrook Hospital, University of Toronto (courtesy of David Hunter).

dwell time for the electric charge in the well of the CCD in a mammographic TDI slot scanning system is about 200 ms. As apparent from Figure 5.44, the dark signal does not pose a serious problem. Another interesting result is that the dark signal for the SELMA devices is dominated by the thermal properties of the silicon (thermal generation in that material) and the contribution of the dark current forced hrough the a-Se layer by the HV bias is very minimal. This observation is important because it allows the used of higher electric fields, or the use of structures with thinner n- like, or even single layer photoconductor structures (see Figure 5.41) to achieve imaging with higher spatial resolution.

5.5.3 Resolution Performance of SELMA X-ray Image Detectors

Photoconductor double layer ni- like structures with different thickness for the n- like layer were manufactured on top of several SELMA CCD chips following the cold deposition method for dark current reduction (see Figure 5.41-a). Photoconductors, having the structure shown in Figure 5.41-c was also produced on several of the SELMA CCD chips. The thickness of the n- like layers in the ni- like structures was in the range from 6 to 50 μm. The x-ray detectors produced in this way were used to study the influence of the blocking layer thickness on the resolution of the detector. It was also interesting to study whether the dark current in an a-Se photoconductor will become high enough to interfere with the functioning of the x-ray detector, especially in the detectors having a double layer photoconductor structure with the thinnest n- like layers and in the detector utilizing a simple single layer structure (Figure 5.41-c).

The MTFs for these detectors were measured and the results were published in [11]. Some of the measured MTFs are shown in Figure 5.45. As intuitively expected, the presence of a thick blocking layer between the pixel electrodes and the x-ray detection layer (i- like layer) deteriorates significantly the resolution performance of the detector. A model was developed to explain the influence of the blocking layer thickness on the MTF of the detector (for details see [11]). The MTF calculated on the basis of that model agrees reasonably well with experimentally measured MTF for the cases of a single layer photoconductor structure, and ni- like structures with n- like layer thicknesses of 30 and 50 μm. Disagreement between the calculated and measured MTFs is observed for ni- like structures having 6 and 16 μm blocking layer thickness. The reasons for the observed disagreements are not clear. Part of them might be related to oversimplifications in the model used to calculate the MTF. Another possible explanation is related to the reproducibility of the charge transport parameters in the produced cold deposited n- like layers. It is known that the quality of a-Se films is related quite strongly to the presence of some trace impurities in the coater. Sometimes conditions that are difficult to account for, such as the history of the vacuum coater system, can have a significant impact on the quality of the produced layers. The reasons for the observed discrepancy will have to be investigated more systematically in the future.

On the positive side, Figure 5.45 demonstrates that SELMA detectors that incorporate

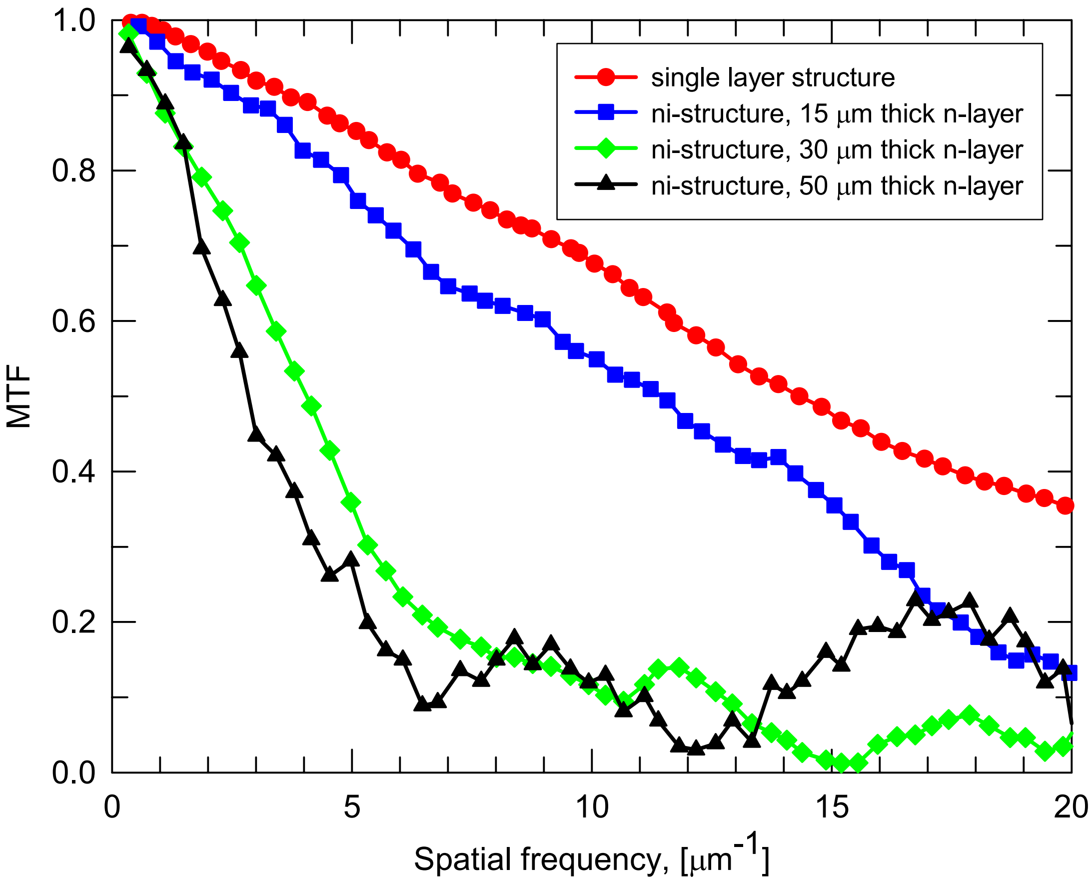

Figure 5.45 Resolution comparison between SELMA x-ray detectors having different a-Se photoconductor structures fabricated on top of the CCD chip. All photoconductor layers were fabricated by the use of the cold deposition technology for dark current reduction. Data were provided by David Hunter, Sunnybrook and Women's Hospital, Toronto.

single layer structure or an ni- like structure with a thin n- like layer are capable of imaging with very high resolution (20 lp/mm).

For all different photoconductor structures involved in the experiments and over the whole rage of applied electric fields (0-5 V/μm), the dark currents forced through the a-Se photoconductor layers in SELMA detectors have never imposed any serious problems for the detector performance.

In Figure 5.46 we have compared the experimentally measured MTF of several commercially available detector systems for mammography with the MTF measured on SELMA x-ray detector utilizing a cold deposited single a-Se photoconductor layer. For all indirect

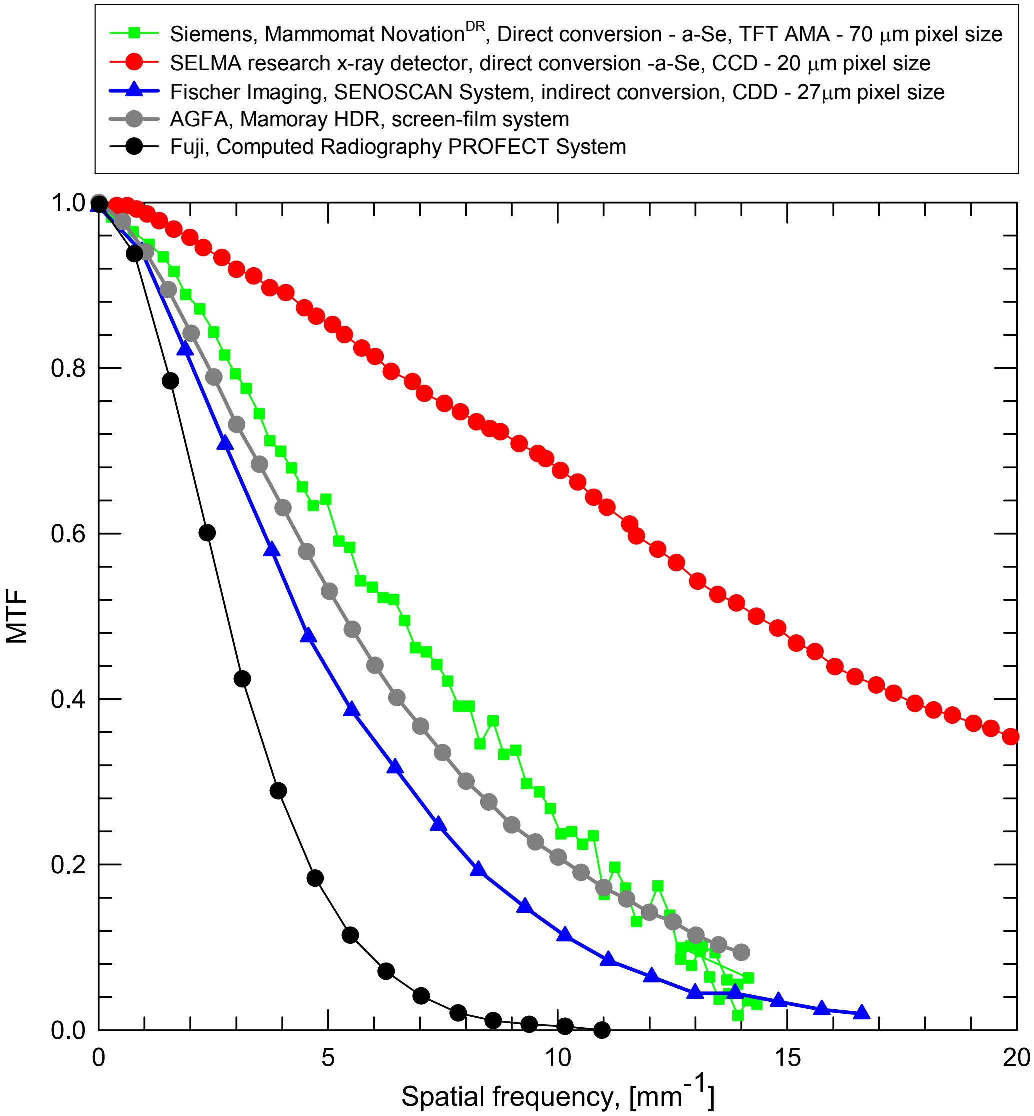

Figure 5.46 Comparison between the MTF measured for SELMA x-ray research detector and for several commercially available detector systems. Data were selectively extracted from: [164] for Siemens Mammomat Novation^{DR} system, [11] for single photoconductor layer SELMA research detector, [166] for Fischer Imaging SenoScan system, and [165] for both AGFA Mamoray HDR screen-film system and FUJI PROFECT computed radiography system.

systems, the lateral spread of light emitted during the scintillation events produced by the x-rays interacting with the phosphor layer (or during the laser readout of the plate for computed radiology system) limits the resolution of such detectors somewhere in the range 10-14 lp mm^{-1}. Note that this limitation is almost totally due to the intrinsic resolution of the phosphor. Both the intrinsic resolution of the film in AGFA screen-film system and of the CCD in the detector of Senoscan imaging system is above 18 lpmm^{-1}.

The red MTF curve for the SELMA detector in Figure 5.46 lies above the MTF curves for all other competing detector systems. This is a clear indication that the SELMA detectors have excellent spatial resolution, much better than those of the other detector systems presented in Figure 5.46. The highest spatial resolution of SELMA detector is due to the smallest pixel size of the CCD readout circuit and to the fact that a-Se has much superior intrinsic resolution than CsI(Tl).

5.5.4 Imaging Performance Evaluation of SALLY Prototype X-ray Detector

SALLY detectors were actually capable of acquiring x-ray images. They have a pixel pitch of 25 μm and an image area of approximately 10 × 5 mm. The a-Se photoconductor layer produced on SALLY chips had the simple single layer structure or double layer ni-structure (see Figure 5.41-a and Figure 5.41-b) of total thickness around 200 μm. The n- like layers in the ni- like structures were very thin (1-2 μm) because that allows imaging with a high spatial resolution and without any associated with the dark current problems up to 1000 V photoconductor bias voltage. Two of the first static images acquired with a SALLY detector are shown in Figure 5.47. These were taken in an attempt to image a PCB (left image) and an apple seed (right image). These preliminary x-ray images demonstrate the potential of SALLY detectors for high resolution imaging of soft tissue. Although some positioning problems are present (only part of the apple seed is in the image field) together with some defects in the particular CCD, one can notice a lot of details in the PCB image and, more importantly, in the image of the seed. The tiny HV wire and the conducting glue making the electrical contact with the top Pt electrode can also be very clearly seen in the image.

The spatial resolution of an x-ray image detector can be routinely evaluated by imaging of commercially available resolution phantoms. These phantoms have built in line patterns with different spatial frequencies. Taking x-ray images of the line patterns provides a fast and convenient way to study the spatial resolution of an x-ray detector.

Figure 5.48 shows x-ray images of small areas of a resolution phantom taken with a SALLY detector. The imaged line pattern areas have spatial frequencies of 3, 5 and 16 lp mm^{-1}. Since the lines in all the images can be clearly distinguished the experiment confirms that the spatial resolution of SALLY detector is indeed close to 20 lpmm^{-1}.

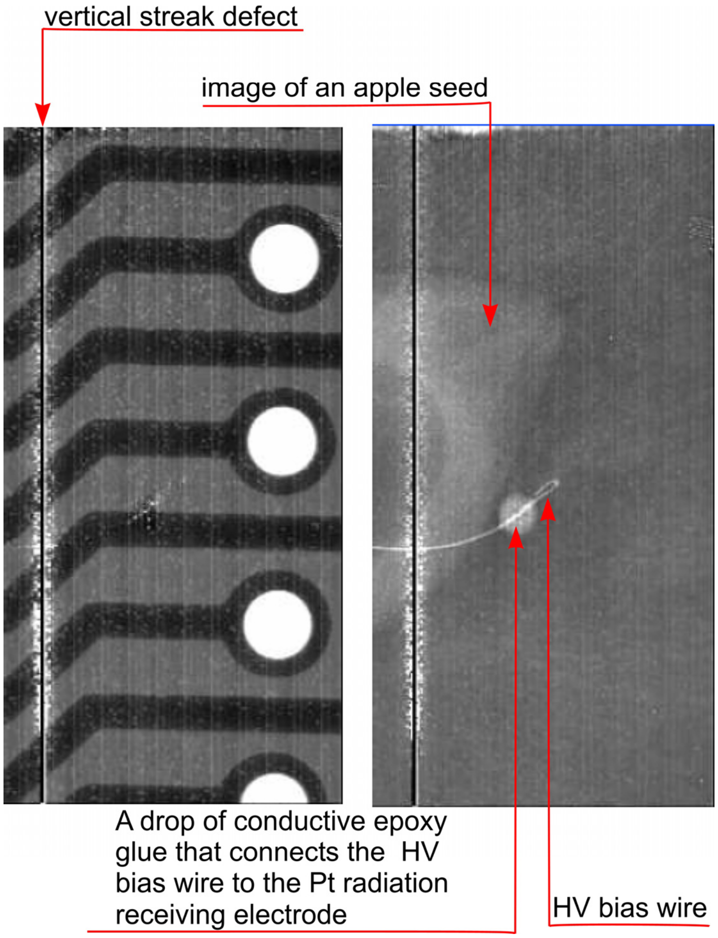

Figure 5.47 Image of a printed circuit board (PCB) with the holes and the metal tracks (on the left) and attempt to image an apple seed (on the right). Both images are obtained with the energy of the x-rays in the mammographic range with a SALLY detector. The CCD has a vertical streak defect. The HV bias wire and the epoxy glue holding it to the top contact are also visible. Image courtesy of David Hunter, Sunnybrook and Women's Hospital, University of Toronto.

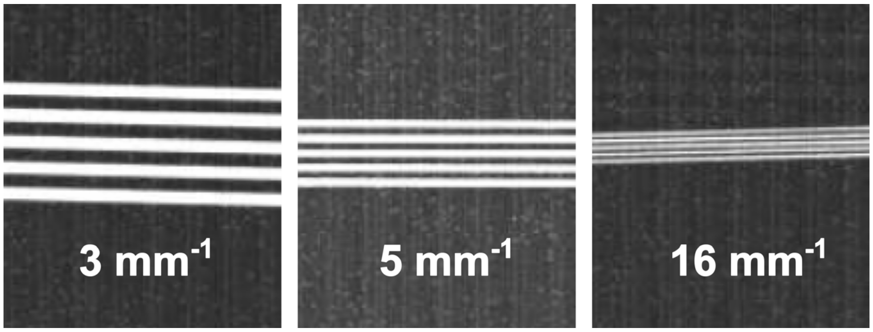

Figure 5.48 Spatial resolution evaluation for a SALLY x-ray image detector based on resolution phantom imaging. The line pattern x-ray images were taken in snap shot mode and are differently scaled. Images courtesy of David Hunter, Sunnybrook and Women's Hospital, University of Toronto.

Figure 5.49 presents x-ray images showing a part of a resolution bar pattern. The images were taken on a Faxitron® Specimen Radiography System and on the SALLY prototype imaging device. The resolution displayed can be seen on the numbers on the left side in the images and ranges from about 5 lp/mm to 8 lp/mm. The choice of window and level that allows fair conditions for detector performance comparison are somewhat subjective and difficult because the Faxitron images could be stretched to emphasize any existing resolution. Such adjustment was not necessary with the SALLY prototype imaging system. The image taken with the SALLY detector was comprised of 100 separate image sections taken in a step and shoot mode. There are alignment offsets. Also the bias wire is seen in the image segments. The wire appears 6

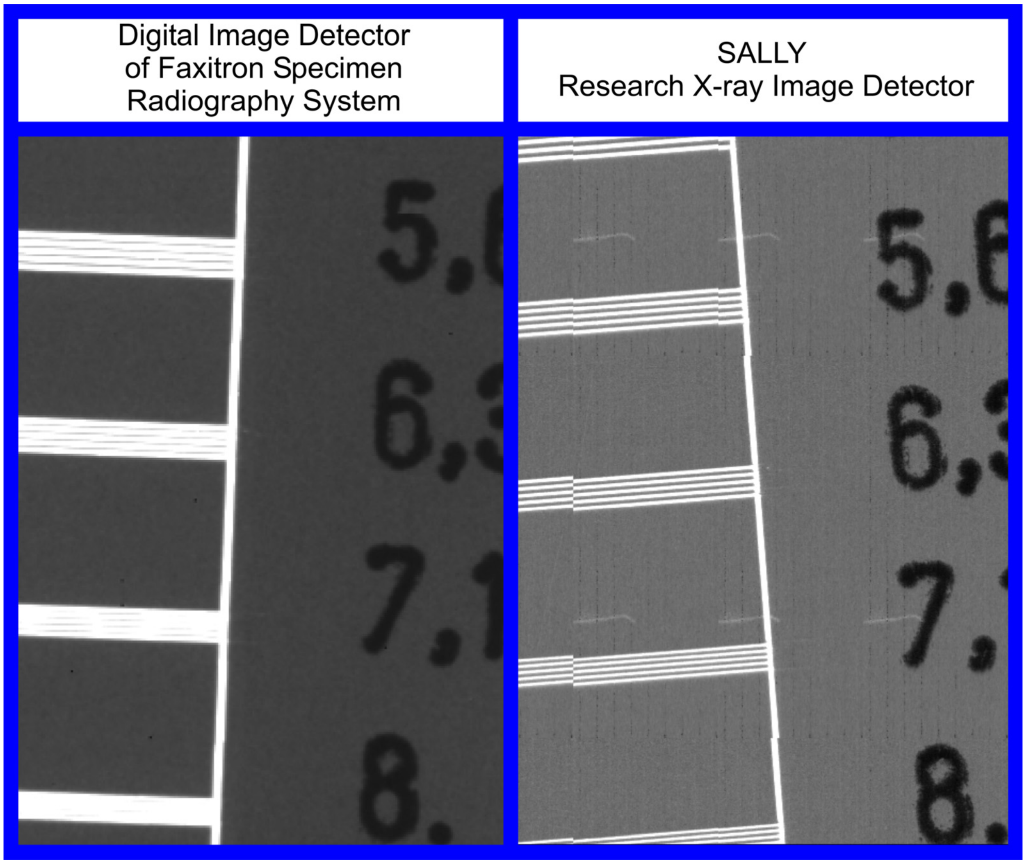

Figure 5.49 SALLY-FAXITRON image comparison. The image on the left was taken with the digital detector FAXITRON® Specimen Radiography System. The image on the right was taken by SALLY prototype detector system in a step and shoot mode. The SALLY image consists of many "stitched" together images and has some alignment problems. The HV bias wire can be seen in the image. This particular SALLY CCD shows some small vertical streak defects. Images courtesy of David Hunter, Sunnybrook and Women's Hospital, University of Toronto.

times in two rows situated just above the patterns with frequency 5.6 lp mm^{-1} and 7.1 lp mm^{-1} in the portion of the SALLY image shown in

Figure 5.49. The SALLY CCD in this particular detector has some vertical streak defects appearing as very thin dark vertical lines.

However, in terms of resolution, the SALLY image is clearly superior (see the amount of fine structure in the "numbers" that can be observed in the image taken with SALLY detector). This was expected because the digital x-ray image detector in Faxitron system is specified to have resolution of only 10 lp mm^{-1}.

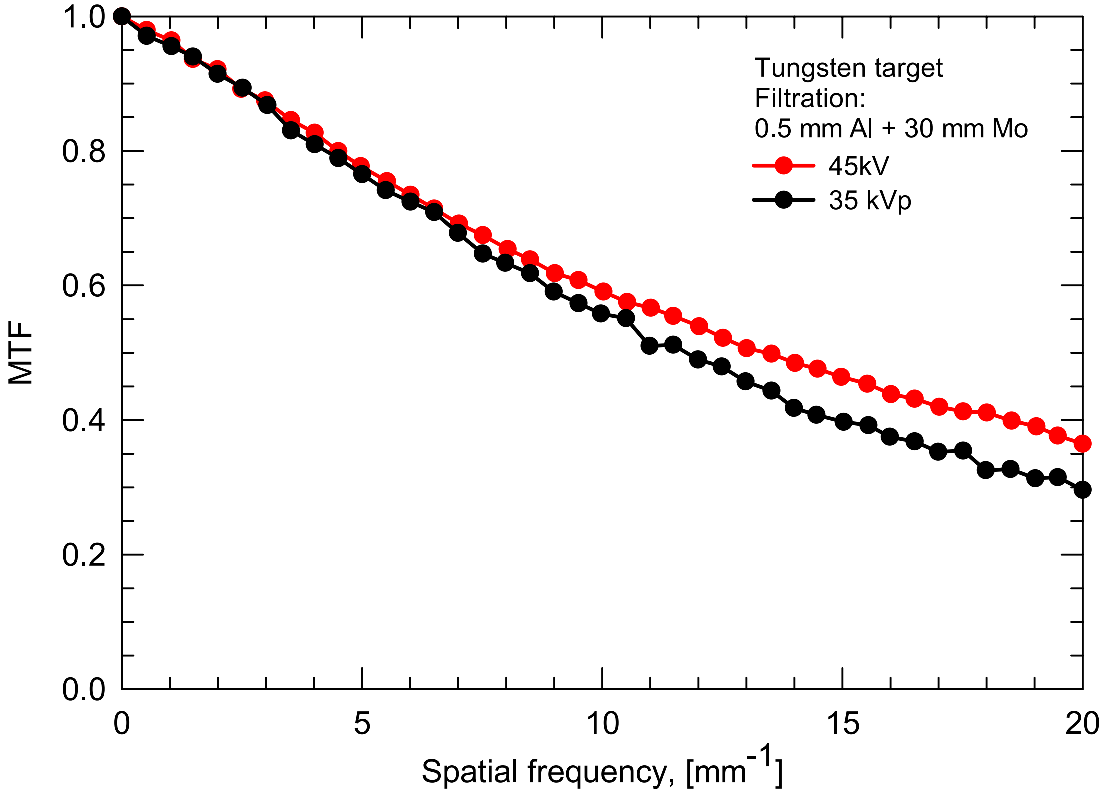

Figure 5.50 MTFs for a single layer SALLY prototype detector measured for two different qualities of the x-ray beam. Data courtesy David Hunter, Sunnybrook and Women's Hospital, Toronto.

MTF and DQE of the SALLY x-ray image detector were measured to further characterize the performance of these prototype detectors. Two MTF curves measured for different x-ray beam qualities are shown in Figure 5.50. These MTF are very similar to the MTF curves for the SELMA detector shown in Figure 5.46 and simply confirm that the SALLY detector is capable of imaging with a resolution that is much higher than the one achievable with the commercial detector systems with MTFs shown in Figure 5.46.

The DQE efficiency for the SALLY detector was measured by David Hunter, Sunnybrook Hospital, University of Toronto under the following conditions: 35 kV tube potential, tungsten target, 0.5 mm Al + 0.03 mm Mo filtration, mean energy of the x-ray beam 22 keV, and 28.8 mR exposure. The measured DQE is shown in Figure 5.51 together with DQEs

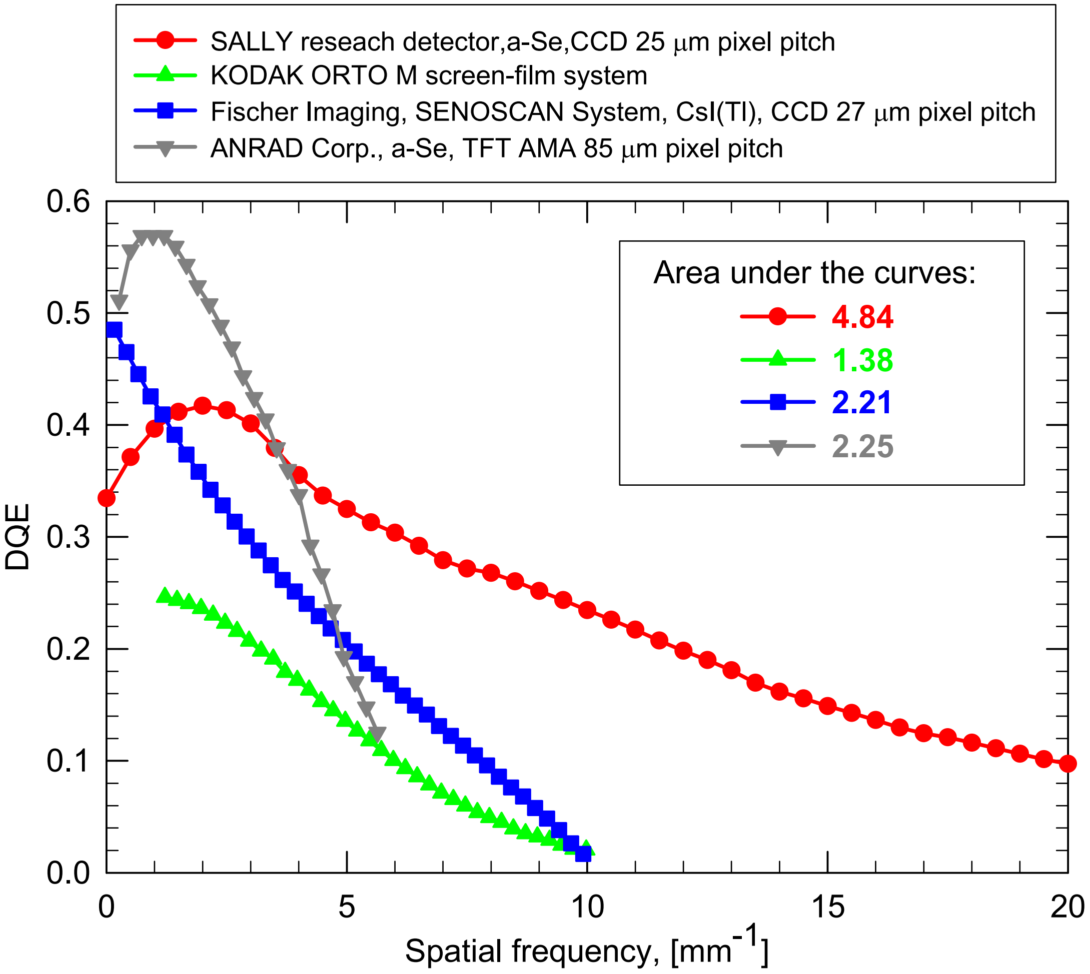

Figure 5.51 Comparison between a DQE curve measured for SALLY detector and DQE curves reported in the literature for several commercial detector systems for mammography. The conditions of the measurements were selected to be as close to each other as possible. SALLY DQE data courtesy David Hunter, Sunnybrook and Women's Hospital, Toronto. The DQE data for KODAK ORTO M screen film system and for Fischer Imaging System were taken from [166]. The DQE data for ANRAD Corp. detector were taken form [167].

for several other detector systems reported in the literature and measured under similar experimental conditions. As seen from the figure, the values for the DQE measured on the

SALLY detector are somewhat lower at spatial frequencies up to 3.5 lp mm^{-1} when compared with the DQE values reported for ANRAD Corp. detector. Since this is the first time the DQE on a SALLY detector has been measured, we are not sure whether the observed relatively low values are objective or they are due to factors connected with this particular detector. For example, we have observed structural noise generated by defects in the particular CCD (vertical columns) and structural noise that appears in the image due to defects in the top electrode. The relative contribution of these two noise sources and the electronic noise in the measured DQE values are to be studied in the future.

The task of comparing the DQE curves is not an easy one. However, over an ensemble of images (a large set of mammograms) what is likely to matter is the integral over the DQE curve [166]. Thus, if we use the area under the DQE curve as a measure of system effectiveness, Figure 5.51 clearly demonstrate the superior performance of SALLY detector over the rest of the detector systems shown in the same figure.

5.5.5 Summary

In subsection 5.4 we have proposed and described a technology for dark current reduction in a-Se x-ray photoconductor layers based on the cold deposition technique. The results from the first practical implementation of this technology were described in this subsection (0). The prototype detectors based on SELMA and SALLY experimental readout CCD chips have demonstrated an excellent imaging performance, as it was described in subsections 5.5.3 and 5.5.4. This performance is in part due to the properties of the photoconductor layers fabricated on the CCD chips in our laboratory. The development of an a-Se photodetector layer which has negligibly small dark current at high electric fields was a key factor in the realization of the high resolution x-ray detectors.

6. SUMMARY AND CONCLUSIONS

6.1 Introduction

The objective of this work was to find a suitable way for dark current reduction in a-Se photoconductor devices for application in high resolution medical x-ray image detectors through studying the electrical properties and durk currents in various metal/a-Se/metal devices as a function of deposition conditions, alloying and other technological parameters.

Based on the results of the work described above, a new technology for the fabrication of multilayer a-Se structures with low dark currents was proposed and tested in a prototype a-Se based high-resolution x-ray image detectors. The new technology eliminates the need of doping with alkali elements to suppress the hole transport in the n- like layer and the complications associated with alkali doping. Consequently, the fabrication method proposed by us can have several potential advantages over the existing technologies for the fabrication of a-Se based multilayer photoconductor structures with low dark currents. The initial test results on the imaging performance of the prototype detectors were very promising (A patent application was filed [168].).

6.2 Effects of Alloying and Doping on Charge Transport in Vacuum Deposited a-Se Films

The effects of alloying and doping with several elements on charge transport in vacuum deposited a-Se films were studied by TOF and IFTOF techniques. The results from these investigations will be summarized below.

6.2.1 Effects of Arsenic

It was found that arsenic addition in the amounts 0.1-0.7 wt % increases the electron lifetime and decreases electron mobility when added both to pure and stabilized (Se:As:Cl) selenium. Overall, As increases the electron mobility-lifetime products (ranges) because the fractional increase in the electron lifetime is more than the observed decrease in the electron mobility. In very limited number of cases, when As is added to pure Se with extremely good starting electron transport, there can be deviations from the tendency described above. In such cases, the electron transport can remain unaffected or can even deteriorate.

The effect of As addition on hole transport is opposite to the effect on electron transport. Arsenic leaves the hole mobility relatively unchanged but causes the hole lifetime to decrease; as a result, the hole mobility-lifetime product also decrease as the amount of added As increases.

6.2.2 Effects of Chlorine

The effects of Cl addition on charge transport in vacuum deposited selenium films are somewhat opposite to those of As.

Chlorine in the amounts 2-70 ppm drastically deteriorates electron transport in selenium both when added to pure or stabilized (Se:As) material. The effect is dominated by the decrease in the electron lifetime, since Cl in the amounts specified above does not strongly affect the electron mobility especially in cases when added to stabilized a-Se material.

When Cl is added to stabilized selenium (Se:As) it forces a significant increase in the hole lifetimes, leaving hole mobility unchanged. The total effect in such cases is a significant increase in the hole range. However, when Cl is added to pure Se, the effect on hole transport is not so clear. In such cases Cl tends to decrease the hole mobility slightly, while the effect on the hole lifetime shows significant variations with the starting pure Se material and alloying conditions. Anything between a slight increase to slight decrease in the hole lifetime can be observed. The magnitude of the effect is much smaller compared with the case when Cl is added to stabilized a-Se.

6.2.3 Combined Alloying with Arsenic and Chlorine

Our results show that combined alloying with As (0.1-0.7 wt %) and Cl (2-60 ppm) can be a very effective tool for the control of the carrier ranges in vacuum deposited films from stabilized a-Se. The addition of As generally improves the electron transport in the films at the expense of deteriorated hole transport. The deterioration of hole transport caused by the As dopant can be compensated for by the addition of Cl. Thus the combined addition of As and Cl results in improved mobility-lifetime products for both electrons and holes. In general terms, these results are in good agreement with the ones previously published in the scientific literature.

The main difficulty accompanying the alloying process is the very strong dependence on the properties of the starting pure Se material which makes the exact determination of the right amounts of As and Cl additions needed a very difficult task. The simultaneous addition of As and Cl in arbitrarily big amounts will not have the same beneficial effect on the carrier transport. Our experiments indicate that, when added in large amounts both As (above 1 wt %) and Cl (above 100 ppm) force changes in a-Se which result in dispersive transport in the films for both types of charge carriers.

6.2.4 Effects of Oxygen

The effects of oxygen on charge transport in films produced from pure Se were investigated. This was motivated by the fact that oxygen impurities are very likely to be present in any pure (99.999%) a-Se as a "side effect" of the technological processes used for the recovery and purification of Se.

Unlike previously published reports in the scientific literature, we have found that the addition of oxygen even in amounts smaller than 50 ppm can have a very strong impact on both electron and hole transport in a-Se films. We observe that oxygen deliberately added to pure Se in amounts specified above causes a deterioration in electron transport and improves hole transport. Both effects are caused mainly by changes in the carrier lifetimes.

The effect strongly resembles that due to the addition of Cl into Se:As:Cl alloys; however when Cl is added to pure Se it causes deterioration of the electron transport but the effect on hole transport is relatively small and not clear (it can be in both directions).

We have initial data that indicate that in films produced from oxygen containing selenium, charge transport changes differently as the films age compared to the changes in charge transport in ageing films produced from stabilized a-Se. As a result of ageing, the charge transport for both electron and holes slightly improves in films produced from Se:As:Cl alloys. In the films produced from oxygen containing pure Se, the electron mobility-lifetime product increases as the films age while the hole range decreases. Such changes correlate well with the data published in the literature, which demonstrates that oxygen is switches its bonding configuration in ageing a-Se films.

6.2.5 Charge Transport in N- and P- Like Layers in Commercial a-Se PIN- Like Structures

Charge transport in n- and p- like layers in commercial a-Se based pin- like structures was also investigated. The n- like layers were produced from Se:As material with alkali doping, while the p- like layers were produced with heavy Cl doping or by the evaporation of As_2Se_3. Details on the concentration of dopants were not supplied for the investigated commercial pin- like structures.

We have found that electron ranges in the p- like layers is 2-3 orders of magnitude smaller than the hole range. At the same time, hole ranges in the n- like layers is only, at most, one order of magnitude smaller than the electron range in that layer. Thus, a-Se based n- like s with good qualities are harder to manufacture than a-Se p- like layers.

Our TOF measurements on the pin- like structures have also shown that the hole transport in the p- like layer is much worse that the hole transport in the i- like layer and at the same time the electron transport in the n- like layer is much worse than the electron transport in the i- like layer. The latter peculiarities are "side effects" of heavy As or Cl doping and/or fabrication conditions.

6.3 Effects of Preparation Conditions on Charge Transport in a-Se Films

The influence of preparation conditions on charge transport in vacuum evaporated a-Se films was investigated in the course of this work. The emphasis was placed on the two parameters that can be easily changed in every vacuum system – the boat temperature and the substrate temperature.

6.3.1 Effects of Boat Temperature on Charge Transport in Vacuum Deposited Films from Pure Selenium

Due to fractionation issues, it is not possible to freely vary the boat temperature when films from stabilized a-Se are to be prepared and this is the reason that the dependence of charge transport parameters on the boat temperature was studied for films produced from pure Se material. In our coater, for source-to-substrate distance of 16 cm, variations of boat temperature in the range 190-250 °C changes the evaporation rate in the range 0.1-10 μm/min and the composition of the Se vapor as well.

For films deposited at high substrate temperatures ($T_{\text{substarte}} > T_g$), variations of boat temperature and hence in the evaporation rate in the ranges specified above did not cause any systematic change in charge transport properties of the produced films. We observe a big scatter in the data which can be attributed to the huge sensitivity of the properties of the films produced from pure Se material to the residual atmosphere in the chamber and hence to the coater history.

6.3.2 Effects of Substrate Temperature on Charge Transport in Vacuum Deposited a-Se Films

Charge transport in vacuum deposited films produced from stabilized a-Se and from pure Se was investigated as a function of the substrate temperature in the range 0-80 °C.

We have found that good quality a-Se films can be produced by evaporating Se on a cold substrate ($T_{\mathrm{substrate}} < T_{\mathrm{g}}$). The production process involves two steps: first, the evaporation of the film onto a cold substrate and second, mild ($T_{\mathrm{annealing}} \sim T_{\mathrm{g}}$) annealing with a duration from one to several hours. Films produced using the procedure described above have resistance to crystallization similar to the one observed for films produced on hot substrates as estimated with DSC measurements.

It has been demonstrated that the mild post annealing process does not improve the hole transport in the studied films while electron transport does not deteriorate due to the annealing.

The decrease in the substrate temperature has a huge impact on the hole transport. It decreases the hole range about two and more orders of magnitude. At the same time, the electron transport remains relatively unaffected. Films produced at sufficiently low substrate temperatures demonstrate clearly an n- like type transport ($\mu_h \tau_h < \mu_e \tau_e$). It is possible to achieve deep trap limited hole transport if the substrate temperature during the deposition is kept well below the glass transition temperature, which depends on the material. The latter behavior of the charge transport has been observed for films produced from Se:As, Se:As:Cl and pure Se materials.

The temperatures at which the transport switches from p- like type to n- like type and the temperature at which the hole transport becomes deep trap limited depend on the material. Films evaporated on substrates kept at temperatures 20-30 °C from alloys that contain only As have, in most cases, deep trap limited hole transport. The films produced from Cl containing alloys demonstrate deep trap limited hole transport only if produced on substrates kept at temperatures around 0 °C or lower.

We have found that the changes in the Se structure related to the deposition of the film onto a cold substrate are quite persistent. For example, if Se:As alloy is evaporated onto a cold substrate (4°C), and then the material is reclaimed and re-evaporated onto hot substrates (60°C) the resulting films demonstrate hole transport that bares no resemblance to the one observed in films produced directly from the starting Se:As material on substrate kept at 60°C. At the same time the charge transport in films produced from cold reclaimed material on hot substrates is very close to the one observed in films produced directly from the starting material on a cold substrate (4°C).

6.4 Dark Currents in Metal/a-Se/Metal Devices

Dark currents in single layer metal/a-Se/metal devices have been investigated towards achieving a better understanding of the mechanisms that control the currents.

6.4.1 Dark Current *I-t* Curves

We have presented results from different experiments on dark currents in metal/a-Se/metal devices. We have studied the *I-t* curves in a-Se films as a function of the material from which the films are produced, as well as a function of the preparation conditions. We have observed decays in the *I-t* curves that are as long as 20000 s and even after that it is difficult to say that the dark current becomes constant. The magnitude of the decay and the shape of the *I-t* curves depend on the applied bias, on the Se material, and on the metals from which the top and bottom electrodes are produced. We not been able to observed fully symmetrical *I-t* curves with respect to the polarity of the applied bias even when the metal/a-Se/metal device was produced to be symmetrical. For some materials and preparation conditions the dark currents are bigger when the top electrode is positive, for other materials and preparation conditions, the dark currents are bigger when the top electrode is negative.

The substrate temperature plays an important role in determining the properties of the film. Films produced at sufficiently high substrate temperatures have higher dark currents when the top electrode is negatively biased, while the opposite is generally true if the films are produced at sufficiently low substrate temperatures. The asymmetric dark currents for negative and positive bias can be explained with the asymmetric properties of the top and bottom metal/a-Se interface and/or with asymmetric non-uniform distribution of various microcrystalline inclusions and/or other carrier traps across the thickness of the a-Se films. A major factor that can contribute to the asymmetry between the top and bottom metal/a-Se interface is probably the formation of a thin continuous layer of polycrystalline trigonal Se between the bottom electrode and the a-Se film produced at high substrate temperatures.

In our samples we observe a process of "contact formation" which basically is a permanent change in the electrical properties of the contacts after the application of high electric field across the sample for the first time, or after mild annealing ($T_{annealing} \sim T_g$) of the metal/a-Se/metal structure. We observe a decrease in the dark currents at low fields when the bias voltage is applied after the contact has been "formed".

The process of contact "formation" in our films must have a very close origin to the processes that are taking place during the high temperature fabrication step in polycrystalline Se rectifier production technology. In any case, the formation of metal selenides, the crystallization of Se at the interface, and the formation of metal contacts to the Se crystalline inclusions present at the interface must be the most important factors that lead to the observed contact "formation" process in our films.

We have also observed "abnormal" *I-t* curves that appear in a-Se samples having a non-uniform structure such as pin- like devices or films produced on an Al surface in which the native Al_2O_3 layer plays the role of an insulating film. The "abnormal" *I-t* curves exhibit a clear maximum in the current. The time at which the maximum in the current appears is voltage depended. Such type of behavior has been described for various ceramic films and is associated with space-charge limited ion currents. Such explanation is unlikely for a-Se samples. The peak in the current most probably appears as a result of injection at the contacts being modified by the a growing space charge region in the film which, in its turn, affects the kinetics of space charge region formation.

6.4.2 Dark Current *I-V* Curves

We observe that the dark current *I-V* curves are strongly non-linear. Our data suggest that that the *I-V* curves measured on single layer metal/a-Se/metal devices can contain several regions for which $I(V) \propto V^n$. The value of the exponent *n* is different in the different regions. Over the range of film thicknesses and over the range of electric fields covered in our experiments we observe two distinct regions with different values of n in the measured *I-V* curves; $1.1 \leq n \leq 1.9$ for the lower field region and $3.1 \leq n \leq 4.4$ for higher field region.

We do not have a ready explanation for the observed *I-V* curves in single layer a-Se samples. Previously, it was thought that the dark currents in a-Se are not space charge limited [14]. However, the theory of SCLCs applied to an insulator having a suitable distribution of traps in the bandgap can predicts *I-V* curves that have shapes which are close to the ones experimentally observed by us.

We have tested the hypothesis that "space charge regions gradually form in a-Se films left under bias" by using several different techniques. Our results suggest that significant space charge build up is possible in films biased up to 2 V/μm.

The space charge can cause significant changes in the internal electric field in the sample and that was illustrated by monitoring the changes in the dark current as a result of stepwise changes in the bias across the sample. The internal electric field in some cases, can become stronger than the externally applied one. For example, a stepwise decrease in the voltage can cause currents in the opposite direction to that normaly expected for the applied bias to flow in the sample as the space charge regions in the film relax to their new equilibrium state.

The changes is the internal electric field in samples left under bias were also probed with hole TOF experiments. The changes in the shape of the recorded TOF waveforms at different times after the bias application clearly indicate changes in the internal electric filed profile, which in its turn indicates build up of space charge in the samples.

The persistent photocurrent after x-ray exposure is probably another proof that space charge regions in the films play important role in determining the electronic state of the a-Se sample. Internal space charge regions that form as a result of the x-ray exposure ,or that have been perturbed as a result of the x-ray exposure, start their relaxation to the equilibrium state after the cessation of the exposure. Such processes can very well be the reason for the observed persistent currents in the sample after the end of the exposure.

All these result suggest that the dark currents in a-Se films observed in our experiments can very well be non equilibrium space charge limited currents.

6.4.3 Effects of Substrate Temperature on the Magnitude of the Dark Currents

Effects of substrate temperature during film fabrication process on the magnitude of the dark currents in metal/a-Se/metal structures were studied. We have found that the magnitude of the dark currents in films produced by deposition onto cold substrates and subsequent post annealing have much lower dark currents than the films produced on hot substrates. Our measurements indicate that films produced by cold deposition and annealing have lower hole lifetimes and hence bigger concentration of deep hole traps, most significant part of which have appeared as a result of the cold fabrication process. Dark current measurements, however, confirmed that the deep hole traps that appear as a result of the deposition on a cold substrate do not act as centers for thermal generation of carriers in the film. Thus we can assume that the thermal generation component of dark currents is one and the same for the cold and hot deposited films. The observed decrease in the dark current is most probably due to the fact that the cold deposited films can trap deeply much bigger amount of holes then the films deposited on hot substrates. The result can be explained by assuming that a region of positive space charge that develops due to trapped holes near the positively biased electrode acts to decrease the electric field near that electrode and thus the rate of hole injection from the electrode decreases. Another potential explanation is related to a possible modification of the properties of substrate/a-Se interface related to the deposition on cold substrates, which makes injection of holes by the bottom electrode more difficult.

The reduction of the magnitude of the dark currents as a result of deposition on cold substrates does not have a simple explanation. However, the technological importance of these results is significant because they prove that the cold deposition process is very suitable for the production of a-Se based n- like layers.

6.4.4 Effects of Electrode Metal on the Dark Currents

The influence of the metal from which the top electrode has been produced on dark currents in metal/a-Se/metal devices in which the top electrode carries the negative bias was investigated. Several metals were investigated as top electrodes: Al, Au and Pt. It was found that the Pt top electrode results in the lowest dark current densities under all other conditions being the same. We observe a negative correlation between the work function of the metal used to produce the top electrode and the dark current in the metal/a-Se/metal structure, which means that metals with higher work functions lead to lower dark currents in the samples when all other conditions ate the same.

We do not have a complete explanation for the facts described above. However, the results do have technological importance paving the way to decrease the dark current in a-Se photoconductor layers operating under negative biasvoltages up to 5 times by simply fabricating the top contact from Pt.

6.5 A Novel Technology for Dark Current Reduction in a-Se Based Photoconductor Layers

The research during the PhD program of study has enabled us to propose and test a novel technological method for dark current reduction in a-Se photoconductor structures. The rational of the method is the same as in the previously existing techniques for dark current reduction. The idea is to introduce a thin buffer (trapping) layer between the positive electrode and the a-Se photoconductor that reduces the carrier injection from the electrode.

We have proven that an efficient hole trapping layer (n- like layer) can be fabricated in two steps: deposition of a-Se on a cold substrate and mild post-annealing. Such a cold deposited n- like layer can replace the alkali metal doped Se:As n- like layers in commercially used multilayer structures. The new method makes possible imaging with simple single, or double ni-, and in- like structures. The electron injection by the negative electrode is minimized by the proper selection of the electrode metal. Thus, the simple cold deposited single and double layer structures can be produced by evaporation of only one suitably chosen Se:As alloy. We control the different charge transport properties of the i- like layer and n- like layer by changing the deposition conditions during fabrication. In particular, we change the substrate temperature to switch from an n- like layer production to an i- like layer production and vice versa. Thus, a simple single boat evaporation system can be used for the production of the photoconductor structure.

In all previous methods, materials with different chemical compositions were used for the production of the different layers, which requires the use of multiple boat evaporation. In addition, materials suitable for the fabrication of buffer layers have to be synthesized and produced, which on its own is a complicated task.

We have proven that simple ni- like structures proposed in this work reduce the dark currents to approximately the same level as can be achieved with commercial pin- like structures based on alkali metal doped n- like layers or double layer structures containing Sb_2S_3 as charge transport layers.

The cold deposited n- like layers have potential advantages over the alkali metal doped n- like s that are related to the absence of alkali metal doping. The advantages include better electron mobilities and lifetimes in the cold deposited n- like layers, and potentially better long term stability in terms of resistance against crystallization and the undesirable drift of the alkali ions in the structure.

6.6 Results from the Application of the New Technology for Dark Current Reduction to Prototype X-ray Image Detectors

Simple single layer and double layer photoconductor ni-structures were fabricated according to the newly proposed method on a series of prototype x-ray image detectors with CCD readout. Both SELMA and SALLY prototype detectors have demonstrated an excellent imaging performance, in particular very high spatial resolution. Dark currents in the selenium photoconductor layer were not a problem for the detector operation at all tested electric fields. Various x-ray images of phantoms were taken to demonstrate the operation of the prototype detectors. The imaging performance of the prototype detectors was also investigated in terms of measuring the MTF and DQE of the detectors.

6.7 Suggestions for Future Work

The engineering focus of the research work was placed on the minimization of the dark current in metal/a-Se/metal structures for application in digital x-ray image detectors. The research indeed resulted in a technology for dark current reduction which was successfully implemented on prototype image detectors with very high resolution. However, our understanding of properties of a-Se is far from being complete.

It is known that certain elements added to a-Se in very small amounts (ppm range) can drastically change the hole and electron transport in a-Se. Elements that were investigated in the work are Cl and O. Probably, other additives in very small amounts can have similar in magnitude effects on the charge transport. Finding such additives in the form of pure chemical elements or chemical compounds will be a topical research task for the future with potential practical importance.

The mechanisms by which the impurities affect the electronic transport in a-Se are also unknown. Most of the researchers tend to explain their results in terms changing concentrations of charged defects in a-Se under the influence of the introduced impurities. That is one possibility. However, other possibilities also exist. For example, the impurities can be inhibiting or promoting the formation of different nano- and micro- crystalline inclusions in a-Se that act as carrier traps. Further, research will have to investigate such possibilities.

It is not clear why exactly the hole lifetime decreases as a result of the deposition of a-Se on a cold substrate which is another question that has to be answered in the future. It seems that our results cannot be explained in terms of charged over- and under- coordinated effects. The hypothesis about the formation of microcrystalline inclusions that seems capable of explaining our results have been based on data that are nearly 30 years old. It will be useful to perform new electron microscope studies on the concentration of nano- and micro- crystalline inclusions in the a-Se film as a function the preparation conditions. It will also be interesting to study the distribution of these inclusions across the sample thickness.

The cold deposition technology for dark current reduction has to be further studied for potential problems when the technology is scaled up to produce large area detectors and for long-term stability. It will be useful to test the technology with CCD detectors capable of fast TDI readout. Long term stability of the devices have to be further studied because processes similar to photo-dissolution of the Pt top electrode encouraged by the high electric fields and the x-ray irradiation might have the potential to affect the photoconductor structure.

APPENDIX

APPENDIX A

The Slot Scanning Technique for X-ray Imaging. Time Delayed Integration Readout Technique. Pixel Structure of a Direct Conversion X-ray Detector with CCD Readout

Introduction

The purpose of this appendix is to briefly illustrate the basics of the slot scanning technique for x-ray imaging and compare it with conventional snapshot radiography. Almost all x-ray detectors designed to be used with slot scanning x-ray machines are based on CCDs and utilize the time delayed integration (TDI) readout technique. The principles of the TDI mode of operation are explained later in this appendix together with an example pixel structure of a direct conversion detector with a CCD readout circuit.

The Slot Scanning Technique for X-ray Imaging

Conventional radiology or flat panel detector based digital radiology system for snapshot imaging is schematically shown in Figure A.1. The system requires a wide primary x-ray beam to spread over a sizable area of interest according to the dimensions of the object to be imaged. The image is taken with one single exposure with a duration that is typically a fraction of a second. In the case of a digital system, the image is available to the radiographer about 2 seconds after the x-ray exposure. Such systems efficiently utilize all the x-rays generated by the x-ray tube and do not require any mechanically moving parts, which make the x-ray tube and the rest of the system relatively easy to design and not so expensive to manufacture.

However, there are certain limitations arising from fundamental physics which prevent the application of such systems in certain cases; imaging of very big objects and digital imaging with very high spatial resolution being two examples.

For a number of different reasons the size of the x-ray field cannot exceed about 40 × 40 cm. So the imaging of big objects like a full body imaging and the examination of large patients become very difficult. If a digital detector is used, it has to be bigger than the object to be imaged. The number of pixels increases very rapidly with the size of the detector. The

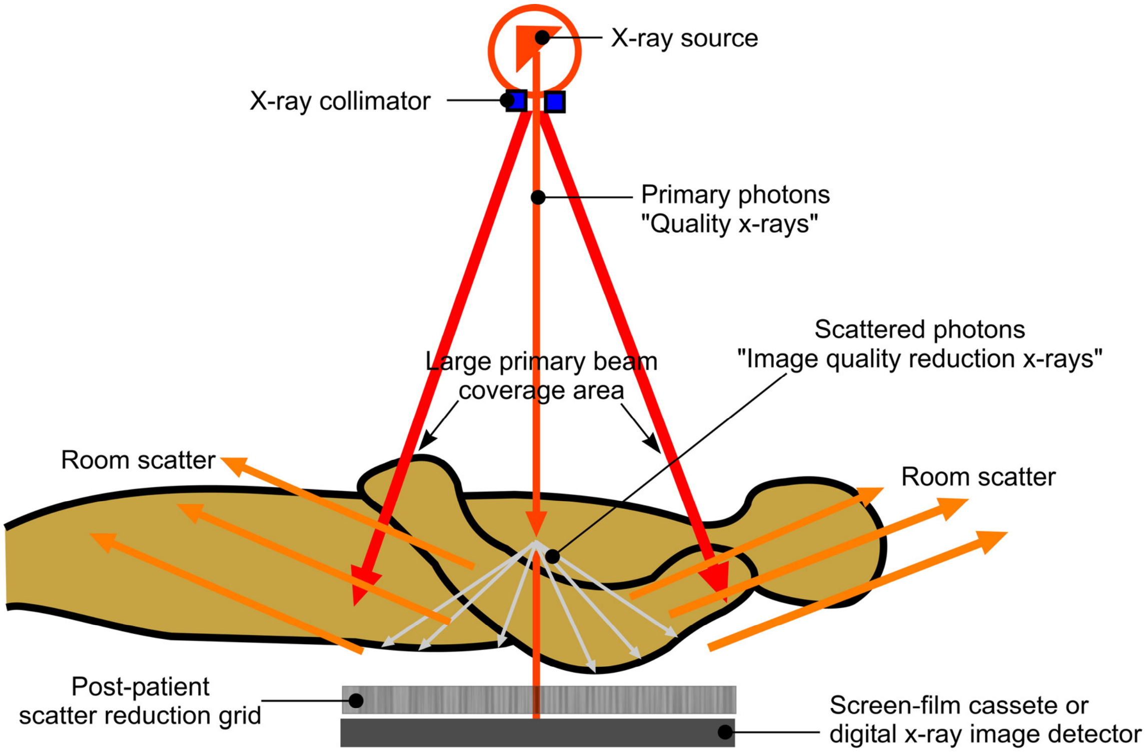

Figure A.1 Principles of operation of conventional radiology or other digital radiology/computer radiology systems for projection radiography. The diagram is taken from reference [169].

complexity of the readout circuit grows as well. For a number of reasons, the production of flat panel detectors with a huge number of pixels is very difficult. When a very large number of pixels are involved, the production process tends to have a very low yield; the price of such big area detector will be prohibitively large.

The number of pixels becomes unreasonably large also in the cases when very high resolution is required. Consider mammography, for example. The field of interest is about 20 × 20 cm in other words relatively small. The smallest objects of interest in mammography are 80-100 μm (various micro calcifications in the breast). Quality imaging of such small objects becomes possible if the pixel size is 20 μm or less. The number of pixels for the above-mentioned area becomes 6.4×10^7 assuming 25 μm pixel pitch. Such flat panel imagers cannot be manufactured with the currently available technology.

In many cases, the quality of the x-rays is deteriorated by the Compton scatter in the object (Figure A.1). Partial reduction of the scattered radiation is achieved by inserting a post patient scatter rejection grid in front of the detector (see Figure A.1). This is a compromise with the performance of the system but is required to maintain the image quality. The radiographer in this case has to increase the patient exposure to counteract the adverse effects of body scatter and grid absorption.

The higher radiation exposures together with the wide x-ray beam spread causes relatively high amounts of scattered radiation throughout the room where the x-ray machine is installed, and in adjacent areas. The premise where such an x-ray equipment is to be installed has to be designed and built in a special way so that the requirements for radiation safety of the patient and of the personnel are met.

In the *slot (line) scanning technique*, the image of the objects is formed line by line, very much like the image in a fax machine or a computer scanner. The coordinate perpendicular to the scan direction corresponds simply to the position of the pixel in the line detector. The coordinate along the scan direction is determined by the parameters of the relative motion of the object with the respect to the x-ray detector. In most of the systems, the patient is immobile and the x-ray source moves synchronously with the detector to scan the area of interest. The major parts and the basics of the slot scanning technique for x-ray imaging are illustrated in Figure A.2. A specially designed x-ray beam controlling mechanism creates a fanned x-ray beam of primary photons. Only the primary x-ray beam strikes the solid-state x-ray detector (in the case of Figure A.2 indirect conversion CsI(Tl) with 60 μm pixel size CCD readout circuit operating in Time Delayed Integration Mode). The result is the elimination of the influence of the scattered radiation on the image. This means that no anti-scatter grid is required regardless of the patient size.

Such slot scanning systems will produce higher quality “scatter free” digital images with high resolution (theoretically expected to be 8 lp/mm). The most important result is the highly reduced patient dose as shown in Table A.1.

Table A.1 compares the slot scanning system with full field radiography based on screen film cassettes. The trend will remain the same even if a digital detector is used to capture the image in the full field snapshot technique because in the slot scanning technique there is no need to compensate for the effects of the scattered radiation on the image. In the slot scanning technique, the area of the detector is highly reduced. This enables the production of very high-resolution line detectors with small pixel sizes (smaller than 20 μm). The dose efficient

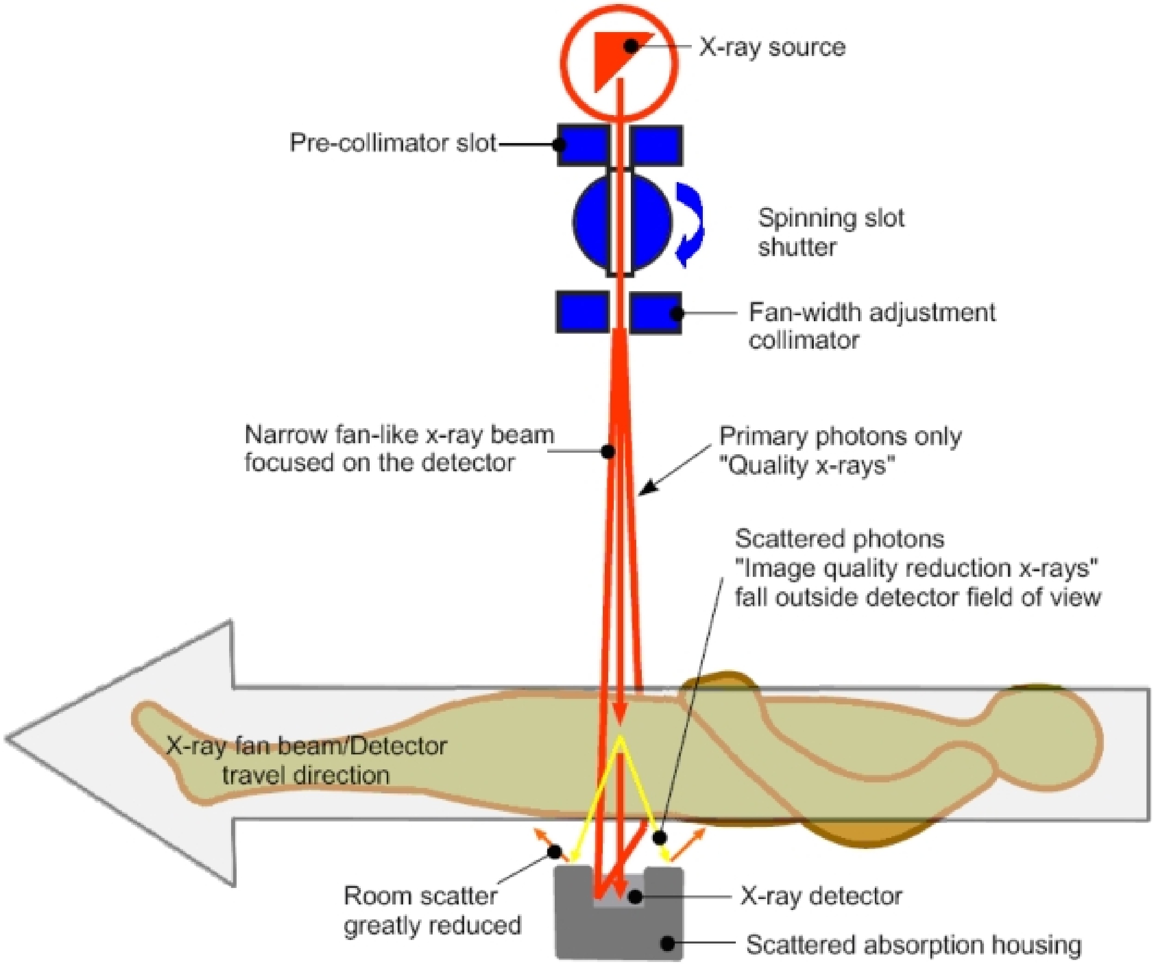

Figure A.2 A slot scanning technique for x-ray imaging as implemented in STATSCAN (LODOX Inc) digital radiography system. The diagram is taken from [169].

elimination of the effects of scattered radiation together with the possibility to produce detectors with small pixel size makes the slot scanning technique very suitable for applications in mammography. At the moment several slot-scanning systems for mammography are commercially available on the market by Fisher, Philips and others. All of them are based on the indirect conversion detectors with a CCD image readout circuit.

In concluding this section we have to mention that the major drawback of the slot scanning technique is the inefficient use of the beam produced by the x-ray tube. A full body scan needs ~15 s to complete and a mammogram is produced in ~6s. During all that time the x-ray tube has to operate, which means extensive x-ray tube heating and wear off. Another disadvantage is the presence of the mechanically moving parts. This causes some inconvenience during examination, and adds significantly to the price of a slot scanning system.

Table A.1 Patient dose comparison between full field radiography based on film-screen cassettes and the slot scanning imaging technique as implemented in STATSCAN machine, LODOX Inc.

Procedure	Guidance Dose *, mR	Statscan™ Dose **, mR	Statscan™ Dose as % of conventional	Ratio
Spine	15000	1640	11	9.1
Abdomen AP	5000	409	8	12.2
Pelvis	5000	409	8	12.2
Skull	2500	210	8	11.9
Full Body AP	1500	150	10	10.0
Extremity	450	60	13	7.5
Chest AP	200	142	71	1.4

*** Typical Patient Radiation Doses in Diagnostic Radiology- 75th percentile, Dept of Radiology, Baylor College of Medicine, AAPM/RSNA Physics Tutorial 1998 (CR & High Speed Film)**
**** Statscan Skin Entrance Radiation Doses measured for "Large" Patient (120kg – 150kg)**

Time Delayed Integration CCD Readout Mode

Area-array Charge-Coupled Device (CCD) image sensors consist of a two dimensional matrix of charge collection sites. Analog voltages corresponding to the charge at each site are read from the CCD by applying clocking signals to transfer the charge in each row of sites to the succeeding row (parallel transfer), and eventually to a serial register, that does not participate in the charge collection process during the exposure, from which charges are clocked and transferred in the orthogonal direction to the detector and amplifier. In the more common two-dimensional imaging mode, after a charge collection time interval (exposure), each sensitive site of the CCD is read out and represents one pixel of the acquired image. Thus a CCD of *x* columns and *y* rows yields an image of *x* by *y* pixels.

A line array CCD sensor consists of a one-dimensional sensitive structure analogous to the serial register, detector, and amplifier of the area array CCD sensor. By repeatedly exposing and reading a line array CCD sensor, while moving the sensor in a direction orthogonal to the array, a two dimensional image can be reconstructed. The resulting image has a maximum width in pixels equal to the number of charge collection sites of the sensor, but a theoretically unlimited length, which corresponds to the length of the scan. This, of course, is the basic principle behind common scanning devices such as FAX machines and document copiers.

Obviously, the slot scanning technique for x-ray imaging described above can use a linear array CCD as detector readout circuit. However, in order to increase the sensitivity and the scanning speed (so as to decrease the patient dose) all commercial devices utilize area array CCD sensors operated in Time Delay Integration (TDI) mode as the readout circuit.

TDI is a somewhat similar in operation to the means of acquiring a continuous two-dimensional image using an area array CCD sensor. If the row by row transfer of charge in the sites proceeds at a rate equal to and in the same direction as the apparent motion of the subject being imaged, accumulation of charge integrates during the entire time required for the row of charge to move from the top of the sensor to the serial register (or to the storage area of the device, in the case of a frame transfer CCD). This integration time provides an increase in the sensitivity over the line array CCD sensor, proportional to the number of rows of sites of the area array sensor. Like the two dimensional image acquired using a line array sensor, the TDI image has a maximum width in pixels equal to the number of sites in a row of the sensor and a length limited only by the maximum storage capacity of the system collecting the data.

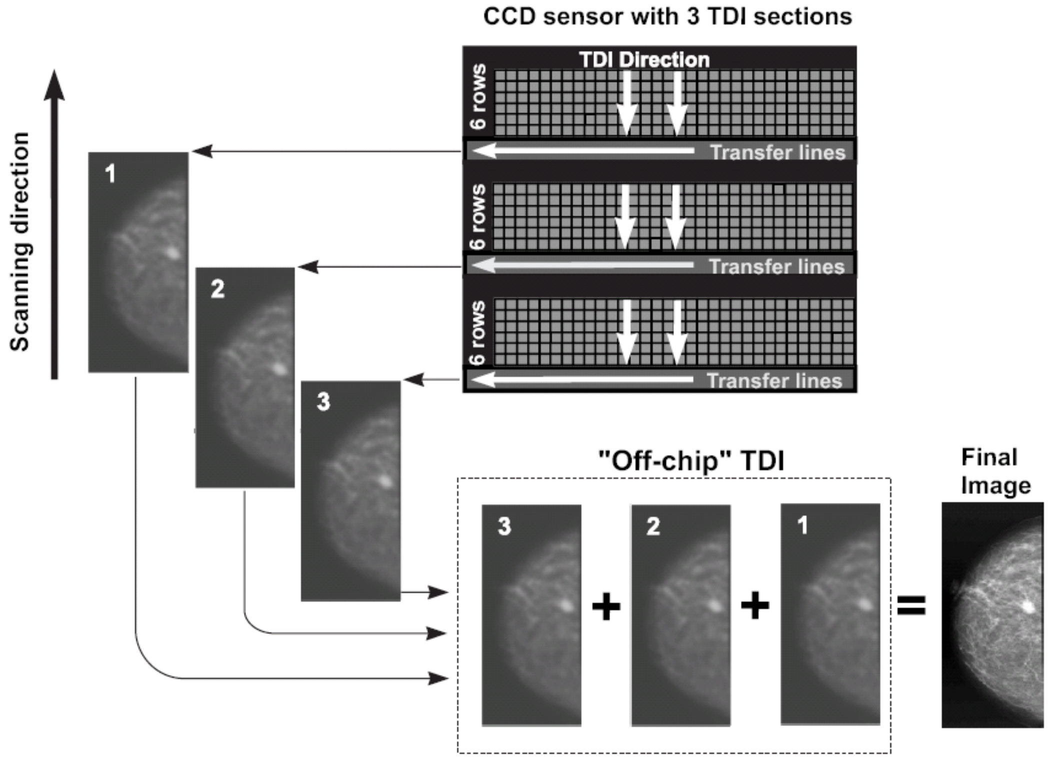

Figure A.3. Schematic representation of a two stage TDI process. The CCD sensor has 3 TDI sections each performing TDI over 6 rows. The signals from the 3 sections are transferred off-chip and integrated together with appropriate delay to form the final image. After [170]). The figure is not to scale.

The factor that limits the sensitivity of a CCD sensor operating in TDI mode is the capacity of the charge collection sites. If the number of rows is too big, the charge generated during the exposure at certain detector elements will exceed the capacity of the charge collection sites and the signal will saturate. Further increase in the sensitivity is possible if the CCD sensor is designed and fabricated in sections as shown in Figure A.3.

Each section consists of several rows and performs normal TDI over these rows. The signals from all sections are transferred off-chip and added with an appropriate delay to form the final image.

The maximum dose in mammography can be 1000 mR or more. This corresponds to approximately 7.6×10^8 electron-hole pairs per pixel if Si is used as x-ray photoconductor. Unfortunately CCD well capacity is quite limited; with maximum charge storage levels about an order of magnitude lower ($\sim10^7$ electron-hole pairs) than required. To accommodate such large signals, CCD sensors with 24 sections (8 rows per section) have been successfully realized [170].

Pixel Structure of a Direct Conversion X-ray Detector with CCD Readout

The direct conversion detectors that utilize CCD sensors as image readout circuits are usually fabricated as two separate parts. The first part is the working media of the detector. This is an array of detector elements where the interaction of the x-rays with the image detector takes place. A portion of the incident energy of the x-rays is converted into electric charges. These charges are then injected into the wells of a CCD sensor which is the second part of the image detector. The charges in the wells are then clocked out of the sensor, measured and transferred to a computer to form the image. A schematic cross section of such detector is shown in Figure A.4. The most difficult fabrication stage involved is the indium bump bonding that forms electrical contacts between the CCD and the detector array. The process requires the formation of small indium bumps and very precise alignment and mating. It becomes a complicated process with a low yield when small pixel size is required. One advantage when a-Se is used as a photoconductor is that indium bump bonding process is not required. Instead the CCD sensor is placed in a vacuum chamber and its electroded surface is conveniently coated with an a-Se layer with the required thickness. After the latter deposition, the radiation receiving electrode is fabricated on top of the a-Se photoconductor. Obviously this process is much simpler and can be used with any pixel size. The cross section of a pixel in this particular case is shown in Figure

A.5. This actually is the pixel architecture was used in one of the test detector fabricated in the course of the PhD work (see more Apendix B for more details).

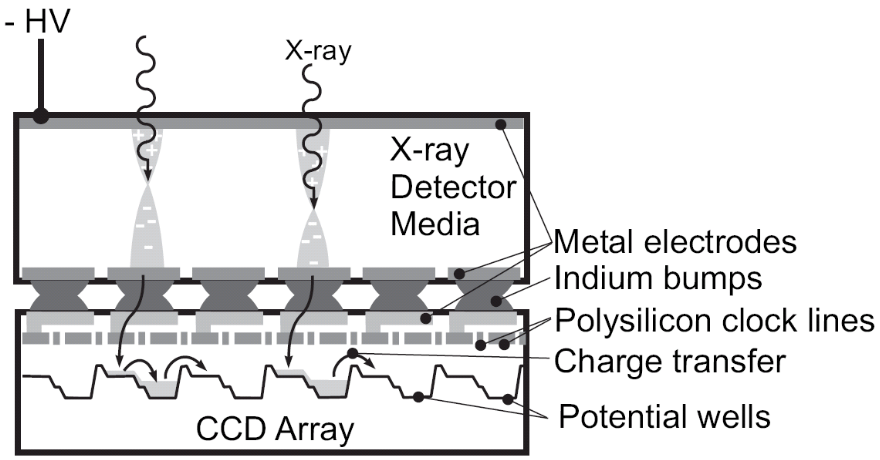

Figure A.4. Cross-sectional view of a direct conversion image detector with CCD readout circuit. After [170].

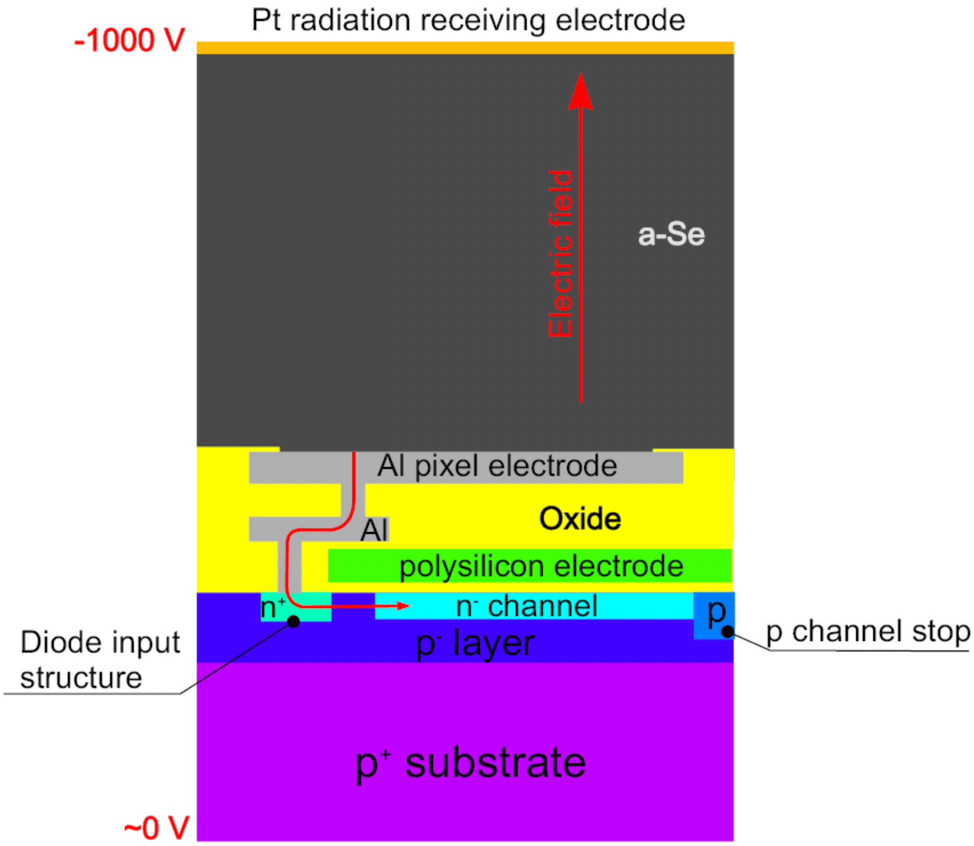

Figure A.5 Cross section of one detector element in an test x-ray detector [11]. The drawing is not to scale.

REFERENCES

1 C. Delaney, E. Finch , "Radiation detectors", *Claderon Press*, Oxford, 1992

2 G. Knoll, "Radiation detection and measurements", 2nd Edition, *John Wiley&Sons*, New York, 1989

3 Z. Jaworowski, "Radiation risks and ethics", *Physics Today*, **52**, 9, pp. 24-29, 1999

4 S. Kasap, J. Rowlands, "Direct-conversion flat-panel x-ray image detrectors", *Proceedings of IEE – Cirquits, Devices, Systems,* **149**, 2, pp. 85-96, 2002

5 S. Kasap, J. Rowlands, "Direct conversion flat panel x-ray image sensors for digital radiography", *Proceedings of IEEE*, **90**, 4, pp. 591-604, 2002

6 J. Rowlands, S. Kasap, "Amorphous semiconductors usher in digital x-ray imaging", *Physics Today*, **50**, pp. 24-30, 1997

7 J. Rowlands, J. Yorkston, "Flat panel detectors for digital radiography", in: J. Beutel, H. Kundel, R. van Metter (Eds.), Medical imaging: physics and psychophysics, *SPIE*, **1**, pp. 223–328, 2000

8 S. Kasap, J. Rowlands, "X-ray photoconductors and stabilized a-Se for direct conversion digital flat panel x-ray image detectors", *Journal of Material Science: Materials for Electronics*, **11**, pp. 179-199, 2000

9 W. Zhao, D. Hunt, K. Tanioka, J. Rowlands, "Amorphous selenium flat panel detectors for medical applications", *Nuclear Instruments and Methods in Physics Research A*, **549**, pp.205-209, 2005

10 V. Nagarkar, T. Gupta, S. Miller, Y. Klugerman, M. Squillante, G. Entine, "Structured CsI(Tl) scintillators for x-ray imaging applications", *IEEE Transactions on Nuclear Science*, **45**, 3, pp. 492 – 496, 1998

11 D. Hunter, G. Belev, G. DeCresenzo, S. Kasap, J. Mainprize, G. Mawdsley, J. Rowlands, C. Smith, T. Tumer, V. Verpakhovski, S. Yin, M. Yaffe, "High-Resolution (20 cycles/mm) digital x-ray mammography using amorphous selenium directly coupled to CCD readout devices", *Proceedings of the SPIE*, **5368**, pp. 466-477, 2004

12 M. Hoheisel , L. Bätz, "Requirements on amorphous semiconductors for medical x-ray detectors", *Journal of Non-Crystalline Solids*, **266-269**, pp. 1152-1157, 2000

13 T. Tümer, S. Yin, V. Cajipe, H. Flores, J. Mainprize, G. Mawdsley, J. Rowlands, M. Yaffe, E. Gordon, Hamilton, J. William, D. Rhiger, S. Kasap, P. Sellin, K. Shah, "High-resolution pixel detectors for second generation digital mammography", *Nuclear Instruments and Methods in Physics Research A*, **497** , pp. 21-29, 2003

14 R. Johanson, S. Kasap, J. Rowlands, B. Polischuk, "Metallic electrical contacts to stabilized amorphous selenium for use in x-ray image detectors", *Journal of Non-Crystalline Solids*, **227-230**, pp.1359-1362, 1998

15 P. Luke, "Unipolar charge sensing with coplanar electrodes - application to semiconductor detectors", *IEEE Transactions on Nuclear Science*, **42**, 4, pp. 207-213, 1995

16 H. Barrett, J. Eskin, H. Barber, "Charge transport in arrays of semiconductor gamma-ray detectors", Physical Review Letters, **75**, 1, pp.156-159, 1995

17 J. Eskin, H. Barrett, and H. Barber, "Signals induced in semiconductor gamma-ray imaging detectors", Journal of Applied Physics, **85**, 2, pp. 647-659, 1999

18 M. Kabir and S. Kasap, "Charge collection and absorption-limited x-ray sensitivity of pixellated x-ray detectors", *Journal of Vacuum Science & Technology A: Vacuum, Surfaces, and Films*, **22**, 3, pp. 975-980, 2004

19 G. Lucovsky, "Physics of Selenium and Tellurium", edited by E. Gerlach and P. Grosse, Springer-Verlag, New York, 1979

20 A. Feltz, "Amorphous Inorganic Materials and Glasses"*,* VCH Publisher, New York, 1993

21 V. Minaev, S. Timoshenkov, V. Kalugin, "Structural and phase transformations in condensed selenium", *Journal of Optoelectronics and Advanced Materials,* **7**, 4, pp. 1717-1741, 2005 and the references therein

22 Y. Miyamoto, "Structure and phase transformation of rhombohedral selenium composed of Se_6 molecules", *Japanese Journal of Applied Physics,* **19**, 10, pp. 1813-1819, 1980

23 K. Murphy, M. Altman, B. Wunderlich, "The monoclinic-to-trigonal transformation in selenium", *Journal of Applied Physics,* **48**, 10, pp. 4122-4131, 1977

24 A. Eisenberg, A.V Tobolsky, "Equilibrium polymerization of selenium", *Journal of Polymer Science*, **46**, 147, pp. 19-28, 1960

25 R. Keezer and M. Bailey, "The structure of liquid Se from viscosity measurements", *Materials Research Buletin*, **2**, 2, pp. 185-192, 1967

26 P. Jóvári, R. Delaplane, L. Pusztai, "Structural models of amorphous selenium", *Physical Review B*, **67**, pp.172201-1 - 172201-4, 2003

27 S. Yannopoulos, K. Andrikopoulos, "Raman scattering study on structural and dynamical features of non crystalline selenium", *Journal of Chemical Physics*, **121**, 10, pp. 4747-4758, 2004

28 A. Popov, "Correlation between the molecular structure and properties of amorphous selenium", *Journal of Physics C: Solid State Physics*, **9**, pp. L675-L677, 1976

29 E. Montrimas, B. Petrétis, "The relation between deep trapping levels and the structure of Se layers", *Journal of Non-Crystalline Solids*, **15**, pp.96-106, 1974

30 C. Juhasz, V. Gembala, S.O. Kasap, "Growth characteristics of vacuum coated thick a-Se films for device applications", *Journal of Vacuum Science and Technology A*, **18**, 2, pp.665-670, 2000

31 T. Takahashi, K. Ohno, and Y. Harada, "Highly disordered amorphous selenium studied by ultraviolet photoemission spectroscopy", *Physical Review B*, **21**, 8, pp. 3399-3404, 1980

32 A. Kolobov, H. Oyanagi, K. Tanaka, "Structural study of amorphous selenium by in situ EXAFS: observation of photoinduced bond alternation ", *Physical Review B*, **55**, 2, pp. 726-734, 1997

33 S. Agarwal, “Nature of localized states in amorphous semiconductors: a study by electron spin resonance”, *Physical Review B*, **7**, pp. 685-691, 1973

34 D. Adler and E. Yoffa, "Electronic structure of amorphous semiconductors", *Physical Review Letters,* **36**, pp. 1197-1200, 1976

35 R. Street and N. Mott, "States in the gap of glassy semiconductors", *Physical Review Letters,* **35,** 19, pp**.** 1293-1296, 1975

36 M. Kastner, D. Adler, H. Fritzsche, "Valance-alternation model for localized gap states in lone pair semiconductors", *Physical Review Letters,* **37,** 22, pp. 1504-1507,1976

37 D. Vanderbilt, J. Joannopoulos, "Calculation of defect states in amorphous selenium", *Physical Review Letters,* **42,** 15 pp.1012-1015, 1979

38 D. Vanderbilt and J. Joannopoulos, "Total energies in selenium III: Defects in glass", *Physical Reveiw B,* **27**, 10, pp.6311-6321, 1983

39 P. Anderson, "Model for the electronic structure of amorphous semiconductors", *Physical Reveiw Letters*, **34**, 15, pp. 953-955 ,1975

40 X. Zhang, D. Drabold, "Evidence for valence alternation and a new structural model of amorphous selenium", *Journal of Non-Crystalline Solids*, **241**, pp. 195-199, 1998

41 A. Kolobov, M. Kondo, H. Oyanagi, A. Matsuda, K. Tanaka, "Negative correlation energy and valence alternation in amorphous selenium: an in situ optically induced ESR study", *Physical Review B*, **58**, 18, pp. 12004-12010, 1998

42 R. Steudel, "Hypervalent defects in amorphous selenium and similar lone-pair semiconductors", *Journal of Non-Crystalline Solids*, **83**, pp. 63-79, 1986

43 D. Hohl and R. Jones, "First-principles molecular-dynamics simulations of liquid and amorphous selenium", *Physical Review B*, **43**, 5, pp. 3856-3870, 1991

44 S. Dembovsky and E. Chechetkina, "Glassy state clarified through chemical bonds and their defects", *Journal of Non-Crystalline Solids*, **85,** 3, pp. 346-357, 1986

45 A. Zyubin, F. Grigor'ev, S. Dembovsky, "Quantum-chemical simulation of the influence of defects on the infrared spectrum and the electronic structure of a-Se", *Semiconductors*, **37**, 5, pp. 598-603, 2003

46 R. Hyman, "Electrical conductivity of hexagonal selenium", *Proceedings of the Physical Society*, Section B, **69**, 7, pp. 743-747, 1956

47 M. Cutler, "Liquid Semiconductors", New York: Academic Press, Chapter 1, 1977

48 P. Nielsen, "Density of states of amorphous selenium by vacuum photoemission", *Physical Review B*, **6**, 10, pp.3739-3749, 1972 and the references therein

49 F. Greuter, "Electronic surface properties of a liquid semiconductor: selenium", *Journal of physics C: Solid State Physics*, **28**, pp. 2527-2537, 1985

50 M. Abkowitz, "Density of states in a-Se from combined analysis xerographic potentials and transient transport data", *Philosophical Magazine Letters,* **58,** 1, pp. 53-57, 1988

51 J. Marshall, A. Owen, “Drift mobility studies in vitreous arsenic triselenide”, *Philosophical Magazine*, **24**, pp. 1281-1290, 1971

52 S. Kasap, C. Juhasz, "Time-of-flight drift mobility maesurements on chlorine-doped amorphous selenium films", *Journal of Physics D: Applied Physics*, **18**, pp. 703-720, 1985

53 T. Orlowski, M. Abkowitz, "Subnanosecond transient photocurrents in a-Se and a-Si:H", *Journal of Non-Crystalline Solids*, **77**, 1, pp. 439-442, 1985

54 R. Blakney, H. Grunwald, "Trapping process in amorphous selenium", Physical Review , **159**, 3, pp. 664-671, 1967

55 T. Yashar, "Transient polarization currents in amorphous selenium", *PhD Thesis Princeton University*, 1968

56 J. Noolandi, “Multiple-trapping model of anomalous transit-time dispersion in a-Se”, *Physical Review B*, **16**, pp. 4466-4473, 1977

57 Y. Hoshino, H. Miyata, "Thermally stimulated currents in amorphous selenium: relationship to the trapping levels and the non-crystallyne state", *Journal of Applied Physics*, **52**, 10, pp. 6214-6217, 1980

58 H. Song, G. Adriaenssens, E. Emelianova, V. Arkhipov, "Distribution of gap states in amorphous selenium thin films", *Physical Review B*, **59**, pp. 10607-10613, 1999

59 N. Qamhieh, M. Benkhedir, M. Brinza, J. Willekens, G. Adriaenssens, "Steady-state photoconductivity in amorphous selenium glasses", *Journal of Physics: Condensed Matter*, **16**, pp. 3827–3833, 2004

60 M. Benkhedir, M. Brinza, G. Adriaenssens, "Electronic density of states in amorphous selenium", *Journal of Physics: Condensed. Matter,* **16** , pp. 5253-5264, 2004

61 M. Benkhedir, M. Aida, G. Adriaenssens, "Defect levels in the band gap of amorphous selenium", *Journal of Non-Crystalline Solids*, **344**, 3, pp. 193-198, 2004

62 N. Qamhieh, M. Benkhedir, M. Brinza, G. Adriaenssens, "Low-tempereture steady-state photoconductivity in amorphous selenium films", *Journal of Optoelectronics and Advanced Materials*, **7**, 4, pp. 1781-1784, 2005

63 M. Benkhedir, M. Brinza, J. Willekens, K. Haenena, M. Daenena, M. Nesladeka, G. Adriaenssens, "Gap-state spectroscopy in amorphous selenium", *Journal of Optoelectronics and Advanced Materials*, **7**, 5, pp. 2223-2230 , 2005

64 M. Benkhedir, M. Brinza, N. Qamhieh, G. Adriaenssens, "Discrete defect levels in amorphous selenium bandgap", *Journal of Non-Crystalline Solids*, **352**, 9-20, pp. 1543-1546, 2006

65 E. Emelianova, M. Benkhedir, M. Brinza and G. Adriaenssens, "Analysis of electron time-of-flight photocurrent data from a-Se", *Journal of Applied Physics*, **99**, pp. 083702-1 - 083702-4, 2006

66 V. Arkhipov, M. Iovu, A. Rudenko, S. Shutov, "An analysis of the dispersive charge transport in vitreous $0.55As_2S_3$:$0.45Sb_2S_3$", *Physica Status Solidi A*, **54**, 1, pp. 67-77, 1979

67 J. Marshall, J. Berkin, C. Main, "Calculation of localized-state energy distributions from transient-photoresponse data", *Philosophical Magazine B*, **56**, 5, pp. 641-652, 1987

68 H. Michael, G. Adriaenssens, E. Davis, "Extended-state mobility and its relation to the tail-state distribution in a-Si:H", *Physical Review B*, **34**, 4, pp. 2486-2489, 1986

69 K. Koughia, B. Fogal, G. Belev, R. Johanson, S. Kasap, "Density of states in the mobility gap of stabilized a-Se from electron time-of-flight photocurrent analysis", *Journal of Non-Crystalline Solids*, **338-340**, pp. 569-573, 2004

70 K. Koughia, Z. Shakoor, S. Kasap, and J. Marshall, "Density of localized electronic states in a-Se from electron time-of-flight photocurrent measurements", *Journal of Applied Physics*, **97**, 3, pp. 033706-1 - 033706-11, 2005

71 K. Koughia, S. Kasap, "Density of states of a-Se near the valence band", *Journal of Non-Crystalline Solid,* **352**, 9-20, pp.1539-1542, 2006

72 H. Naito, T. Iwai, M. Okuda, T. Matsushita, A. Sugimura, "Computer simulation study of tail state distribution in amorphous selenium", *Journal of Non-Crystalline Solids*, **114**, pp. 112-114, 1986

73 V. Ivanov, "On the approximate solution of operator equations of the first kind", *Zhurnal Vychislitelnoi Matematiki i Matematicheskoi Fiziki*, **6**, 6, pp. 1089–1094, 1966

74 T. Nagase, K. Kishimoto, H. Naito, "High resolution measurement of localized state distributions from transient photoconductivity in amorphous and polymeric semiconductors", *Journal of Applied Physics*, **86**, 9, pp. 5026-5035, 1999

75 S. Reynolds, C. Main, D. Webb, S. Grabtchak, "Bandwidth considerations in modulated and transient photoconductivity measurements to determine localized state distributions", *Journal of Applied Physics*, **88**, 1, pp. 278-282, 2000

76 G. Roberts, "Electrical conduction in single crystal trigonal selenium", *Journal of Physics C: Solid state Physics*, **4**, pp. 1348-1359, 1971

77 J. Hartke, P. Regensburger, "Electronic states in vitreous selenium", *Physical Review*, **139**, pp. A970-A980,1965

78 E. Davis, "Optical absorption, transport and photoconductivity in amorphous selenium", *Journal of Non-Crystalline Solids*, **4**, pp. 107-116, 1970

79 H. Adachi, K. Kao, "Dispersive optical constants of amorphous selenium $Se_{1-x}Te_x$ films", *Journal of Applied Physics*, **51**, pp. 6326-6331, 1980

80 D. Pai, R. Enck, “Onsager mechanism of photogeneration in amorphous selenium”, *Physical Review B*, **11**, pp. 5163-5174, 1975

81 K. Klein, “Bandgap dependence and related features of radiation ionization energies in semiconductors”, *Journal of Applied Physics*, **39**, 4, pp. 2029-2038, 1968

82 W. Que, J. Rowlands, "X-ray photogeneration in amorphous selenium: geminate versus columnar recombination", *Physical Review B* , **51,** pp. 10500-10507**,** 1995

83 I. Blevis, D. Hunt, J. Rowlands, "Measurement of x-ray photogeneration in amorphous selenium", *Journal of Applied Physics*, **85**, pp. 7958-7963, 1999

84 S. Kasap, C. Haugen, M. Nesdoly, J. Rowlands, "Properties of a-Se for use in flat panel x-ray image detectors", *Journal of Non-Crystalline Solids,* **266-269**, pp. 1163-1167 , 2000

85 G. Belev, S. Kasap, “Amorphous selenium as an x-ray photoconductor”, *Journal of Non-Crystalline Solids*, **345-346**, pp. 484-488, 2004

86 M Lachaine, B. Fallone, "Monte carlo simulations of x-ray induced recombination in amorphous selenium", *Journal of Physics D: Applied Physics*, **33**, pp. 1417-1423, 2000

87 J. Marshall, A. Owen, "The hole drift mobility of vitreous selenium*", Physica Status Solidi A*, **12**, 1, pp. 181-191, 1972

88 W. Spear, “Transit time measurements of charge carriers in amorphous selenium films”, *Proceedings from the Physical Society of London*, **B70**, pp. 669-675, 1957

89 M. Abkowitz, D. Pai, “Photoelectronic behavior of a-Se and some a-Se:As alloys in their glass transition regions”, *Physical Review B*, **18**, pp. 1741-1750, 1978

90 G. Juska, A. Matulionis, J. Viscakas, “Measurement of thermal release and transit time in case of multiple trapping”, *Physica Status Solidi*, **33**, pp. 533-539, 1969

91 M. Abkowitz, “Evidence of the defect origin of states which control photoelectric behavior of amorphous chalcogenides”, *Journal of Non-Crystalline Solids*, **66**, pp. 315-320, 1984

92 M. Abkowitz, “Relaxation induced changes in electrical behavior of glassy chalcogenide semiconductors”, *Polymer Engineering Science*, **24**, pp. 1149-1154, 1984

93 M. Abkowitz, J. Markovics, “Evidence of equilibrium native defect populations in amorphous chalcogenides from analysis of xerographic spectra”, *Philosophical Magazine B*, **49**, pp. L31-L36, 1984

94 S. Kasap, J. Rowlands, “Review: x-ray photoconductors and stabilized a-Se for direct conversion digital flat-panel x-ray image detectors”, *Journal of Materials Science: Materials in Electronics*, **11**, pp.179-198, 2000

95 D. Pai, "Time-of-flight study of the compensation mechanism in a-Se alloys”, *Journal of Imaging Science and Technology*, **41**, pp. 135-142, 1997

96 W. Spear, “Drift mobility techniques for the study of electrical transport properties in insulating solids ”, *Journal of Non-Crystalline Solids,* **1***,* pp. 197-214, 1968

97 H. Scher, E. Montroll, “Anomalous transit-time dispersion in amorphous solids”, *Physical Review B*, **12**, pp. 2455-77, 1975

98 J. Marshall, “Carrier diffusion in amorphous semiconductors”, *Reports on Progress in Physics*, **46**, pp. 1235-1282, 1983

99 J. Noolandi, “Equivalence of multiple-trapping model and time-dependent random walk”, *Physical Review B*, **16**, pp. 4474-479, 1977

100 F. Schmidlin, “Theory of trap-controlled transient photoconduction”, *Physical Review B*, **16**, pp. 2362-2385, 1977

101 G. Seinhaeve, R. Barclay, G. Adriaenssens, and J. Marshall, "Post transit time-of-flight as a probe of the density of states in hydrogenated amorphous silicon", *Physical Review B*, **39**, pp. 10196-10205, 1989

102 G. Seinhaeve, G. Adriaenssens, H. Michiel, H. Overhof, "Analysis of time-of-flight transit times based on the multiple-trapping model of charge-carrier transport", *Philosophical Magazine B*, **58**, 4, pp. 421-432, 1988

103 J. McWhirter, E. Pike, "On the numerical inversion of the laplace transform and similar Fredholm integral equations of the first kind", *Journal of Physics A: Matematical and General*, **11**, 9, pp. 1729-1745, 1978

104 R. Blakney, H. Grunwald, "Small-signal current transients in insulators with traps", *Physical Review,* **159**, 3, pp. 658-664, 1967

105 C. Main, R. Brüggemann, D. Webb, S. Reynolds, "Determination of gap-state distributions in amorphous semiconductors from transient photocurrents using a fourier transform technique", *Solid State Communications*, **83**, pp. 401-405, 1992

106 C. Main, S. Reynolds, "An enhanced resolution technique for determination of the distribution of localized states in semiconductors from transient photocurrents", *Applied Physics Letters*, **76**, pp. 3085-3087, 2000

107 J. Mort, A. Troup, M. Morgan, S. Grammatica, J.C. Knights, R. Lujan, "Geminate recombination in a-Si:H", *Applied Physics Letters*, **38**, 4, pp. 277-279, 1981

108 S. Kasap, C. Juhasz, "Transient photoconductivity probing of negative bulk space charge evolution in halogenated amorphous selenium films", *Solid State Communications*, **63**, pp. 553-556, 1987

109 K. Dolezalek, W. Spear, "Carrier recombination in orthorhombic sulphur", *Journal of Physics and Chemistry of Solids*, **36**, 7-8 pp. 819-825 ,1975

110 D. Gibbons, W. Spear, "Electron hopping transport and trapping phenomena in orthorhombic sulphur crystals", *Journal of Physics and Chemistry of Solids*, **27,** 11-12, pp. 1917-1925, 1966

111 G. Juska, S. Vengris, K. Arlauskas, "Electron lifetime in amorphous selenium", *Physica Status Solidi A*, **48**, 2, pp. K149-K151, 1978

112 W. Spear, H.L. Steemers, H. Mannsperber, "Carrier lifetimes in amorphous silicon junctions from delayed and interrupted field experiments", *Philosophical Magazine B*, **48**, 5, pp. L49-54, 1983

113 S. Kasap, B. Polischuk, D. Dodds, "An interrupted field time-of-flight (IFTOF) technique in transient photoconductivity measurements", *Review of Scientific Instruments*, **61**, 8, pp. 2080-2087, 1990

114 S. Kasap, R. Thakur, D. Dodds, “Method and apparatus for interrupted transit time transient photoconductivity measurements”, *Journal of Physics E: Scientific Instrumentation*, **21**, pp.1195-1202, 1988

115 W. Helfrich, P. Mark, “Space charge limited currents in anthracine as a means of determining the hole drift mobility”, *Zeitschrift Fur Physik*, **166**, pp. 370-385, 1962

116 B. Polischuk, S.O. Kasap, “A high-voltage interrupted-field time-of-flight transient photoconductivity apparatus”, *Measurement Science & Technology*, **2**, pp. 75-80, 1991

117 B. Fogal, "Electronic Transport Properties of Stabilized Amorphous Selenium X-ray Photoconductors", *MSc Thesis*, University of Saskatchewan, Canada, 2005

118 S. Kasap, V. Ajyah, B. Polischuk, A. Bhattacharyya, Z. Liang, "Deep-trapping kinematics of charge carriers in amorphous semiconductors: a theoretical and experimental study", *Physical Review B*, **43**, pp. 6691-6705, 1991

119 S. Kasap, "Charge-carrier deep-trapping kinetics in high-resistivity semiconductors", *Journal of Physics D: Applied Physics*, **25**, pp. 83-93, 1992

120 M. Tabak, W. Hillegas, "Preparation and transport properties of vacuum evaporated selenium films", *Journal of Vacuum Science and Technology*, **9**, pp. 387-390, 1972

121 S. Kasap, C. Juhasz, "Charge transport in selenium based xerographic photoreceptors", *Photographic Science Engineering*, **26**, 5, pp. 239-244, 1982

122 S. Kasap, B. Polischuk, "Application of the interrupted field time-of-flight transient photoconductivity to investigate sample inhomogeneities: Cl doped amorphous Se:Te and Se:As films", *Canadian Journal of Physics*, **73**, pp. 96-100, 1995

123 C. Juhasz, S. Vaezi-Nejad, S. Kasap, "Electron and hole drift mobility in amorphous selenium based photoreceptors", *Journal of Imaging Science*, **29**, pp. 144-148, 1985

124 S. Kasap, K. Koughia, B. Fogal, G. Belev, R. Johanson, "The influence of deposition conditions and alloying on the electronic properties of amorphous selenium", *Semiconductors*, **37**, 7, pp. 789–794, 2003

125 G. Belev, B. Fogal, K. Koughia, R. Johanson, S. Kasap, "Dependence of charge-carrier ranges in stabilized a-Se on preparation conditions and alloying", *Journal of Material Science: Materials in Electronics*, **14**, pp. 841-842, 2003

126 S. Kasap, in "Handbook of imaging materials", 2nd edition, edited by A. Diamond and D. Weiss, Marcel Dekker, New York, Chapter 9, 2002

127 N. Mott, "Conduction in non-crystalline materials: II. Localized states in a pseudogap and near extremities of conduction and valence Bands", *Philosophical Magazine*, **19**, pp. 835-852, 1969

128 W. Lacourse, V. Twaddell, J. Mackenzie, "Effects of impurities on the electrical conductivity of slassy selenium", *Journal of Non-Crystalline Solids*, **3**, pp. 234-236, 1970

129 V. Twaddell, W. Lacourse, J. Mackenzie, "Impurity effects on the structure and electrical properties of non-crystalline selenium", *Journal of Non-Crystalline Solids*, **8-10**, pp. 831-836, 1972

130 Y. Takasaki, E. Maruyama, T. Uda, T. Hirai, "Molecular doping in a-Se", *Journal of Non-Crystalline Solids*, **59-60**, pp. 949-952, 1983

131 O. Oda, A. Onozuka, I. Tsuboya, "Effects of oxygen on electrophotographic properties of selenium", *Journal of Non-Crystalline Solids*, **83**, pp. 49-62, 1986

132 F. Jansen, "The effects of oxygen and chlorine on the interfacial crystallization of amorphous selenium films", *Journal of Vacuum Science and Technology*, **18**, 2, pp. 215-218, 1981

133 J. Szabo, W. Sears, K. Colbow, "The influence of residual gas on the properties of evaporated selenium films", *Semiconductor Science and Technology*, **5**, pp. 695-701, 1990

134 M. Abkowitz, "Structure and mobility in molecular and atomic glasses", *Annals of New York Academy of Science*, **371**, pp. 170-180, 1981.

135 M. Tabak, W. Hillegas, "Preparation and transport properties of vacuum evaporated selenium films", *Journal o Vacuum Science and Technology*, **9**, 1, pp. 387-390, 1971

136 D. Tonchev, S. Kasap, "Influence of Cl doping on the thermal properties of amorphous Se", *Physics and Chemistry of Glasses*, **43**, 1, pp. 66-71, 2002

137 A. Zyubin, O. Kondakova, S. Dembovsky, "Quantum chemical modeling of chlorine-doped defects in a-Se", *PhysicaB*, **308-310**, pp. 1061-1064, 2001

138 S. Kasap, B. Polischuk, "Application of the interrupted field time-of-flight transient Photoconductivity to Investigate Sample Inhomogeneities: Cl doped amorphous Se:Te and Se:As films", *Canadian Journal of Physics*, **73,** pp. 96-100, 1995

139 S. Vaezi-Nejad, C. Juhasz, "Electrical properties of amorphous semiconductor selenium and its alloys: II. Heterojunction multilayers", *Semiconductor Science and Technology*, **3**, pp. 664-674, 1988

140 V. Illarionov, L. M. Lapina, "The associated states of selenium in the gas phase", *Dokady Akademii Nauk,* **114**, 1021, pp. 615-619, 1957

141 S. Touihri, G. Safoula, J.C. Bernède, "Diode devices based on amorphous selenium films", *Physica Status Solidi A*, **159**, pp. 569-578, 1997

142 J. Bernède, S. Touihri, G. Safoula, "Electrical characteristics of an aluminum/amorphous selenium rectifying contact", *Solid-StateElectronics*, **42**, 10, pp. 1775-1778, 1998

143 E. Montrimas, B. Petrètis, "The structure of vacuum evaporated selenium layers", *Physica Status Solidi A*, **15**, pp. 361-366, 1973

144 J. Hartke, “Drift mobilities of electrons and holes and space-charge-limited currents in amorphous selenium films”, *Physical Review B*, **125**, 4, pp. 1177-1192, 1962

145 H. Lanyon, “Electrical and optical properties of vitreous selenium”, *Physical Review,* **130**, 1, pp. 134-143, 1963

146 G. Pfister, A. Lakatos, “One-carrier and two-carrier steady state space-charge-limited currents in amorphous selenium”, *Physical Review B*, **6**, 8, pp. 3012-3018, 1972

147 A. Rizo, G. Miccocci, A. Tepore, “Space-charge-limited currents in insulators with two sets of traps distributed in energy: theory and experiment”, *Jornal of Applied Physics*, **48**, 8, pp. 3415-3424, 1977

148 L. Müller, M. Müller, “Current-voltage characteristics at high fileds in amorphous selenium thin layers”, *Journal of Non-Crystalline Solids*, **4**, pp. 504-509, 1970

149 A. Sapega, H. Lanyon, “Charge transport through the cadmium-selenium interface”, *Physica Status Solidi A*, **11**, pp. 713-719, 1972

150 F. Kamel, P. Gonon, L. Ortega, F. Jomni, B. Yangui, “Space charge limited transient currents and oxygen vacancy mobility in amorphous $BaTiO_3$ thin films”, *Journal of Applied Physics*, **99**, pp. 094107-1 -094107-5, 2006

151 M. Lampert, P. Mark, “Current injection in solids”, Academic Press, New York and London, Chapter 6, 1970

152 R. Waser, M. Klee, “Theory of conduction and breakdown in perovskite thin films” *Integrated Ferroelectrics*, **2**, 1-4, pp. 23-40, 1992

153 S. Wolters, J. van der Schoot, “Kinetics of charge trapping in dielectrics”, *Journal of Applied Physics*, **58**, pp. 831-837, 1985

154 J. Simmons, G. Taylor, “Dielectric relaxation and its effect on the isothermal electrical characteristics of defect insulators”, *Physical Review B,* **6**, 12, pp. 4793-4802, 1972

155 H. Neumann, G. Arlt, “Maxwell-Wagner relaxation and degradation of $SrTiO_3$ and $BaTiO_3$ ceramics”, *Ferroelectrics*, **69,** pp.179-186 (1986)

156 L. Dissado, R. Hill,” Non-exponential decay in dielectrics and dynamics of correlated systems”, *Nature*, **279**, pp.685-689, 1979

157 C. Haugen, “Charge transport in stabilized a-Se films used in x-ray image detectors”, PhD Thesis, University of Saskatchewan, Canada, 1999

158 B. Fogal, R. Johanson, G. Belev, S. O'Leary, S. Kasap, "X-ray induced effects in stabilized a-Se x-ray photoconductors", *Journal of Non-Crystalline Solids*, **299-302**, pp. 993-997, 2002

159 S. Kasap, "X-ray sensitivity of photoconductors: application to stabilized a-Se", *Journal of Physics D: Applied Physics*, **33**, pp.2853-2865, 2000

160 E. Rhoderick, R. Williams, "Metal-semiconductor contacts", 2nd edition, edited by P. Hammond and R. Grimsdale, Clarendon Press, Oxford, Ch.1, p.48, 1988

161 B. Polischuk, J. Alain, "Method of producing multilayer plate for x-ray imaging", *United States Patent #6 171 643*, January 9, 2001

162 K. Shima, M. Sato, N. Uchida, Y. Shimura, K. Sato, H. Kishimoto, "X-ray detection plate and x-ray detector", United States Patent #6 642 534 B2, November 4, 2003

163 G. Belev, S. Kasap, "Reduction of the dark current in stabilized a-Se based x-ray detectors", *Journal of Non-Crystalline Solids,* **352,** 9-20, pp. 1616-1620, 2006

164 M. Hoheisel, L. Bätz, T. Mertelmeier, J. Giersch, A. Korn, "Modulation transfer function of a selenium-based digital mammography system", *IEEE Transactions on Nuclear Science*, **53**, 3, pp. 1118-1122, 2006

165 P. Monnin, D. Gutierrez, S. Bulling, D. Lepori, J. Valley, F. Verdun, "A comparison of the performance of modern screen-film and digital mammography systems", *Physics in Medicine and Biology*, **50**, pp. 2617-2631, 2005

166 G. Besson, A. Koch, M. Tesic, R. Sottoriva, P. Prieur-Drevron, B. Munier, E. Calais, P. DeGroot, "Design and evaluation of a slot-scanning full-field digital mammography system", *Proceedings of SPIE*, **4682**, pp. 457-468, 2002

167 A. Albanese, A. Bevilacqua, R. Campanini, E. Iampieri, N. Lanconelli, M. Rossi, D. Romani, V. Salomoni, P. Vignoli, "Characterization of an FFDM unit based on a-Se direct conversion detector", *Proceedings of IWDM 2002 Bremen, Germany*, pp. 69-71, 2002

168 G. Belev, S.O. Kasap, "Dark current reduction in metal/a-Se/metal for application as an x-ray photoconductor layer in digital image detectors", *International PCT Patent Application No PCT/CA2006/000004*, international filing date 04/01/2006, priority date 18/01/2005

169 Statscan^{TM} – critical imaging system, 12296 LODOX Inc brochure, downloaded from www.lodox.com/downloads/PDF/StatscanBrochureCom.pdf, August 2005

170 J. Mainprize, N. Ford, S. Yin, T. Tumer, M. Yaffe, "Image quality of a prototype direct conversion detector for digital mammography", *SPIE Medical Imaging Conference Proceeding*, **3659**, pp. 118-127, 1999